

マス・フォア・インダストリ研究 No.5



Mathematical Backgrounds and Future Progress of
Practical Inverse Problems

Institute of Mathematics for Industry
Kyushu University

編集 藤原 宏志
滝口 孝志

九州大学マス・フォア・インダストリ研究所

About the Mathematics for Industry Research

The Mathematics for Industry Research was founded on the occasion of the certification of the Institute of Mathematics for Industry (IMI), established in April 2011, as a MEXT Joint Usage/Research Center – the Joint Research Center for Advanced and Fundamental Mathematics for Industry – by the Ministry of Education, Culture, Sports, Science and Technology (MEXT) in April 2013. This series publishes mainly proceedings of workshops and conferences on Mathematics for Industry (MfI). Each volume includes surveys and reviews of MfI from new viewpoints as well as up-to-date research studies to support the development of MfI.

October 2014

Yasuhide Fukumoto

Director

Institute of Mathematics for Industry

**Mathematical Backgrounds and Future Progress of
Practical Inverse Problems**

Mathematics for Industry Research No.5, Institute of Mathematics for Industry, Kyushu University

ISSN 2188-286X

Editors: Hiroshi Fujiwara, Takashi Takiguchi

Date of issue: 1 March 2016

Publisher:

Institute of Mathematics for Industry, Kyushu University

Motooka 744, Nishi-ku, Fukuoka, 819-0395, JAPAN

Tel +81-(0)92-802-4402, Fax +81-(0)92-802-4405

URL <http://www.imi.kyushu-u.ac.jp/>

Printed by

Social Welfare Service Corporation Fukuoka Colony

1-11-1, Midorigahama, Shingu-machi Kasuya-gun, Fukuoka, 811-0119, Japan

TEL +81-(0)92-962-0764 FAX +81-(0)92-962-0768

Mathematical Backgrounds and Future Progress of

Practical Inverse Problems

Organized by

Hiroshi Fujiwara (Kyoto University)

Takashi Takiguchi (National Defence Academy of Japan)

Preface

Inverse problems have been investigated for a long time. However, depending on our social environments and life styles, their practical demands have been continuously changing; new problems are created day after day. Mathematical science gives a method to understand their structures and requirements systematically. It often reveals relations between different modalities and leads innovations.

This volume contains several recent topics on inverse problems from practical problems to theoretical viewpoints. They were discussed in the conference “Mathematical Backgrounds and Future Progress of Practical Inverse Problems”, which was held at Institute of Mathematics for Industry (IMI) in Kyushu University during 10th–13th, November, 2015.

One of the aims of the conference has been to make an opportunity of collaborative research between two fields; non-destructive testing of concrete structures, and non-invasive diagnostic methods of human bodies. The former arises in civil engineering for safety of our society, and the latter arises in medical science to realize healthy lives.

In particular, we concentrate on the tomographic techniques, which have been recognized as an effective modality in both fields and have been developed independently. Recently, depending on the progress of measurement devices, high-resolution image reconstruction has been expected and various algorithms have been investigated based on experiments in each field. On the other hand, many mathematical methods are studied for tomographic methods involved with electromagnetic phenomenon and acoustic properties. Hence we shall study their backgrounds and experimental methods, and give systematic understanding of their empirical strategies by considering them based on mathematical models.

To this end, we invited researchers and engineers from both companies and universities, and asked them to present not only recent topics, but also fundamental knowledges in each fields. All presentations contains valuable aspects and proposals, and we also found new relations beyond fields and objects throughout the conference. We hope that this volume helps you to understand each research foundation, viewpoints and directions.

Finally we would like to express our sincere thanks to the secretaries of IMI. Without their kind supports, the conference would not have succeeded.

1st, March, 2016.

Hiroshi Fujiwara (Kyoto University)

Takashi Takiguchi (National Defence Academy of Japan)

Mathematical Backgrounds and Future Progress of Practical Inverse Problems

November 10–13, 2015

Lecture Room M W1-C-513, West Zone 1, Ito Campus,
Institute of Mathematics for Industry, Kyushu University
744 Motooka Nishi-ku Fukuoka 819-0395, Japan

November, 10th (Tue.)

- | | |
|-------------|---|
| 13:20 | Opening |
| 13:30–14:30 | Kenji Hashizume (West Nippon Expressway Shikoku Company Limited)
Inspection of bridges, tunnels, and pavement by using cameras |
| 14:30–15:00 | Discussion |
| 15:00–16:00 | Takashi Ohe (Okayama University of Science)
Reconstruction of slowly-moving dipole wave sources from boundary observations |
| 16:00–16:30 | Discussion |

November, 11th (Wed.)

- | | |
|-------------|--|
| 10:30–11:30 | Naoya Oishi (Kyoto University)
Inverse problems in emission tomography |
| 11:30–12:00 | Discussion |
| 13:00–14:00 | Shinpei Okawa, Takeshi Hirasawa, Toshihiro Kushibiki and Miya Ishihara
(National Defense Medical College)
Numerical and experimental studies on quantification of the optical properties by use of photoacoustic measurement |
| 14:00–14:30 | Discussion |
| 14:30–15:30 | Kuo-Ming Lee (National Cheng Kung University)
Integral equations method in inverse problem |
| 15:30–16:00 | Discussion |

12 November (Thu.)

- 10:30–11:30 Alexandru C. Tamasan (University of Central Florida)
Current density based impedance imaging from minimal data
- 11:30–12:00 Discussion
- 13:00–14:00 Takeaki Shimokawa (ATR)
Hierarchical Bayesian estimation method for diffuse optical tomography
- 14:00–14:30 Discussion
- 14:30–15:30 Gentarō Taga (The University of Tokyo)
Phase dynamics of spontaneous activity in the cerebrovascular system of human infants
- 15:30–16:00 Discussion

13 November (Fri.)

- 10:30–11:30 Noriyuki Mita (Polytechnic University of Japan) and Takashi Takiguchi (National Defense Academy of Japan)
Development of ultrasonic tomography for concrete structures
- 11:30–12:00 Discussion
- 12:00 Closing

Organizers : Hiroshi Fujiwara (Kyoto University) and Takashi Takiguchi (National Defense Academy of Japan)

The workshop is supported by IMI (Kyushu University), and partially supported by JSPS Grant-in-Aid for Scientific Research (C) (No.26400198), (C) (No.26400184).

Table of Contents

Inspection of bridges, tunnels, and pavement by using cameras ······	1
<i>Kenji Hashizume</i>	
Reconstruction of slowly-moving dipole wave sources from boundary observations ······	27
<i>Takashi Ohe</i>	
Inverse problems in emission tomography ······	55
<i>Naoya Oishi</i>	
Numerical and experimental studies on quantification of the optical properties by use of photoacoustic measurement ······	81
<i>Shinpei Okawa, Takashi Hirasawa, Toshihiro Kushibiki, and Miya Ishihara</i>	
Integral equations method in inverse problem ······	111
<i>Kuo-Ming Lee</i>	
On current density based impedance imaging from minimal data ······	145
<i>Alexandru Tamasan</i>	
Hierarchical Bayesian estimation method for diffuse optical tomography ···	181
<i>Takeaki Shimokawa</i>	
Phase dynamics of spontaneous activity in the cerebrovascular system of human infants ······	203
<i>Gentaro Taga</i>	
Development of ultrasonic tomography for concrete structures ······	205
<i>Noriyuki Mita and Takashi Takiguchi</i>	

Inspection of bridges, tunnels, and pavement by using cameras

Kenji Hashizume

West Nippon Expressway Shikoku Company Limited

I. Outline

A lot of resources and costs would be necessary for infrastructure developments and rehabilitations. So the followings are very important: (i) managing, repairing, and renewing the developed infrastructures efficiently and effectively, and (ii) eliminating serious accidents triggered by the deteriorations and damages, and realizing the society without any anxiety. This is necessary for the utilization of the limited resources and the sustainable development of the society. For the given purpose, the efficient and effective inspections and maintenance practice shall be necessary. The inspection method using cameras for the bridges, tunnels, and pavements inspections with objective evaluations and keeping their records is now proposed.

II. Bridge Inspections

We now explain the “J-System” (Figure-1) for the inspection method using the infrared cameras.

The reinforced concrete fulfill its role with the joint functioning of rebar and concrete for the concrete structure. When the rebar gathers rust in the concrete, cracks appear on the concrete surface along the rebar, the surface concrete spalls, and so its durability is to be reduced. We have been inspecting the cracks triggered by the concrete delaminations along the rebar through the hammering. The infrared cameras inspection is the new one detecting the damaged areas such as concrete delaminations and cracks through photographing the concrete surface by using infrared cameras from remote palaces, and keeping the records of the concrete surface conditions using digital cameras. The inspections of bridges surface by infrared cameras are done by the passive method, and the followings are the important elements;



figure -1 J-system

i. Cameras Quality (Is the cameras suitable for the inspection environment?)

Inspections are done basically during night, so it is important to extend the surveillance hours of the day and increase the annual surveillance days by using the camera with a short- wave type which has no the environmental reflections during night and with a enforcing-cooling- system type with a small thermal resolution.

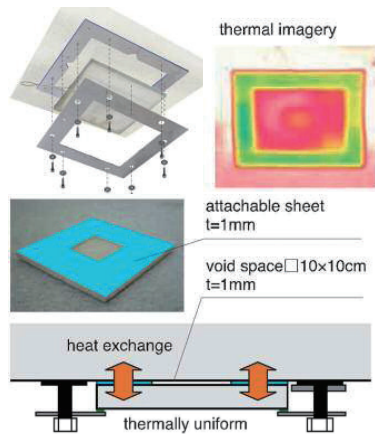


figure -2 J-system EM(S)

ii. judgment on time zone of the day when inspections can be done (Do we inspect at a suitable time ?)

We implement the night- time inspection basically, because there are various bridge types and bridge members which are not suitable to inspect during daytime. The time zone of the day when inspection is possible is based on data of the EMS (Environment Measuring System)(Figure-2) mounted on the inspection bridges.

iii. Simple and Objective Evaluation Method (Is it possible and easy to evaluate objectively?)

There could be, for individuals, differences among the inspection judgments because it is sometime impossible to judge the damage evaluation such as delamination and spalling for the bridge members and damaged parts only by looking at the infrared images. It is also impossible to judge the crack's depth along the rebar. However, the red, yellow, and blue cracks' judgment- images at the 1, 2, 3 cm depth from the surface are shown at the camera monitor (Figure -3).


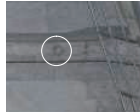
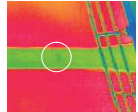
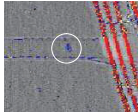


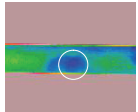
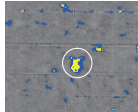


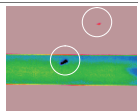
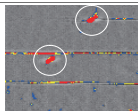
Damage grade	Visible image	Infrared image	3 level indication
Observation Abnormal sound 			
Caution Possibility of falling down near future 			
Warning Require emergency measure 			

figure -3 J-System Monitor Image

III. Tunnel and Pavement Inspection

We now explain the “L & L System” (Figure-4) inspection method which uses the Line Censor Camera and Laser Marker. Line Censor cameras mount the visual image sensors, and can photograph seamless and continuous imageries. They can also be applied for the tunnel and pavement inspections. Light Cutting method is photographing the laser marker images from a upper and oblique position by using the laser which is irradiated vertically down on measuring surfaces and obtain the object shape. This method is used for road surface profile measuring.



figure -4 L&L System

i. Tunnel Inspection

It is possible to obtain the fine and colorful continuous images (Figure-5) of tunnel lining by using Line Censor cameras mounted on the inspection cars with high speed (less than 100km/h). The cracks of tunnel lining can be detected up to 0.2mm, and water leakage and lime isolation can be also found. The damage spreading drawings and their diagonal charts can easily be produced based on the captive pictures, and so we inspect only the areas where further close and detail investigations are necessary. And we can clearly watch the conditions of rusted accessories in tunnels, and so it is now possible to apply them for the accessories inspections.

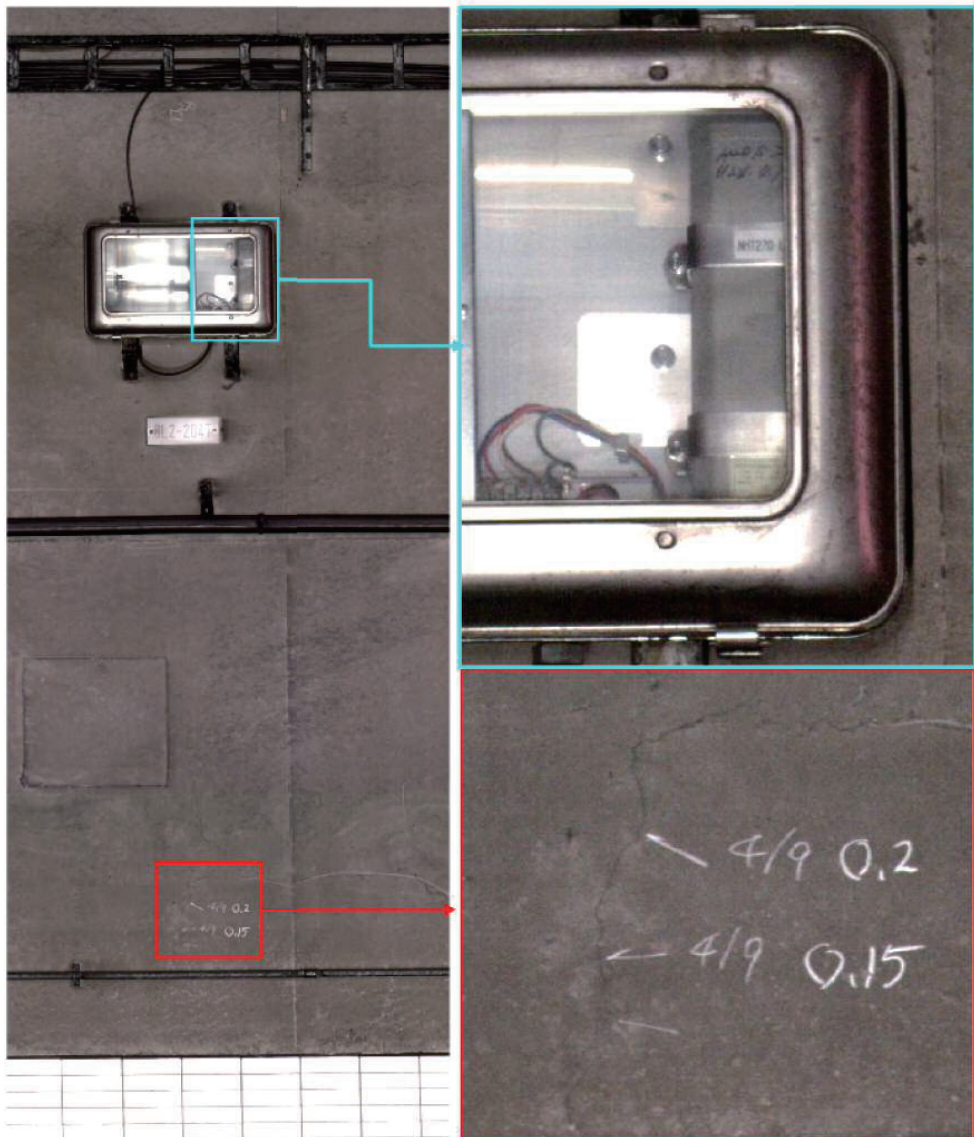


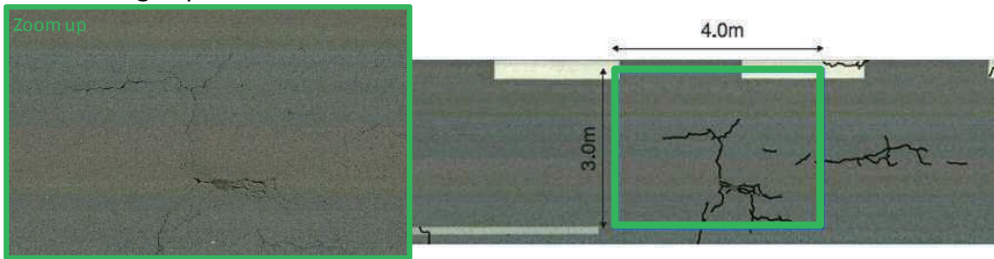
figure -5 Visual image with cracks and the accessories

ii. Pavement Inspection

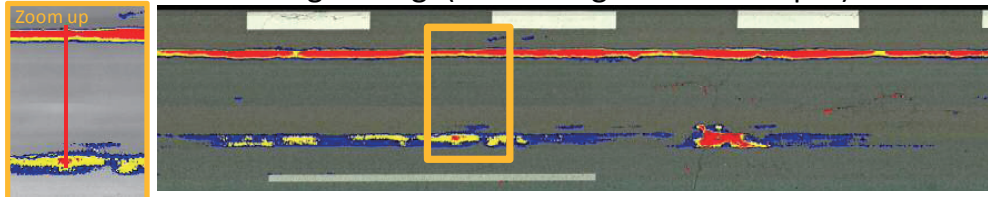
We can inspect the pavement conditions such as cracks and potholes, and conditions of bridge expansion joints by using Line Censer cameras mounted on the vehicle with high speed (less than 100km/h). At the same time, we can also measure rutting, bumps, and upheaval through using laser cameras, and measure road surface profile such as height, and also evaluate the evenness, bump and IRI values.

We can also display the grade evaluation for the cracks, rutting, bumps, evenness, and IRI values obtained by the road surface measurements, and we can also easily sort and extract some of the data with abnormal ranges which show more than a certain threshold (Figure-6). Thus, the repairing and renewal plans of road pavement and the bumps will be made easier.

Visual image (pavement)



Processed surface height image (red: rutting 10mm or deeper)



Transversal cross section (Left red line) Cracks can be detected as a difference of height.

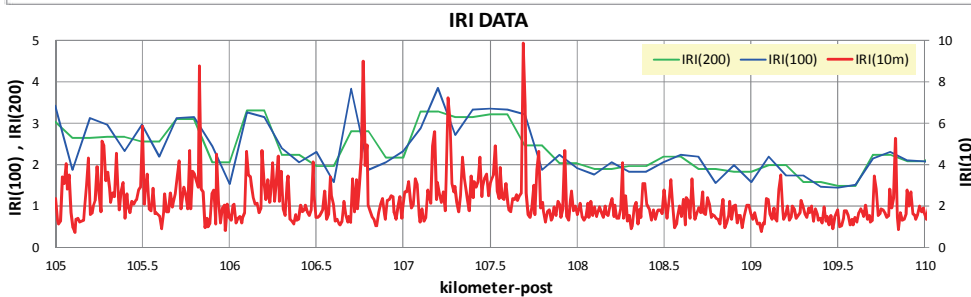
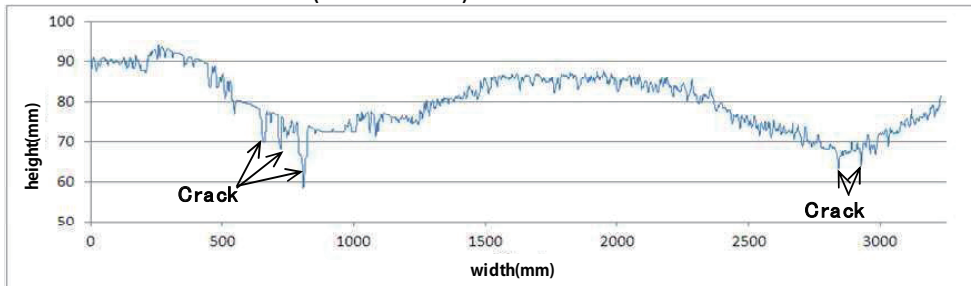


figure -6 Pavement evaluation

Also, we can measure the inner damages such as layer delamination and cracks of pavement by using infrared cameras (Figure-7).

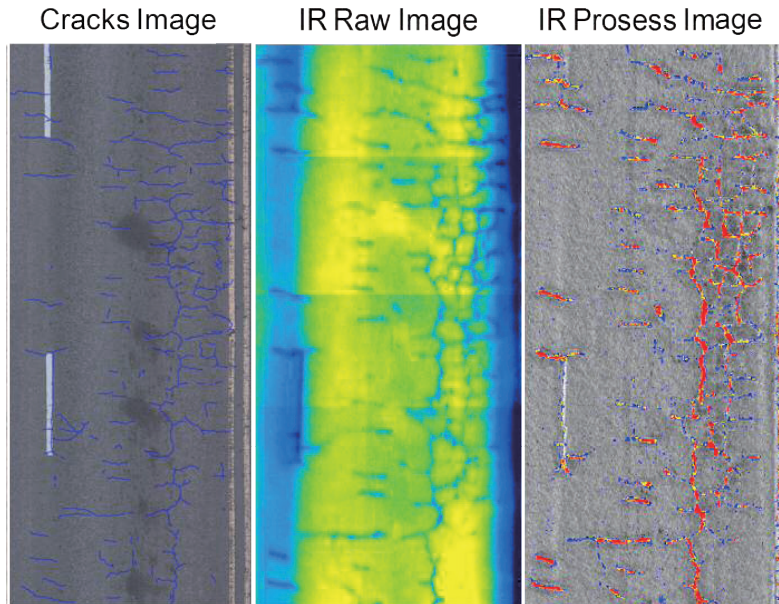


figure -7 Pavement IR evaluation

IV. Conclusion

The bridges, tunnels, and pavement inspections by cameras can be used for the assistances for the on-site inspections or their alternatives, and we can maintain the objective evaluations and predict the future damages through their annual transitions. Also the repairing plan can be made easily and efficiently.

The proposed inspection method using the cameras makes it possible to use, select and combine those inspection tools economically and effectively in accordance with budgets and utilizations patterns of each organization based on their different road structure maintenance and repairing standards.

Inspection of bridges, tunnels, and pavement by using cameras



West Nippon Expressway Shikoku Company Limited.

Contents

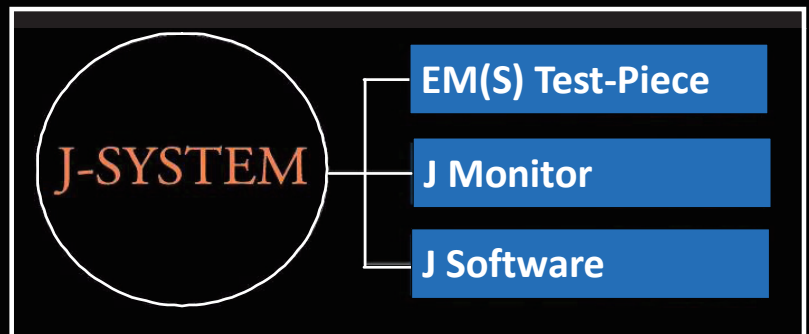
- I . Approach and issues for preventing concrete accident flaking
 - I -1. Bridge
 - (reinforced concrete structure)
 - I -2. Tunnel
 - (unreinforced concrete structure)
- II . Approach and issues for identity of pavement damages



J -SYSTEM



A new concrete inspection and assessment method with safer manipulating, higher performance, and lower cost based on infrared thermography technology.

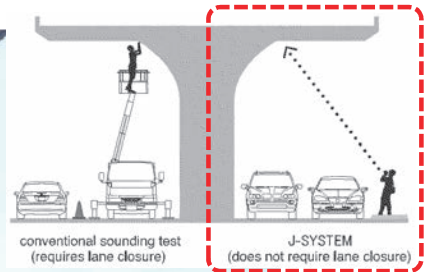


Sounding inspection for prevention measure against flaking



Present method needs a lot of costs and time

Infrared inspection situation



Visible image camera

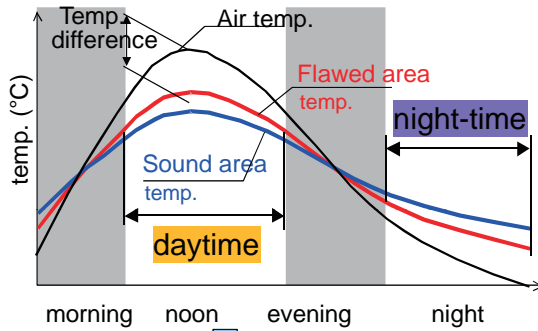
Monitor

Infrared camera

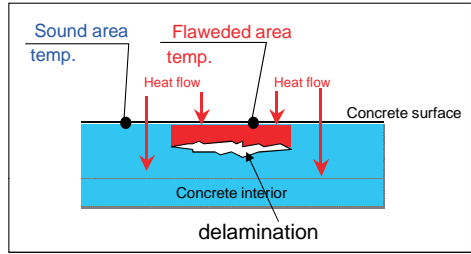
Battery

Basic Theory of Infrared Thermography

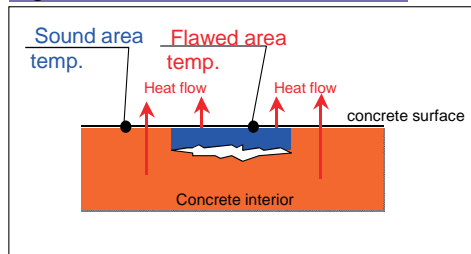
Inspection must be done when the temperature difference between air and concrete is large enough.



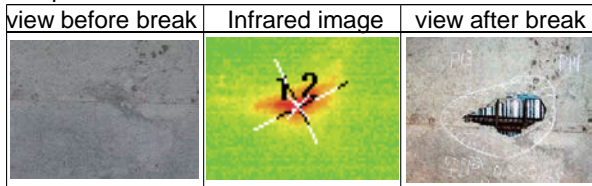
daytime : sound < flawed < air



night-time : sound > flawed > air



Temp. differences creates thermal anomalies



Relationship between Inspection time, and bridge type or part

Direction of heat flow and temperature in damage part

Section	Surface to be inspected	Direct effect	Indirect effect
All bridges			
Metal bridge		Surface to be inspected is not directly exposed to sunlight	
Box beam bridge		Surface to be inspected is not directly exposed to sunlight	

Inspection time should be selected by bridge type or part

Inspection time period of each bridge type

Seto Inland Sea climate during summer/autumn

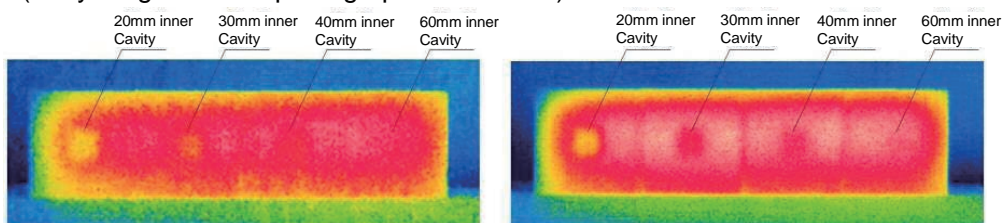
Inspection time period

Bridge type	Section	Time											
		6	8	10	12	14	16	18	20	22	24	2	4
All bridges	Wall balustrade		█	█	█			█	█	█	█	█	█
RC bridge	Overhang									█	█	█	█
	Floor slab			█	█	█	█				█	█	█
Me bridge	Overhang	█								█	█	█	█
	Floor slab	█								█	█	█	█
Box beam bridge	Overhang	█								█	█	█	█
	Floor slab										█	█	█
PC bridge	Overhang	█								█	█	█	█
	Girder			█	█	█	█				█	█	█
	Floor slab	█								█	█	█	█

Almost all bridge types and bridge sections can be investigated during night time.

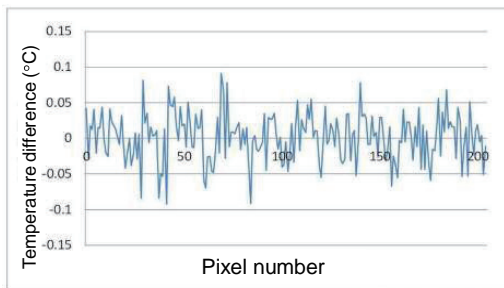
Images of damage from different minimum detected temperatures

Thermal images of different minimum detected temperatures (NETD)
(Daily range = 10°C: photographed at 0 a.m.)

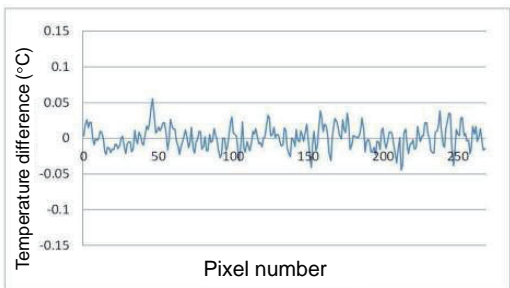


a) Thermal image photographed by Camera A

b) Thermal image photographed by Camera B



a) Temperature variation of Camera A

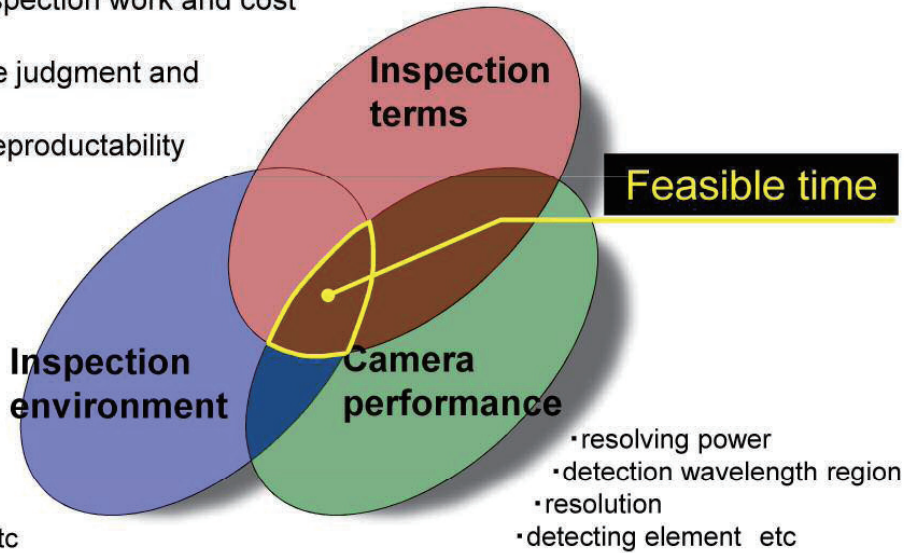


b) Temperature variation of Camera B

Issues for accurate infrared inspection

- clarification of inspection depth
- quality guarantee and prevention of missing damage
- high efficient inspection work and cost performance
- efficient damage judgment and objectivity
- recording and reproductability

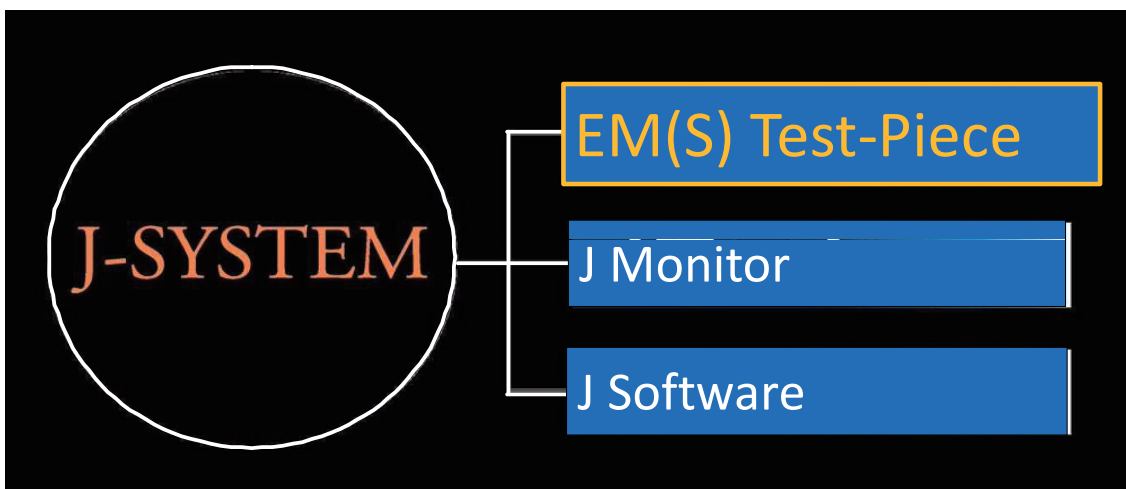
- kind of bridge, part
- detection depth
- photographing distance etc



- daily range
- solar radiation
- wind and rain etc

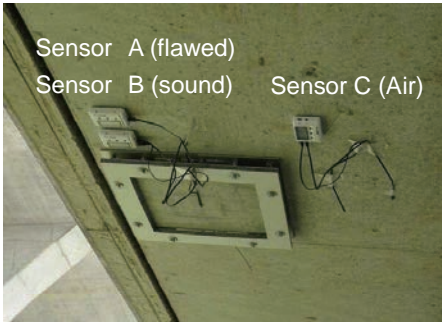
- resolving power
- detection wavelength region
- resolution
- detecting element etc

EM(S): On-the-spot Test Piece

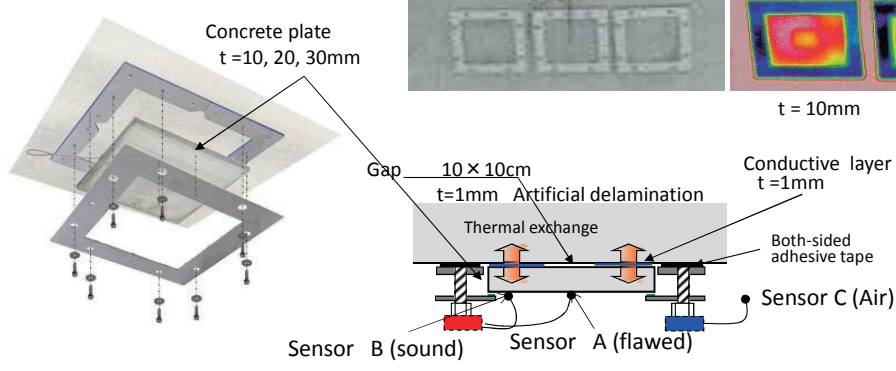
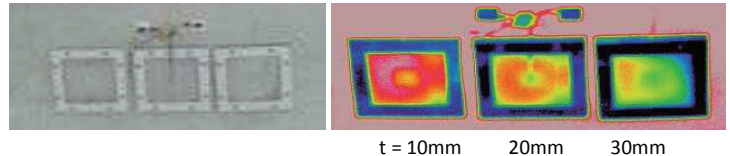
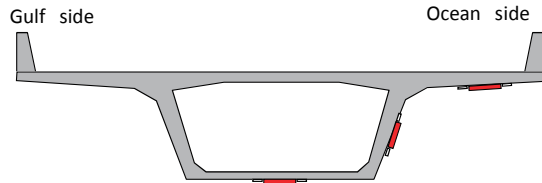


To ensure thermal condition of real structure for infrared testing before and during infrared inspection

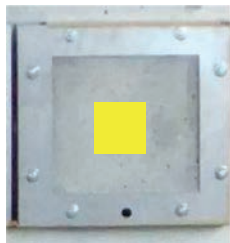
EM(S) : On-the-spot Test-Piece



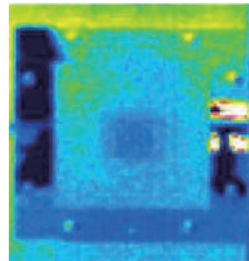
To obtain real temperature data under actual conditions element by element



Do we inspect at a suitable time ?

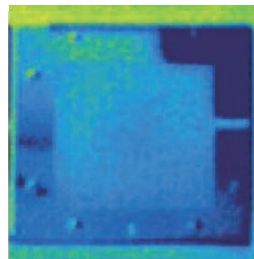


EM(S)



IR Image
Central cavity is observed.
⇒ OK

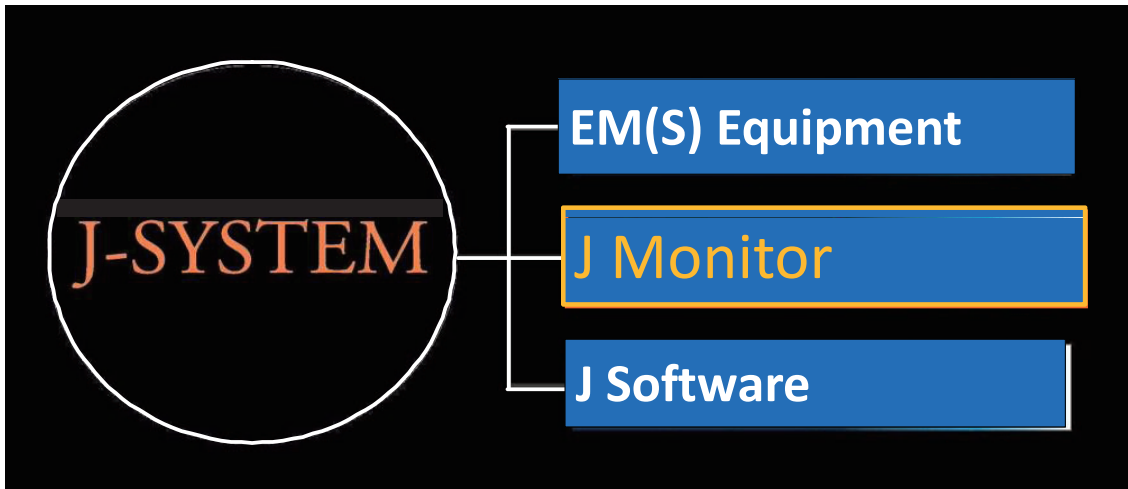
Checking central Void



IR Image
Cavity is not observed.
⇒ NG

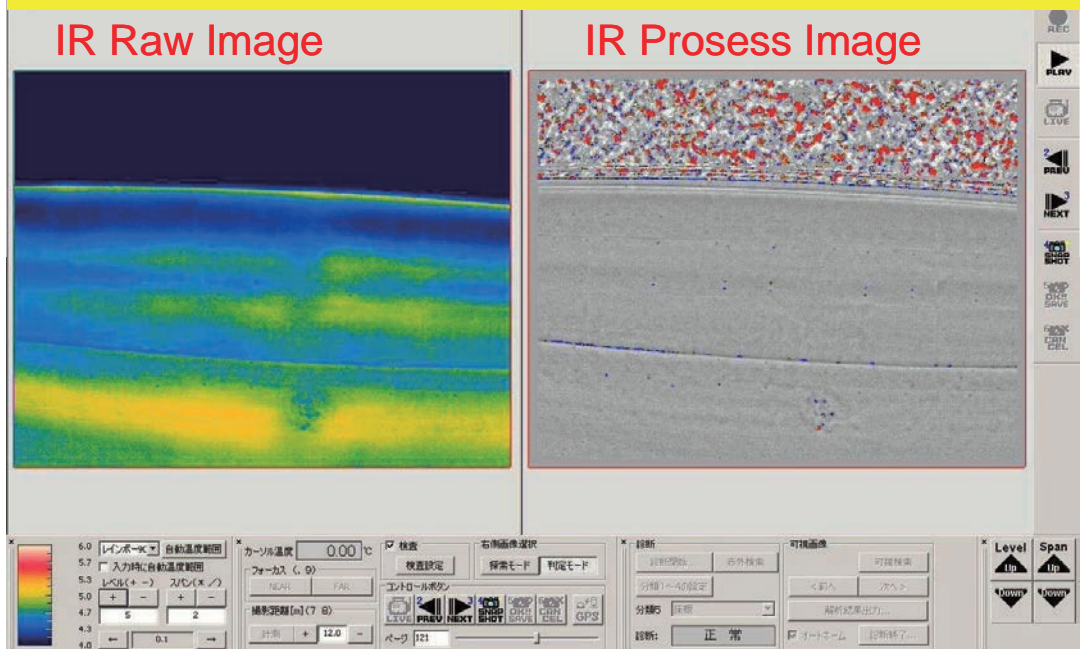
The thermal environment should be precisely obtained by an EM(S) device before any investigation

J Monitor : A Display for IR images in Real Time



J Monitor

J Monitor



J Software: Infrared Image Processing Software

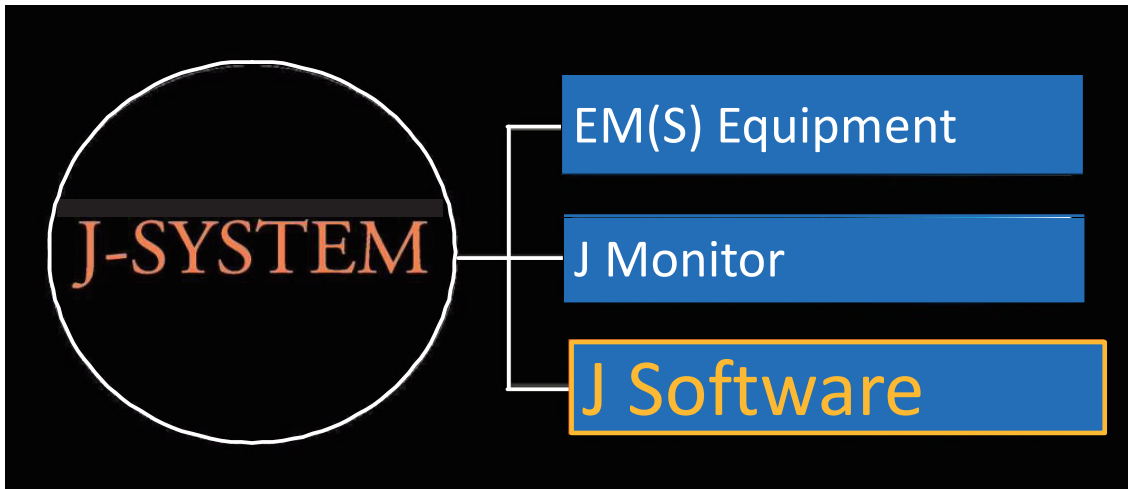
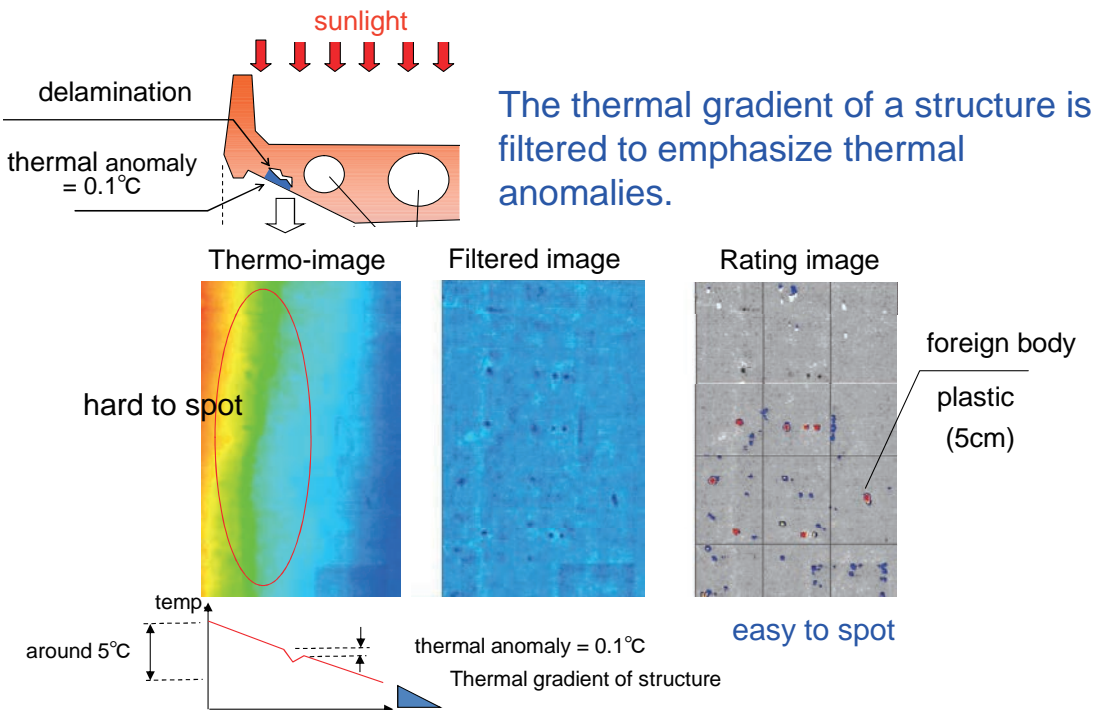


Image Emphasizing Thermal Anomalies



J Software: Damage Ratings

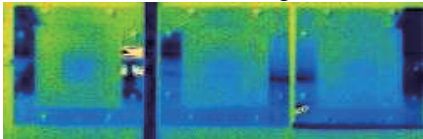
Temperature distribution is interpreted into damage ratings by using a comprehensive database of temperature patterns.

Visible image: EM(S) test-piece



1cm 2cm 3cm

IR raw image



IR Process image

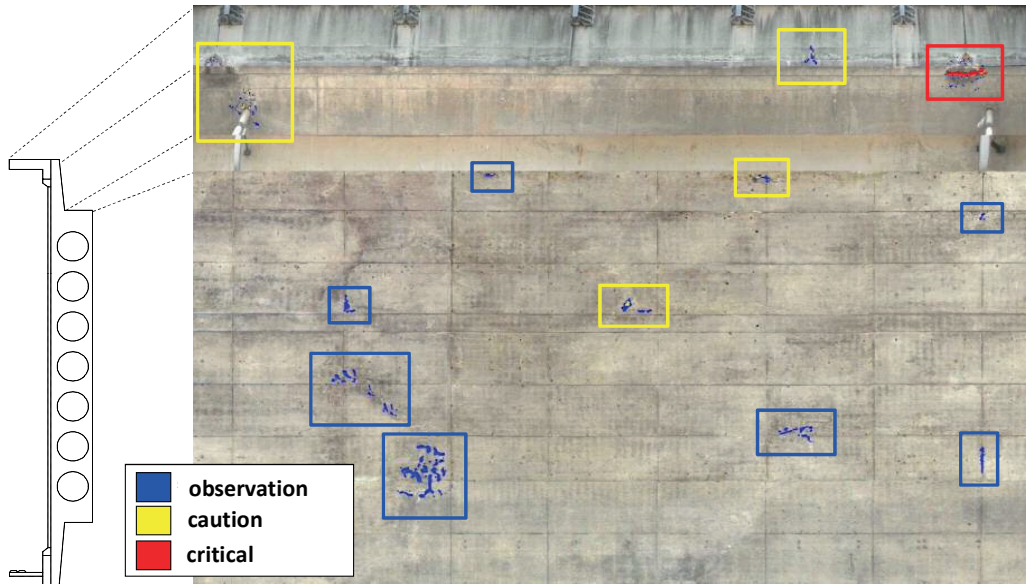


Damage level	
Damage pattern	indication
	<p>Observation (Insignificant)</p>
	<p>Caution</p>
	<p>Critical Emergency measures required</p>

Comparison Between New and Conventional



Is it possible and easy to evaluate objectively?



Your resources can be focused on the areas that need the most work.

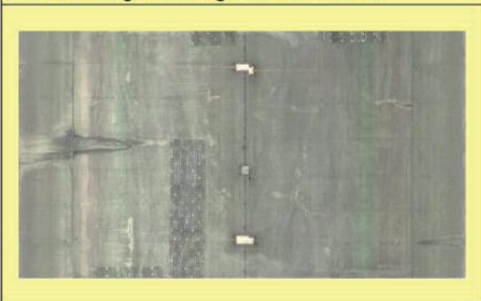
Tunnel Inspection

Flow chart for tunnel inspection

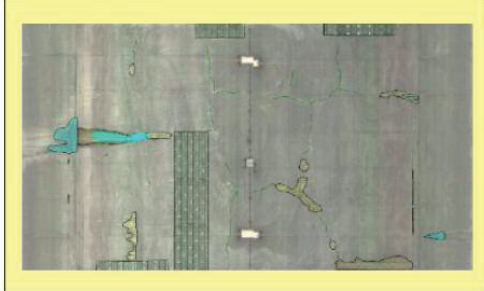
I . The captured image of the tunnel



II . Creating an image of the tunnel



III . Analyzing



IV . Inspection

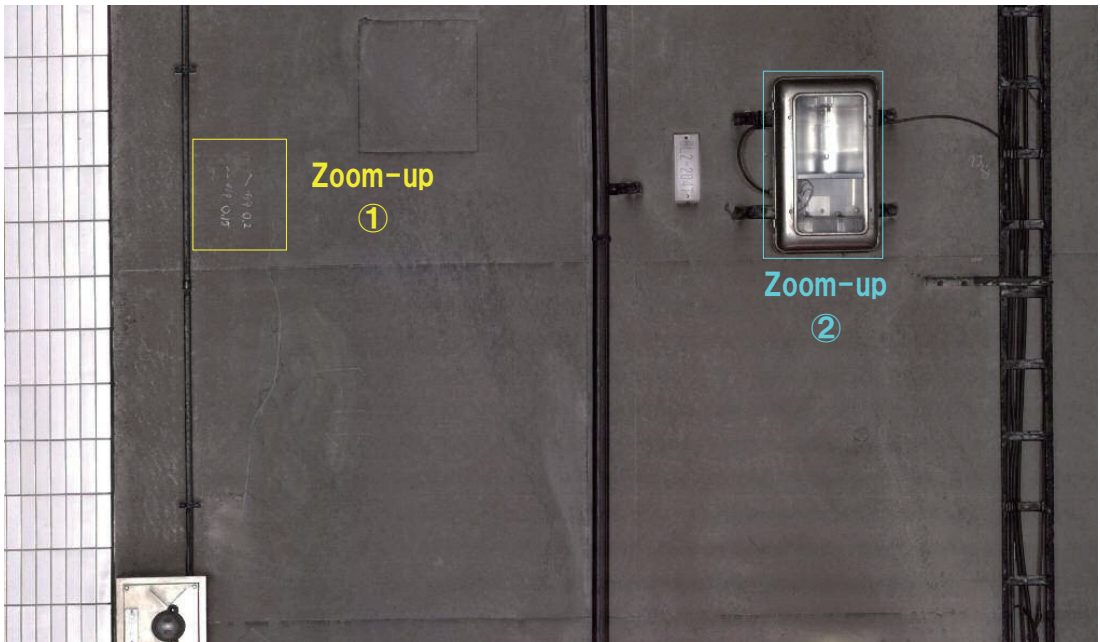


Investigation of cracking and other damages

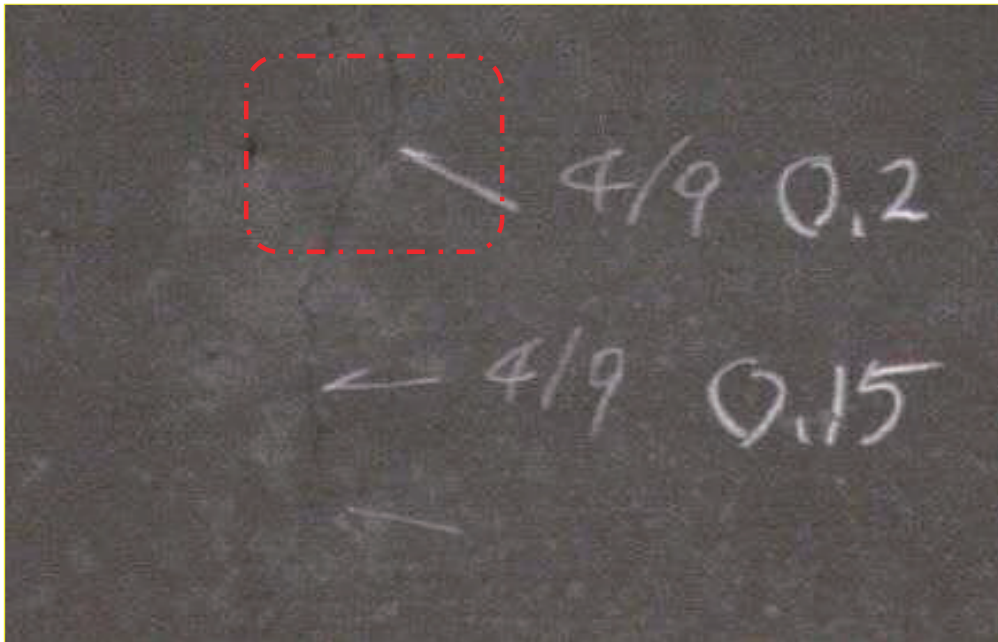


- The width, length, and number of cracks, efflorescence, and water leakage can be investigated with high precision.
- Color images allow the inspection of corrosion and damage to the accessories attached to the tunnel lining.
- High-precision photography/analysis enables a comparison between the previous investigation and the current damage progress.

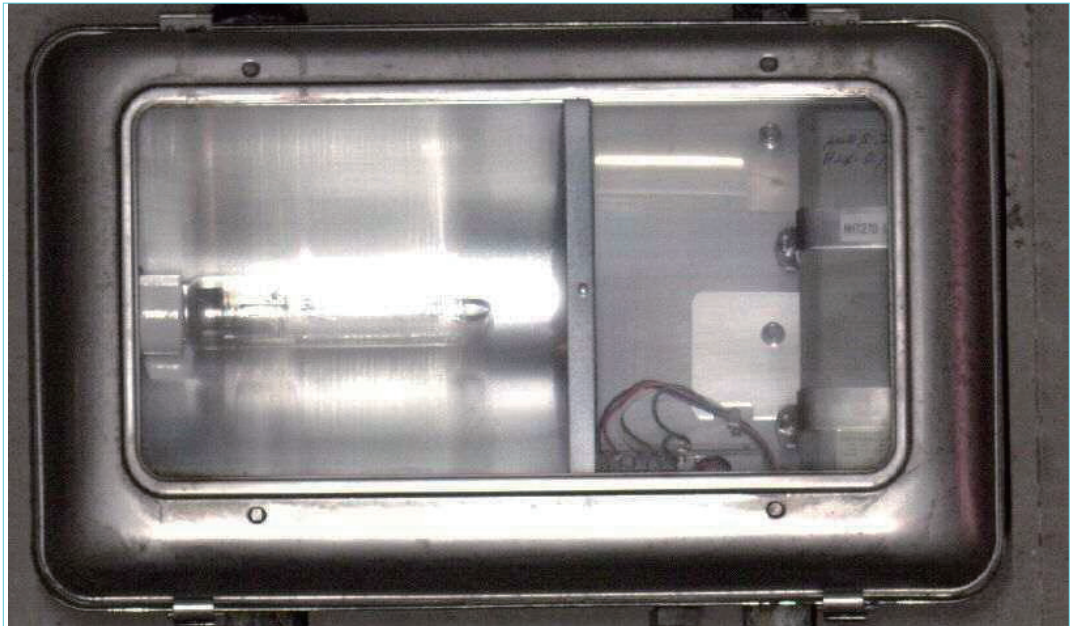
Visual image (tunnel)



Zoom-up visual image (Cracks)



Zoom-up visual image (tunnel lighting)



Pavement Inspection

Data Acquisition by Periodic Inspection

Road Surface Measurement (3 Elements)

Company-owned
vehicle



Cracks



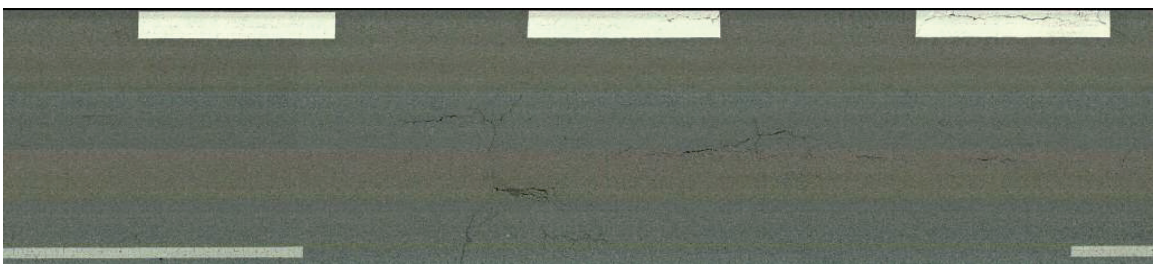
Ruts



Flatness



Visual image (pavement)



Accuracy at a speed of 100km/h

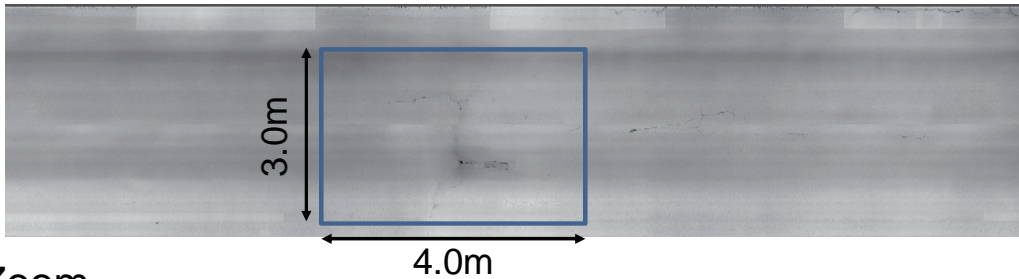
~ Detecting cracks ~

Shooting width=4.5m(Color image)

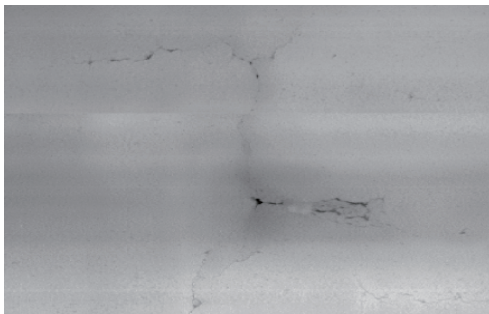
Resolution 0.8mm x 0.8mm/pixel

Height image

Surface height image



Zoom



Accuracy at a speed of 100km/h

~Rutting Measurement~

Shooting width=4.4m

Dimension of rutting:1mm or less

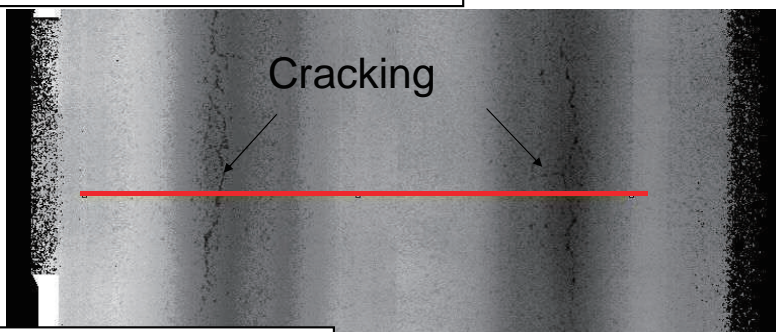
Resolution 1.68mm(Transversal)

5.60mm (Longitudinal)

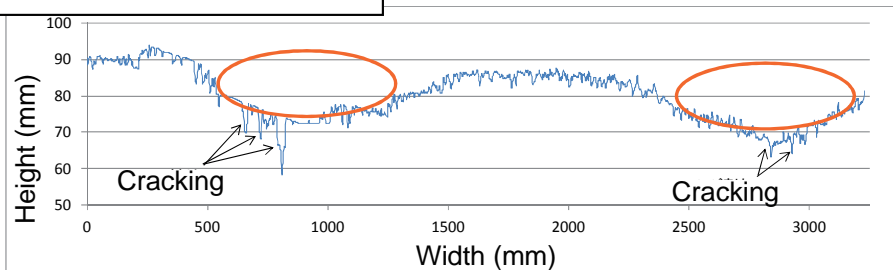
0.50mm (Depth)

Ruts

Height image (Black part is low.)

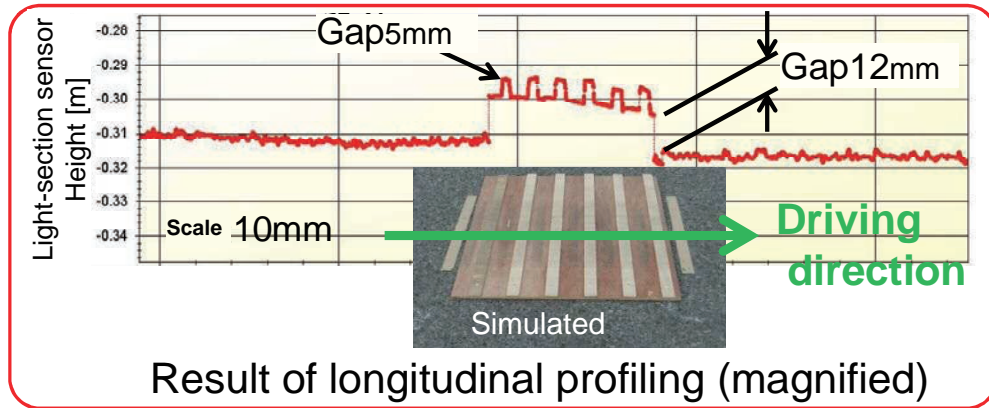
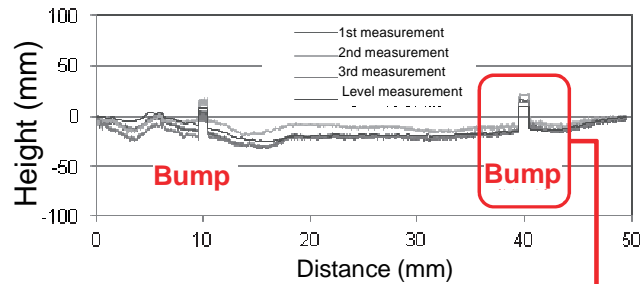


Ruts on the red line above



Flatness (Longitudinal profiling)

High-resolution allows us to accurately profile the longitudinal shape of a microscopic bump.



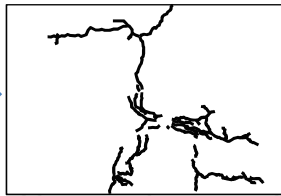
Pavement analyzing
To suggest a new
pavement evaluation

Bumps Analyzing

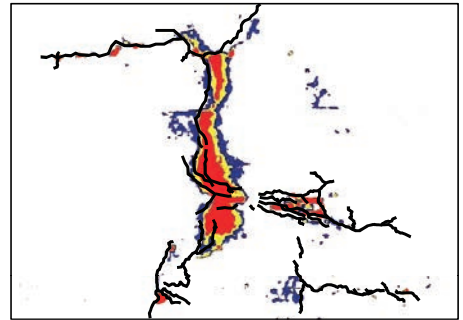
Detecting cracks Abstracting cracks from visual image



Visual image

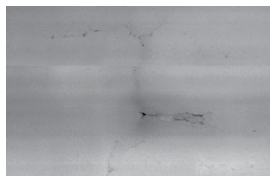


Abstracting crack image

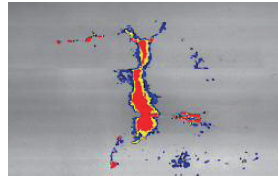


Crack+Processed image (red:bumps 5mm or deeper)

Detecting rutting Abstracting rutting from visual image



Surface height image

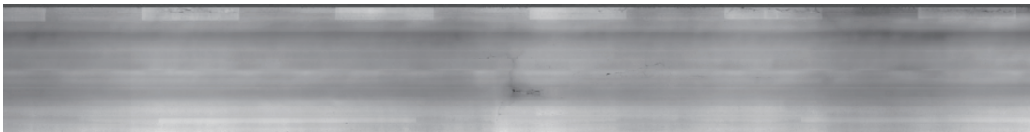


Processed surface height image

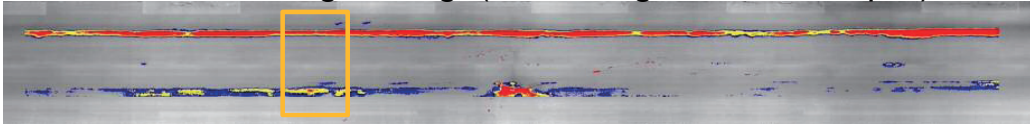
Depth of a rutting is contrasted through special software, called J-soft.

Rutting Area Analysing

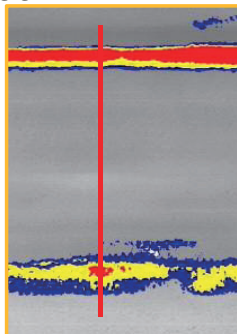
Surface height image



Processed surface height image (red: rutting 10mm or deeper)

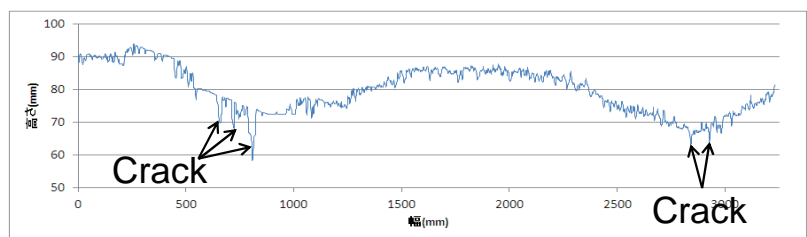


Zoom

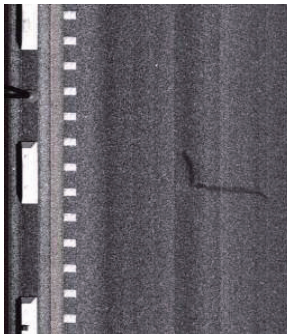


Transversal cross section (Left red line)

Cracks can be detected as a difference of height.



New proposal using image analysis (Blistering)



Visible image

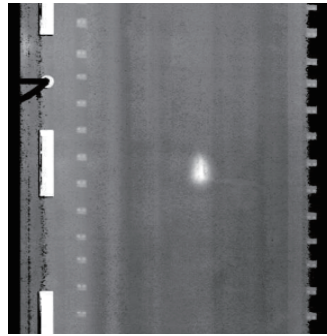
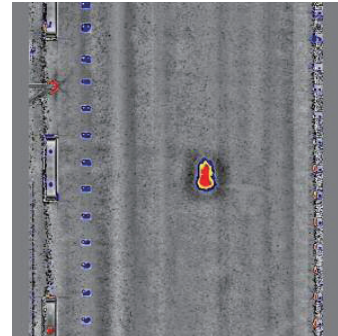
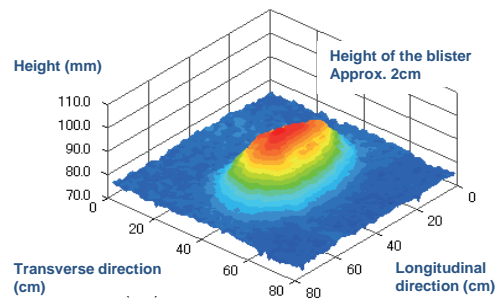


Image of road surface height



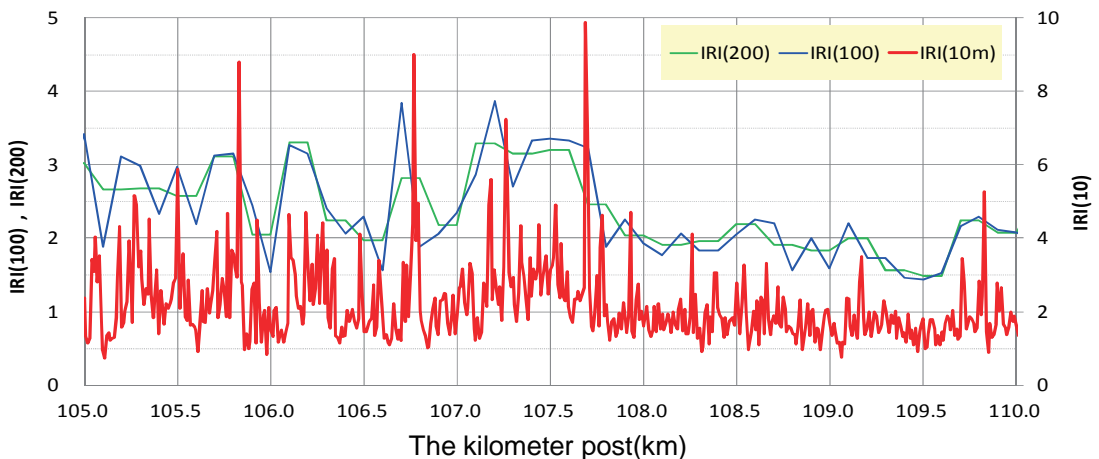
Analyzed image

The form of partial damage such as blistering can be replicated.



Analyzing highly accurate longitudinal profile

Future: IRI can be measured thanks to no speed dependanc



Reconstruction of slowly-moving dipole wave sources from boundary observations

Takashi Ohe

Department of Applied Mathematics, Faculty of Science, Okayama University of Science
e-mail: ohe@xmath.ous.ac.jp

Abstract

Inverse source problem is an important mathematical model of many problems in science, engineering, and medical fields. In this talk, we consider an inverse source problem for three dimensional wave equation, and discuss a reconstruction procedure for wave sources. In general, uniqueness of the solution of inverse source problem is not guaranteed, and so some *a priori* conditions are imposed for sources, for examples, point sources, dipole sources. Here, we assume that the wave source is expressed by a linear combination of some dipole sources, and they moves slowly relative to the wave propagation speed. Under these assumptions, we consider a problem to reconstruct the number, locations, and moments of dipole sources from boundary observations.

For this problem, we apply a technique based on the reciprocity gap functional. The reciprocity gap functional is widely used for various inverse problems. We use the same kind of reciprocity gap functionals used in the reconstruction of point sources[19], and propose a reconstruction procedure for the number, locations, and moments of unknown dipole sources. We show the effectiveness of our method by some numerical examples. We also show some open problems in the reconstruction procedure, and discuss further possibilities of our method.

1 Introduction

Inverse source problem is one of important problems in mathematical sciences for its wide applications in science, engineering fields[9, 10, 13, 15, 22, 23, 24]. Especially, inverse source problem for wave equation has many important applications such as passive sonars, estimation of seismic source, and so on[1, 4]. In this report, we discuss an inverse source problem for scalar wave equation in a three dimensional domain.

We show the formulation of our inverse problem. Let Ω be a bounded domain in \mathbb{R}^3 with smooth boundary Γ . Let $u(\mathbf{r}, t)$ be the solution of initial- and boundary-value problem of the scalar wave equation:

$$\left\{ \begin{array}{ll} \frac{1}{c^2} \frac{\partial^2 u}{\partial t^2}(\mathbf{r}, t) - \Delta u(\mathbf{r}, t) = F(\mathbf{r}, t), & (\mathbf{r}, t) \in \Omega \times (0, T), \\ u(\mathbf{r}, t) = 0, & (\mathbf{r}, t) \in \Gamma \times (0, T), \\ u(\mathbf{r}, 0) = 0, & \mathbf{r} \in \Omega, \\ \frac{\partial u}{\partial t}(\mathbf{r}, 0) = 0, & \mathbf{r} \in \Omega, \end{array} \right. \quad (1)$$

where $c > 0$ and $T > 2 \cdot \text{diag}\Omega > 0$ are given constants, and $F(\mathbf{r}, t)$ is the source term defined in $\Omega \times (0, T)$. Suppose that $F(\mathbf{r}, t)$ is unknown, and consider the problem to reconstruct it from observations of the normal derivative $\phi = \frac{\partial u}{\partial \nu}$ on $\Gamma \times (0, T)$. This problem is called an *inverse source problem for scalar wave equation*.

Unfortunately, uniqueness of the solution of this inverse problem is not guaranteed in general. Therefore we usually set some assumptions and restrictions for the source term. The point source model is one of popular models that guarantee the uniqueness of the solution of inverse problems, and widely discussed in theoretical and numerical points of views[5, 7, 8, 11, 12, 16, 18, 19]. The point source model is represented by three kind of parameters, the number of point sources K , location $\mathbf{p}_k(t)$ and magnitude $\lambda_k(t)$ of each point source as follows:

$$F(\mathbf{r}, t) = \sum_{k=1}^K \lambda_k(t) \delta(\mathbf{r} - \mathbf{p}_k(t)), \quad (2)$$

where δ denotes the Dirac's delta distribution. Therefore, for point mass model, the problem is reduced to reconstruct these parameters from observation ϕ .

Reconstruction methods, specifically in numerical reconstruction methods, can be classified into two categories, one is an iterative method, and the other is a non-iterative method. Comparing iterative and non-iterative methods, the later has an advantage in the necessary computation resources since we need not to solve the partial differential equation.

In non-iterative reconstruction methods, some papers discussed algebraic method based on the reciprocity gap functional. The reciprocity gap functional is widely used for various inverse problems[2, 3, 6, 7, 8]. We also discussed some inverse problems based on the reciprocity gap functional[18, 19, 20].

In practical applications, point source model describes non-directional sources. However, in the real world, there are many kind of sources that have directional property, such as dipole antenna, audio speaker, and so on[1, 4, 8, 14, 17, 21]. One mathematical model for such kind of sources is the dipole source model that is expressed by

$$F(\mathbf{r}, t) = \sum_{k=1}^K \mathbf{m}_k(t) \cdot \nabla_{\mathbf{r}} \delta(\mathbf{r} - \mathbf{p}_k(t)), \quad (3)$$

where K denotes the number of dipole sources, $\mathbf{p}_k(t) = (p_{k,x}(t), p_{k,y}(t), p_{k,z}(t))$ the location of k -th dipole source, and $\mathbf{m}_k(t) = (m_{k,x}(t), m_{k,y}(t), m_{k,z}(t))$ the dipole moment that expresses the direction of k -th sources. Then, our problem is to reconstruct these parameters from observations ϕ on Γ . In Figure 1, we illustrate the situation our problem. The main interest of this report is to develop the algebraic reconstruction method for dipole sources based on the reciprocity gap.

2 Reconstruction of wave sources

2.1 Reciprocity gap functional

We first explain what the reciprocity gap functional for scalar wave equation is. The reciprocity gap functional is base on the weak formulation of the partial differential equation. The weak form of the initial- and boundary value problem of the scalar wave equation (1) is expressed as to find a function $u \in C^1((0, T); L^2(\Omega))$ that satisfies

$$\begin{aligned} & \frac{1}{c^2} \int_{\Omega} \frac{\partial u}{\partial t}(\mathbf{r}, T) v(\mathbf{r}, T) dV(\mathbf{r}) - \frac{1}{c^2} \int_{\Omega} u(\mathbf{r}, T) \frac{\partial v}{\partial t}(\mathbf{r}, T) dV(\mathbf{r}) \\ & - \int_0^T \int_{\Gamma} \frac{\partial u}{\partial \nu}(\mathbf{r}, t) v(\mathbf{r}, t) dS(\mathbf{r}) dt \\ & + \int_0^T \int_{\Omega} u(\mathbf{r}, t) \left(\frac{1}{c^2} \frac{\partial^2 v}{\partial t^2}(\mathbf{r}, t) - \Delta v(\mathbf{r}, t) \right) dV(\mathbf{r}) dt = \mathcal{F}(v), \end{aligned} \quad (4)$$

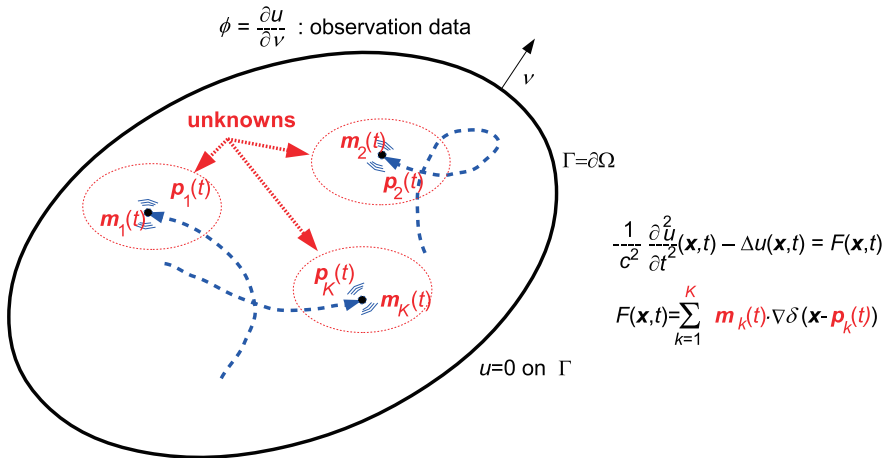


Figure 1: Inverse source problem for dipole sources in scalar wave equation.

for any $v \in H^2((0, T); H^2(\Omega))$, where \mathcal{F} is a linear functional defined by

$$\mathcal{F}(v) \equiv \int_0^T \int_{\Omega} F(\mathbf{r}, t) v(\mathbf{r}, t) dV(\mathbf{r}) dt. \quad (5)$$

Let $\mathcal{W} \subset H^2((0, T); H^2(\Omega))$ be a set of complex-valued functions that satisfy the homogeneous scalar wave equation

$$\frac{1}{c^2} \frac{\partial^2 v}{\partial t^2}(\mathbf{r}, t) - \Delta v(\mathbf{r}, t) = 0, \quad (\mathbf{r}, t) \in \Omega \times (0, T), \quad (6)$$

and vanishing condition

$$v(\mathbf{r}, T) = \frac{\partial v}{\partial \nu}(\mathbf{r}, T) = 0, \quad \mathbf{r} \in \Omega. \quad (7)$$

From the observations ϕ on Γ , we define the reciprocity gap functional $\mathcal{R}_{\phi}(\cdot)$ on \mathcal{W} by

$$\mathcal{R}_{\phi}(v) = - \int_0^T \int_{\Gamma} \phi(\mathbf{r}, t) v(\mathbf{r}, t) dS(\mathbf{r}) dt, \quad v \in \mathcal{W}. \quad (8)$$

Since $v \in \mathcal{W}$ satisfies the homogeneous scalar wave equation (6) and the vanishing condition (7), we obtain

$$\begin{aligned} & \frac{1}{c^2} \int_{\Omega} \frac{\partial u}{\partial t}(\mathbf{r}, T) v(\mathbf{r}, T) dV(\mathbf{r}) - \frac{1}{c^2} \int_{\Omega} u(\mathbf{r}, T) \frac{\partial v}{\partial t}(\mathbf{r}, T) dV(\mathbf{r}) \\ & + \int_0^T \int_{\Omega} u(\mathbf{r}, t) \left(\frac{1}{c^2} \frac{\partial v}{\partial t}(\mathbf{r}, t) - \Delta v(\mathbf{r}, t) \right) dV(\mathbf{r}) dt = 0. \end{aligned} \quad (9)$$

Hence, we derive the equation

$$\mathcal{R}_{\phi}(v) = - \int_0^T \int_{\Gamma} \frac{\partial u}{\partial \nu} v(\mathbf{r}, t) dS(\mathbf{r}) dt = \mathcal{F}(v), \quad v \in \mathcal{W}. \quad (10)$$

Equation (10) suggests that we may reconstruct the source term F from $\mathcal{R}_\phi(v)$ for suitable choice functions $v \in \mathcal{W}$. From the equation (10), the reciprocity gap functionals are expressed by

$$\mathcal{R}_\phi(v) = \sum_{k=1}^K \int_0^T \lambda_k(t) v(\mathbf{r}, t) |_{\mathbf{r}=\mathbf{p}_k(t)} dt, \quad (11)$$

for point source model (2), and

$$\mathcal{R}_\phi(v) = - \sum_{k=1}^K \int_0^T \mathbf{m}_k(t) \cdot \nabla v(\mathbf{r}, t) |_{\mathbf{r}=\mathbf{p}_k(t)} dt, \quad (12)$$

for dipole source model (3).

2.2 Restriction for dipole sources

In [18] and [19], we have already proposed a reconstruction method of point sources using the reciprocity gap functional. In our reconstruction procedure, we use the reciprocity gap functionals for the following three sequences of functions in W :

$$f_n(\mathbf{r}, t; \tau, \varepsilon) = (x + iy)^n \rho_\varepsilon \left(t + \frac{z}{c} - \tau \right), \quad n = 0, 1, 2, \dots, \quad (13)$$

$$g_n(\mathbf{r}, t; \tau, \varepsilon) = - \frac{\partial}{\partial t} f_n(\mathbf{r}, t; \tau, \varepsilon), \quad n = 0, 1, 2, \dots, \quad (14)$$

$$\begin{aligned} h_n(\mathbf{r}, t; \tau, \varepsilon) &= z \left(\frac{\partial}{\partial x} - i \frac{\partial}{\partial y} \right) f_n(\mathbf{r}, t; \tau, \varepsilon) \\ &\quad - (x - iy) \frac{\partial}{\partial z} f_n(\mathbf{r}, t; \tau, \varepsilon), \quad n = 1, 2, 3, \dots, \end{aligned} \quad (15)$$

where $\tau \in \mathbb{R}$, $0 < \varepsilon \ll 1$ and ρ_ε denotes a mollifier function with support $[-\varepsilon, \varepsilon]$ and satisfies $\int_{-\infty}^{\infty} \rho(s) ds = 1$. We note that τ is a time parameter that plays an important role in the reconstruction procedure. As a first step, we consider to apply these sequences to the reconstruction of dipole sources.

However, the expressions of reciprocity gap functionals $\mathcal{R}_\phi(f_n)$, $\mathcal{R}_\phi(g_n)$, $\mathcal{R}_\phi(h_n)$ for dipole source are very complicated. As an example, we show the expression of $\mathcal{R}_\phi(f_n)$ below:

$$\begin{aligned} \mathcal{R}_\phi(f_n)(\tau) &= -n \sum_{k=1}^K \alpha_k(t_k(\tau)) (m_{k,x}(t_k(\tau)) + i m_{k,y}(t_k(\tau))) (p_{k,x}(t_k(\tau)) + i p_{k,y}(t_k(\tau)))^{n-1} \\ &\quad + \frac{n}{c} \sum_{k=1}^K \alpha_k(t_k(\tau)) (m'_{k,z}(t_k(\tau)) \alpha_k(t_k(\tau)) + m'_{k,z}(t_k(\tau)) \alpha'_k(t_k(\tau))) \\ &\quad \quad \quad \times (p_{k,x}(t_k(\tau)) + i p_{k,y}(t_k(\tau)))^n \\ &\quad + \frac{n}{c} \sum_{k=1}^K m_{k,z}(t_k(\tau)) \alpha_k^2(t_k(\tau)) (p_{k,x}(t_k(\tau)) + i p_{k,y}(t_k(\tau)))^{n-1} + O(\varepsilon), \end{aligned} \quad (16)$$

where $t_k(\tau)$ denotes the solution t_k to the nonlinear equation $\tau = t_k + \frac{p_{k,z}(t_k)}{c}$, and $\alpha_k(t) = 1 / \left(1 + \frac{p_{k,z}(t)}{c} \right)$. The expressions become more complicated for $\mathcal{R}_\phi(g_n)$ and $\mathcal{R}_\phi(h_n)$.

To make the problem simply, we add the following assumption to the dipole source model (3).

- The z -component of dipole moment vanishes entirely, i.e. $m_{k,z}(t) \equiv 0$.
- Dipole sources move slowly relative to the wave propagation speed, i.e. $\frac{|\mathbf{p}'_k(t)|}{c} \ll 1$ for all k .
- For any instant τ , $(p_{k,x}(t_k(\tau)), p_{k,y}(t_k(\tau))) \neq (p_{j,x}(t_j(\tau)), p_{j,y}(t_j(\tau)))$ if $k \neq j$.

Under these assumptions, the expression of the reciprocity gap functional for the sequence of functions f_n , g_n , and h_n are simplified as follows:

$$\begin{aligned} \mathcal{R}_\phi(f_n)(\tau) &= -n \sum_{k=1}^K (m_{k,x}(t_k(\tau)) + im_{k,y}(t_k(\tau)))(p_{k,x}(t_k(\tau)) + ip_{k,y}(t_k(\tau)))^{n-1} \\ &\quad + \sum_{k=1}^K O(|\mathbf{p}'_k|/c) + O(\varepsilon), \quad n = 1, 2, \dots, \end{aligned} \quad (17)$$

$$\begin{aligned} \mathcal{R}_\phi(g_n)(\tau) &= n \sum_{k=1}^K (m'_{k,x}(t_k(\tau)) + im'_{k,y}(t_k(\tau)))(p_{k,x}(t_k(\tau)) + ip_{k,y}(t_k(\tau)))^{n-1}, \\ &\quad + \sum_{k=1}^K O(|\mathbf{p}'_k|/c) + O(\varepsilon), \quad n = 1, 2, \dots \end{aligned} \quad (18)$$

$$\begin{aligned} \mathcal{R}_\phi(h_n)(\tau) &= 2n(n-1) \sum_{k=1}^K (m_{k,x}(t_k(\tau)) + im_{k,y}(t_k(\tau)))(p_{k,x}(t_k(\tau)) + ip_{k,y}(t_k(\tau)))^{n-2} \\ &\quad \times p_{k,z}(t_k(\tau)) \\ &\quad + \frac{1}{c} \sum_{k=1}^K \overline{(m'_{k,x}(t_k(\tau)) + im'_{k,y}(t_k(\tau)))} (p_{k,x}(t_k(\tau)) + ip_{k,y}(t_k(\tau)))^n \\ &\quad + \frac{n}{c} \sum_{k=1}^K (m'_{k,x}(t_k(\tau)) + im'_{k,y}(t_k(\tau))) \\ &\quad \quad \times \overline{(p_{k,x}(t_k(\tau)) + ip_{k,y}(t_k(\tau)))} (p_{k,x}(t_k(\tau)) + ip_{k,y}(t_k(\tau)))^{n-1} \\ &\quad + \sum_{k=1}^K O(|\mathbf{p}'_k|/c) + O(\varepsilon), \quad n = 2, 3, \dots \end{aligned} \quad (19)$$

We consider a reconstruction procedure for dipole sources based on these expressions.

2.3 Identification of the number of dipole sources

Firstly, we consider the identification of the number K of dipole sources from $\mathcal{R}_\phi(f_n)$. Neglecting small terms $\sum_{k=1}^K O(|\mathbf{p}'_k|/c) + O(\varepsilon)$, $\mathcal{R}(f_n)$ is approximated by

$$\mathcal{R}(f_n)(\tau) = -n \sum_{k=1}^K (m_{k,x}(t_k(\tau)) + im_{k,y}(t_k(\tau)))(p_{k,x}(t_k(\tau)) + ip_{k,y}(t_k(\tau)))^{n-1}. \quad (20)$$

For each $L \in \mathbb{N}$ and $\mu \in \mathbb{N}$, we define the square matrix $H_{L,\mu} \in \mathbb{C}^{L \times L}$ by

$$H_{L,\mu}(\tau) = ((H_\mu)_{\alpha,\beta}) = \left(-\frac{1}{(\mu+\alpha+\beta-2)} \mathcal{R}_\phi(f_\mu) \right), \quad (21)$$

where α, β denote the row and column indices, respectively. Using the same discussion for point source model in [7], we obtain

$$\begin{cases} \det H_{L,1} \neq 0, & \text{for } L \leq K(\tau), \\ \det H_{L,1} = 0, & \text{for } L > K(\tau), \end{cases} \quad (22)$$

where $K(\tau)$ is the number of dipole sources which satisfy $|\mathbf{m}_k(t_k(\tau))| \neq 0$ for every instant τ . Hence, we can identify the number of dipole sources which do not vanish at instant $t_k(\tau)$ using $\mathcal{R}_\phi(f_n)(\tau)$. Hereafter, we denote $K(\tau)$ by K for simplicity.

2.4 Reconstruction of locations \mathbf{p}_n and moments \mathbf{m}_n

Next, we consider the reconstruction of locations and moments of dipole sources using reciprocity gap functionals $\mathcal{R}_\phi(f_n)$, $\mathcal{R}_\phi(g_n)$ and $\mathcal{R}_\phi(h_n)$. We reconstruct these parameters by the following three steps:

Step 1. Reconstruct x and y components of the location of dipole sources, i.e. $p_{k,x}(t_k(\tau))$ and $p_{k,y}(t_k(\tau))$, and reconstruct dipole moments $\mathbf{m}_k(t_k(\tau))$ using reciprocity gap functionals $\mathcal{R}_\phi(f_n)(\tau)$, $n = 1, 2, \dots, 2K$.

Step 2. Estimate $\mathbf{m}'_k(t_k(\tau))$ using $\mathcal{R}_\phi(g_n)(\tau)$, $n = 1, 2, \dots, K$, where \mathbf{m}'_k denotes the derivative in time of \mathbf{m}_k .

Step 3. Reconstruct z component of location of each dipole source, i.e. $p_{k,z}(t_k(\tau))$, using $\mathcal{R}_\phi(h_k)(t_k(\tau))$, $n = 2, 3, \dots, K + 1$.

We describe the detail of each step.

Step 1.

Let us introduce complex numbers

$$\xi_k = \xi_k(t_k(\tau)) \equiv p_{k,x}(t_k(\tau)) + ip_{k,y}(t_k(\tau)), \quad k = 1, 2, \dots, K, \quad (23)$$

$$a_k = a_k(t_k(\tau)) \equiv m_{k,x}(t_k(\tau)) + im_{k,y}(t_k(\tau)), \quad k = 1, 2, \dots, K. \quad (24)$$

Then the equation (17) is rewritten as

$$\mathcal{R}_\phi(f_n)(\tau) = -n \sum_{k=1}^K a_k \xi_k^{n-1} + \sum_{k=1}^K O(|\mathbf{p}'_k|/c) + O(\varepsilon), \quad n = 1, 2, \dots. \quad (25)$$

Assume that $a_k \neq 0$ for $k = 1, 2, \dots, K$. Then, and neglecting smaller terms and using same discussions for point source model[7], we can reconstruct ξ_n , $n = 1, 2, \dots, K$ as eigenvalues of $H_{K,1}^{-1} H_{K,2}$, where $H_{L,\mu}$ is defined in (21). After the reconstruction of ξ_k , $k = 1, 2, \dots, K$, we can reconstruct a_k , $k = 1, 2, \dots, K$ as a solution of the linear equation

$$\sum_{k=1}^K \xi_k^{n-1} a_k = -\frac{1}{n} \mathcal{R}_\phi(f_n)(\tau), \quad n = 1, 2, \dots, K. \quad (26)$$

We note that the equation (26) is uniquely solvable since we assumed that $(p_{k,x}(t_k(\tau)), p_{k,y}(t_k(\tau))) \neq (p_{j,x}(t_j(\tau)), p_{j,y}(t_j(\tau)))$ for $k \neq j$.

Step 2.

Under the assumption that $m_{k,z}(t) \equiv 0$, the reciprocity gap functionals $\mathcal{R}_\phi(g_n)$ can be expressed as

$$\begin{aligned}
& \mathcal{R}_\phi(g_n)(\tau) \\
&= n \sum_{k=1}^K (m'_{k,x}(t_k(\tau)) + im'_{k,y}(t_k(\tau)))(p_{k,x}(t_k(\tau)) + ip_{k,y}(t_k(\tau)))^{n-1} \\
&\quad + \sum_{k=1}^K O(|\mathbf{p}'_k|/c) + O(\varepsilon) \\
&= n \sum_{k=1}^K a'_k(t_k(\tau)) \xi_k^{n-1} + \sum_{k=1}^K O(|\mathbf{p}'_k|/c) + O(\varepsilon), \quad n = 1, 2, \dots.
\end{aligned} \tag{27}$$

Neglecting smaller terms $O(|\mathbf{p}'_k|/c) + O(\varepsilon)$ and since we have already reconstructed parameters $p_{k,x}(t_k(\tau))$ and $p_{k,y}(t_k(\tau))$, we can uniquely estimate $a'_k(t_k(\tau))$, i.e. $m'_{k,x}(t_k(\tau))$ and $m'_{k,y}(t_k(\tau))$ from $\mathcal{R}_\phi(g_n)(\tau)$, $n = 1, 2, \dots, K$.

Step 3.

Under the assumption $m_{k,z}(t) \equiv 0$ and neglecting smaller terms in the reciprocity gap functionals $\mathcal{R}_\phi(h_n)$, we obtain

$$\begin{aligned}
& \mathcal{R}_\phi(h_n)(\tau) \\
&= 2n(n-1) \sum_{k=1}^K (m_{k,x}(t_k(\tau)) + im_{k,y}(t_k(\tau)))(p_{k,x}(t_k(\tau)) + ip_{k,y}(t_k(\tau)))^{n-2} \\
&\quad \times p_{k,z}(t_k(\tau)) \\
&\quad + \frac{1}{c} \sum_{k=1}^K \overline{(m'_{k,x}(t_k(\tau)) + im'_{k,y}(t_k(\tau)))} (p_{k,x}(t_k(\tau)) + ip_{k,y}(t_k(\tau)))^n \\
&\quad + \frac{n}{c} \sum_{k=1}^K (m'_{k,x}(t_k(\tau)) + im'_{k,y}(t_k(\tau))) \\
&\quad \quad \times \overline{(p_{k,x}(t_k(\tau)) + ip_{k,y}(t_k(\tau)))} (p_{k,x}(t_k(\tau)) + ip_{k,y}(t_k(\tau)))^{n-1} \\
&= 2n(n-1) \sum_{k=1}^K a_k(t_k(\tau)) \xi_k(t_k(\tau))^{n-2} p_{k,z}(t_k(\tau)) \\
&\quad + \frac{1}{c} \sum_{k=1}^K \overline{a'_k(t_k(\tau))} \xi_k(t_k(\tau))^n + \frac{n}{c} \sum_{k=1}^K a'_k(t_k(\tau)) \overline{\xi_k(t_k(\tau))} \xi_k(t_k(\tau))^{n-1}, \quad n = 2, 3, \dots,
\end{aligned} \tag{28}$$

In (28), only $p_{k,z}(t_k(\tau))$, $k = 1, 2, \dots, K$ are unknown. From (28), we can derive the following linear equation for $q_k = q_k(t_k(\tau)) \equiv p_{k,z}(t_k(\tau)) a_k(t_k(\tau))$, $k = 1, 2, \dots, K$:

$$\sum_{k=1}^K \xi_k^{n-2} q_k = \frac{1}{2n(n-1)} (\mathcal{R}_\phi(h_n)(\tau) - d_n(\tau)), \tag{29}$$

where

$$\begin{aligned}
d_n(\tau) &= \frac{1}{c} \sum_{k=1}^K \overline{a'_k(t_k(\tau))} \xi_k(t_k(\tau))^n + \frac{n}{c} \sum_{k=1}^K a'_k(t_k(\tau)) \overline{\xi_k(t_k(\tau))} \xi_k(t_k(\tau))^{n-1}, \\
& n = 2, 3, \dots.
\end{aligned} \tag{30}$$

Therefore, we can uniquely estimate q_k , $k = 1, 2, \dots, K$ from $\mathcal{R}_\phi(h_n)(\tau)$, $n = 2, 3, \dots, K+1$ and obtain $p_{k,z}(t_k(\tau)) = q_k(t_k(\tau))/a_k(t_k(\tau))$.

3 Numerical Experiments

In this section, we show some numerical experiments for our reconstruction method. We consider the case where the domain $\Omega = \{\mathbf{r} \mid |\mathbf{r}| = 1\}$, and the wave propagation speed $c = 1$.

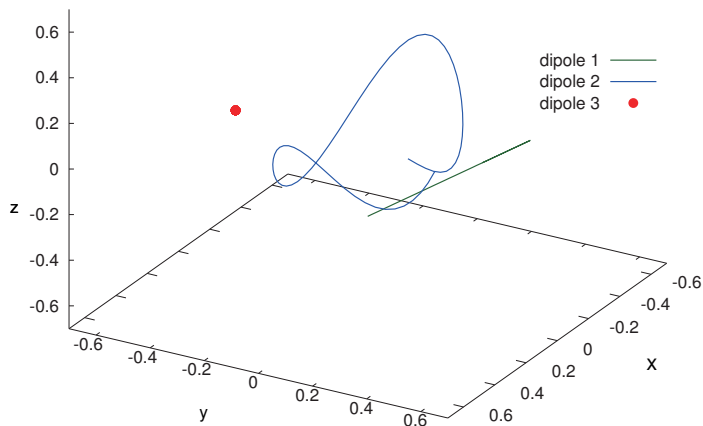
We set the number of dipole sources $K = 3$. Each dipole source moves as following, and the trajectories of locations of dipole sources are shown in Figure 2.

Dipole 1: Moves on a line segment.

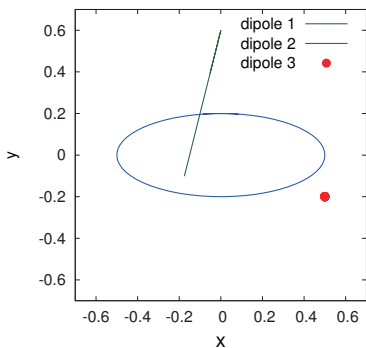
Dipole 2: Moves on a ellipsoid-like shape.

Dipole 3: Fixed on $(0.5, -0.2, 0.3)$.

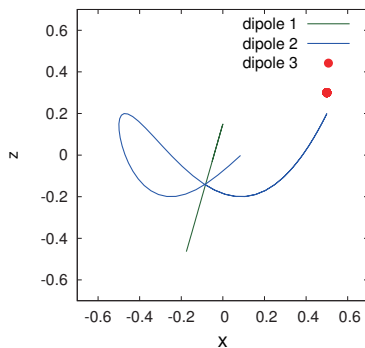
In our experiments, moving speed of dipole sources is restricted as $\max \frac{|\mathbf{P}'_k(t)|}{c} = 15\%$. Moment of each dipole changes in time as shown in Figure 3. To give the observation data, we solve the initial- and boundary-value problem (1) by boundary integral equation method. We give observation data on 384 points on Γ with time step $\delta t = 0.1$. To simulate practical observation condition, we add 0.0%, 1.0%, 5.0% and 10.0% random noise to observation data.



(a) Diagonal view



(b) xy -view



(c) xz -view

Figure 2: Trajectories of dipole sources.

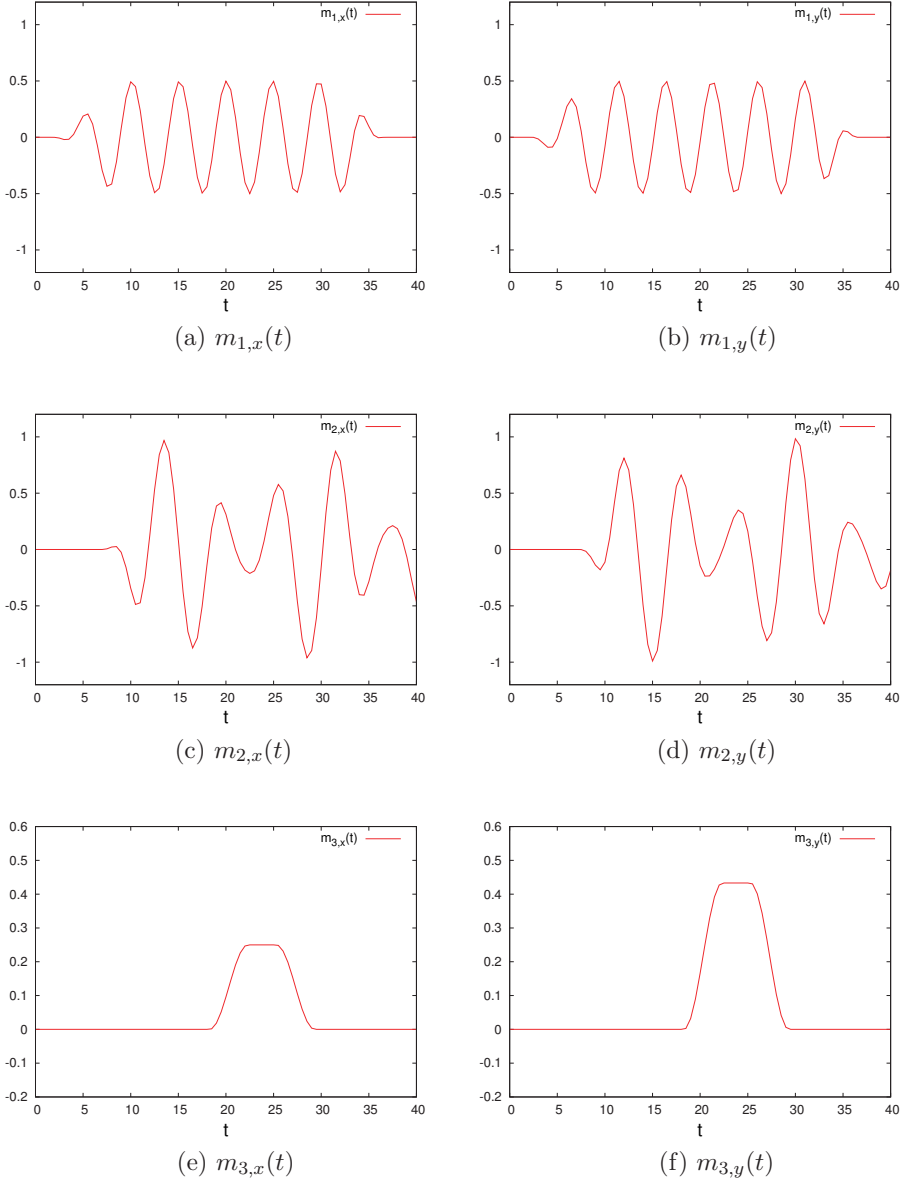


Figure 3: Time-profiles of moments of dipole sources.

Firstly, we show the reconstruction result for noise-free case. In Figure 4, we give the trajectories of reconstructed dipole sources. We displays the time-profile of location of each reconstructed dipole source in Figures 5 and 6, and dipole moment in Figure 7. From these figures, we may understand that our method gives precise reconstruction for both locations and moments of dipole sources.

Next, we examine our method for noisy observation cases. Figures 8-11, 12-15, 16-19 show the reconstruction results of trajectories, time-profile of locations, and moments of dipoles for observations with 1.0%, 5.0% and 10.0% noise cases, respectively. Also Table 1 shows the errors of reconstruction results for noisy observation cases. In Table 1, we use average of absolute values for errors of locations, and relative errors with respect to L^2 -norm for errors of dipole moments. From Figures 8-11, 12-15, 16-19 and Table 1, we consider that our method gives reliable reconstruction results if noise is smaller than 5%, but noise is larger than 10%, the reconstruction result becomes bad.

Table 1: Errors of reconstruction results from observations with various noises.

Noise		dipole 1	dipole 2	dipole 3
0.0 %	location	0.0260	0.0360	0.0250
	moment	14.6 %	12.7 %	26.6 %
1.0 %	location	0.0264	0.0387	0.0254
	moment	14.1 %	12.7 %	26.8 %
5.0 %	location	0.0328	0.0648	0.0758
	moment	16.6 %	16.2 %	42.4 %
10.0 %	location	0.0462	0.0922	0.0706
	moment	23.3 %	21.4 %	45.0 %

4 Conclusions and open problems

In this report, we consider a reconstruction method for slowly-moving dipole sources in three dimensional scalar wave equation. We apply the reciprocity gap functional for three types of functions, and propose a procedure to reconstruct parameters of dipole sources. We examine our reconstruction method by some numerical experiments, and find that our method gives good estimates of locations and moments of dipole sources under noisy observation condition.

We have many open problems for our problem and method as shown in below:

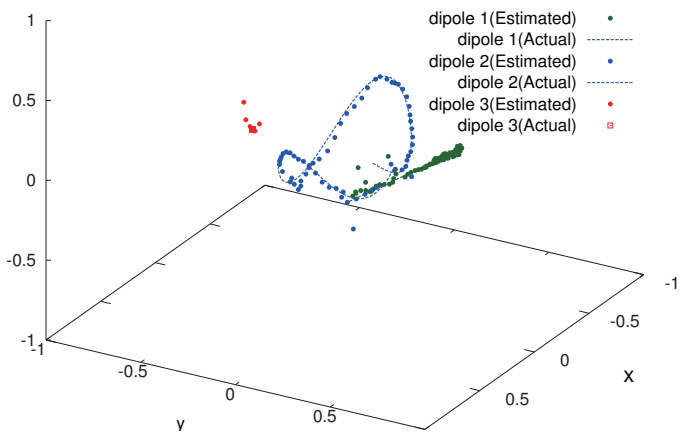
- Remove an assumption that dipoles move slowly.
- Remove an assumption that moments of dipoles have no z -components.
- Limited aperture cases (i.e., we observe $\partial u / \partial \nu$ on $\Gamma_u \subset \Gamma$).
- Extend results to reconstruct quadrapoles.

References

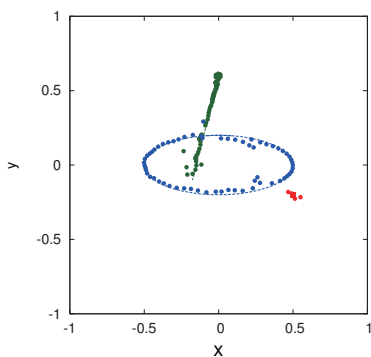
- [1] Ando, S., An Autonomous Three-Dimensional Vision Sensor with Ears *IEICE Trans. Inf. & Syst.* **E78-D** (1995), 1621–1629
- [2] Andrieux, S. and Ben Abda, A., Identification of planar cracks by complete overdetermined data: inversion formulae, *Inverse Problems*, **12** (1996), No. 5, 553–563.

- [3] Ben Abda, A., Delbary, F. and Haddar, H., On the use of the reciprocity-gap functional in inverse scattering from planar cracks, *Math. Models Methods Appl. Sci.*, **15** (2005), No. 10, 1553–1574.
- [4] Ben-Menahem, A. and Singh, S. J. 2000 *Seismic Waves and Sources (2nd ed)*, Dover, (2000).
- [5] Bruckner, G. and Yamamoto, M., Determination of point wave sources by pointwise observations: stability and reconstruction *Inverse Problems* **16**, (2000), 723–748.
- [6] Colton, D. and Haddar, H., An application of the reciprocity gap functional to inverse scattering theory, *Inverse Problems*, **21** (2005), No. 1, 383–398.
- [7] El Badia, A. and Ha-Duong, T., An inverse source problem in potential analysis, *Inverse Problems*, **16**, (2000), No. 3, 651–663.
- [8] El Badia, A. and Ha-Duong, T. Determination of point wave sources by boundary measurements, *Inverse Problems*, **17**, (2001), No. 4, 1127–1139.
- [9] Isakov, V. *Inverse Source Problems*, Mathematical Surveys and Monographs, **34**, American Mathematical Society, (1990).
- [10] Isakov, V. *Inverse Problems for Partial Differential Equations (2nd. Ed.)*, Applied Mathematical Sciences, **127**, Springer, (2006).
- [11] Komornik, V. and Yamamoto, M., Upper and lower estimates in determining point sources in a wave equation *Inverse Problems*, **18**, (2002), 319–329.
- [12] Komornik, V. and Yamamoto, M., Estimation of point sources and applications to inverse problems *Inverse Problems*, **21**, (2005), 2051–2070.
- [13] Kubo, S., *Inverse Problems*, Baifu-kan, (1992).
- [14] Lu, Z-L. and Kaufman, L. (eds.) *Magnetic Source Imaging of the Human Brain*, Lawrence Erlbaum Associates, (2003).
- [15] Mueller, J.L. and Siltanen, S., *Linear and Nonlinear Inverse Problems with Practical Applications*, Computational Science and Engineering Series, SIAM, (2012).
- [16] Nara, T. and Ando, S., An inverse potential analysis via projection onto the Riemann sphere, *Bulletin of JSIAM*, **13**, (2003), No. 3, 45–57 (in Japanese).
- [17] Nara, T., Algebraic reconstruction of the general-order poles of a meromorphic function, *Inverse Problems*, **28**, (2012), No. 2, 025008, 19 pp.
- [18] Ohe, T., A numerical method for an inverse source problem for a scalar wave equation without optimisation procedures, *Inverse problems for practice, the present and the future*(eds. Takiguchi, T. and Fujiwara H.), MI Lecture Note, **54**, 67–76.
- [19] Ohe, T., Inui, H. and Ohnaka, K., Real-time reconstruction of time-varying point sources in a three-dimensional scalar wave equation, *Inverse Problems*, **27**, (2011), No. 11, 115011, 19 pp.
- [20] Ohe, T. and Ohnaka, K., Determination of locations of point-like masses in an inverse source problem of the Poisson equation, *J. Comput. Appl. Math.*, **54**, (1994), No. 2, 251–261.
- [21] Sarvas, J., Basic mathematical and electromagnetic concepts of the biomagnetic inverse problem *Phys. Med. and Bio.*, **32**, (1987), 11–22.

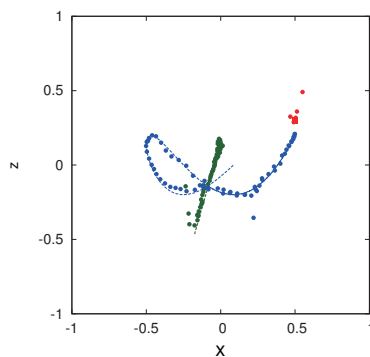
- [22] Tanaka, T. (ed.), *Inverse Problems in Engineering Mechanics IV*, Elsevier, (2003).
- [23] Uhlmann, G. (ed.), *Inside Out, Inverse Problems and Applications*, Cambridge University Press, (2003).
- [24] Uhlmann, G. (ed.), *Inside Out II, Inverse Problems and Applications*, Cambridge University Press, (2013).



(a) Diagonal view



(b) xy -view



(c) xz -view

Figure 4: Reconstruction results of trajectories of dipole sources from noise-free observations.

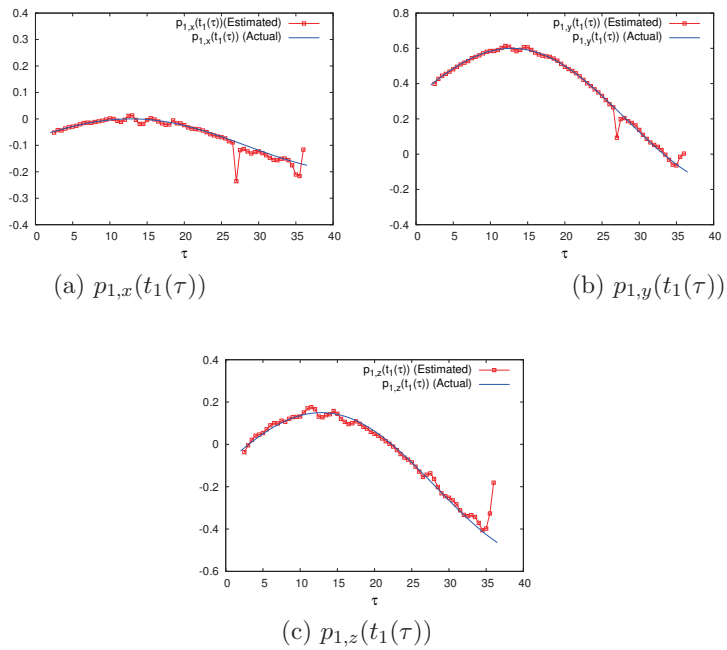


Figure 5: Reconstruction results of time-profiles of locations of dipole sources $\mathbf{p}_1(t_1(\tau))$ from noise-free observations.

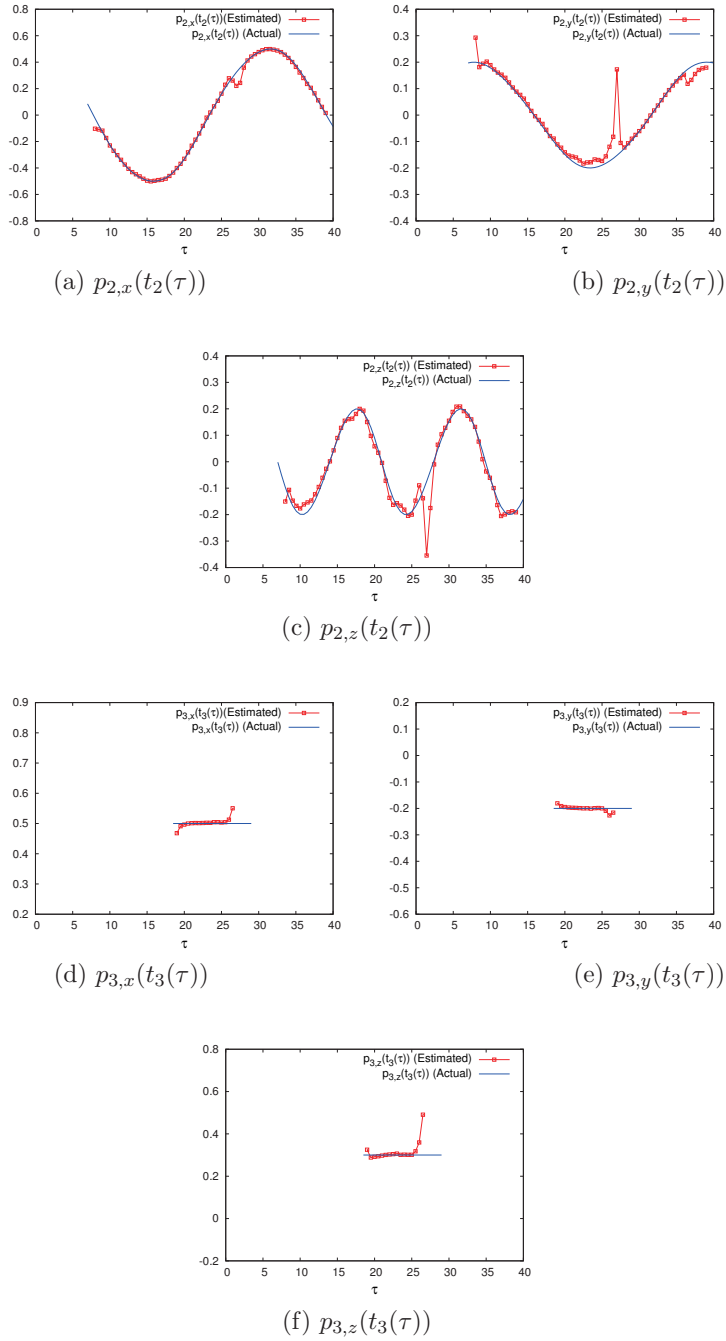
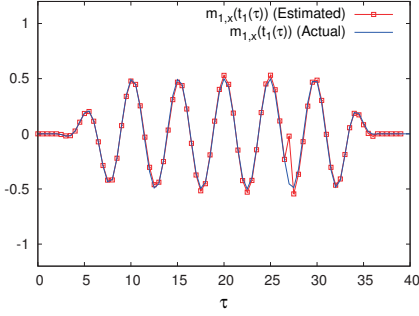
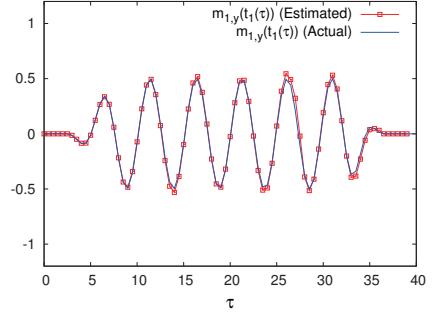


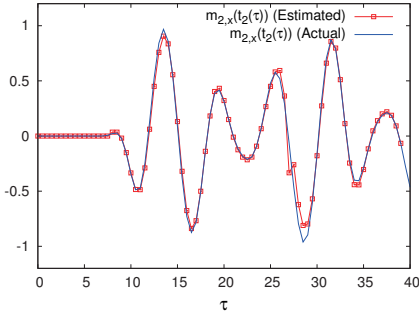
Figure 6: Reconstruction results of time-profiles of locations of dipole sources $\mathbf{p}_2(t_2(\tau))$ and $\mathbf{p}_3(t_3(\tau))$ from noise-free observations.



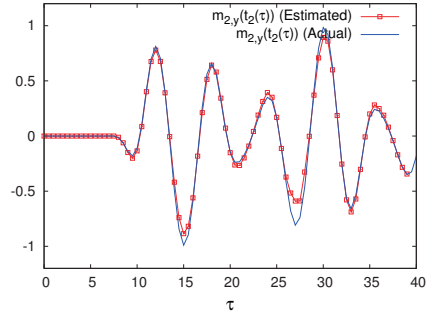
(a) $m_{1,x}(t_1(\tau))$



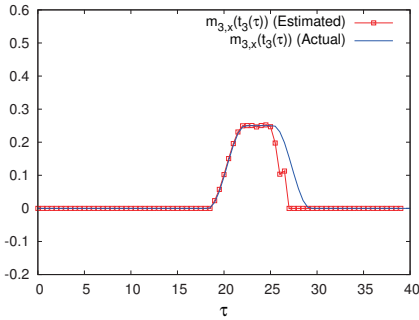
(b) $m_{1,y}(t_1(\tau))$



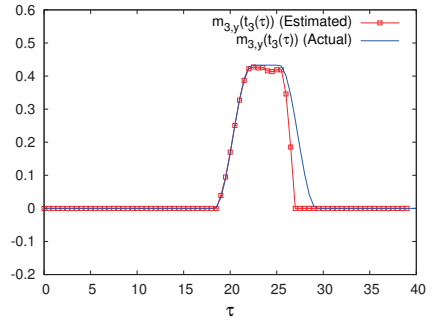
(c) $m_{2,x}(t_2(\tau))$



(d) $m_{2,y}(t_2(\tau))$

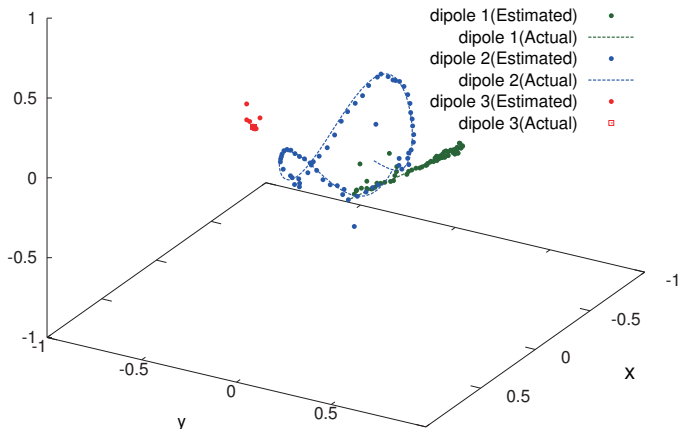


(e) $m_{3,x}(t_3(\tau))$

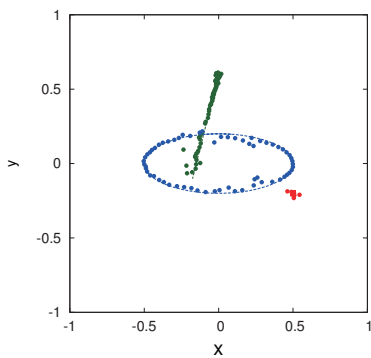


(f) $m_{3,y}(t_3(\tau))$

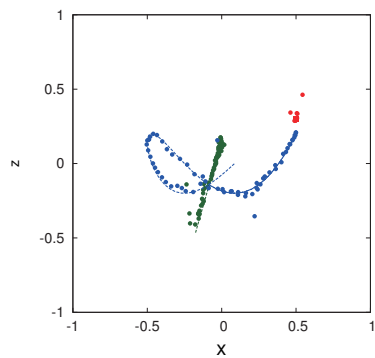
Figure 7: Reconstruction results of time-profiles of moments of dipole sources from noise-free observations.



(a) Diagonal view



(b) xy -view



(c) xz -view

Figure 8: Reconstruction results of trajectories of dipole sources from observations with 1.0% noise.

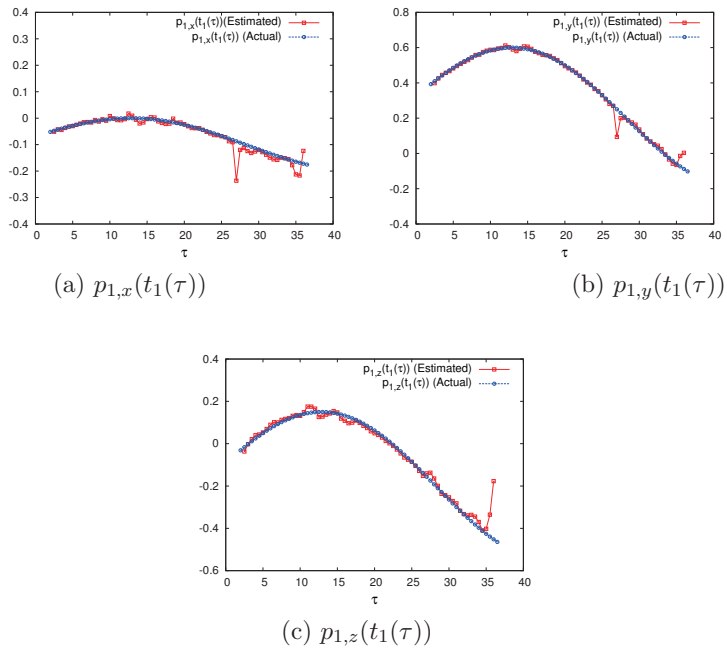


Figure 9: Reconstruction results of time-profiles of locations of dipole sources $\mathbf{p}_1(t_1(\tau))$ from observations with 1.0% noise.

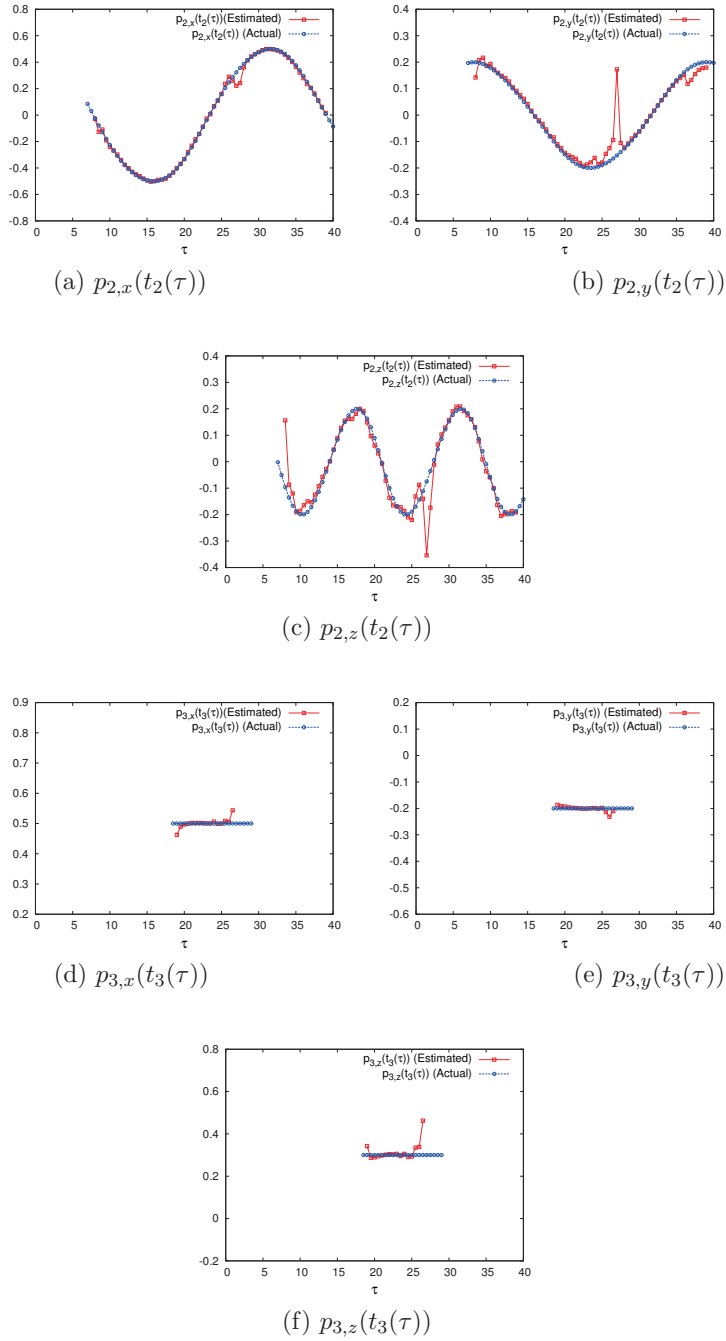
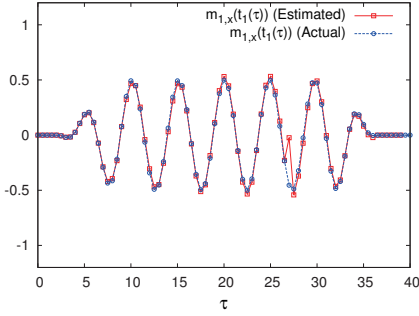
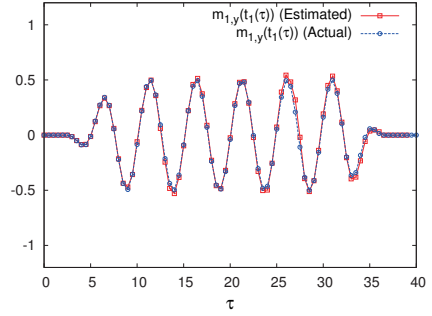


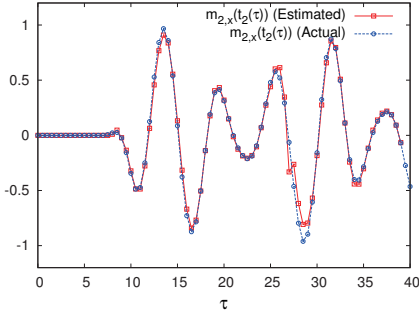
Figure 10: Reconstruction results of time-profiles of locations of dipole sources $\mathbf{p}_2(t_2(\tau))$ and $\mathbf{p}_3(t_3(\tau))$ from observations with 1.0% noise.



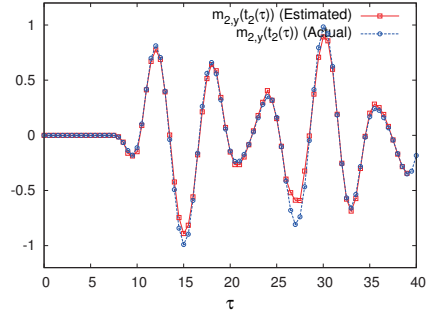
(a) $m_{1,x}(t_1(\tau))$



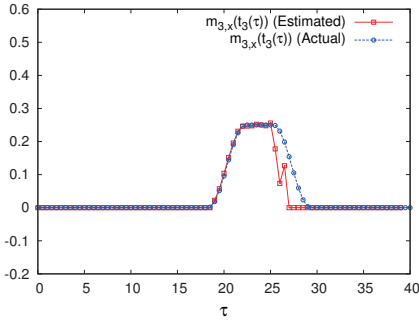
(b) $m_{1,y}(t_1(\tau))$



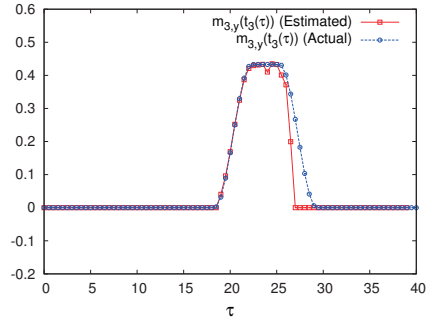
(c) $m_{2,x}(t_2(\tau))$



(d) $m_{2,y}(t_2(\tau))$

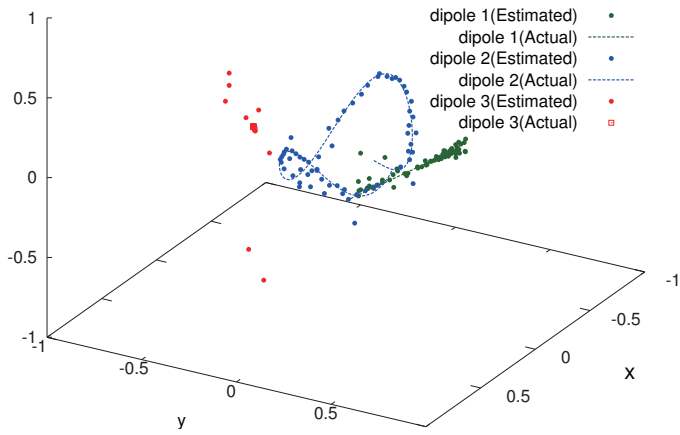


(e) $m_{3,x}(t_3(\tau))$

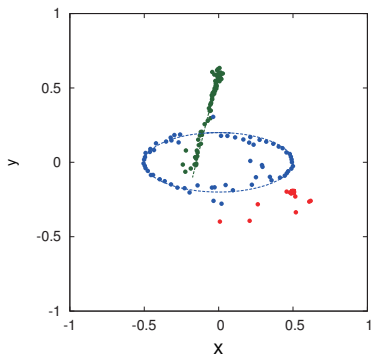


(f) $m_{3,y}(t_3(\tau))$

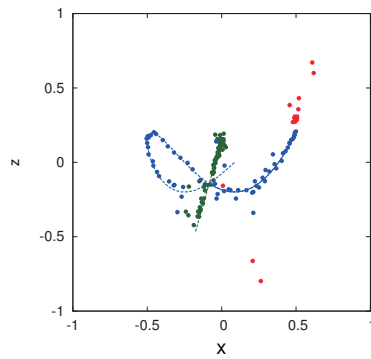
Figure 11: Reconstruction results of time-profiles of moments of dipole sources from observations with 1.0% noise.



(a) Diagonal view



(b) xy -view



(c) xz -view

Figure 12: Reconstruction results of trajectories of dipole sources from observations with 5.0% noise.

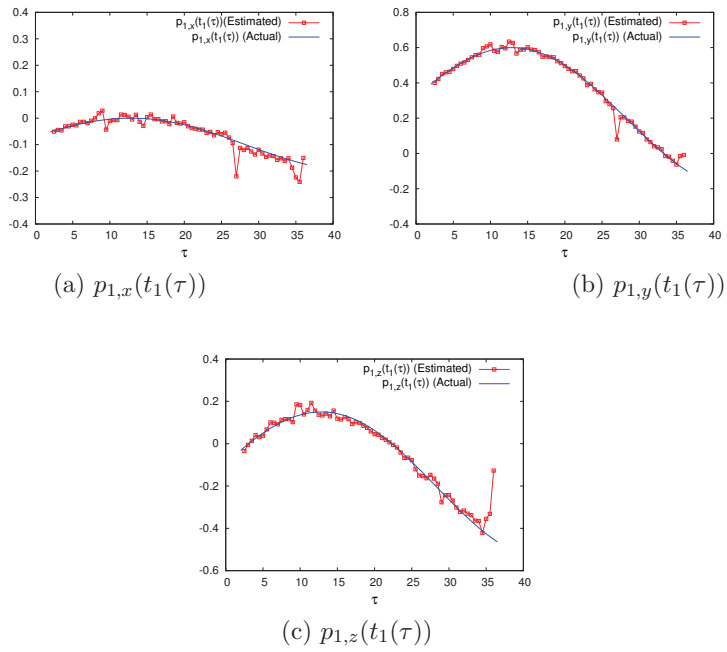


Figure 13: Reconstruction results of time-profiles of locations of dipole sources $\mathbf{p}_1(t_1(\tau))$ from observations with 5.0% noise.

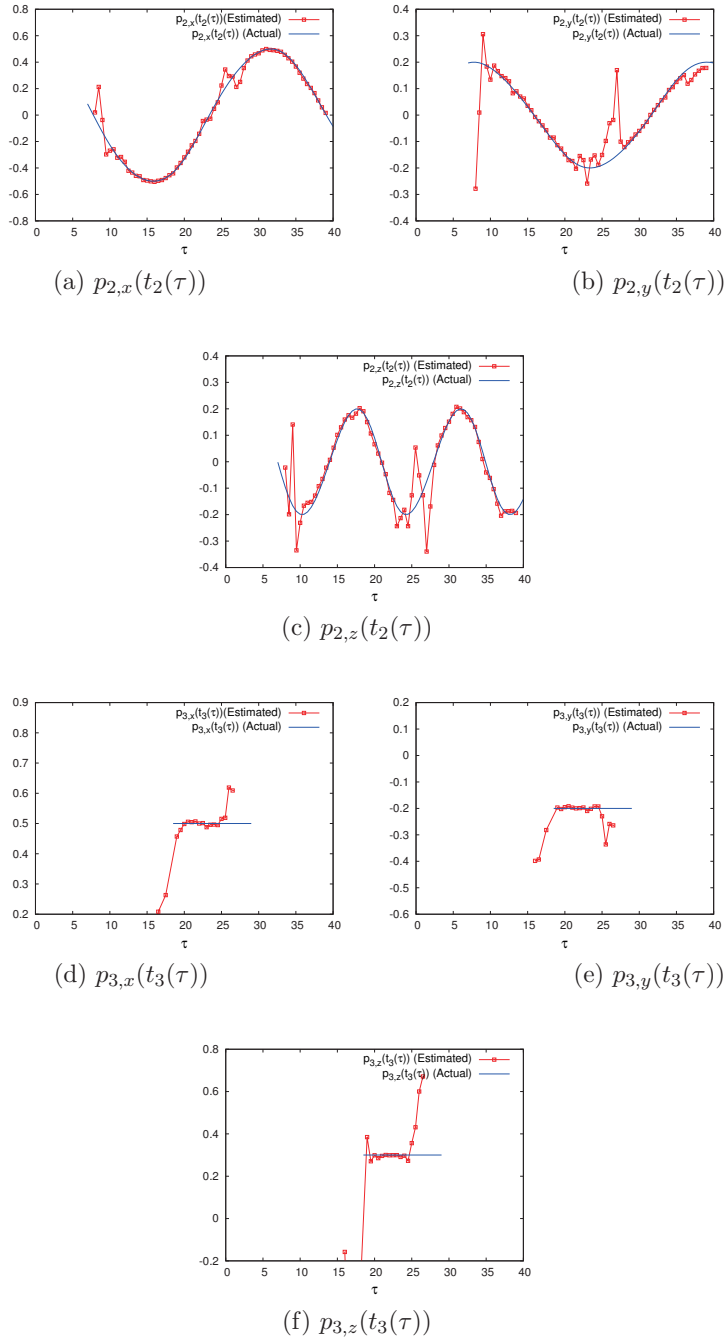
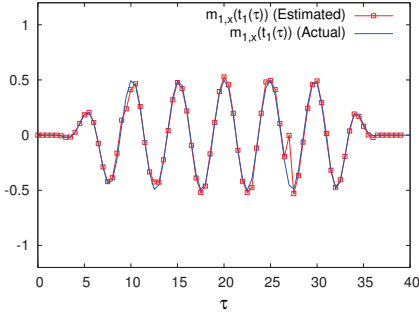
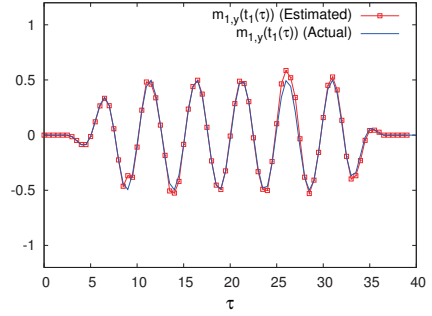


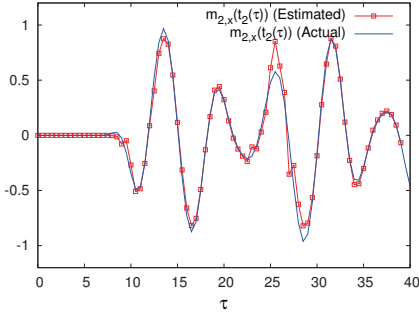
Figure 14: Reconstruction results of time-profiles of locations of dipole sources $\mathbf{p}_2(t_2(\tau))$ and $\mathbf{p}_3(t_3(\tau))$ from observations with 5.0% noise.



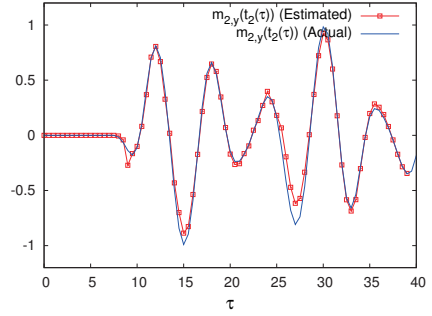
(a) $m_{1,x}(t_1(\tau))$



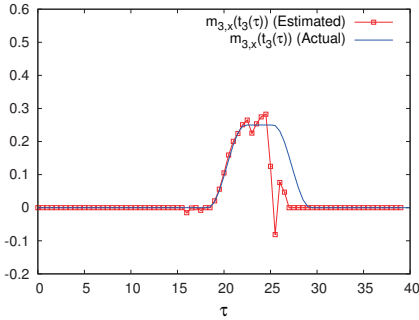
(b) $m_{1,y}(t_1(\tau))$



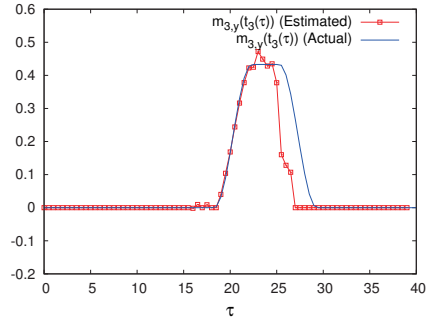
(c) $m_{2,x}(t_2(\tau))$



(d) $m_{2,y}(t_2(\tau))$

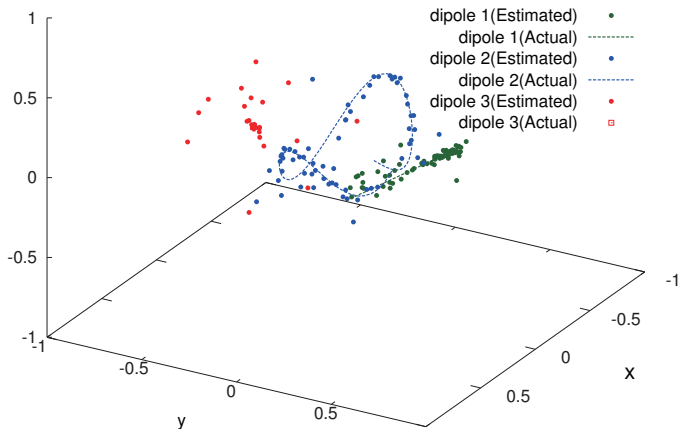


(e) $m_{3,x}(t_3(\tau))$

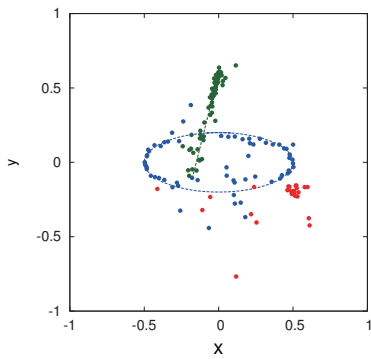


(f) $m_{3,y}(t_3(\tau))$

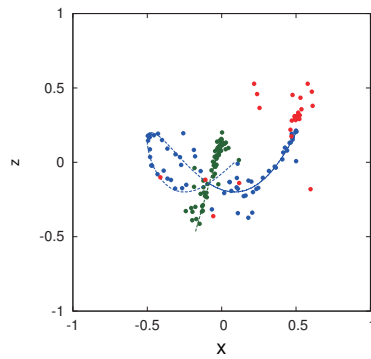
Figure 15: Reconstruction results of time-profiles of moments of dipole sources from observations with 5.0% noise.



(a) Diagonal view



(b) xy -view



(c) xz -view

Figure 16: Reconstruction results of trajectories of dipole sources from observations with 10.0% noise.

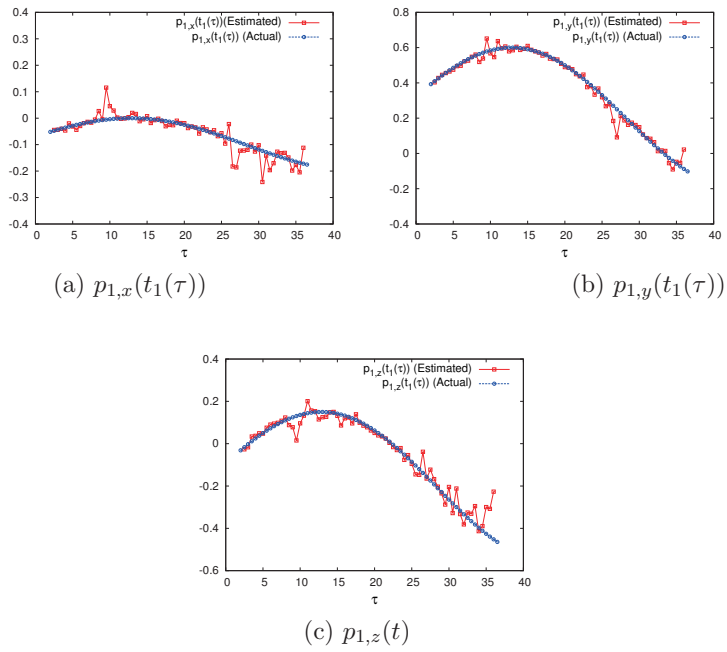


Figure 17: Reconstruction results of time-profiles of locations of dipole sources $\mathbf{p}_1(t_1(\tau))$ from observations with 10.0% noise.

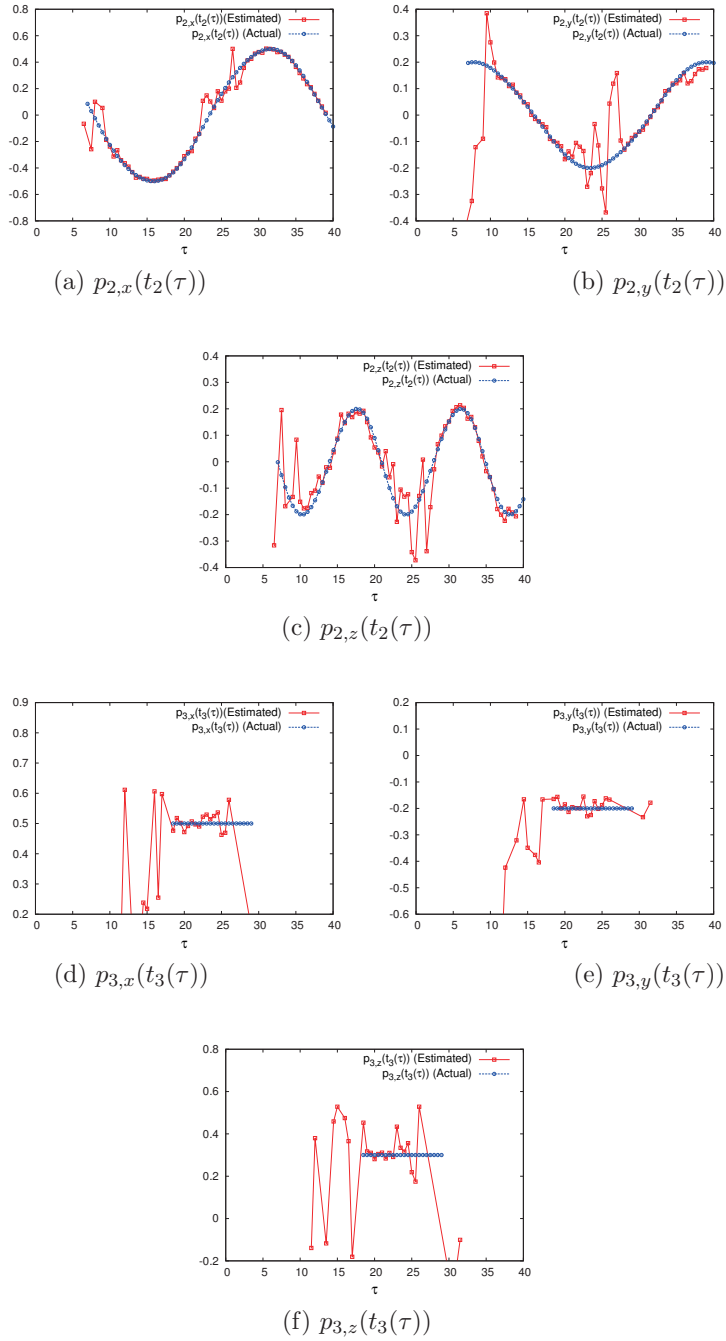
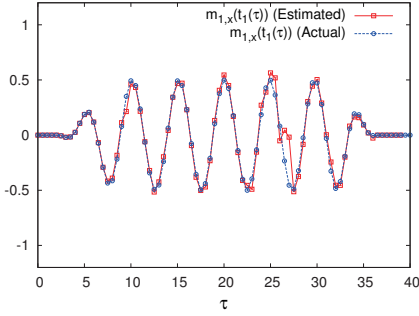
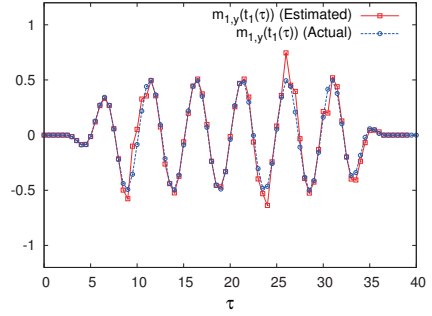


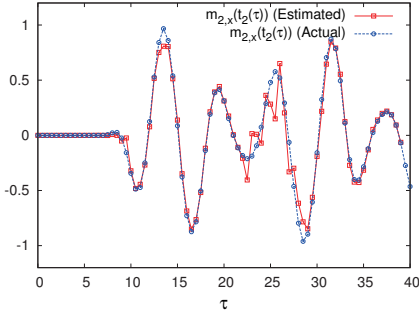
Figure 18: Reconstruction results of time-profiles of locations of dipole sources $\mathbf{p}_2(t_2(\tau))$ and $\mathbf{p}_3(t_3(\tau))$ from observations with 10.0% noise.



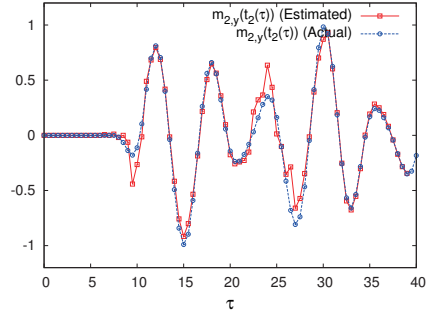
(a) $m_{1,x}(t_1(\tau))$



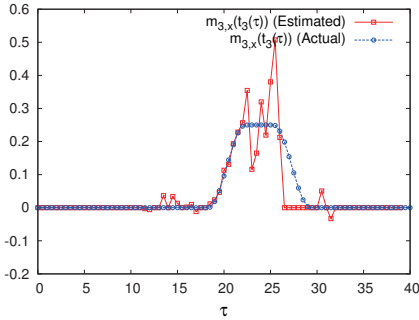
(b) $m_{1,y}(t_1(\tau))$



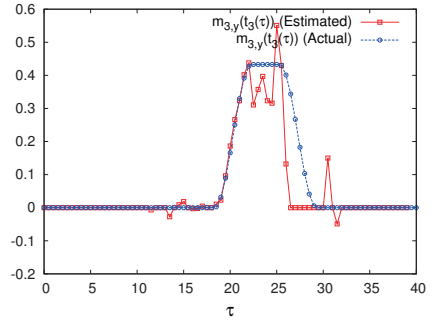
(c) $m_{2,x}(t_2(\tau))$



(d) $m_{2,y}(t_2(\tau))$



(e) $m_{3,x}(t_3(\tau))$



(f) $m_{3,y}(t_3(\tau))$

Figure 19: Reconstruction results of time-profiles of moments of dipole sources from observations with 10.0% noise.

Inverse problems in emission tomography

Naoya Oishi

Department of Psychiatry, Human Brain Research Center
Kyoto University Graduate School of Medicine
Shogoin Kawahara-cho 54, Sakyo-ku, Kyoto 606-8397, Japan
E-mail: noishi@kuhp.kyoto-u.ac.jp

Abstract

The article reviews methods for image reconstruction from projections (inverse problems) in emission tomography with introducing medical imaging, especially neuroimaging, and an overview of emission tomography.

Key words - emission tomography, positron emission tomography, single photon emission computed tomography, inverse problem

1 Introduction

Emission tomography is a medical imaging technique based on the tracer principle by George de Hevesy who got Nobel Prize in Chemistry 1943. It can utilize ionizing radiation emitted by radiotracers injected into the body specifically targeting molecular pathways in tissue in vivo. Positron emission tomography (PET) and single photon emission computed tomography (SPECT) are representative examples of emission tomography and widely used as non-invasive diagnostic imaging in clinical medicine. Photons emitted from the radiotracer in the body are detected by the detectors as independent events in SPECT and, in PET, the two photons, which are detected by the detectors in coincidence, from the annihilation of positrons originally emitted from the radiotracer are the basis of image formation. The image reconstruction process from projections in emission tomography is an inverse problem for the photon transport equation. The main advantage of PET and SPECT is the ability to provide information about regional tissue function, which usually precedes structural changes measured by magnetic resonance imaging (MRI) or computed tomography (CT)

in the course of the disease. Clinical applications of PET and SPECT are found in oncology, neurology, psychiatry, cardiology, and so on and play an important role in malignant tumor detection, disease diagnosis, and treatment strategy. Therefore, further advances of emission tomography not only in instrumentation for data collection but also in more effective methods for solving the inverse problem from the measured data, can improve patient outcomes.

Photons emitted from radiotracers undergo a number of interactions with matter. In the range of PET and SPECT, emitted photon interactions with matter occur in the following three ways: photoelectric effect, Compton scattering, and Rayleigh scattering. The majority of primary emitted photons are either completely absorbed without reaching the detectors or deviate from their original emission directions. It causes events to be either lost or misplaced, which distorts the projection data and degrades the quantitative accuracy of reconstructed images. Thus, these attenuation and scattering effects make the image reconstruction process in emission tomography a difficult ill-posed inverse problem.

The first part of the article briefly introduces medical imaging, especially neuroimaging. In the next part, an overview of emission tomography including PET and SPECT is described. The last part reviews methods for imaging reconstruction from projections in emission tomography.

2 Introduction to medical imaging and neuroimaging

Medical imaging is widely used not only for a clinical medicine but for a basic research. It can also be applied not only for human but for animal. Many medical imaging methods are non-invasive and various methodologies have been developed for target organs such as brain.

Neuroimaging depicts not only the structure but also the function of the nervous system, including brain. Neuroimaging falls into two broad categories:

1. Structural imaging
2. Functional imaging.

Magnetic resonance imaging (MRI), and computed tomography (CT) are the representatives of structural imaging. Positron Emission Tomography (PET), single photon emission CT (SPECT), functional MRI (fMRI), and functional near-infrared spectroscopy (fNIRS) are the representatives of functional imaging. Figure 1 shows various kinds of current neuroimaging not only in humans but also in small animals.

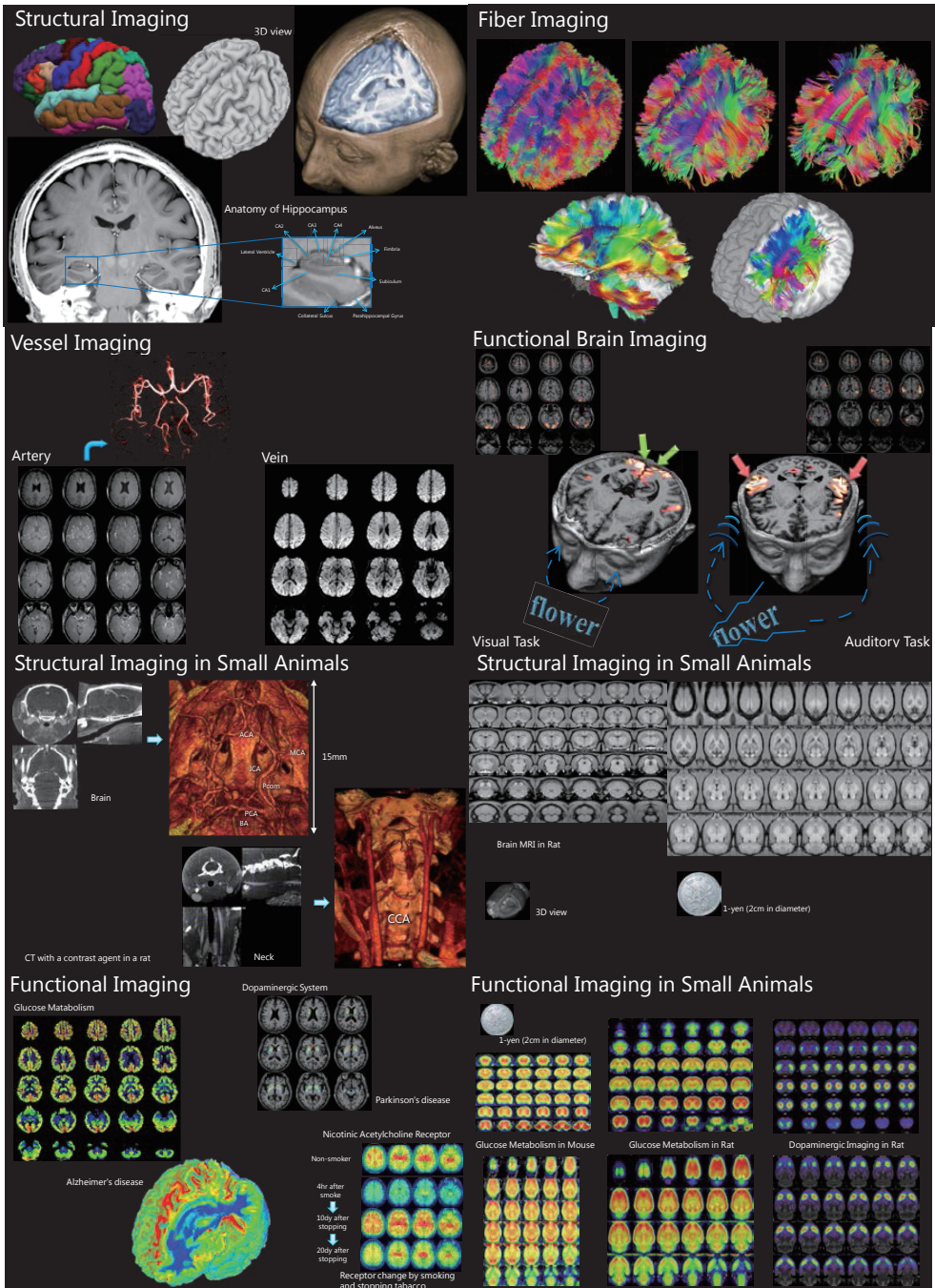


Figure 1. Various kinds of current neuroimaging in humans and animals

2.1 CT and MRI

CT is a structural imaging method that employs computer-based tomographic reconstruction to delineate bodily structures based on their ability to block an x-ray beam. CT examinations are preferable for patients who are claustrophobic or unable to remain still for longer durations, as is required for MRI imaging. On the other hand, MRI provides higher resolution to underlying tissue structure and water content, which allows for the detection of subtle anatomical and vascular changes associated with dementia. However, MRI is contraindicated in patients who have any ferromagnetic objects, are claustrophobia, or unable to remain still for longer durations. Table 1 shows a comparison chart between CT and MRI. Figure 2 shows representative human brain MRI.

	CT Scan	MRI
Radiation exposure	2 - 10 mSv (same as the background radiation in 3 to 5 years).	None
Cost	Less than MRIs (about half the price of MRI)	More expensive than CT
Time taken for complete scan	Less than 30 sec. less sensitive to patient movement than MRI.	Depending on sequences (1 - 20 min). totally 30 min.
Details of bony structures	Provides good details about bony structures	Less detailed compared to X-ray
Details of soft tissues	A major advantage is to image bone, soft tissue and blood vessels all at the same time.	Much higher soft tissue detail as compare to CT scan.
Intravenous Contrast Agent	Allergic reaction is rare but more common than MRI contrast. Risk of contrast induced nephropathy.	Very rare allergic reaction.
Comfort level for patient	Seldom creates claustrophobia	Anxiety caused by claustrophobia is common, as is annoyance over staying on a hard table for a long time.
Limitation for Scanning patients	CT is not recommended for pregnant women or children unless absolutely necessary.	Patients with Cardiac Pacemakers, tattoos and metal implants are contraindicated. Any ferromagnetic object may cause trauma/burn.

Table 1. A comparison chart between CT and MRI.

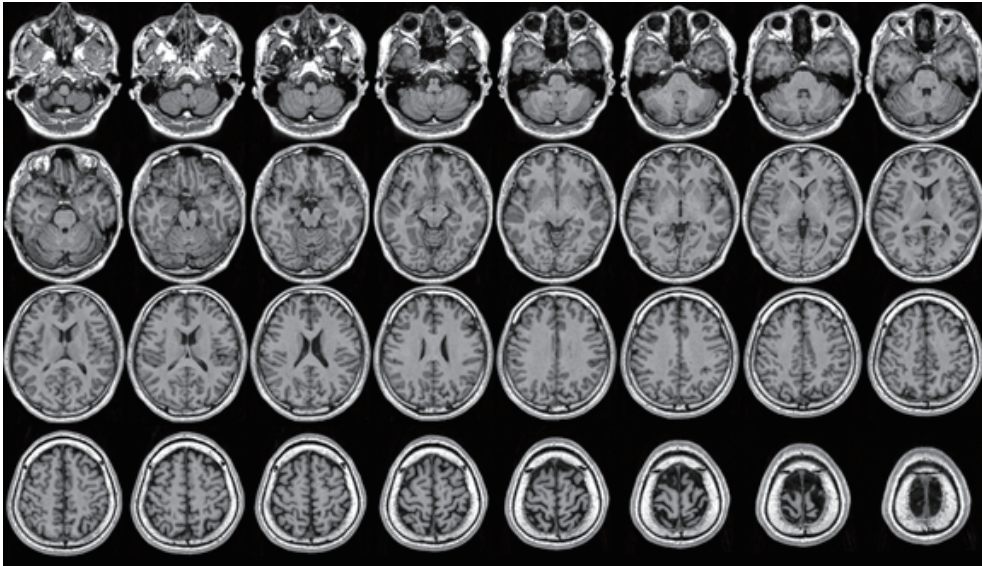


Figure 2. Representative human brain MRI.

2.2 PET and SPECT

In contrast to CT and MRI, PET and SPECT are chemical or functional imaging techniques. Table 2 shows a comparison chart between PET and SPECT. There are a lot of clinical applications in PET and SPECT. For example, using a radio-labeled analogue of glucose, ^{18}F -fluorodeoxyglucose (^{18}F -FDG), PET depicts glucose metabolism distribution. Also using a radio-labeled tracer, ^{123}I -isopropyl-iodoamphetamine (^{123}I -IMP), SPECT depicts cerebral blood flow distribution. They are usually used for diagnosing dementia, for example. Figure 3 shows a representative case of cerebral blood flow SPECT imaging in Alzheimer's disease and figure 4 also shows a representative case of cerebral blood flow SPECT imaging in dementia with Lewy bodies. Figure 5 shows a difference of reductions in cerebral blood flow between Alzheimer's disease and dementia with Lewy bodies. Thus, SPECT imaging reveals remarkable different patterns in regional cerebral blood flow between two representative causes of dementia, while structural changes by MRI or CT do not because functional changes usually precede structural ones. Figure 6 shows a comparison between SPECT (left) and PET (right) in a patient with Alzheimer's disease. Spatial resolution in PET is usually higher than that in SPECT.

Recent advances in PET and SPECT tracers, pathological biomarkers can be imaged by PET. The human amyloid PET imaging by ^{11}C -PiB was reported in 2004 by Klunk WE et al. Extracellular deposits of amyloid plaques are specific pathological findings in Alzheimer's disease

and amyloid plaques precedes clinical symptoms more than 10 years ago. Therefore, non-invasive detection of amyloid plaques can be useful for early diagnosis and early intervention. Figure 7 shows representative amyloid plaque-negative (left) and -positive (right) cases by human brain amyloid PET by ^{11}C -PiB. We can easily differentiate frontotemporal lobar degeneration, which is one of the common causes of dementia, from Alzheimer's disease by amyloid PET imaging. Thus, we can currently estimate brain pathology non-invasively.

	PET	SPECT
Principles	Emits positrons	Emits gamma radiations
Tracers	Physiological	Non-physiological
Supply	Usually in-house production (except ^{18}F -FDG)	Usually by vendors
Spatial resolution	Higher	Lower
Sensitivity	Higher	Lower
Cost	More expensive scanner	Less expensive scanner
Half-life of radiotracers	Limited half-life of radiotracers	Longer lived radiotracers

Table 2. A comparison chart between PET and SPECT.

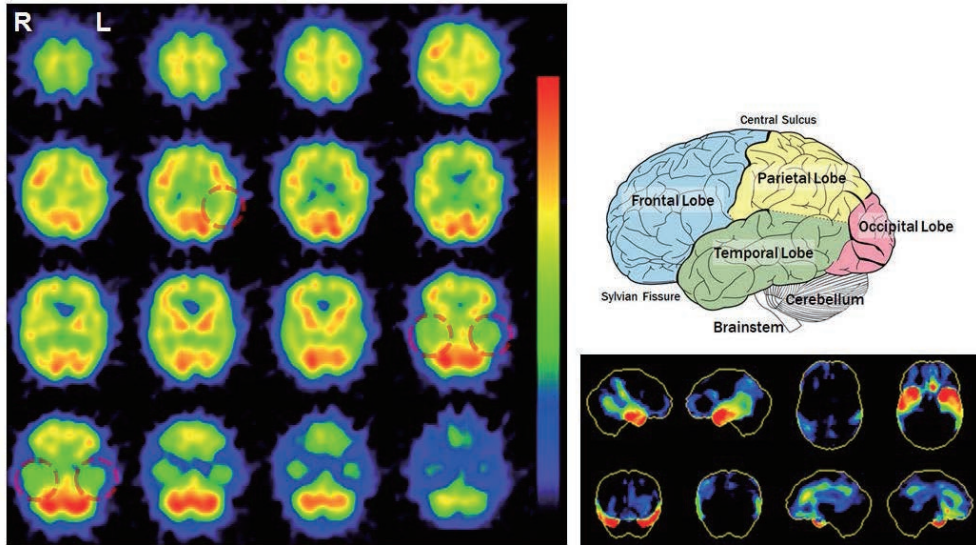


Figure 3. Cerebral blood flow images by ^{123}I -isopropyl-iodoamphetamine (^{123}I -IMP) SPECT in Alzheimer's disease. The patient was 81 year-old female. She developed a symptom of forgetfulness six years ago. Her mini-mental state examination (MMSE) score was 18/30. Regional cerebral blood flow in the temporal and parietal lobes were remarkably reduced.

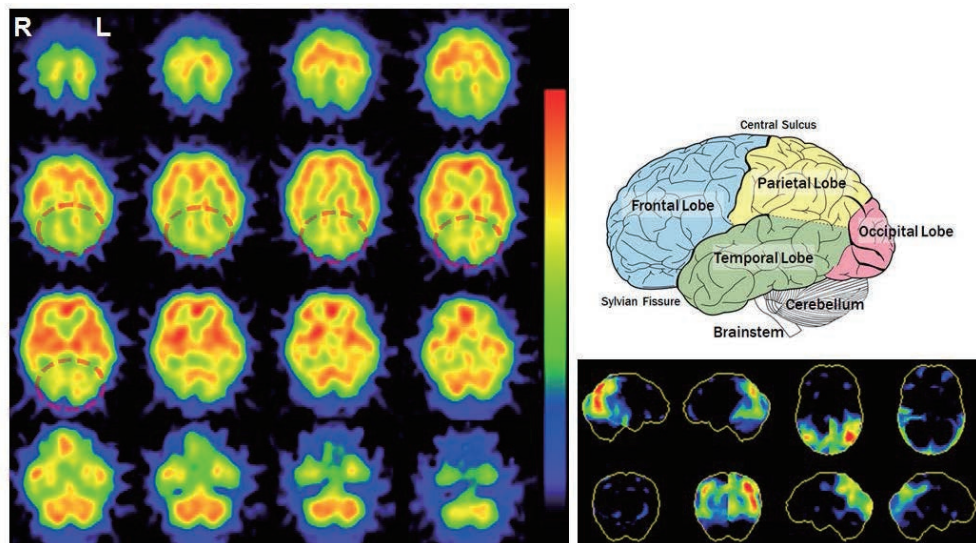


Figure 4. Cerebral blood flow images by ^{123}I -isopropyl-iodoamphetamine (^{123}I -IMP) SPECT in dementia with Lewy bodies. The patient was 70 year-old female. She developed symptoms of tremor, bradykinesia, and rigidity 12 years ago, visual hallucination five years ago, and forgetfulness two

years ago. Her mini-mental state examination (MMSE) score was 26/30. Regional cerebral blood flow in the occipital and parietal lobes were remarkably reduced.

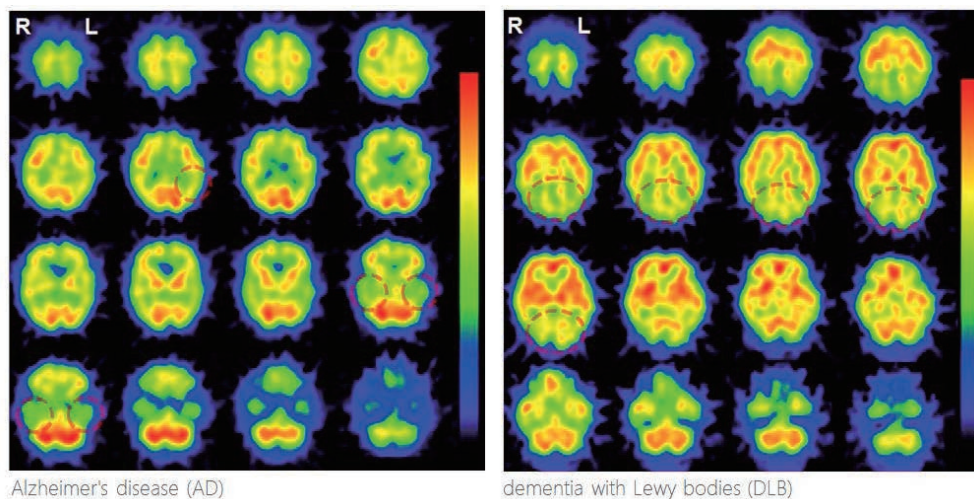


Figure 5. A difference of reductions in cerebral blood flow between Alzheimer's disease (left) and dementia with Lewy bodies (right).

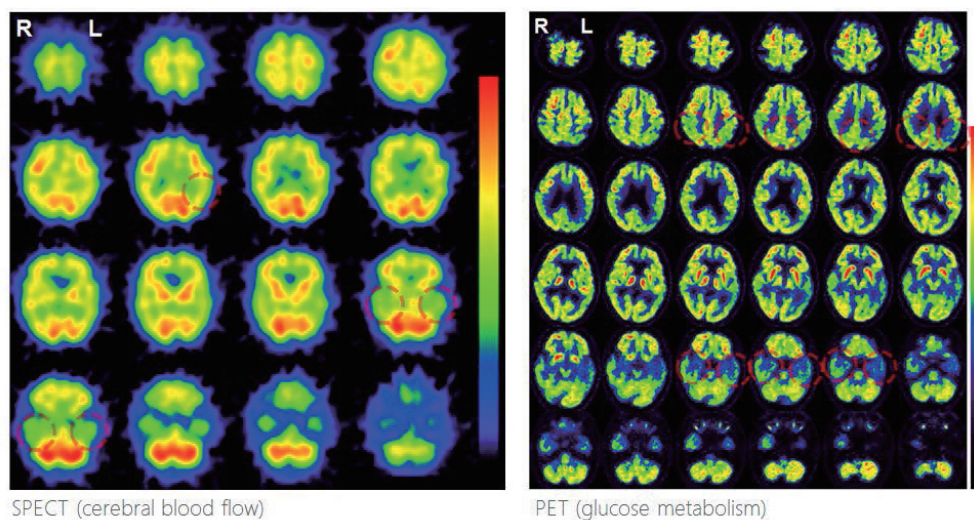
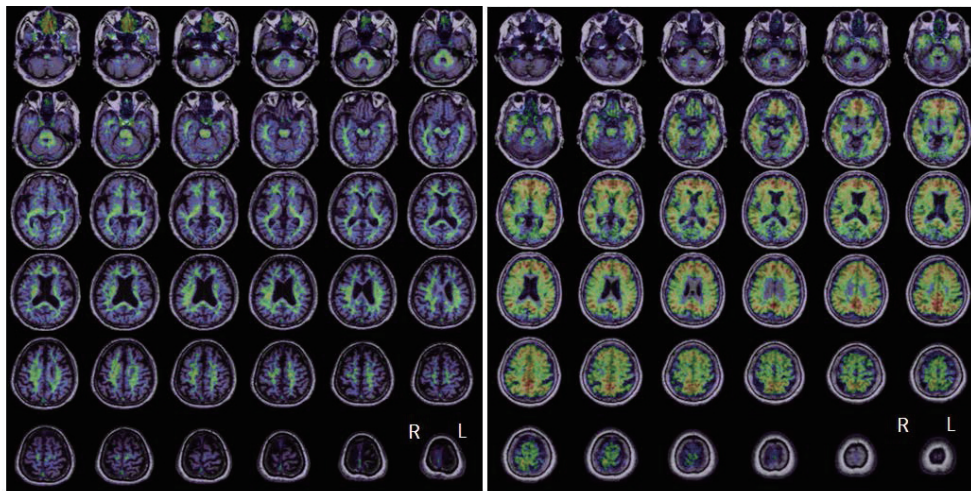


Figure 6. A comparison between SPECT (left) and PET (right) in a patient with Alzheimer's disease. Spatial resolution in PET is higher than that in SPECT.



Negative case (frontotemporal lobar degeneration)

Positive case (Alzheimer's disease)

Figure 7. Representative amyloid plaque-negative (left) and -positive (right) cases by human brain amyloid PET by ^{11}C -PiB. The PET images were overlaid on a structural MRI. We can easily differentiate frontotemporal lobar degeneration, which is one of the common causes of dementia, from Alzheimer's disease by amyloid PET imaging.

3 Emission tomography

Several forms of electromagnetic radiation (EMR) are used in medical imaging (Figure 8). Other new forms of EMR can be used for innovative imaging technology. Emission tomography is a medical imaging technique based on ionizing radiation (gamma-ray). It is often called "nuclear medicine". The fundamental principles of emission tomography are based on the history of nuclear physics, especially around the early 20th century (Figure 9). The X-ray was discovered by Wilhelm Conrad Röntgen in 1895 (Nobel Prize in 1901). The natural radioactivity was discovered by Antoine-Henri Becquerel in 1896 (Nobel Prize in 1903). The electron was discovered by Joseph John Thomson in 1897 (Nobel Prize in 1906). The alpha particle was discovered by Ernest Rutherford in 1899 (Nobel Prize in 1908). The positron was discovered by Carl David Anderson in 1932 (Nobel Prize in 1936). The neutron was discovered by James Chadwick in 1932 (Nobel Prize in 1935).

Emission tomography is a medical imaging technique based on the tracer principle by George de Hevesy (1885 - 1966) who got Nobel Prize in Chemistry 1943 "for his work on the use of isotopes as tracers in the study of chemical processes". Radioactive elements have identical chemical properties as the nonradioactive form (Figure 10). Radioactive compounds participate in organism's physiological processes in the same way as the non-radioactive substances. It can utilize ionizing radiation emitted by radiotracers injected into the body specifically targeting molecular pathways in tissue *in vivo* (Figure 11). A radioactive tracer is a chemical compound in which one or more atoms have been replaced by a radioisotope. Because it is applied in minimal amount, it has no pharmacologic effect *in vivo*. It can also be used to explore the mechanism of biochemical reactions by tracing the path that the radioisotope follows from reactant to product. For example, 370 MBq of ^{11}C -tracer necessary for a brain scan with ^{11}C -Raclopride (D_2 -receptor ligand) has no pharmacologic effect *in vivo* because it corresponds only to 100 picogram total mass injected.

Positron emission tomography (PET) and single photon emission computed tomography (SPECT) are representative examples of emission tomography and widely used as non-invasive diagnostic imaging in clinical medicine. Table 3 shows representative PET & SPECT tracers for human brain. Not only cerebral blood flow and metabolism but also neurotransmitter functions and neuropathological changes can be depicted non-invasively. PET and SPECT are functional imaging techniques, which provide information about metabolic and physiological processes. The reconstructed images reveal radiopharmaceutical distribution map and selected metabolic processes become visible. They are widely used in clinical routine as nuclear medicine in neurology, oncology, cardiology, and so on.

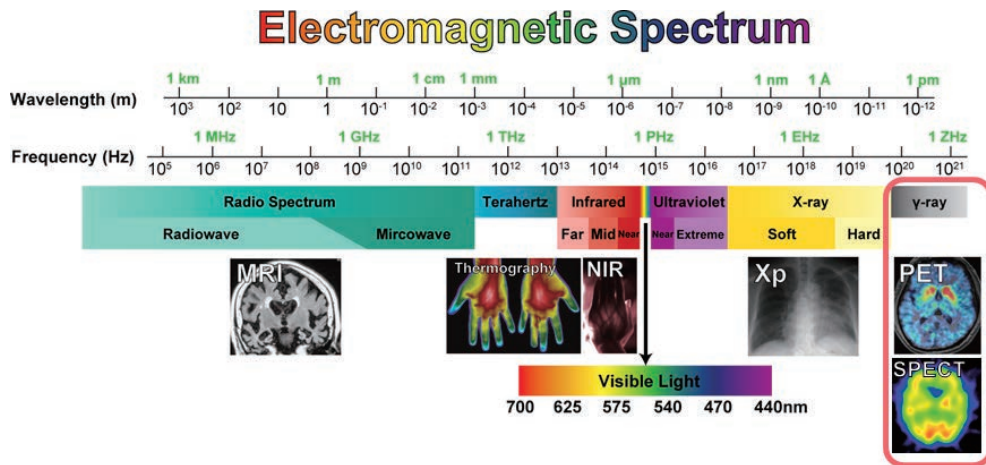


Figure 8. Electromagnetic spectrum for medical imaging. PET and SPECT use gamma-rays.

History of nuclear physics

- X-ray discovered by Wilhelm Conrad Röntgen in 1895 (Nobel Prize in 1901)
- Natural radioactivity discovered by Antoine-Henri Becquerel in 1896 (Nobel Prize in 1903)
- Electron discovered by Joseph John Thomson in 1897 (Nobel Prize in 1906)
- Alpha particle discovered by Ernest Rutherford in 1899 (Nobel Prize in 1908)
- Positron discovered by Carl David Anderson in 1932 (Nobel Prize in 1936)
- Neutron discovered by James Chadwick in 1932 (Nobel Prize in 1935)

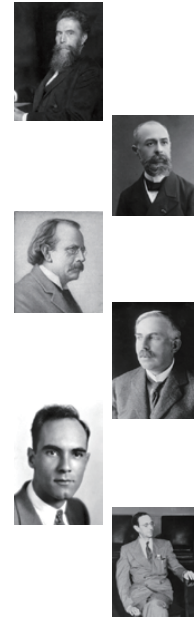


Figure 9. History of nuclear physics. All photos were cited from Wikipedia (<https://en.wikipedia.org/wiki/Wikipedia>).

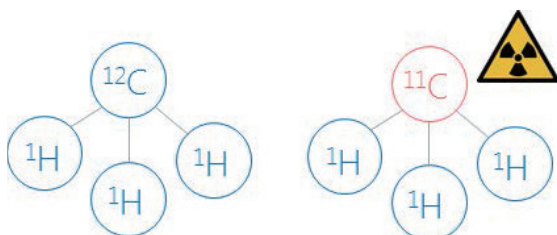


Figure 10. Radioactive elements (right) with identical chemical properties as the nonradioactive form (left).



Figure 11. Gamma-decay of selected radioactive elements can be used to track the flow and distribution of important substances in the body. Illustrations of the middle column were from 11. http://intranet.tdmu.edu.te.ua/data/kafedra/internal/pediatria2/classes_stud/en/med/lik/ptn/Propaedeutic%20pediatrics/3/Theme%2010%20Urinary%20system%20in%20children.htm.

Measuring functions			Tracers for PET	Tracers for SPECT
Cerebral blood flow and metabolism	Blood flow		$^{15}\text{O-H}_2\text{O}$	$^{99\text{m}}\text{Tc-HMPAO}$, $^{99\text{m}}\text{Tc-ECD}$, $^{123}\text{I-IMP}$
	Glucose metabolism		$^{18}\text{F-FDG}$	
	Oxygen metabolism		$^{15}\text{O-O}_2$	
Neurotransmitter functions	Cholinergic	Nicotinic acetylcholine receptor	$^{11}\text{C-nicotine}$, $2\text{-}^{18}\text{F-FA}$, $6\text{-}^{18}\text{F-FA}$	$^{123}\text{I-5IA}$
		Muscarinic acetylcholine receptor	$^{11}\text{C-scopolamine}$, $^{11}\text{C-benztropine}$, $^{11}\text{C-NMPB}$	$^{123}\text{I-QNB}$, $^{123}\text{I-IDEX}$
		Acetylcholinesterase activity	$^{11}\text{C-MP4A}$, $^{11}\text{C-MP4P}$, $^{11}\text{C-PMP}$	
		Butyrylcholinesterase activity	$^{11}\text{C-BMP}$, $^{11}\text{C-MP4B}$	
	Dopaminergic	Dopamine metabolism	$^{18}\text{F-DOPA}$	$^{123}\text{I-BZM}$
		Transporter	$^{11}\text{C-CFT}$, $^{18}\text{F-CFT}$, $^{11}\text{C-PE2I}$	$^{123}\text{I-}\beta\text{-CT}$, $^{123}\text{I-LFP-CT}$
		D ₁ receptor	$^{11}\text{C-SC23390}$	
		D ₂ receptor	$^{11}\text{C-raclopride}$, $^{11}\text{C-FLB457}$	
	Serotonergic	5-HT _{1A} receptor	$^{11}\text{C-WAY100635}$, $^{18}\text{F-MPPF}$	
		5-HT _{2A} receptor	$^{18}\text{F-altanserin}$	
		Transporter	$^{11}\text{C-DASB}$	
	GABAergic	Central benzodiazepine receptor	$^{11}\text{C-flumazenil}$	$^{123}\text{I-loxazepam}$
	Glutamate	Metabotropic glutamate receptor	$^{11}\text{C-ABP688}$	
	Noradrenergic	Transporter	$^{11}\text{C-RTI}$	
	Opioid		$^{11}\text{C-diprenorphine}$	
Neuropathology	Beta amyloid	$^{11}\text{C-PiB}$, $^{18}\text{F-AV45}$, $^{18}\text{F-FDDNP}$, $^{11}\text{C-BF227}$, $^{18}\text{F-GE067}$		
	Tau	$^{11}\text{C-PBB3}$, $^{18}\text{F-THK-5117}$		
	Alpha synuclein	$^{11}\text{C-BF227}$		
	Activated microglia	Peripheral benzodiazepine receptor	$^{11}\text{C-PK11195}$, $^{11}\text{C-DAA1106}$	

(Modified from Oishi N, 2011)

Table 3. PET & SPECT tracers for human brain. Tracers enclosed in red rectangles are clinically available in Japan. The table was modified by Oishi N 2011.

3.1 Principle of SPECT

In SPECT, data collection is based on the recording of photons detected independently from each other. Single-photon detection relies on the use of physical collimation in order to obtain directional information for the incident photons (Figure 12).

The following three types of decay are considered in SPECT tracers:

1. isomeric transition
2. electron capture
3. β decay

^{67}Ga , $^{99\text{m}}\text{Tc}$, ^{123}I , ^{111}In , ^{201}Tl , and ^{131}I are important radiotracers for SPECT. The first gamma camera called Anger camera (NaI-scintillator and photo multipliers) was invented by Hal Oscar Anger (1920-2005) in 1957. NaI (Tl), CsI, CsF, CaF₂ (Eu), BaF₂, BGO, CdWO₄, LaCl₃ (Ce), LaBr₃ (Ce), YAP are important gamma scintillator for SPECT.

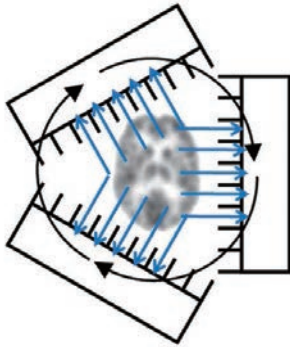
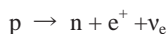


Figure 12. Detection of photons is performed by a gamma camera comprising a single or multiple detector heads.

3.2 Principle of PET

PET is based on the coincident detection of a pair of positron annihilation γ -rays (Figure 13). It provides biochemical information about a human body by using positron-emitter-labeled pharmaceuticals. It also has higher performance for resolution and quantitative accuracy compared with a SPECT system.

The positron is the anti-particle of electron and its charge is positive ($m = 9.1 \times 10^{-28}$ g ; $e = 4.8 \times 10^{-19}$ C). Positrons are emitted from unstable nuclei which are proton-rich. A positron (e^+) and a neutrino (ν_e) are emitted from a nucleus by the β^+ decay:



A positron travels a short distance and is annihilated with an electron in a substance. The positron-range depends on the positron energy. The positron-range contributes uncertainty to the localization of the originating nucleus and imposes a lower limit in the spatial resolution of PET. Positron range increases when increasing initial energy of the positron. When a positron is combined with an electron, they are annihilated and produce two 511-keV γ -rays. They are emitted in the direction of around 180 degrees to each other. A deviation from the strict 180-degree angle between the two photons contributes a further uncertainty to the localization of the annihilation, which can reduce spatial resolution. The reduction depends on the distance between the two coincidence detectors. ^{11}C , ^{15}O , ^{18}F , ^{64}Cu , ^{68}Ga , ^{76}Br , ^{124}I , ^{89}Zr are important radionuclides for PET. The scintillation detectors for PET convert radiation to visible light, detected by PMT, SiPMT or APD-, PIN-diodes. Semiconductor detectors (CdTe or ZnCdTe) are also used for PET. NaI (Tl), BaF₂, BGO, LSO are examples of gamma scintillator for PET. When two photons are detected by two opposing detectors simultaneously (i.e. within a narrow time interval of typically 4–12 ns, state-of-the-art

interval of a 200ps–2ns), their originating positron annihilation event is placed along the volume defined by the two detectors, which is called a line of response (LOR). The following four types of possible coincidences in PET are considered: (Schibli R. 2013) (Figure 14)

1. True coincidences
2. Scatter coincidences
3. Random coincidences
4. γ -coincidences

In true coincidences, the line drawn between the two hit detector elements for that event passes through the point of origin. Scatter coincidences, where one or both 511-keV photons undergo Compton scatter, random coincidences, which occur when two distinct radionuclei contribute one detected photon, and γ -coincidences, which occur when a 511 keV photon and a γ -photon are detected, are undesirable coincidences for PET. These photons can interact with electrons of the surrounding medium, which causes either the photoelectric absorption or scattering of the photons. Photons are detected by tracking their energy loss inside the crystals because of photoelectric absorption and Compton-scattering events, discarding those events that are outside a given energy range. However, photons can transfer their energy after arbitrary number of bounces, possibly occurring in several crystals away from their incident location known as inter-crystal scattering, or simply leave the system unnoticed, described by detector sensitivity. The system registers a coincidence hit if two photons are detected in the given time window and energy range.

The following physical effects should be considered for PET reconstructions:

1. Positron range
2. Acolinearity of the annihilation γ -ray
3. Detector efficiency non-uniformity
4. Crystal size (Sampling interval)
5. Statistical Error
6. Counting Loss
7. Detector Penetration (Depth of Interaction)

The positron range results in positional inaccuracies in tomography reconstruction. Because the mean free-path length of positrons is typically in a range of up to a few millimeters in tissues, positron range is one of the most important limiting factors of the resolution in PET. The spatial density on Cartesian axis x of the annihilation of a positron born in the origin can be approximated by the following:

$$P(x) = C e^{-k_1 x} + (1 - C) e^{-k_2 x}$$

Parameters C, k_1, k_2 depend on the actual radiotracer (Levin CS, 1999). The material of the object, and can be determined by fitting this function onto data measured or simulated e.g. with a Monte-Carlo simulation-based open source software named GATE (Jan S, 2004;

<http://www.opengatecollaboration.org>) (Milan M, 2014). Because of the conservation of momentum, the initial directions of the photons have an angular uncertainty, known as acollinearity. The acollinearity angle is a Gaussian distribution that has been measured to approximately 0.5 degrees FWHM, which introduces a 2-3 mm and a 0.3-0.4 mm positional inaccuracy to human and small animal PET imaging, respectively. The image blur due to the acollinearity angle can be more severe when the inner diameter of the PET ring is increased (Burdette DJ, 2009; Milan M, 2014).

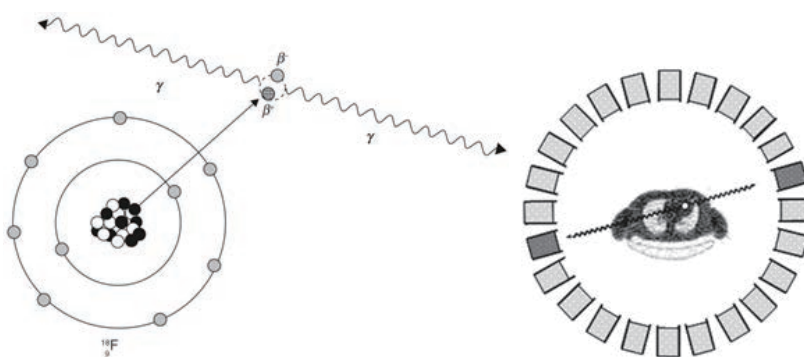


Figure 13. Positron emission and annihilation (left) and detection of annihilation photons by two opposing detectors in coincidence (right). (Livieratos L. 2012)

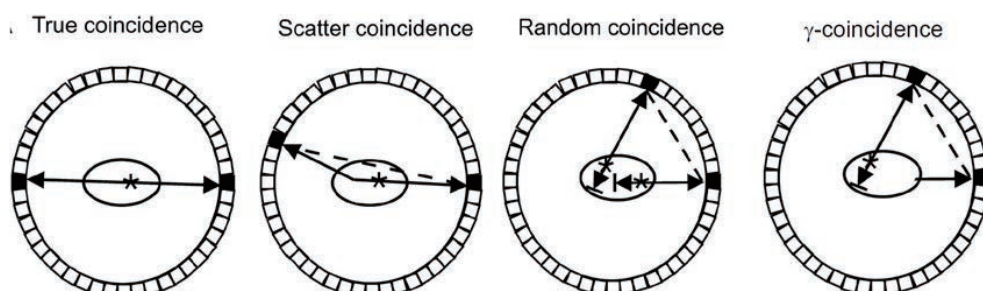


Figure 14. Four types of possible coincidences in PET (Schibli R. 2013)

4 Inverse problems in emission tomography

The image reconstruction process from projections in emission tomography is an inverse problem for the photon transport equation if electromagnetic wave properties such as polarization can be ignored. Photons emitted from radiotracers undergo a number of interactions with matter. In the range of PET and SPECT, emitted photon interactions with matter occur in the following three ways: photoelectric effect, Compton scattering, and Rayleigh scattering. The majority of primary emitted photons are either completely absorbed without reaching the detectors or deviate from their original emission directions. It causes events to be either lost or misplaced and distorts the projection data and degrades the quantitative accuracy of reconstructed images. Thus, these attenuation and scattering effects make the image reconstruction process in emission tomography a difficult ill-posed inverse problem.

The advent of computed tomography (CT) in 1973 was the beginning of the new mathematical discipline of imaging. It leads to a mathematical sophistication that was unheard of in imaging before. Before inverse problems in emission tomography, those in computed tomography are reviewed.

4.1 Inverse problems in CT

Allan Cormack reinvented it for tomography in 1963. Cormack proposed using Radon transform, which was invented in 1917 for pure mathematical reasons, to reconstruct the density of the body from X-ray images from different directions and won the Nobel Prize in Medicine in 1979. He gave a mathematical formula to do the reconstruction and implemented his ideas by building and testing a prototype CT scanner. Godfrey Hounsfield shared the prize for his independent work deriving an algorithm and making a medical CT scanner.

The simplest mathematical model of CT assumes that the scanner measures the line integrals of the absorption coefficient $f(x)$. This gives rise to the Radon transform:

$$(Rf)(\theta, s) = \int_{x \cdot \theta = s} f(x) dx, \quad \theta \in S^1, s \in \mathbf{R}^1$$

and the mathematical problem is to invert R (Natter F. 2006). In principle, this was solved by Radon's 1917 inversion formula

$$f = R^* K g, \quad g = R f$$

where R^* is the backprojection (the adjoint of R),

$$(R^*g)(x) = \int_{S^1} g(\theta, x \cdot \theta) d\theta$$

and K the composition of the derivative and the Hilbert transform (Natter F. 2006):

$$(Kg)(s) = \frac{1}{4\pi^2} \int \frac{g'(t)}{s-t} dt.$$

CT is formulated as an inverse problem for the photon transport equation. Introducing the density $u(x, \theta)$ of the particles at $x \in \Omega$ travelling in direction $\theta \in S^1$ we have in $\Omega \times S^1$

$$\theta \cdot \nabla u(x, \theta) + f(x)u(x, \theta) = \delta(x - x_0)\delta(\theta - \theta_0)$$

and, in the absence of exterior radiation,

$$u(x, \theta) = 0, \quad x \in \partial\Omega, \quad \theta \cdot \nu_x \leq 0$$

with ν_x the exterior normal at $x \in \partial\Omega$. It is a reasonable problem that admits a unique solution under natural conditions. The inverse problem of CT consists in finding f from

$$u(x, \theta), \quad x, x_0 \in \partial\Omega, \quad \theta = (x - x_0)/|x - x_0|.$$

The inverse problem reduces immediately to the Radon transform since

$$u(x, \theta) = H((x - x_0) \cdot \theta) \delta((x - x_0) \cdot \theta^\perp) \delta(\theta - \theta_0) e^{\int_{x_0}^x f ds}.$$

(Natter F. 2006)

The photon transport equation ignores such electromagnetic wave properties as polarization, and such particle properties as inelastic collisions although it is generally sufficient to describe the interaction of electro-magnetic radiation in tissue for many medical imaging modalities. It needs several following assumptions:

1. The system is assumed to be steady-state.
2. Effects of scatter and diffraction are assumed to be zero.
3. Emissions from internal sources are assumed to be zero.

4.2 Inverse problems in SPECT

SPECT is also formulated as an inverse problem for the photon transport equation. Introducing the density $u(x, \theta)$ of the particles at $x \in \Omega$ travelling in direction $\theta \in S^1$ with the attenuation $a(x)$, we have in $\Omega \times S^1$

$$\theta \cdot \nabla u(x, \theta) + a(x)u(x, \theta) = f(x) \quad \text{in } \Omega \times S^1 \quad (4.2.1)$$

$$u(x, \theta) = 0, \quad x \in \partial\Omega, \quad \theta \cdot \nu_x \leq 0 \quad (4.2.2)$$

A radiotracer is injected and the radiation is measured outside the body in a tomographic fashion. We seek the distribution $f(x)$ of the radiopharmaceutical agent. Two following inverse problems are proposed (Natter F. 2006):

Inverse problem 1: Find a and f from $u(x, \theta)$, $x \in \partial\Omega$, $\theta \in S^1$.

Inverse problem 2: Assume a to be known. Find f from $u(x, \theta)$, $x \in \partial\Omega$, $\theta \in S^1$.

The inverse problem 1 is non-linear. It is not uniquely solvable. However, if a is modelled by a few parameters, these parameters can be determined in favorable circumstances (Natter F. 2006). The inverse problem 2 (a so-called inverse source problem) is linear. It corresponds to the case in which the attenuation a of the body is known. The inverse problem 2 reduces to the attenuated Radon transform

$$(R_a f)(\theta, s) = \int_{x \cdot \theta = s} f(x) e^{-\int_a^\infty a(x+s'\theta) ds'} dx \quad (4.2.3)$$

since the solution of (4.2.1), (4.2.2) is

$$u(x, \theta) = \int_{-\infty}^0 f(x + s\theta) e^{\int_a^\infty a(x+s'\theta) ds'} ds$$

which is just a reparameterization of (4.2.3) (Natter F. 2006). If a is constant on the support of f , an inversion formula for R_a has been known for a long time. However, it has been an open problem whether R_a is always injective for about 20 years. It was an important breakthrough that Novikov recently gave an explicit formula for the inverse of R_a for arbitrary Hölder continuous a (Novikov RG, 2000; 2002). R_a admits an explicit inversion formula very similar to Radon's inversion formula: If $g = R_a f$, then

$$f = \frac{1}{4\pi} Re \operatorname{div} R_{-a}^* (\theta e^{-h} H e^h g)$$

where H is the Hilbert transform, $h = 1/2(I + iH)R_a$ and R_a^* is the (weighted) backprojection

$$\begin{aligned} (R_a^* g)(x) &= \int_{S^1} e^{-(Da)(x, \theta^\perp)} g(\theta, x \cdot \theta) d\theta \\ (Da)(x, \theta) &= \int_0^\infty a(x + s\theta) ds. \end{aligned}$$

This formula was obtained by Novikov in 2000. Natterer later supplied a simpler proof of Novikov's formula (Natterer F, 2001). Novikov also proved injectivity for the attenuated Radon transform with the angle variable θ restricted to an arbitrarily small open set (Novikov RG, 2002). The Novikov's explicit inversion formula was applied not only to parallel beam geometries but also nonparallel ones, which are often used in the current SPECT scanners (Li T, 2005; Boman J. 2004; Natterer F. 2006).

4.3 Inverse problems in PET

Photons can interact with electrons of the surrounding medium, which results in either the absorption or scattering of the photons. Because the mean free-path length of γ -photons inside tissues is comparable to the diameter of the human chest (it is 10 cm in water for a 511 keV photon), accurate attenuation and scattering models become crucial especially for human PET: a roughly 30–50% of the photons get scattered before reaching the detectors, depending on the scanner geometry and the size of the subject (Burdette DJ, 2009; Milan M, 2014). To describe photon–volume interaction, it is considered how the photons go through participating media. Let us consider the radiant intensity I on a linear path of equation $\vec{l}(t)=\vec{l}_0 + \vec{\omega}t$. The change of radiant intensity I on differential length dt and of direction $\vec{\omega}$ depends on the following different phenomena (Burdette DJ, 2009; Milan M, 2014):

1. Absorption
2. Out-scattering
3. Emission
4. In-scattering

1. Absorption

The intensity is decreased if photons collide with the electrons or atomic cores and are absorbed due to the photoelectric effect. The effect is proportional to the number of photons entering the path, i.e. the intensity and the probability of this type of collision. If the probability of such collision in a unit distance is σ_a , called absorption cross section, then the probability of collision along distance dt is $\sigma_a(\vec{l})dt$. Thus, the total intensity change due to absorption is $-I(\vec{l})\sigma_a(\vec{l})dt$. The probability of the absorption due to the photoelectric effect depends on the material (grows rapidly with the atomic number) and is inversely proportional to the cube of the photon energy:

$$\sigma_a(\epsilon_0) \approx \frac{\sigma_a(1)}{\epsilon_0^3}.$$

where $\epsilon_0 = E_0/(m_e c^2)$ is the incident photon energy E_0 relative to the energy of the electron. m_e is the rest mass of the electron, c is the speed of light, and $m_e c^2 = 511$ keV is the energy of the resting electron (Burdette DJ, 2009; Milan M, 2014).

2. Out-scattering

The radiation is scattered out from its path if photons collide with the material and are reflected after collision. The effect is proportional to the number of photons entering the path, and the probability of such type of collisions in a unit distance, which is described by the scattering cross section σ_s . The total out-scattering term is $-I(\vec{l})\sigma_s(\vec{l})dt$ (Burdette DJ, 2009; Milan M, 2014).

3. Emission

The intensity can be increased by the photons emitted by the medium. This increase in a unit distance is expressed by the emission density $I^e(\vec{l})$. We usually assume that the emission is isotropic, i.e. it is independent of the direction (Burdette DJ, 2009; Milan M, 2014).

4. In-scattering

Photons originally flying in a different direction can be scattered into the considered direction. The expected number of scattered photons from differential solid angle $d\omega_{in}$ equals to the product of the number of incoming photons and the probability that a photon is scattered in distance dt , and the conditional probability density that the photon changes its direction from solid angle $d\omega_{in}$ to $\vec{\omega}$ provided that scattering happens. The conditional probability density is called the phase function $P(\vec{\omega}_{in}, \vec{\omega})$, which depends on the angle θ between the incident and scattered directions:

$$\frac{d\sigma_s}{d\omega} = \sigma_s(\vec{x}) \cdot P(\vec{\omega}_{in}, \vec{\omega}), \quad P(\vec{\omega}_{in}, \vec{\omega}) = P(\vec{\omega}_{in} \cdot \vec{\omega}) = P(\cos \theta).$$

Taking into account all incoming directions Ω of a sphere, the radiance increase due to in-scattering is:

$$\sigma_s(\vec{l}) dt \left(\int_{\Omega} I^{in}(\vec{l}, \vec{\omega}_{in}) P(\vec{\omega}_{in} \cdot \vec{\omega}) d\omega_{in} \right).$$

(Burdette DJ, 2009; Milan M, 2014).

There are two types of scattering during photon traveling:

1. Rayleigh scattering
2. Compton scattering

1. Rayleigh scattering

If the photon energy does not change during collision, i.e. elastic scattering, which happens when the photon collides with an atomic core or a base state, not excited electron, then the scattering is said to be coherent or Rayleigh scattering. Rayleigh scattering was discovered by John William Strutt, 3rd Baron Rayleigh (Nobel Prize for Physics in 1904). Rayleigh scattering can be described by the Rayleigh phase function

$$P_{RS}(\cos \theta) = \frac{3}{16\pi} (1 + \cos^2 \theta)$$

if the particle size is much smaller (at least 10 times smaller) than the wavelength of the radiation wave, which is the case of electrons and photons less than 1 MeV energy. As typical detectors are sensitive in the 100–600 keV range, photons outside this range can be ignored. In this energy range

and typical materials like water, bone and air, Compton scattering is far more likely than Rayleigh scattering, thus Rayleigh scattering can be ignored (Burdette DJ, 2009; Milan M, 2014).

2. Compton scattering

If energy is exchanged between the photon and the electron during scattering, i.e. inelastic scattering, the scattering is said to be incoherent or Compton scattering. Compton scattering was discovered by Arthur Holly Compton (Nobel Prize for Physics in 1927). The energy change is defined by the Compton law:

$$\epsilon = \frac{1}{1 + \epsilon_0(1 - \cos \theta)}$$

where $\epsilon = E_1/E_0$ expresses the ratio of the scattered energy E_1 and the incident energy E_0 , and $\epsilon_0 = E_0/(m_e c^2)$ is the incident photon energy relative to the energy of the electron. The differential of the scattering cross section, i.e. the probability density that the photon is scattered from direction $\vec{\omega}$ to $\vec{\omega}_{in}$, is given by the Klein-Nishina formula :

$$\frac{d\sigma_s^{CS}}{d\omega} \propto \epsilon + \epsilon^3 - \epsilon^2 \sin^2 \theta$$

where the proportionality ratio includes the classical electron radius and the electron density of the material (Burdette DJ, 2009; Milan M, 2014). Instead of using these physical parameters explicitly, the measured cross section of Compton scattering on energy level 511 keV, i.e. $\epsilon_0 = 1$ for the representation of the material should be used. From this, the phase function that is supposed to be normalized can be found as:

$$P_{KN}(\cos \theta) = \frac{\epsilon + \epsilon^3 - \epsilon^2 \sin^2 \theta}{\int_{\Omega} \epsilon + \epsilon^3 - \epsilon^2 \sin^2 \theta d\omega}$$

The energy dependence of the Compton scattering cross section can be computed from the scaling factor in the Klein-Nishina formula:

$$\sigma_s^{CS}(\epsilon_0) = \sigma_s^{CS}(1) \cdot \frac{\int_{\Omega} \epsilon(\epsilon_0) + \epsilon^3(\epsilon_0) - \epsilon^2(\epsilon_0) \sin^2 \theta d\omega}{\int_{\Omega} \epsilon(1) + \epsilon^3(1) - \epsilon^2(1) \sin^2 \theta d\omega}$$

The ratio between $\sigma_s^{CS}(\epsilon_0)$ and $\sigma_s^{CS}(1)$ is depicted as a function of relative energy ϵ_0 (Burdette DJ, 2009; Milan M, 2014).

Taking into account all contributions, intensity $I(\vec{l}, \vec{\omega}, \epsilon)$ of a particle flow at energy level ϵ satisfies an integro-differential equation:

$$\vec{\omega} \cdot \vec{\nabla} I(\vec{l}, \vec{\omega}, \epsilon) = \frac{dI}{dt} = -\sigma_t(\vec{l}, \epsilon) I(\vec{l}, \vec{\omega}, \epsilon) + I^e(\vec{l}, \epsilon) + \int_{\Omega} I(\vec{l}, \vec{\omega}_{in}, \epsilon_{in}) \frac{d\sigma_s(\vec{l}, \vec{\omega}_{in} \cdot \vec{\omega}, \epsilon_{in})}{d\omega_{in}} d\omega_{in}$$

where $\sigma_t(\vec{l}, \epsilon) = \sigma_a(\vec{l}, \epsilon) + \sigma_s(\vec{l}, \epsilon)$ is the extinction parameter that is the sum of the absorption cross section and the scattering cross section, $I^e(\vec{l}, \epsilon)$ is the source intensity, Ω is the directional sphere, ϵ_{in} and ϵ are the incident and scattered photon energies, respectively. Scattered photon energy ϵ is equal to incident photon energy ϵ_{in} for coherent scattering. For incoherent scattering, the scattered and incident photon energies are related via scattering angle $\cos \theta = \vec{\omega} \cdot \vec{\omega}_{in}$ as stated by the Compton law (Milan M, 2014).

References

- Bal G, Tamasan A. Inverse source problems in transport equations. *SIAM J. Math. Anal.* 39:57–76,2007
- Boman J, Stromberg JO. Novikov's Inversion Formula for the Attenuated Radon Transform—A New Approach. *The Journal of Geometric Analysis.* 14:185–98,2004
- Burdette DJ. A study of the effects of strong magnetic fields on the image resolution of pet scanners. PhD Thesis. 2009
- Kösters T, Natterer F. Scatter Correction in PET Using the Transport Equation. *Nuclear Science Symposium Conference Record, 2006. IEEE.* 6:3305–9, 2006
- Li T, You J, Wen J, Liang Z. An efficient reconstruction method for nonuniform attenuation compensation in nonparallel beam geometries based on Novikov's explicit inversion formula. *IEEE Trans Med Imaging.* 24:1357–68,2005
- Livieratos L. Basic Principles of SPECT and PET Imaging. in *Radionuclide and Hybrid Bone Imaging.* Springer, pp. 344–359, 2012.
- Milan M. GPU-based particle transport for pet reconstruction. PhD Thesis. 2014
- Natterer F. Inversion of the attenuated Radon transform. *Inverse Problems.* 17:113–119,2001
- Natterer F. Scatter correction in PET based on transport models. *Angewandte Mathematik und Informatik.* 2004
- Natterer F. *Imaging and Inverse Problems of Partial Differential Equations.* 2006
- Novikov RG. An inversion formula for the attenuated X-ray transformation. *Ark Mat.* 40:145–167,2002
- Schibli R. PET and SPECT: Physical principles and basic strategies of radiotracer development for preclinical and clinical use. 2013.
- Zvolský M. *Tomographic Image Reconstruction. An Introduction.* Lecture on Medical Physics. 2013

Numerical and experimental studies on quantification of the optical properties by use of photoacoustic measurement

Shinpei Okawa, Takeshi Hirasawa, Toshihiro Kushibiki, and Miya Ishihara

Department of Medical Engineering, National Defense Medical College, 3-2 Namiki,
Tokorozawa, Saitama 359-8513, Japan
okawa@ndmc.ac.jp

Abstract

Photoacoustic (PA) imaging in various biomedical applications were summarized, and some studies on the quantification of the optical properties of the biological tissues from the PA pressure wave were reported in this presentation. The optical properties such as scattering and absorption coefficients depend on the concentration of the photon absorbers in the biological tissues, such as oxy- and deoxy-hemoglobin, which can be useful for monitoring patients' conditions and diagnosing cancers. We have tried to estimate the optical properties of rabbit organs *in vitro*. The PA pressure wave from the sample of organs was measured to estimate the optical properties of the organs. Additionally, the image reconstruction of the distribution of the absorption coefficient has been tried. We tested the reconstruction algorithm to investigate the influences of some approximations used in the algorithm by some numerical simulations and phantom experiments. The effect of the regularization technique minimizing L_1 -norm of the solution was also investigated.

1 Introduction

The optical properties such as the scattering and absorption coefficients determine the light propagation in the biological medium which scatters and absorbs the light [1]. The optical properties depend on the concentration of the photon absorbers in the biological tissues, such as oxy- and deoxy-hemoglobin, which can be useful for monitoring patients' conditions and diagnosing cancers. Biomedical optical measurement technologies such as diffuse optical tomography and optical topography employing near-infrared spectroscopic technique have been developed in recent years [2,3]. The optical techniques are noninvasive and transportable so that they can be applied to various medical imaging and diagnoses, such as breast cancer diagnosis and monitoring brain activities which are associated with the changes in local blood concentration [4-6].

One of the technical issues of the optical techniques is the low spatial resolution. The biological medium scatters light so strongly that it is difficult to locate the changes in the absorption. Compared

to the ultrasound imaging, the optical techniques can not image the imaging target deeply inside the biological medium owing to the scattering by the tissues.

On the other hand, photoacoustic (PA) imaging employing optical and ultrasound technologies has been studied to resolve the technical issues of the optical technique [7,8]. In the PA measurement, light is used to excite the PA pressure wave, which is detected by the ultrasound transducer. By applying the sophisticated ultrasound imaging technique, the image of the photon absorber generating the PA pressure wave can be obtained with higher spatial resolution.

This paper summarizes the presentation by the authors in Institute of Mathematics for Industry, Kyushu University. In the presentation, the PA imaging in various biomedical applications were introduced, and the quantification of the optical properties of the biological tissues from of the photoacoustic (PA) pressure wave are reported. From the features of the PA pressure wave, the scattering and absorption coefficient of the biological tissues. The image reconstruction by using the equations describing the propagation of the light and PA pressure wave was discussed with numerical simulation and phantom experiment. The presentation slides are included at the end of this paper.

2 PA measurement and its applications

The PA pressure wave is generated by the irradiation of pulse laser light. The light energy absorbed by the biological tissues is transformed to heat. As a result, the thermal expansion of the heated tissue causes ultrasound referred to as the PA pressure wave propagating in the biological medium. Since the PA pressure wave depends on the distribution of the light energy absorbed by the tissues, the detected PA pressure wave contains the information about the absorption and scattering coefficients of the tissues. The amplitude depends on the absorbed light energy. The time of arrival depends on the distance between the photon absorber and the detector. Therefore the image of the distribution of the photon absorbers can be reconstructed from the PA signals (Slide 3).

To obtain the PA image, there are two approaches. One of the approaches is PA microscopy (PAM) [8], which does not need image reconstruction. To obtain the microscopy image, the PA pressure source needs to be located. One method called acoustic-resolution PAM (AR-PAM) uses acoustic lens to specify which the PA wave comes from. And the other is optical-resolution PAM (OR-PAM) which uses optical lens to specify the position of the PA pressure source (Slide 4). The spatial resolution of the PAM image is so high that they can image organelle (cell nucleus) and cells. But they cannot image deep region of the biological tissues, because the light is diffused by the tissues.

Another approach is PA computed tomography with image reconstruction based on the equations of light and PA pressure wave propagation [8]. In the reconstruction of the tomographic image image reconstruction method conventionally used in the medical ultrasound imaging can be used basically. One can use the circular backprojection and delay-and-sum backprojection [9] (Slide 5).

The methods calculate the distance between the detector and the source. By adding up the PA amplitude in the pixel at the calculated distance, the true source position is highlighted. Xu et al. proposed the universal backprojection method for media with various shapes [10].

A lot of applications of the PA imaging have been reported. Wang et al. presented the PA measurement methods and obtained PA images in their review article [11]. The oxygen saturations of the blood vessels in mouse ear are obtained by OR-PAM. Oxy and deoxy hemoglobin have different optical properties, so by use of two wavelength of the light, it is possible to quantify oxy and deoxy-hemoglobin. The blood vessels in palm are imaged by the AR-PAM. This is the tomographic image of the sentinel lymph node of rat stained by methylene blue [12]. The change in hemoglobin concentration in rat brain was imaged by PA computed tomography. Cell-nuclear images of *ex vivo* and *in vivo* tissue were acquired with ultraviolet photoacoustic microscopy at a wavelength of 250 nm [13]. The epithelial cells in the *ex vivo* lip of a mouse were imaged by Yao et al. The PA image of melanoma cells in a scaffold were acquired at 14 days post-seeding by Zhang et al [14].

The group in University College London succeeded in precise PA imaging of blood vessels in human palm and small animals by using the Fabry-Perot film ultrasound transducer and the light with wavelengths from 590 nm to 800 nm [15,16]. The group in National Defense Medical College applied PA imaging for monitoring the neurovascular bundles and cancers in prostate [17]. By monitoring the blood vessels neighboring to the nerve fibers during the prostatectomy, it is expected that the sexual function of the patient will be preserved. The imaging from organelle to organs is possible by photoacoustic technology [11] with appropriate wavelength of the pulse laser and ultrasound transducer.

3 Quantitative PA measurement

The PA pressure wave depends on the absorbed light energy. Therefore, the optical properties of the imaging target can be quantified from the detected PA pressure wave. The optical properties, such as the absorption and scattering coefficients depend on the constituent and concentration of the photon absorber such as oxy- and deoxy-hemoglobin in the imaging target [1] (Slides 7, 8). So, by the quantitative PA measurement, the condition of the target containing the photon absorber can be investigated quantitatively.

To achieve the quantitative PA measurement, the equations describe the generation and propagation of the PA pressure wave. The light propagation in the biological medium is the radiative transport of the energy. So the radiative transfer equation (RTE) describes the phenomenon in the biological medium accurately [18-21] (Slide 9). The absorption and scattering coefficients are the parameters of the RTE. Some methods to approximate the light propagation are known.

Monte Carlo method approximates the light propagation statistically [22]. It tracks the movements of photon packets. The movement of the photon packet is determined by use of the

optical properties and the probability density function called the scattering phase function. Photon diffusion equation (PDE) is derived from the first-order approximation using spherical harmonic expansion of RTE [18]. When the PDE is used, the isotropic scattering and isotropic light source are assumed (Slide 9).

On the other hand, the propagation of the PA pressure wave is described by the PA pressure wave equation [8] (Slide 10). The speed of the sound in tissues is close to the speed in water. The source term is the absorbed light energy which is described as the product of the absorption coefficient and the fluence rate. The efficiency of the transform the energy to pressure is represented by Grüneisen parameter.

Based on the equations, we have been trying to quantify the optical properties by use of PA measurement, because the optical properties reflect the condition of tissues. For example, the optical properties of breast tissues have been reported [23-29]. And the cancer tissue has larger absorption coefficient owing to increase of blood concentration caused by angiogenesis. The optical properties can be useful for medical diagnoses (Slide 11).

There is another important reason to quantify the optical property. The amplitudes of the PA pressure waves from the cancers can be different even when the conditions of cancers are identical. The PA pressure from the cancer near the light source is large while the PA pressure from the cancer in deeper region is small. This is because the light intensity, which determines the energy absorbed by the imaging target, decreased rapidly while propagating. This means that diagnosis only with the amplitude of PA pressure may lead to misdiagnosis. The optical properties should be quantitatively evaluated in medical diagnosis by solving the inverse problem in the PA measurement based on the equations about the light and PA pressure wave propagation (Slides 12-14).

4 In vitro approach to quantify the optical properties

To diagnose the tissue conditions, we need to know the optical properties of normal and diseased tissues. Additionally, the optical properties of the biological tissues are crucial to solve the forward process in the noninvasive image reconstruction. Therefore, we have tried a method to estimate the optical properties [30].

Before we tested the estimation method of the optical properties, we have examined that the photoacoustic pressure wave was varied by depending on the optical properties in the numerical simulations. The absorbed light energy distribution was calculated in the cylindrical region by Monte Carlo method. The circular light source was assumed. Then the PA pressure wave was simulated from the simulated absorbed light energy distribution. The maximum, minimum and the full width at half maximum of the simulated PA pressure wave were investigated. These features of the PA pressure wave are varied by depending on the optical properties in the cylindrical region.

In the measurement of the actual biological tissues, we made the lookup table which related the

features of PA signal to the optical properties. The features were the maximum, minimum and the temporal interval between them. The lookup table was made by measuring the liquid sample with known optical properties. Then, we measured the PA pressure wave from tissue sample. And we found the absorption and reduced scattering coefficients which minimized the difference between measured features and lookup table data (Slide 16).

We used the pulse laser with 532 nm wavelength. It was green light. The light illuminated the tissue sample pack in the sample holder via optical fiber (Slide 17). The PA pressure was detected by a ring shaped piezoelectric film of P(VDF-TrFE) (KF piezo-film, Kureha Corp., Tokyo, Japan) surrounding the optical fiber. By measuring the PA pressure wave from the biological tissues sampled from the organs of chicken and rabbits, the absorption and reduced scattering coefficients were estimated (Slide 18). The reduced scattering coefficients of the chicken muscles, which looked white, were larger than the absorption coefficient. This result seems reasonable. When an object looks white, it scatters the visible lights with wide range of the wavelengths strongly (Slide 19).

On the other hand, the red tissue such as liver of the chicken had large absorption coefficient. The red color indicated that the object strongly absorbed the light except red light, so green light was absorbed strongly in this experiment. The similar results were obtained by the rabbit organs (Slide 20). The estimation method using lookup table relating the feature of the PA pressure wave with the optical properties obtained the reasonable results. The precision of the method will be improved in future work.

5 In vivo approach to image the optical properties

By the quantitative PA tomography (QPAT), we can diagnose the tissue condition noninvasively. QPAT reconstructs the optical properties based on light propagation model [31-37]. Currently, we have been testing our image reconstruction algorithm with very simple experimental setup [38-40]. Our algorithm uses 2D PDE and linearization. The algorithm will be able to reconstruct the image quickly enough to use in clinical practice (Slide 22).

We investigated the error caused by our image reconstruction method when it was used for imaging 3D medium [41]. The PA pressure was measured by the PA probe combining optical fiber and ring-shaped piezoelectric film like this. So the illumination and detection was carried out at identical position. The measurements were done at 11 positions. From the measure PA pressure, the changes in the absorption coefficient distribution are reconstructed to find pixel having diseased tissues with large absorption coefficient (Slide 23).

According to the photoacoustic wave equation, the PA pressure wave was linear to the source of the PA pressure wave which is the light energy absorbed by the photon absorber. The source was expanded about the background absorption coefficient, and the relation between the PA pressure

wave and the changes in the absorption coefficient from the background was linearized. The differential coefficient is calculated based on the 2D PDE with the finite element method [42]. To eliminate the background signal, the signals measured at different positions were subtracted. Then the set of the subtracted data was formulated as the forward equation which linearly related to the changes in absorption coefficient from the background. Based on the forward equation, the inverse problem is solved with the Tikhonov regularization (Slides 24, 25).

In the numerical simulation, the light energy absorbed by the target photon absorber was calculated by the 2D photon diffusion equation with squared medium and by the 3D MC simulation with cylindrical medium. The target photon absorber with 2-mm side and various absorption coefficients was placed at the depths of 5, 7, or 9 mm. And the proposed 2D PDE based linearized image reconstruction was tried. Then, the reconstructed absorption coefficient of the photon absorber was investigated (Slide 26).

In the calculated distribution of the absorbed light energy calculated with both of 2D PDE and 3D RTE, it was shown that the targeted photon absorber strongly absorbed the light energy. However, it can be seen that the absorbed light energy decreased more rapidly in 3D MC simulation (Slide 27). This caused the error in the reconstructed absorption coefficient of the target. Because of the difference between the light propagation models with 2D PDE and 3D MC simulation, the absorption coefficient reconstructed from the PA pressure wave calculated with 3D MC simulation became smaller than that with 2D PDE, although the photon absorbers were reconstructed at the correct position successfully from the PA pressure waves calculated with 2D PDE and 3D MC simulation. The 2D PDE-based reconstruction cannot overcome the difference in light propagation model.

The error caused by the linearization in the algorithm was also observed in the simulation. The reconstructed absorption coefficient became larger when the true absorption coefficient of the target increased. So the reconstructed image was quantitative to some extent. But, the error in the reconstructed value became larger as the true value increased. The amplitude of PA pressure wave changes nonlinearly with large absorption coefficient. So the linearized algorithm can not recover large absorption coefficient correctly (Slide 28).

To check the validity of the numerical simulation, we tried to reconstruct the image of the liquid phantom made of water, intralipid [43] and indocyanine green (ICG). The target photon absorber was a tube containing ICG with higher concentration. The depth of the photon absorber was varied as 5, 7 and 9 mm. A Ti:sapphire laser pumped by the second harmonic of a Q-switched Nd:YAG laser (LT-2211, LS-2134, Lotis Tii, Minsk, Belarus) operated at 765 nm wavelength was used. The pulse laser light illuminated the phantom via the optical fiber which was introduced into the center of the ring shaped piezoelectric film P(VDF-TrFE) to detect the PA pressure wave. The illumination and detection were carried out at 11 positions (Slide 29).

In the reconstructed images of the phantom, the photon absorbers were reconstructed at the correct positions at the depths of 5, 7 and 9 mm. The deeper the photon absorber existed, the smaller the reconstructed value was. This result agreed with the previous numerical simulation using the 3D Monte Carlo simulation. The results suggested that the error in the image reconstructed by 2D PDE-based algorithm can be predicted and may be corrected by use of the simulation data (Slides 30, 31).

We also investigated the effect of the regularization method [44]. The sparsity regularization minimizing L_1 -norm and the Tikhonov regularization were compared. The regularization parameter λ was selected by use of L-curve [45]. Following three regularization methods were tested: (1) the sparsity regularization and λ at the corner of the L-curve, (2) the Tikhonov regularization and λ at the flat point of the L-curve where the difference in the regularization was minimized, and (3) the Tikhonov regularization and λ at the corner of the L-curve (Slide 32).

The numerical simulation was carried out. In the images reconstructed with the regularization methods (1) and (2), the photon absorber was clearly reconstructed. But, the artifacts which caused by noise were reconstructed by the method (3). The ratios of the reconstructed absorption coefficient to its standard deviation (SD) were examined for the cases with the absorption coefficient of 0.6, 1.1 and 1.7 mm^{-1} and the cases with the depth of 5, 7, and 9 mm. Each of the regularization methods reconstructed absorption coefficient with small SD. The ratios of the reconstructed absorption coefficient to the artifacts were investigated. The method (1) with the sparsity regularization reconstructed smaller artifact than the others (Slides 33, 34).

In the phantom experiment, the results agreed with the numerical simulations. It was demonstrated that the sparsity regularization reconstructed the photon absorber with reducing the influence of noise effectively (Slide 35).

6 Conclusion

Photoacoustic (PA) imaging technology provides precise images in biomedical research field by exploiting the optical and acoustical techniques. The PA pressure wave reflects the optical properties of the biological tissues which are useful for medical diagnoses. From the features of the PA pressure wave, it can be possible to estimate the optical properties. Non-invasive and quantitative PA tomography considering the light propagation in biological medium will support the medical diagnosis by quantifying the optical properties. It is important to understand that some errors occurred owing to the light propagation model approximations in image reconstruction algorithm. Adequate regularization technique improves the robustness of the image reconstruction to noise.

Acknowledgment

This work was partly supported by AMED Collaborative Research Based on Industrial Demand (In vivo Molecular Imaging: Towards Biophotonics Innovations in Medicine) and JSPS KAKENHI 15K06125. Dr. Kiguna Sei and Mr. Seishiro Tatsukawa in National Defense Medical College contributed to the experiment presented in the section 4. The authors thank the organizers, Prof. Takashi Takiguchi and Prof. Hiroshi Fujiwara, for their kind support and fruitful discussions.

References

- [1] S. L. Jacques, “Optical properties of biological tissues: a review,” *Phys. Med. Biol.* **58**, R37–R61 (2013).
- [2] A. P. Gibson, J. C. Hebden, and S. R. Arridge, “Recent advances in diffuse optical imaging,” *Phys. Med. Biol.* **50**, R1-R43 (2005).
- [3] D. A. Boas, D. H. Brooks, E. L. Miller, C. A. DiMarzio, M. Kilmer, R. J. Gaudette, and Q. Zhang, “Imaging the Body with Diffuse Optical Tomography,” *IEEE Signal Process. Mag.* **18**(6), 57-75 (2001).
- [4] D. A. Boas, A. M. Dale, and M. A. Franceschini, “Diffuse optical imaging of brain activation: approaches to optimizing image sensitivity, resolution, and accuracy,” *NeuroImage* **23**, S275–S288 (2004).
- [5] A. P. Gibson, T. Austin, N. L. Everdell, M. Schweiger, S. R. Arridge, J. H. Meek, J. S. Wyatt, D. T. Delpy, J. C. Hebden, “Three-dimensional whole-head optical tomography of passive motor evoked responses in the neonate” *Neuroimage* **30**(2), 521-528 (2006).
- [6] T. Yates, C. Hebden, A. Gibson, N. Everdell, S. R. Arridge, and M. Douek, “Optical tomography of the breast using a multi-channel time-resolved imager,” *Phys. Med. Biol.* **50**, 2503-2517 (2005).
- [7] M. Xu and L. V. Wang, “Photoacoustic imaging in biomedicine,” *Rev. Sci. Instrum.* **77**, pp. 041101-1-22 (2006).
- [8] C. Li and L. V. Wang, “Photoacoustic tomography and sensing in biomedicine,” *Phys. Med. Biol.* **54**, R59-R97 (2009).
- [9] J. I. Sperl, K. Zell, P. Menzenbach, C. Haisch, S. Ketzer, M. Marquart, H. Koenig, M. W. Vogel, “Photoacoustic image reconstruction: a quantitative analysis,” *Proc. SPIE* **6631**, 663103 (2007).
- [10] M. Xu and L. V. Wang, “Universal backprojection algorithm for photoacoustic computed tomography,” *Phys. Rev. E* **71**, 016706 (2005).
- [11] L. V. Wang and S. Hu, “Photoacoustic Tomography: In Vivo Imaging from Organelles to Organs,” *Science* **335**, 1458-1462 (2012).
- [12] T. N. Erpelding, C. Kim, M. Pramanik, L. Jankovic, K. Maslov, Z. Guo, J. A. Margenthaler, M.

- D. Pashley, and L. V. Wang, "Sentinel Lymph Nodes in the Rat: Noninvasive Photoacoustic and US Imaging with a Clinical US System," *Radiology* **256**(1), 102-110 (2010).
- [13] D.-K. Yao, K. Maslov, K. K. Shung, Q. Zhou, and L. V. Wang, "In vivo label-free photoacoustic microscopy of cell nuclei by excitation of DNA and RNA," *Opt. Lett.* **35**, 4139-4141 (2010).
- [14] Y. Zhang, X. Cai, S.-W. Choi, C. Kim, L. V. Wang, and Y. Xia, "Chronic Label-free Volumetric Photoacoustic Microscopy of Melanoma Cells in Three-Dimensional Porous Scaffolds," *Biomaterials* **31**, 8651-8658 (2010).
- [15] E. Zhang, J. Laufer, and P. Beard, "Backward-mode multiwavelength photoacoustic scanner using a planar Fabry-Perot polymer film ultrasound sensor for high-resolution three-dimensional imaging of biological tissue," *Appl. Opt.* **47**(4), 561-577 (2008).
- [16] website of Photoacoustic imaging group in University College London, <http://www.medphys.ucl.ac.uk/research/mle/index.htm>
- [17] A. Horiguchi, K. Tsujita, K. Irisawa, T. Kasamatsu, K. Hirota, M. Kawaguchi, M. Shinchi, K. Ito, T. Asano, H. Shinmoto, H. Tsuda, and M. Ishihara, "A pilot study of photoacoustic imaging system for improved real-time visualization of neurovascular bundle during radical prostatectomy," *Prostate* **76**(3), 307-315 (2016).
- [18] S. R. Arridge, "Optical tomography in medical imaging," *Inverse Probl.* **15**, R41-R93 (1999).
- [19] A. D. Klose, V. Ntziachristos, and A. H. Hielscher, "The inverse problem based on the radiative transfer equation in optical molecular imaging," *J. Compt. Phys.* **202**, 323-345 (2005).
- [20] T. Tarvainen, V. Kolehmainen, S. R. Arridge, and J. P. Kaipio, "Image reconstruction in diffuse optical tomography using the coupled radiative transport-diffusion model," *J. Quant. Spectrosc. Radiat. Transfer* **112**, 2600-2608 (2011).
- [21] H. Fujii, S. Okawa, Y. Yamada, and Y. Hoshi, "Hybrid model of light propagation in random media based on the time-dependent radiative transfer and diffusion equations," *J. Quant. Spectrosc. Radiat. Transfer* **147**, 145-154 (2014).
- [22] L.-H. Wang, S. L. Jacques, and L. Q. Zheng, "MCML - Monte Carlo modeling of photon transport in multi-layered tissues," *Comput. Meth. Prog. Bio.* **47**, 131-146 (1995).
- [23] D. J. Hawrysz and E. M. Sevick-Muraca, "Development Toward Diagnostic Breast Cancer Imaging Using Near-Infrared Optical Measurements and Fluorescent Contrast Agents," *Neoplasia* **2**(5), 388-417 (2000).
- [24] D. Grosenick, H. Wabnitz, H. H. Rinneberg, T. Moesta, and P. M. Schlag, "Development of a time-domain optical mammography and first in vivo applications," *Appl. Opt.* **38**(13), 2927-2943 (1999).
- [25] T. Durduran, R. Choe, J. P. Culver, L. Zubkov, M. J. Holboke, J. Giammarco, B. Chance, and A. Yodh, "Bulk optical properties of healthy female breast tissue," *Phys. Med. Biol.* **47**, 2847-2861 (2002).

- [26] D. Grosenick, H. Wabnitz, K. T. Moesta, J. Mucke, M. Möller, C. Stroszczynski, J. Stöbel, B. Wassermann, P. M. Schlag, and H. Rinneberg, "Concentration and oxygen saturation of haemoglobin of 50 breast tumors determined by time-domain optical mammography," *Phys. Med. Biol.* **49**, 1165-1181 (2004).
- [27] D. Grosenick, K. T. Moesta, M. Möller, J. Mucke, H. Wabnitz, B. Gebauer, C. Stroszczynski, B. Wassermann, P. M. Schlag, and H. Rinneberg, "Time-domain scanning optical mammography: I. Recording and assessment of mammograms of 154 patients," *Phys. Med. Biol.* **50**, 2429-2449 (2005).
- [28] D. Grosenick, H. Wabnitz, K. T. Moesta, J. Mucke, P. M. Schlag, and H. Rinneberg, "Time-domain scanning optical mammography: II. Optical properties and tissue parameters of 87 carcinomas," *Phys. Med. Biol.* **50**, 2451-2468 (2005).
- [29] M. Herranz and A. Ruibal, "Optical Imaging in Breast Cancer Diagnosis: The Next Evolution," *J. Oncol.* **2012**, 863747 (2012).
- [30] S. Tatsukawa, S. Okawa, K. Sei, T. Hirasawa, T. Kushibiki, M. Fujita, and M. Ishihara, "Estimation of the optical properties of biological tissues from photoacoustic signal," *Optics and Photonics Japan 2015*, 29pA8 (2015) (in Japanese).
- [31] B. Cox, J. G. Laufer, S. R. Arridge, and P. C. Beard "Quantitative spectroscopic photoacoustic imaging: a review," *J. Biomed. Opt.* **17**, 061202-1-22 (2012).
- [32] B. T. Cox, S. R. Arridge, K. P. Köstli, and P. C. Beard, "Two-dimensional quantitative photoacoustic image reconstruction of absorption distributions in scattering media by use of a simple iterative method," *Appl. Opt.* **45**(8), 1866-1875 (2006).
- [33] J. Laufer, B. Cox, E. Zhang, and P. Beard, "Quantitative determination of chromophore concentrations from 2D photoacoustic images using a nonlinear model-based inversion scheme," *Appl. Opt.* **49**(8), 1219-1233 (2010).
- [34] Z. Yuan, Q. Wang, and H. Jiang, "Reconstruction of optical absorption coefficient map of heterogeneous media by photoacoustic tomography coupled with diffusion equation based regularized Newton method," *Opt. Express* **15**(26), 18076-18081 (2007).
- [35] L. Yao, Y. Sun, and H. Jiang, "Transport-based quantitative photoacoustic tomography: simulations and experiments," *Phys. Med. Biol.* **55**(7), 1917 (2010).
- [36] T. Saratoon, T. Tarvainen, B. T. Cox, and S. R. Arridge, "A gradient-based method for quantitative photoacoustic tomography using the radiative transfer equation," *Inverse Problems* **29**, 075006 (2013).
- [37] A. Pulkkinen, B. T. Cox, S. R. Arridge, J. P. Kaipio, and T. Tarvainen, "Quantitative photoacoustic tomography using illuminations from a single direction," *J. Biomed. Opt.* **20**(3), 036015 (2015).
- [38] S. Okawa, T. Hirasawa, T. Kushibiki, and M. Ishihara, "Numerical Evaluation of Linearized

- Image Reconstruction Based on Finite Element Method for Biomedical Photoacoustic Imaging,” *Opt. Rev.* **20**(5), 442-451 (2013).
- [39] S. Okawa, T. Hirasawa, T. Kushibiki, and M. Ishihara, “Reconstruction of the optical properties of inhomogeneous medium from photoacoustic signal with l_p sparsity regularization,” *Proc. SPIE* **8581**, 858135 (2013).
- [40] S. Okawa, T. Hirasawa, T. Kushibiki, and M. Ishihara, “Reconstruction of the optical absorption coefficient from photoacoustic signals measured by scanning coaxial probe with regularization methods,” *Proc. SPIE* **8943**, 89433W (2014).
- [41] S. Okawa, T. Hirasawa, T. Kushibiki, and M. Ishihara, “Influence of the light propagation models on a linearized photoacoustic image reconstruction of the light absorption coefficient,” *Proc. SPIE* **9323**, 93231X (2015).
- [42] M. Schweiger, S. R. Arridge, and D. T. Delpy, “Application of the Finite-Element Method for the Forward and Inverse Model in Optical Tomography,” *J. Math. Imaging Vis.* **3**, 263-283 (1993).
- [43] H. J. van Staveren, C. J. M. Moes, J. van Marie, S. A. Prahl, and M. J. C. van Gemert, “Light scattering in Intralipid-10% in the wavelength range of 400-1100 nm,” *Appl. Opt.* **30**(31), 4507-4514 (1991).
- [44] S. Okawa, T. Hirasawa, T. Kushibiki, and M. Ishihara, “Image reconstruction of the absorption coefficient with l_1 -norm minimization from photoacoustic measurements,” *Quant. Imaging Med. Surg.* **5**(1), 78-85 (2014).
- [45] C. R. Vogel, *Computational Methods for Inverse Problems (Frontiers in Applied Mathematics)* (The Society of Industrial and Applied Mathematics, Philadelphia, 2002).

Slide 1

Numerical and experimental studies on quantification of the optical properties by use of photoacoustic measurement

Shinpei Okawa, Takeshi Hirasawa,
Toshihiro Kushibiki, Miya Ishihara

Dept. of Medical Engineering,
National Defense Medical College

Slide 2

Table of contents

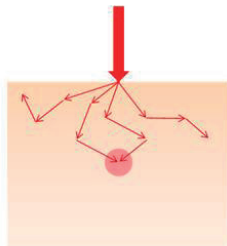
1. Biomedical photoacoustic imaging
Photoacoustic (PA) phenomenon
Biomedical PA imaging
2. Introduction to quantitative PA imaging
Light propagation in biological medium
Propagation of PA pressure wave
Motivation for quantification by PA measurement
3. In vitro approach to quantify the optical properties
PA pressure wave reflects the optical properties - simulation -
A method to estimate the optical properties from PA signal
In vitro estimation of biological tissues - experiment -
4. In vivo approach to image the optical properties
Quantitative photoacoustic tomography
A 2D photon diffusion equation based algorithm
Influences of the approximations on quantification
Sparsity regularization for robust image reconstruction
5. Conclusions

Slide 3

Biomedical photoacoustic imaging

- The image is reconstructed from the detected PA pressure wave.
- PA pressure wave depends on the absorbed light energy.

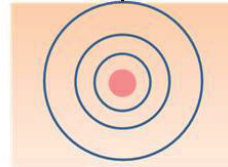
Irradiation of pulse laser light



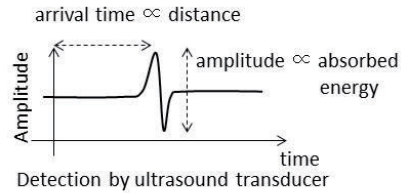
Absorption of the light energy by photon absorber (hemoglobin etc) [fs]



Thermal expansion of the photon absorber [sub ns]



Generation and propagation of PA pressure wave [μ s]



Slide 4

Biomedical photoacoustic imaging

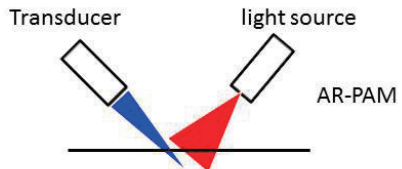
Variety of photoacoustic imaging techniques

PA microscopy (PAM)

imaging method without image reconstruction

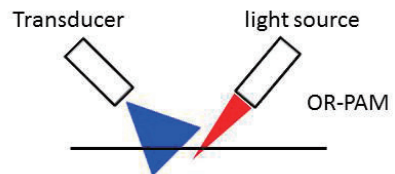
Acoustic-resolution PAM (AR-PAM)

focusing with acoustic lens
imaging depth ~ 3 mm
lateral resolution $50 \sim 500 \mu\text{m}$



Optical-resolution PAM (OR-PAM)

focusing with optical lens
imaging depth ~ 1 mm
lateral resolution $200 \text{ nm} \sim 2 \mu\text{m}$



PA computed tomography (PACT)

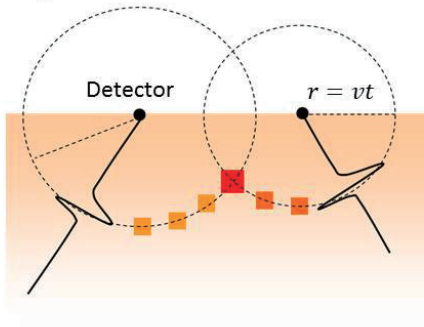
imaging method with image reconstruction

Wang et al, Science 335, 1458 (2012)

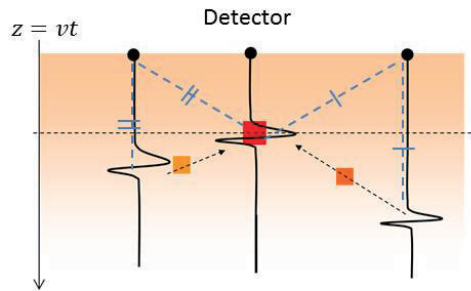
Slide 5

Biomedical photoacoustic imaging

Image reconstruction



Circular back-projection



Delay-and-Sum back-projection

PA amplitude is added to the positions with the equivalent distance calculated with speed of sound and time of arrival.

→ The position of the PA source is highlighted.

J.I. Sperl et al. SPIE vol. 6631, 663103 (2007)

Slide 6

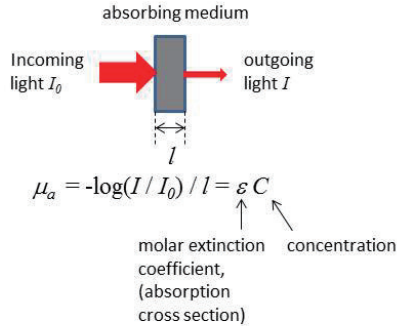
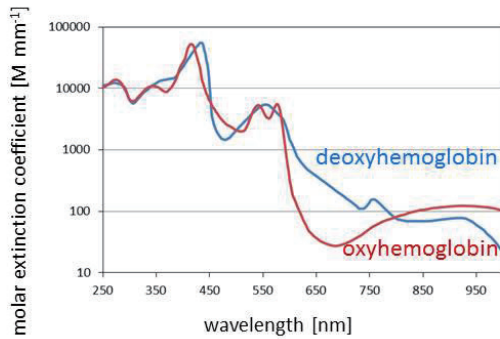
Table of contents

1. Biomedical photoacoustic imaging
Photoacoustic (PA) phenomenon
Biomedical PA imaging
2. Introduction to quantitative PA imaging
Light propagation in biological medium
Propagation of PA pressure wave
Motivation for quantification by PA measurement
3. In vitro approach to quantify the optical properties
PA pressure wave reflects the optical properties - simulation -
A method to estimate the optical properties from PA signal
In vitro estimation of biological tissues - experiment -
4. In vivo approach to image the optical properties
Quantitative photoacoustic tomography
A 2D photon diffusion equation based algorithm
Influences of the approximations on quantification
Sparsity regularization for robust image reconstruction
5. Conclusions

Slide 7

Optical properties of biological medium

μ_a : absorption coefficient [mm^{-1}]



Endogenous chromophores such as hemoglobin have signature absorption spectra.

Tissue $\left\{ \begin{array}{l} \text{Oxy- and deoxy-hemoglobin} \\ \text{water} \\ \text{melanosome} \\ \text{bilirubin} \\ \text{Fat ...} \end{array} \right. \longrightarrow \mu_a = \sum_{i=1}^N \epsilon_i C_i$

Slide 8

Optical properties of biological medium

μ_s : scattering coefficient [mm^{-1}]

$P(\Omega', \Omega), P(\theta)$: scattering phase function
(probability of change the direction Ω to Ω' by scattering)

g : anisotropic factor

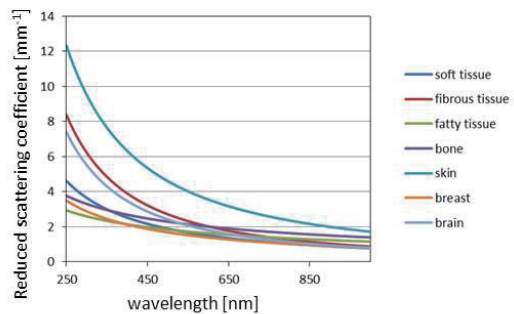
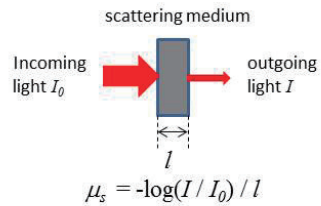
$$g = \langle \cos \theta \rangle = 2\pi \int_0^\pi \cos \theta P(\theta) \sin \theta d\theta$$

$\mu_s' = (1 - g) \mu_s$
: reduced scattering coefficient [mm^{-1}]

$D = 1 / [3(\mu_s' + \mu_a)]$
: diffusion coefficient [mm]

➔ Diffusion approximation

After the sufficient scattering events, the light propagation with $(1-g_1) \mu_{s1}$ is similar to that with $(1-g_2) \mu_{s2}$ when they have identical μ_s' .



Light propagation in biological medium

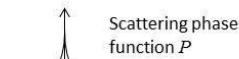
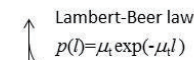
Radiative Transfer Equation (RTE)

$$\{\Omega \cdot \nabla + \mu_a(r) + \mu_s(r)\} I(r, \Omega) = \mu_s(r) \int_s d\Omega' P(\Omega, \Omega') + q(r, \Omega),$$

Direction
Absorption coefficient
Scattering coefficient
Radiance
Scattering phase function
Light source

- Monte Carlo (MC) simulation

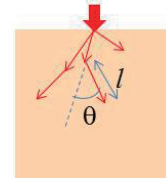
MC simulation tracks movement of photons.
Movement of photons determined statistically.



Probability density functions

Optical properties to be quantified from PA pressure waves

Irradiation of laser light



- Photon Diffusion Equation (PDE)

$$\{-\nabla \cdot D(r) \nabla + \mu_a(r)\} \Phi(r) = q(r),$$

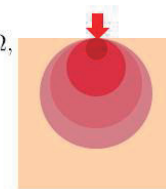
Diffusion coefficient
Absorption coefficient
Fluence rate
Light source

Diffusion Approximation: isotropic scattering, isotropic light source

$$\Phi(r) = \int I(r, \Omega) d\Omega,$$

$$D(r) = \frac{1}{3(\mu_s')},$$

Scattering coefficient



Propagation of PA wave pressure

PA wave equation

$$\left\{ \frac{\partial^2}{\partial t^2} - v^2 \nabla^2 \right\} p(r, t) = \Gamma \frac{\partial}{\partial t} H(r, t),$$

Speed of sound
PA pressure
Grüneisen parameter
Absorbed light energy

$$H = \mu_a \Phi(r) \delta(t),$$

Speed of sound [mm/μs]

water : 1.5
soft tissues : 1.5 - 1.6
bone : 3.3 - 4.0

Grüneisen parameter = $\beta [K^{-1}] v^2 [ms^{-1}] / C_p [J(K kg)^{-1}]$

water : 0.13
oxygenated red blood cell : 0.15
soft tissues : 0.25
(at room temperature)

β : volume expansion coefficient
 v : speed of sound
 C_p : specific heat

Motivation for quantification by PA measurement

Optical properties reflect the conditions of tissues

Optical properties of breast tissues

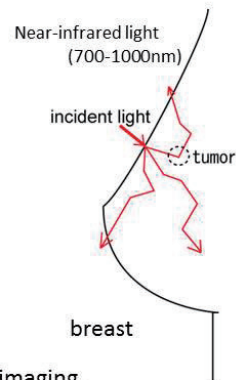
$$\mu_a = 0.001 \sim 0.01 \text{ mm}^{-1}, \mu_s' = 0.5 \sim 1.5 \text{ mm}^{-1}$$

(Hawrysz et al, 2000)

$$\mu_a = 0.0041 \text{ mm}^{-1}, \mu_s' = 0.85 \text{ mm}^{-1} @ 780 \text{ nm}$$

(Durduran et al, 2002)

μ_a of cancer tissue was 2-4 times as large as μ_a of normal tissues due to increase of blood concentration with angiogenesis. (Grosenick et al, 2004)



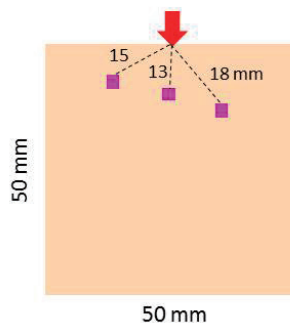
Many reports exist in research with near-infrared diffuse optical imaging.

→ quantification of the absorption coefficient is useful in diagnosis

Motivation for quantification by PA measurement

Simulation

Hemoglobin concentration increases due to angiogenesis in 3 cancers. But they exist at different depths from the light source.



Three cancer regions (1x1 mm) equally have $\mu_a = 0.01 \text{ mm}^{-1}$,

Normal tissues have $\bar{\mu}_a = 0.001 \text{ mm}^{-1}$

Finite element method

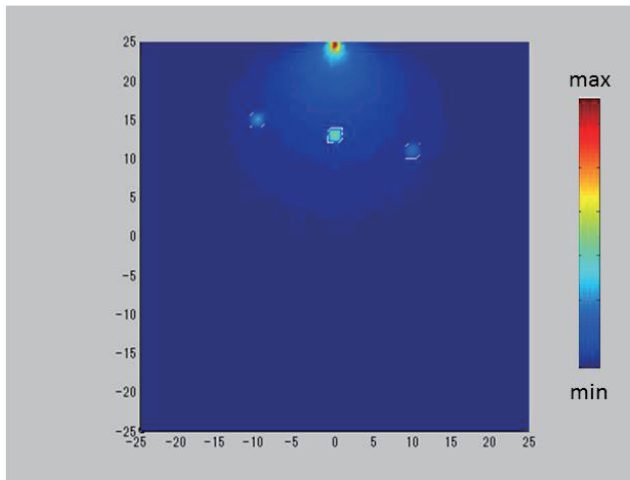
10,201 nodes (0.5 mm spacing), 20,000 elements, 500 time steps with 0.1 μs interval

Slide 13

Motivation for quantification by PA measurement

Simulation

PA amplitudes from the cancers are different, even though the conditions of cancers are identical.



Slide 14

Motivation for quantification by PA measurement

Simulation

Diagnosis only with PA pressure may lead to misdiagnosis. The optical properties should be quantitatively evaluated.

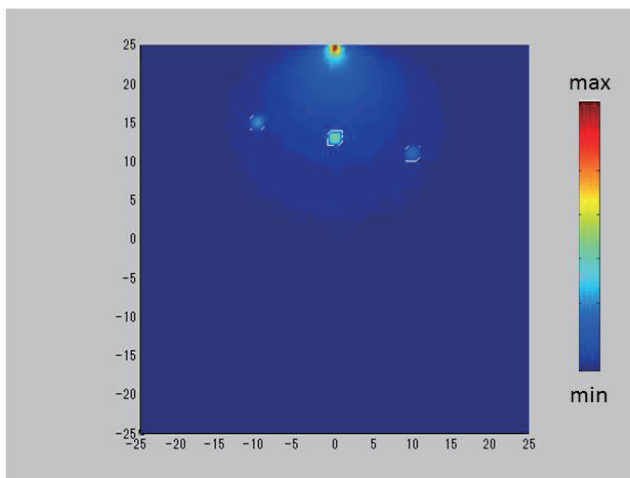
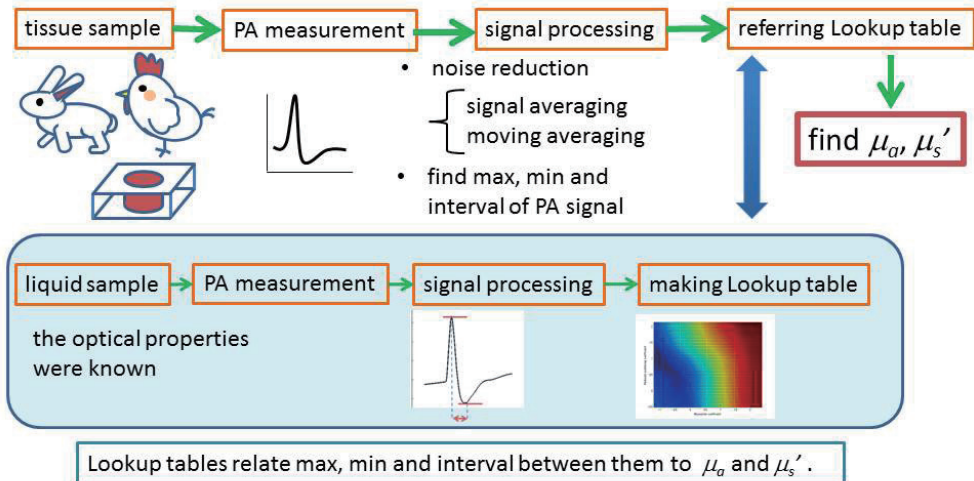


Table of contents

1. Biomedical photoacoustic imaging
 Photoacoustic (PA) phenomenon
 Biomedical PA imaging
2. Introduction to quantitative PA imaging
 Light propagation in biological medium
 Propagation of PA pressure wave
 Motivation for quantification by PA measurement
3. In vitro approach to quantify the optical properties
 PA pressure wave reflects the optical properties - simulation -
 A method to estimate the optical properties from PA signal
 In vitro estimation of biological tissues - experiment -
4. In vivo approach to image the optical properties
 Quantitative photoacoustic tomography
 A 2D photon diffusion equation based algorithm
 Influences of the approximations on quantification
 Sparsity regularization for robust image reconstruction
5. Conclusions

A method to estimate the optical properties from PA signal



$$\min_{\mu_a, \mu_s'} \|M_{\text{measured}} - M_{\text{LT}}(\mu_a, \mu_s')\|^2 \quad M = [m_{\text{max}}, m_{\text{min}}, \Delta t],$$

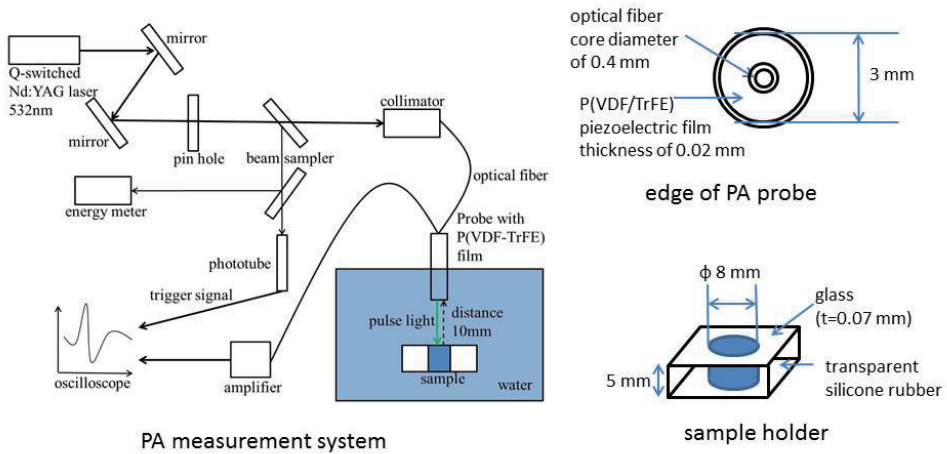
LT: Lookup table

Slide 17

A method to estimate the optical properties from PA signal

Experimental setup

Pulse laser light (wavelength 532 nm, 40~300 $\mu\text{J}/\text{pulse}$)
was used to excite PA pressure wave



Slide 18

In vitro estimation of biological tissue

Measured tissues

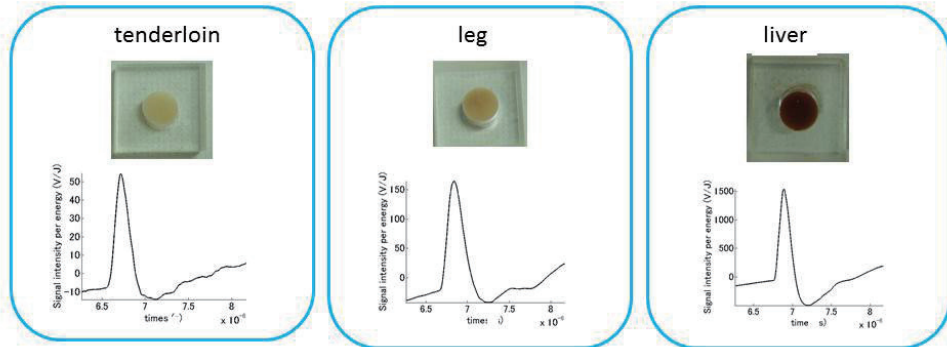
extracted from:

Chicken	Rabbit (with blood removal perfusion)
tenderloin (pectoralis minor)	liver
breast (pectoralis major)	kidney (cortex)
leg (biceps femoris)	lung
liver	fat
	cardiac muscle (left venticle)
	striated muscle (quadriceps femoris)
	smooth muscle (uterus)

Slide 19

In vitro estimation of biological tissue

Chicken



	tenderloin	breast	leg	liver
μ_a (cm ⁻¹)	0.86 ± 0.60	0.78 ± 0.44	2.809 ± 1.32	40.07 ± 3.50
μ_s' (cm ⁻¹)	53.27 ± 51.47	45.71 ± 51.06	12.38 ± 6.330	12.31 ± 2.46

N = 5

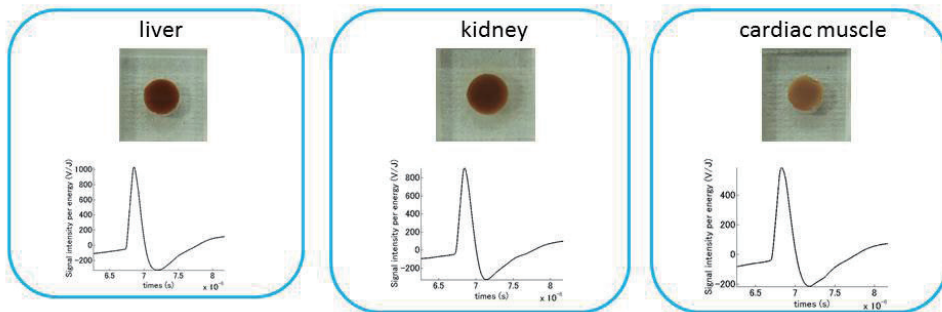
“White” tissue scattered light strongly → large μ_s'

“Red” tissues absorbed green light strongly → large μ_a

Slide 20

In vitro estimation of biological tissue

Rabbit



	liver	kidney	lung	fat
μ_a (cm ⁻¹)	36.37 ± 6.743	17.73 ± 8.837	2.43 ± 1.881	0.636 ± 0.5
μ_s' (cm ⁻¹)	4.171 ± 4.108	17.35 ± 24.09	120.8 ± 21.47	80.67 ± 61.1
	cardiac muscle	striated muscle	smooth muscle	
μ_a (cm ⁻¹)	13.77 ± 12.34	0.544 ± 0.789	1.444 ± 1.121	
μ_s' (cm ⁻¹)	16.15 ± 9.888	82.31 ± 60.71	91.56 ± 61.08	

N = 5

“White” tissue scattered light strongly → large μ_s'

“Red” tissues absorbed green light strongly → large μ_a

Table of contents

1. Biomedical photoacoustic imaging
Photoacoustic (PA) phenomenon
Biomedical PA imaging
2. Introduction to quantitative PA imaging
Light propagation in biological medium
Propagation of PA pressure wave
Motivation for quantification by PA measurement
3. In vitro approach to quantify the optical properties
PA pressure wave reflects the optical properties - simulation -
A method to estimate the optical properties from PA signal
In vitro estimation of biological tissues - experiment -
4. In vivo approach to image the optical properties
Quantitative photoacoustic tomography
A 2D photon diffusion equation based algorithm
Influences of the approximations on quantification
Sparsity regularization for robust image reconstruction
5. Conclusions

Quantitative photoacoustic tomography (QPAT)

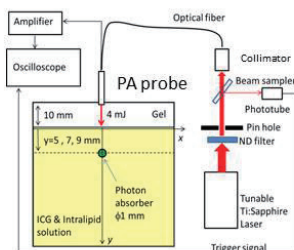
non-invasive measurement
of PA pressure wave



the distribution of μ_a and μ_s .
(concentration of photon absorber)

Image reconstruction based on
the light propagation model

B. Cox et al. Appl. Opt. 45, 1866 (2006).
Z. Yuan et al. Opt. Express, 15, 18076 (2007).
J. Laufer et al. Appl. Opt., 49, 1219 (2010).
T. Saratoon et al. Inverse problems, 29, 075006 (2013).
and so on..

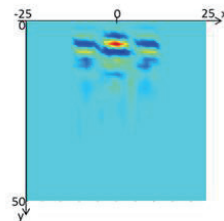


Test of image reconstruction
with a simple experimental setup
for clinical practice

- 2D
- photon diffusion equation (PDE)
- linearization



5 sec / 1 image reconstruction
CPU: Intel Core i7-3820QM 2.7 GHz
RAM: 16.0 GB

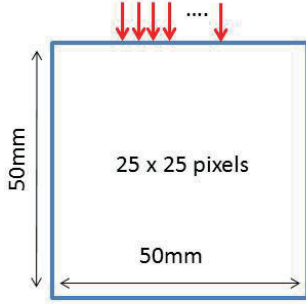


What errors occur by the 2D PDE-based linearized image reconstruction?

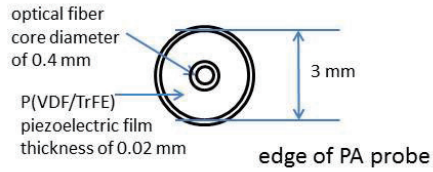
A 2D photon diffusion equation based algorithm

Conditions in measurement for image reconstruction

11 illuminating and detecting positions with 2mm spacing



Illumination and detection (PA measurement) is carried out at identical position by use of optical fiber and piezoelectric film.



Background normal tissues:

$$\mu_a = 0.0023 \text{ mm}^{-1},$$

$$\mu_s' = 0.8 \text{ mm}^{-1}$$

PA measurements are carried out at 11 positions.

Changes in μ_a distribution are reconstructed to find pixel having diseased tissues with large μ_a .

A 2D photon diffusion equation based algorithm

Forward modeling

$$\left\{ \frac{\partial^2}{\partial t^2} - v^2 \nabla^2 \right\} p(r, t) = \Gamma \frac{\partial}{\partial t} H(r, t), \quad H = \mu_a \Phi(r) \delta(t), \quad (\text{PA wave equation})$$

$$\mathbf{m}^i = \mathbf{L} \mathbf{H}^i, \quad \mathbf{m}^i \in \mathbb{R}^T, \quad \mathbf{H}^i \in \mathbb{R}^S, \quad \mathbf{L} \in \mathbb{R}^{T \times S},$$

PA signal measured at i -th detector

distribution of PA source intensities

calculated from 2D photon diffusion equation

$$\mathbf{H}^i \simeq \mathbf{H}(\bar{\mu}_a) + \mathbf{J}^i \Delta \mu_a, \quad \mathbf{J}^i = \frac{\partial \mathbf{H}^i}{\partial \Delta \mu_a}, \quad \mathbf{J}^i \in \mathbb{R}^{S \times N}, \quad \Delta \mu_a \in \mathbb{R}^N,$$

$\bar{\mu}_a$ of background normal tissues

changes in μ_a

$$\mathbf{m}^i - \mathbf{m}^j = \mathbf{L} \mathbf{H}^i - \mathbf{L} \mathbf{H}^j$$

differences between PA signals are used for reconstruction

$$\begin{aligned} &= \mathbf{L} \{ \mathbf{H} + \mathbf{J}^i \Delta \mu_a \} - \mathbf{L} \{ \mathbf{H} + \mathbf{J}^j \Delta \mu_a \} \\ &= \mathbf{G}^{i,j} \Delta \mu_a, \end{aligned}$$

$$\mathbf{m}_{\text{diff}} = \mathbf{G} \Delta \mu_a,$$

$$\begin{pmatrix} m^1 - m^2 \\ m^1 - m^3 \\ \vdots \\ m^1 - m^M \\ m^2 - m^3 \\ \vdots \\ m^2 - m^M \\ \vdots \\ m^{M-1} - m^M \end{pmatrix} = \begin{pmatrix} G^{1,2} \\ G^{1,3} \\ \vdots \\ G^{1,M} \\ G^{2,3} \\ \vdots \\ G^{2,M} \\ \vdots \\ G^{M-1,M} \end{pmatrix} \Delta \mu_a,$$

A 2D photon diffusion equation based algorithm

Inversion process

$$\mathbf{m}_{\text{diff}} = G \Delta \mu_a,$$

↑ measured PA signals ↑ changes in μ_a

$$\begin{pmatrix} m^1 - m^2 \\ m^1 - m^3 \\ \vdots \\ m^1 - m^M \\ m^2 - m^3 \\ \vdots \\ m^2 - m^M \\ \vdots \\ m^{M-1} - m^M \end{pmatrix} = \begin{pmatrix} G^{1,2} \\ G^{1,3} \\ \vdots \\ G^{1,M} \\ G^{2,3} \\ \vdots \\ G^{2,M} \\ \vdots \\ G^{M-1,M} \end{pmatrix} \Delta \mu_a,$$

$$\min_{\Delta \mu_a} \|\mathbf{m}_{\text{diff}} - G \Delta \mu_a\|^2 + \lambda \cdot \|\Delta \mu_a\|_2^2,$$

$$\widehat{\Delta \mu_a} = (G^T G + \lambda \cdot I)^{-1} G^T \mathbf{m}_{\text{diff}}$$



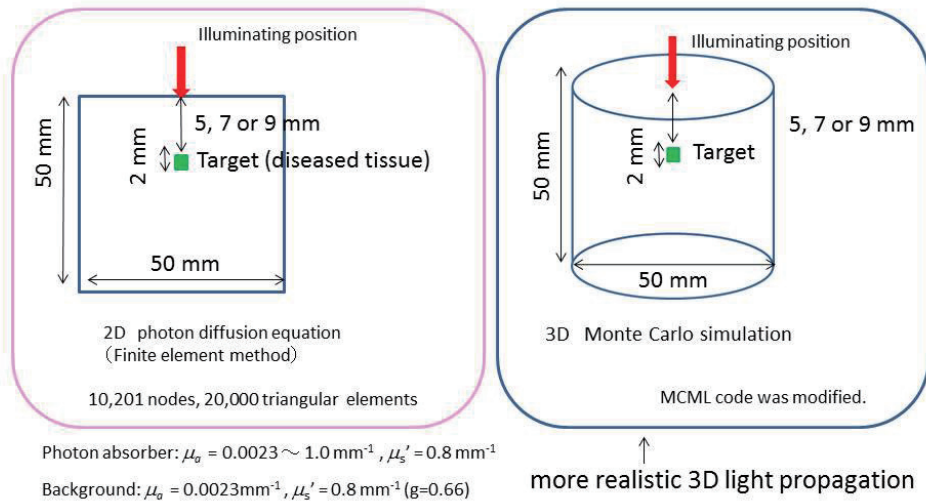
Reconstructed image (distribution of changes in μ_a) reveals diseased tissues with large (or small) μ_a .

A 2D photon diffusion equation based algorithm

Numerical simulations

Conditions

- Light energy absorbed by photon absorber were calculated.
- Reconstructed absorption coefficient of the photon absorber was checked.

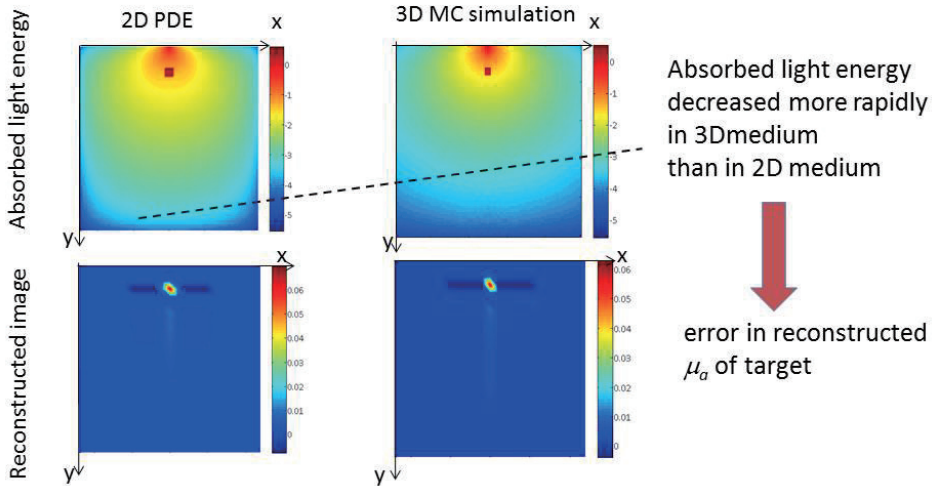


Slide 27

A 2D photon diffusion equation based algorithm

Numerical simulations

Results



photon absorber with depth 7 mm and absorption coeff of 0.1 mm^{-1}

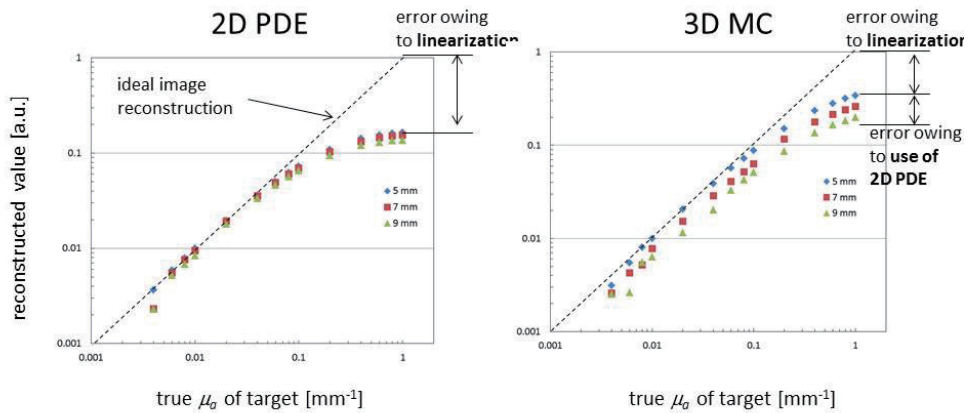
Slide 28

A 2D photon diffusion equation based algorithm

Numerical simulations

Results

reconstructed μ_a from PA signal calculated with:



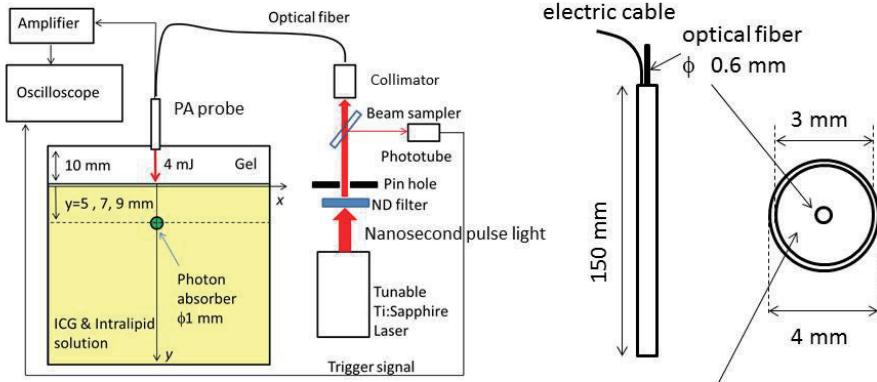
The difference owing to the linearization remained in the reconstructed image as the error.
 The photon absorbers with identical absorption in different depths were reconstructed identically.

Slide 29

A 2D photon diffusion equation based algorithm

Phantom experiment

Conditions



Target: ICG + Intralipid
 $\mu_a = 0.6 \text{ mm}^{-1}$
 (ICG 32.3 μM)
 $\mu_s' = 0.8 \text{ mm}^{-1}$

Background: ICG + Intralipid
 $\mu_a = 0.0023 \text{ mm}^{-1}$
 $\mu_s' = 0.8 \text{ mm}^{-1}$

P(Vdf/TrFE) $t = 0.02 \text{ mm}$
 (Kureha, Tokyo)
PA probe

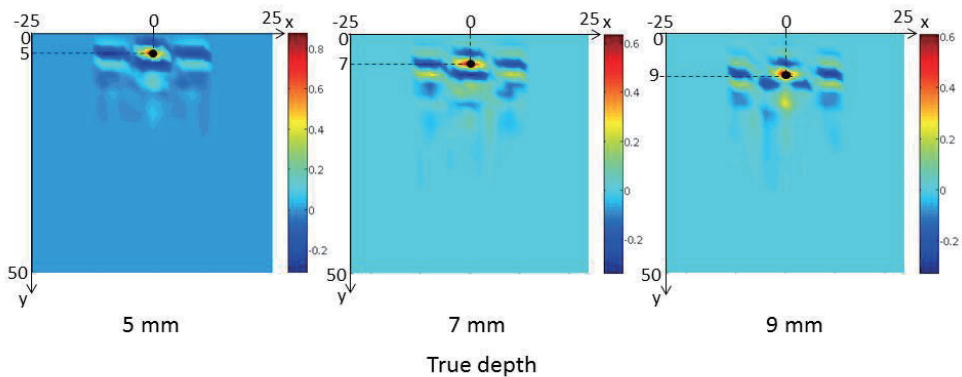
Slide 30

A 2D photon diffusion equation based algorithm

Phantom experiment

Results

Reconstructed images

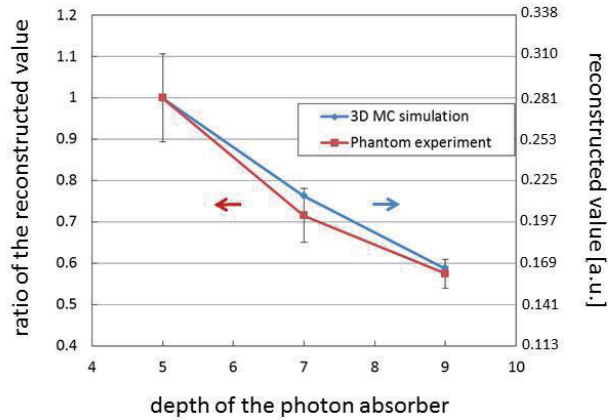


The photon absorbers (red region) were reconstructed at the depth of 5, 7 and 9 mm (black dots).

A 2D photon diffusion equation based algorithm

Phantom experiment

Results



μ_a at deeper position was underestimated.
 The ratio agreed with the ratio in the numerical simulations.
 The reconstructed absorption coefficient can be corrected based on the simulation.

Sparsity regularization for robust image reconstruction

Comparison of regularization methods

$$\min_{\Delta\mu_a} \|m_{\text{diff}} - G\Delta\mu_a\|^2 + \lambda \cdot f(\Delta\mu_a),$$

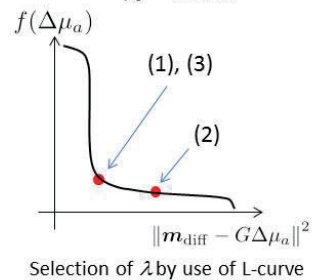
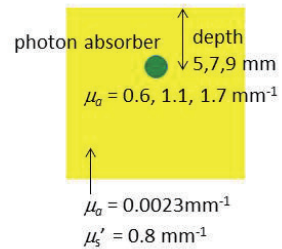
Sparsity regularization: $f(\Delta\mu_a) = \sum_{i=1}^N |\Delta\mu_{a_i}|,$

Tikhonov regularization: $f(\Delta\mu_a) = \sum_{i=1}^N |\Delta\mu_{a_i}|^2,$

regularization methods

	regularization function	λ at
(1)	Sparsity	corner
(2)	Tikhonov	flat point
(3)	Tikhonov	corner

of L-curve

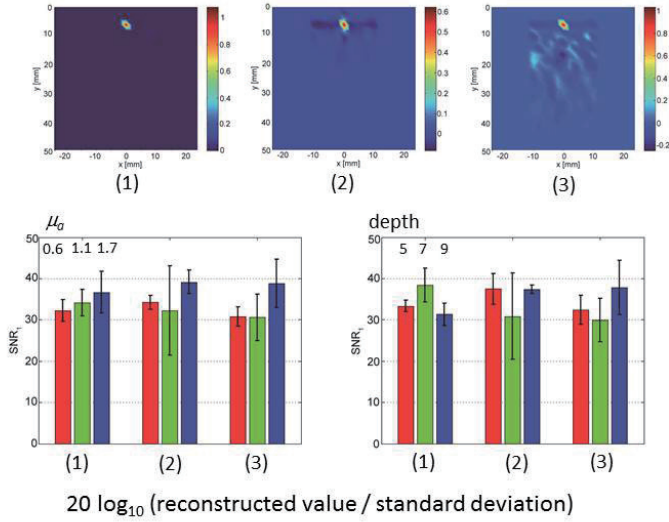


Noise: Gaussian noise with 10 % of the maximum of the measured data

Sparsity regularization for robust image reconstruction

Numerical simulations

Target had true $\mu_a = 1.1 \text{ mm}^{-1}$, Depth 7 mm.

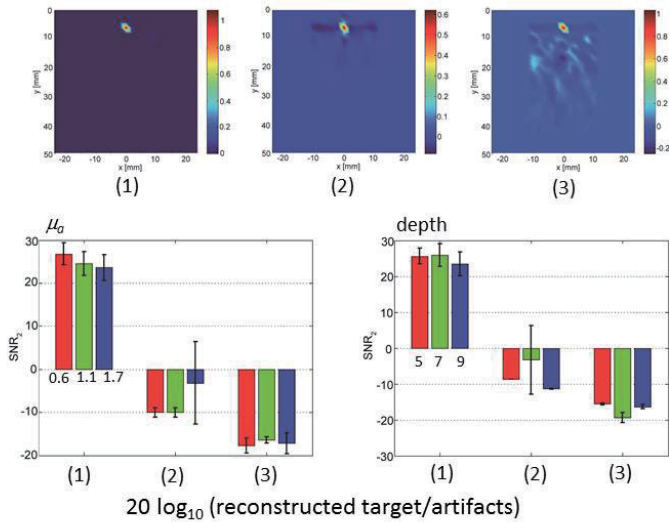


Each of the regularization methods reconstructed target with small SD.

Sparsity regularization for robust image reconstruction

Numerical simulations

Target had true $\mu_a = 1.1 \text{ mm}^{-1}$, Depth 7 mm.



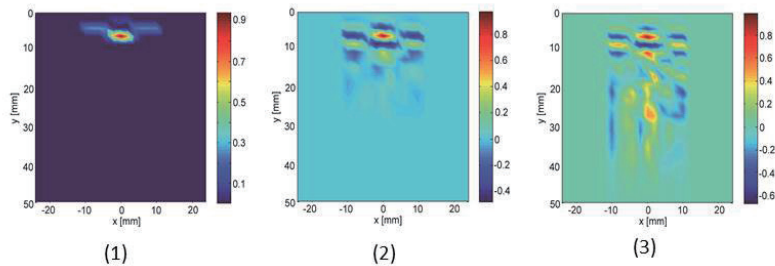
sparsity regularization reconstructed small artifacts.

Slide 35

Sparsity regularization for robust image reconstruction

Phantom experiment

Target had true $\mu_a = 1.1 \text{ mm}^{-1}$, Depth 7 mm.



sparsity regularization reconstructed the photon absorber with reducing the influence of noise effectively.

Slide 36

Conclusion

Photoacoustic (PA) imaging technology provides precise images in biomedical research field by exploiting the optical and acoustical techniques.

The PA pressure wave reflects the optical properties properties which are useful for medical diagnoses.

From the features of the PA pressure wave, it can be possible to estimate the optical properties.

Non-invasive and quantitative PA tomography considering the light propagation in biological medium will support the medical diagnosis.

Some errors occurred owing to the light propagation model.

Adequate regularization technique improves the robustness of the image reconstruction to noise.

Integral equations method in inverse problem

Kuo-Ming Lee*

*Department of Mathematics, National Cheng Kung University
No. 1, Dasyue Rd., Tainan City 70101, Taiwan
kmlee@math.ncku.edu.tw

ABSTRACT

In this talk, we discuss integral equations method in inverse problems and the difficulties that arise. As a model for our discussion, we choose the scattering problem from a sound soft obstacle. The direct problem can be modelled by the exterior Dirichlet problem for the Helmholtz equation satisfying some radiation condition. The corresponding inverse problem is to identify the scatterer with some measured far-field data.

We introduce integral equations method to solve both the direct and the inverse problem. This kind of method transforms the domain into a compact set which is beneficial both from the theoretical and the numerical point of view. For the direct problem, on the one hand, it allows elegant analysis as far as the unique solvability and the stability of the problem is concerned with the power of functional analysis. On the other hand, it reduces the computational cost by decreasing the dimension. In this case, the problem itself is converted into a system of boundary integral equations in the framework of Fredholm integral equation of the second kind with compact integral operators. Thus, the unique solvability of the direct problem follows directly from the Riesz theory.

Difficulties arise when dealing with the inverse problem. In this case, there is a Fredholm integral equation of the first kind with a compact integral operator. Formally, this is only a little bit different from the other equations appears in the direct problem. However, the solving of this kind of equations is ill-posed. This ill-posedness lies in the problem itself, not in the method we use. To overcome this dilemma, we incorporate the idea of regularization.

This talk will consist of four parts: The first part is to introduce integral equations and its solution theory. In the second part, we will briefly discuss inverse problems and ill-posed problems which is followed by regularization theory in the third part. Finally, we will solve the scattering problem based on the the above discussion.

Integral equations method in inverse problem

Lee, Kuo-Ming

Department of Mathematics
National Cheng Kung University

Mathematical Backgrounds and Future Progress of Practical
Inverse Problems
Institute of Mathematics for Industry, Kyushu University, Fukuoka
Nov. 10 - 13 2015

Outline

- 1 Integral Equations
- 2 Solution Theory for Second Kind Fredholm Integral Equations
- 3 Solution Theory for First Kind Fredholm Integral Equations
- 4 Applications of Integral Equations

Section Content

- 1 Integral Equations
 - Main Classifications
 - Historical Remarks
 - Solutions of Integral Equations
 - Basic Linear Functional Analysis
- 2 Solution Theory for Second Kind Fredholm Integral Equations
 - Riesz Theory
 - Fredholm Theory
- 3 Solution Theory for First Kind Fredholm Integral Equations
 - First Kind Fredholm Equations
 - Ill-posed Problems
 - Regularization
- 4 Applications of Integral Equations
 - Inverse Problems
 - Scattering Problem
 - Numerical examples



4 main types of integral equations

• Fredholm Integral Equations

- 1. kind

$$\int_a^b K(x, y)\varphi(y)dy = g(x), \quad x \in I$$

- 2. kind

$$\varphi(x) + \int_a^b K(x, y)\varphi(y)dy = g(x), \quad x \in I$$

• Volterra Integral Equations

- 1. kind

$$\int_a^x K(x, y)\varphi(y)dy = g(x), \quad x \in I$$

- 2. kind

$$\varphi(x) + \int_a^x K(x, y)\varphi(y)dy = g(x), \quad x \in I$$



Historical Remarks I

- **Maxime Bôcher 1908**

The theory of integral equations may be regarded as dating back at least as far as the discovery by Fourier of the theorem concerning integrals which bears his name; for, though this was not the point of view of Fourier, this theorem may be regarded as a statement of the solution of a certain integral equation of the first kind.

Fourier's inversion formula

$$g(x) = \sqrt{\frac{2}{\pi}} \int_0^{\infty} \cos(x\xi) f(\xi) d\xi$$

$$f(x) = \sqrt{\frac{2}{\pi}} \int_0^{\infty} \cos(x\xi) g(\xi) d\xi$$

Historical Remarks II

- **Abel's Integral 1826**

- a mechanical problem : a Tautochrone
- the general accepted begin of the theory of integral equations
- actually an **inverse problem**
- The problem is to find the unknown path in the plane along which a particle will fall, under the influence of gravity alone, so that at each instant the time of fall is a known function of the distance fallen.

$$g(t) = \int_0^t \frac{f(y)}{\sqrt{2a(t-y)}} dy$$

Historical Remarks III

- Joachimstahl's attraction problem 1861
 - also an inverse problem
 - find the law of attraction if one knows the attraction force

$$\frac{g(h)}{2h} = \int_h^\infty \frac{f(r)}{\sqrt{r^2 - h^2}} dr$$

- at the turn of 20. century :
 - Volterra, Fredholm, Hilbert, Schmidt,
 - Introduction of Hilbert spaces
 - Strong connection with the development of functional analysis ¹

¹M. Bernkopf, The development of function spaces with particular reference to their origins in integral equation theory, Arch. History Exact Sci.

3. 1-96 (1966)

Mathematical Backgrounds and Future Progr. / 63

Solutions of Integral Equations

- In general, integral equations do not have a closed form solution.
- The solvability of integral equations is ensured by **functional analytic** approach.
- Numerical approximate solutions.

Mathematical Backgrounds and Future Progr. / 63

Linear Operators

- **linear operator**

X, Y linear spaces. $A: X \rightarrow Y$ is linear iff for all $\alpha, \beta \in \mathbb{C}$

$$A(\alpha f + \beta g) = \alpha A(f) + \beta A(g), \quad \forall f, g \in X$$

- **bounded operator**

X, Y are normed spaces. A is bounded if there exists a constant $C > 0$ such that

$$\|Af\| \leq C\|f\|, \quad \forall f \in X$$

- **compact operator**

A is compact if it maps a bounded set to a relatively compact set.

Integral Operators

- **integral operator**

$$(A\varphi)(x) := \int_G K(x, y)\varphi(y)dy, \quad x \in G \subset \mathbb{R}^m$$

where K is called the **kernel** of the integral operator.

- K is called **weakly singular** iff there exists a constant $M > 0$ and $\alpha \in (0, m]$ such that

$$|K(x, y)| \leq M|x - y|^{\alpha - m}, \quad \forall x, y \in G \subset \mathbb{R}^m, x \neq y$$

- A is compact if K is continuous or weakly singular.

Section Content

- 1 Integral Equations
 - Main Classifications
 - Historical Remarks
 - Solutions of Integral Equations
 - Basic Linear Functional Analysis
- 2 Solution Theory for Second Kind Fredholm Integral Equations
 - Riesz Theory
 - Fredholm Theory
- 3 Solution Theory for First Kind Fredholm Integral Equations
 - First Kind Fredholm Equations
 - Ill-posed Problems
 - Regularization
- 4 Applications of Integral Equations
 - Inverse Problems
 - Scattering Problem
 - Numerical examples



Riesz Theory I

Consider the following integral equation of the second kind with a compact linear operator $A : X \rightarrow X$

$$\varphi - A\varphi = f$$

Let $L := I - A$.

- **First Riesz Theorem**
The nullspace of L is a finite-dimensional subspace.
- **Second Riesz Theorem**
The range of the operator L is a closed linear subspace.

Riesz Theory II

- **Third Riesz Theorem**

There exists a uniquely determined nonnegative integer r , called the **Riesz number** of A such that

$$\{0\} = N(L^0) \subsetneq N(L^1) \subsetneq \cdots \subsetneq N(L^r) = N(L^{r+1}) = \dots,$$

and

$$X = L^0(X) \supsetneq L^1(X) \supsetneq \cdots \supsetneq L^r(X) = L^{r+1}(X) = \dots,$$

Furthermore, we have the direct sum

$$X = N(L^r) \oplus L^r(X).$$

Fundamental Result of Riesz Theory

Theorem 1

Let $A : X \rightarrow X$ be a compact operator on a normed space X . Then $I - A$ is injective if and only if it is surjective. If $I - A$ is injective, then its inverse operator $(I - A)^{-1}$ is bounded.

Solvability of a Second Kind Equation I

Theorem 2

If the homogeneous equation

$$\varphi - A\varphi = 0$$

has only the trivial solution $\varphi = 0$, then for each $f \in X$ the inhomogeneous equation

$$\varphi - A\varphi = f$$

has a unique solution $\varphi \in X$ and this solution depends continuously on f .

Solvability of a Second Kind Equation II

Theorem 3

If the homogeneous equation

$$\varphi - A\varphi = 0$$

has a nontrivial solution $\varphi \neq 0$, then it has only a finite number m of linearly independent solutions $\varphi_1, \varphi_2, \dots, \varphi_m \in X$ and the inhomogeneous equation is either unsolvable or its general solution is of the form

$$\varphi = \tilde{\varphi} + \sum_{i=1}^m \alpha_i \varphi_i$$

where $\tilde{\varphi}$ is a particular solution of the inhomogeneous equation.

Remarks

- Reduction of the solvability of the equation to the solvability of the simpler homogeneous equation $\varphi - A\varphi = 0$.
- No answer to the question of whether the inhomogeneous equation $\varphi - A\varphi = f$ for a given inhomogeneity is solvable in the case where the homogeneous equation has a nontrivial solution.

Bilinear Forms

Definition 1

Let X, Y be linear spaces. A mapping $\langle \cdot, \cdot \rangle: X \times Y \rightarrow \mathbb{C}$ is called a **bilinear form** if

$$\langle \alpha_1\varphi_1 + \alpha_2\varphi_2, \psi \rangle = \alpha_1 \langle \varphi_1, \psi \rangle + \alpha_2 \langle \varphi_2, \psi \rangle \quad (1)$$

$$\langle \varphi, \beta_1\psi_1 + \beta_2\psi_2 \rangle = \beta_1 \langle \varphi, \psi_1 \rangle + \beta_2 \langle \varphi, \psi_2 \rangle \quad (2)$$

for all $\varphi, \varphi_1, \varphi_2 \in X, \psi, \psi_1, \psi_2 \in Y$ and $\alpha_1, \alpha_2, \beta_1, \beta_2 \in \mathbb{C}$.

A bilinear form is called **nondegenerated** if

$$\langle \varphi, \psi \rangle = 0, \quad \forall \varphi \in X \implies \psi = 0$$

$$\langle \varphi, \psi \rangle = 0, \quad \forall \psi \in Y \implies \varphi = 0$$

Dual Systems

Definition 2

Two normed spaces X and Y equipped with a nondegenerated bilinear form $\langle \cdot, \cdot \rangle: X \times Y \rightarrow \mathbb{C}$ are called a **dual system** and denoted by $\langle X, Y \rangle$.

Example 1

$\langle C(G), C(G) \rangle$ is a dual system with the bilinear form

$$\langle \varphi, \psi \rangle := \int_G \varphi(x)\psi(x)dx, \quad \varphi, \psi \in C(G)$$

Adjoint Operators

Definition 3

Let $\langle X_1, Y_1 \rangle$ and $\langle X_2, Y_2 \rangle$ be two dual systems. Then two operators $A: X_1 \rightarrow X_2, B: Y_2 \rightarrow Y_1$ are called **adjoint** (w.r.t. dual systems) if

$$\langle A\varphi, \psi \rangle = \langle \varphi, B\psi \rangle$$

for all $\varphi \in X_1, \psi \in Y_2$.

Theorem 4

Let $\langle X_1, Y_1 \rangle$ and $\langle X_2, Y_2 \rangle$ be two dual systems. If an operator $A: X_1 \rightarrow X_2$ has an adjoint $B: Y_2 \rightarrow Y_1$, then B is uniquely determined, and A and B are linear.

Adjoint Integral Operators

Theorem 5

If A is compact, then the adjoint of A exists and is also compact.

Theorem 6

Let K be a continuous or a weakly singular kernel. Then in the dual system $\langle C(G), C(G) \rangle$ the integral operators defined by

$$(A\varphi)(X) := \int_G K(x, y)\varphi(y)dy, \quad , x \in G, \quad (3)$$

$$(B\psi)(X) := \int_G K(y, x)\psi(y)dy, \quad , x \in G, \quad (4)$$

are adjoint.

Fredholm Theory I

Let $\langle X, Y \rangle$ be a dual system and $A : X \rightarrow X, B : Y \rightarrow Y$ be compact adjoint operators. We have the following theorems

- **First Fredholm Theorem**

$$\dim N(I - A) = \dim N(I - B) < \infty$$

- **Second Fredholm Theorem**

$$(I - A)(X) = \{f \in X : \langle f, \psi \rangle = 0, \psi \in N(I - B)\} \quad (5)$$

$$(I - B)(Y) = \{g \in Y : \langle \varphi, g \rangle = 0, \varphi \in N(I - A)\} \quad (6)$$

Fredholm Theory II

- **Fredholm Alternative**

Either $I - A$ and $I - B$ are bijective

or $I - A$ and $I - B$ have nontrivial nullspaces with finite dimension

$$\dim N(I - A) = \dim N(I - B) \in \mathbf{N}$$

and the ranges are given by

$$(I - A)(X) = \{f \in X : \langle f, \psi \rangle = 0, \psi \in N(I - B)\} \quad (7)$$

$$(I - B)(Y) = \{g \in Y : \langle \varphi, g \rangle = 0, \varphi \in N(I - A)\} \quad (8)$$

Fundamental Results from Fredholm Theory I

Either the homogeneous integral equations

$$\varphi(x) - \int_G K(x, y)\varphi(y)dy = 0, \quad , x \in G, \quad (9)$$

$$\psi(x) - \int_G K(y, x)\psi(y)dy = 0, \quad , x \in G, \quad (10)$$

only have the trivial solutions $\varphi = 0$ and $\psi = 0$ and the inhomogeneous equations

$$\varphi(x) - \int_G K(x, y)\varphi(y)dy = f(x), \quad , x \in G, \quad (11)$$

$$\psi(x) - \int_G K(y, x)\psi(y)dy = g(x), \quad , x \in G, \quad (12)$$

have a unique solution $\varphi \in C(G)$ and $\psi \in C(G)$ for each right-hand side $f \in C(G)$ and $g \in C(G)$, respectively

Fundamental Results from Fredholm Theory II

or the homogeneous integral equations have the same finite number $m \in \mathbf{N}$ of linearly independent solutions and the inhomogeneous integral equations are solvable if and only if the right-hand sides satisfy

$$\int_G f(x)\psi(x)dx = 0$$

for all solutions ψ of the homogeneous adjoint equation and

$$\int_G \varphi(x)g(x)dx = 0$$

for all solutions φ of the homogeneous equation, respectively.

Remark: Sesquilinear Forms

Definition 4

Let X, Y be linear spaces. A mapping $(\cdot, \cdot) : X \times Y \rightarrow \mathbb{C}$ is called a **sesquilinear form** if

$$(\alpha_1\varphi_1 + \alpha_2\varphi_2, \psi) = \alpha_1(\varphi_1, \psi) + \alpha_2(\varphi_2, \psi) \quad (13)$$

$$(\varphi, \beta_1\psi_1 + \beta_2\psi_2) = \bar{\beta}_1(\varphi, \psi_1) + \bar{\beta}_2(\varphi, \psi_2) \quad (14)$$

for all $\varphi, \varphi_1, \varphi_2 \in X, \psi, \psi_1, \psi_2 \in Y$ and $\alpha_1, \alpha_2, \beta_1, \beta_2 \in \mathbb{C}$.

All the discussions in this section remain true for the sesquilinear forms, e.g.

$(C(G), C(G))$ is a dual system with the sesquilinear form

$$(\varphi, \psi) := \int_G \varphi(x)\bar{\psi}(x)dx, \quad \varphi, \psi \in C(G)$$

Section Content

- 1 Integral Equations
 - Main Classifications
 - Historical Remarks
 - Solutions of Integral Equations
 - Basic Linear Functional Analysis
- 2 Solution Theory for Second Kind Fredholm Integral Equations
 - Riesz Theory
 - Fredholm Theory
- 3 Solution Theory for First Kind Fredholm Integral Equations
 - First Kind Fredholm Equations
 - Ill-posed Problems
 - Regularization
- 4 Applications of Integral Equations
 - Inverse Problems
 - Scattering Problem
 - Numerical examples



First Kind Fredholm Equations

Consider the following equation

$$A\varphi = f$$

When A is compact, we are encountered with an **ill-posed problem** since

Theorem 7

A compact operator defined in an infinite dimensional space can not have a bounded inverse.

Hadamard's Postulation of Well-posedness

Hadamard (1902)

A problem is called **well-posed**, if it has the following properties

- ① Existence of a solution.
- ② Uniqueness of the solution.
- ③ (Stability) Continuous dependence of the solution on the data.

otherwise it is called **ill-posed**.

Examples of Ill-Posed Problems

Example 2 (Cauchy Problem for the Laplace Equation)

Find a harmonic function u in $D := \mathbf{R} \times [0, \infty]$ satisfying the following initial conditions

$$u(\cdot, 0) = 0, \quad \frac{\partial}{\partial y} u(\cdot, 0) = f,$$

where f is a given continuous function.

Let $f_n(x) = \frac{1}{n} \sin nx, x \in \mathbf{R}$.

For $n \in \mathbf{N}$, we obtain the solution

$$u_n(x, y) = \frac{1}{n^2} \sin nx \sinh ny, \quad (x, y) \in D.$$

Clearly, $(f_n) \rightarrow 0$, but (u_n) doesn't converge in any reasonable norm.

Example 3 (Fredholm Integral Equation of the First Kind)

$$A\varphi(x) := \int_a^b K(x, y)\varphi(y)dy, \quad x \in [c, d]$$

Solving $A\varphi = f$ is ill-posed if, for example, the kernel K is continuous. If K is continuous, then the operator A will be compact. In this case, the operator A will not have a bounded inverse.

Fredholm integral Equations 2. Kind

$$\varphi(x) - \frac{1}{2} \int_0^1 (x+1)e^{-xy}\varphi(y)dy = e^{-x} - \frac{1}{2} + \frac{1}{2}e^{-(x+1)}, \quad 0 \leq x \leq 1$$

Trapezoidal rule

n	$x = 0$	$x = 0.5$	$x = 1$
4	-0.007146	-0.010816	-0.015479
8	-0.001788	-0.002711	-0.003882
16	-0.000447	-0.000678	-0.000971
32	-0.000112	-0.000170	-0.000243

Simpson's rule

n	$x = 0$	$x = 0.5$	$x = 1$
4	-0.00006652	-0.00010905	-0.00021416
8	-0.00000422	-0.00000692	-0.00001366
16	-0.00000026	-0.00000043	-0.00000086
32	-0.00000002	-0.00000003	-0.00000005

Fredholm integral Equations 1. Kind

$$\int_0^1 (x+1)e^{-xy}\varphi(y)dy = 1 - e^{-(x+1)}, \quad 0 \leq x \leq 1$$

Trapezoidal rule

n	$x = 0$	$x = 0.5$	$x = 1$
4	0.4057	0.3705	0.1704
8	-4.5989	14.6094	-4.4770
16	-8.5957	2.2626	-153.4805
32	3.8965	-32.2907	22.5570
64	-88.6474	-6.4484	-182.6745

Simpson's rule

n	$x = 0$	$x = 0.5$	$x = 1$
4	0.0997	0.2176	0.0566
8	-0.5463	6.0868	-1.7274
16	-15.4796	50.5015	-53.8837
32	24.5929	-24.1767	67.9655
64	23.7868	-17.5992	419.4284

Ill-Posed Problems : Regularization

Definition 5 (Regularization)

Assume X, Y are normed spaces.

Let the operator $A : X \rightarrow Y$ be linear, bounded and injective.

A family of bounded linear operators $R_\alpha : Y \rightarrow X, \alpha > 0$ is called a **regularization scheme** for

$$A\varphi = f,$$

if it satisfies the following pointwise convergence

$$\lim_{\alpha \rightarrow 0} R_\alpha A\varphi = \varphi, \text{ for all } \varphi \in X$$

In this case, the parameter α is called the **regularization parameter**.

Regularization : Error Estimate

Find a stable approximation to the equation

$$A\varphi = f$$

The regularized approximation

$$\varphi_\alpha^\delta := R_\alpha f^\delta$$

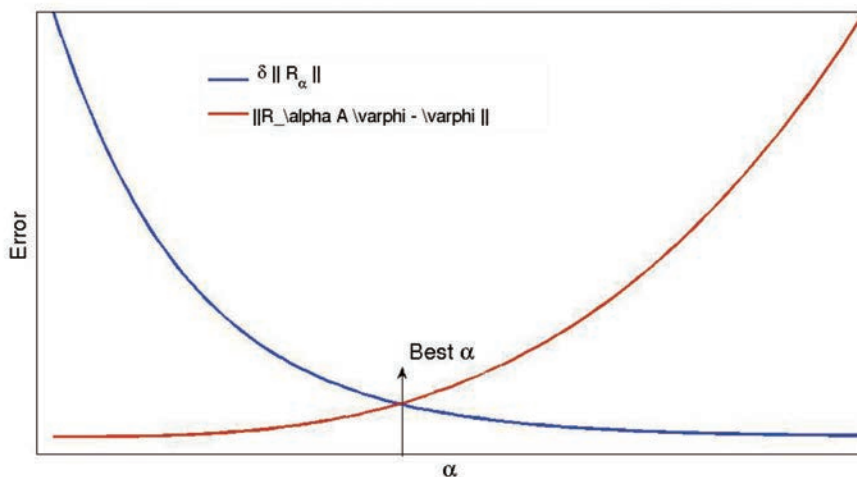
The total approximation error

$$\varphi_\alpha^\delta - \varphi = R_\alpha f^\delta - R_\alpha f + R_\alpha A\varphi - \varphi$$

We have

$$\|\varphi_\alpha^\delta - \varphi\| \leq \delta \|R_\alpha\| + \|R_\alpha A\varphi - \varphi\|$$

Error behavior



Regularization : Choice of α

How to choose the regularization parameter α ?

- ① **a priori** choice based on some information of the solution.
In general not available
- ② **a posteriori** choice based on the data error level δ

Discrepancy Principle of Morozov :

$$\|AR_\alpha f^\delta - f^\delta\| = \gamma\delta, \quad \gamma \geq 1$$

Tikhonov Regularization I

X, Y Hilbert spaces.

Theorem 8

Assume $A : X \rightarrow Y$ compact and linear.

Then for every $\alpha > 0$, the operator

$$\alpha I + A^*A : X \rightarrow X$$

is bijective and has a bounded inverse.

Furthermore, if the operator A is injective, then

$$R_\alpha := (\alpha I + A^*A)^{-1} A^*, \quad \alpha > 0$$

describes a regularization scheme with $\|R_\alpha\| \leq \frac{1}{2\sqrt{\alpha}}$.

Tikhonov Regularization II

Theorem 9

Let $A : X \rightarrow Y$ be a linear and bounded operator. Assume $\alpha > 0$. Then for each $f \in Y$ there exists a unique $\varphi_\alpha \in X$ such that

$$\|A\varphi_\alpha - f\| + \alpha\|\varphi_\alpha\| = \inf_{\varphi \in X} \left\{ \|A\varphi - f\|^2 + \alpha\|\varphi\|^2 \right\}$$

The minimizer φ_α is given by the unique solution of the equation

$$\alpha\varphi_\alpha + A^*A\varphi_\alpha = A^*f$$

and depends continuously on f .

Section Content

- 1 Integral Equations
 - Main Classifications
 - Historical Remarks
 - Solutions of Integral Equations
 - Basic Linear Functional Analysis
- 2 Solution Theory for Second Kind Fredholm Integral Equations
 - Riesz Theory
 - Fredholm Theory
- 3 Solution Theory for First Kind Fredholm Integral Equations
 - First Kind Fredholm Equations
 - Ill-posed Problems
 - Regularization
- 4 Applications of Integral Equations
 - Inverse Problems
 - Scattering Problem
 - Numerical examples

Inverse Problems : Definition

Keller², 1976

Two problems are **inverse** to each other if the formulation of each of them requires all or partial knowledge of the other. Often, for historical reasons, one of the two problems has been studied extensively for some time, while the other is newer and not so well understood. In such cases, the former problem is called the **direct problem**, while the latter is called the **inverse problem**.

²Inverse Problems, Joseph B. Keller, The American Mathematical Monthly, Vol. 83, No. 2. (Feb., 1976), pp. 107-118.

Example 4 (Differentiation)

Direct problem (DP): Given $\varphi \in C([0, 1])$, solve

$$(T\varphi)(x) := \int_0^x \varphi(t) dt, \quad x \in [0, 1]$$

Inverse problem (IP): Given $g \in C([0, 1])$ with $g(0) = 0$, solve

$$T\varphi = g$$

Remark

(IP) has a solution $\varphi \in C([0, 1])$ if and only if $g \in C^1([0, 1])$.

Assume $g^\delta \in C([0, 1])$ with $\|g^\delta - g\|_\infty \leq \delta$, $0 < \delta < 1$.

Define $g_n^\delta(x) := g(x) + \delta \sin \frac{nx}{\delta}$, $x \in [0, 1]$

We have $(g_n^\delta)'(x) := g'(x) + n \cos \frac{nx}{\delta}$, $x \in [0, 1]$

It holds $\|(g_n^\delta)' - g'\|_\infty = n$.

Example 5 (Backward Heat Conduction)

Consider the heat equation

$$\frac{\partial u}{\partial t} = \frac{\partial^2 u}{\partial x^2}, \quad -\infty < x < \infty, t > 0,$$

with initial condition $u(x, 0) = \varphi(x)$

Direct problem: find $u(x, t), t > 0$

$$u(x, t) = \frac{1}{\sqrt{4\pi t}} \int_{-\infty}^{\infty} e^{-(x-y)^2/4t} \varphi(y) dy$$

Inverse Problem : find $u(x, t), t < 0$

$u_n(x, t) = \frac{1}{n} \sin nx e^{-n^2 t}$ solves the heat equation.

$u_n(x, 0) = \frac{1}{n} \sin nx \rightarrow 0$ uniformly. but

$u_n(x, -1) = \frac{1}{n} \sin nx e^{n^2} \rightarrow \pm\infty$

Example 6 (Inverse Obstacle Scattering Problem)

Direct Problem :

Given an impenetrable, smooth, bounded obstacle D .

Find the **far field pattern** u_∞ of the scattered field u^s satisfying the following conditions :

- ① (Helmholtz equation) $\Delta u + k^2 u = 0$ in $\mathbb{R}^n \setminus D$
- ② (Dirichlet BC) $u = 0$ on ∂D .
- ③ (Sommerfeld Radiation Condition, SRC)

$$\lim_{r \rightarrow \infty} r^{(n-1)/2} \left(\frac{\partial u^s}{\partial r} - iku^s \right) = 0, \quad \text{uniformly for all } \hat{x}$$

where the total field u is the superposition of the unknown scattered field u^s and the known incident field $u^i(x) = e^{ik \langle x, d \rangle}$ with incident direction $d \in S^{n-1}$.

Inverse Problem :

Find D from the knowledge of u_∞

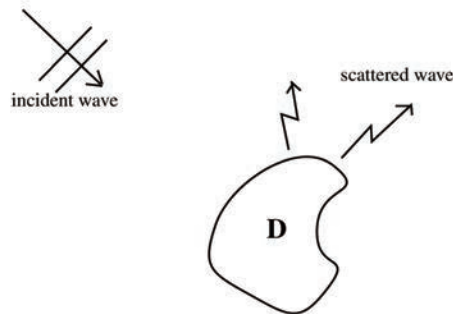
Scattering problem

Object :

time harmonic acoustic scattering

Modelling :

Exterior boundary value problem for the Helmholtz equation



Direct problem

Definition 6

Find: $u^s \in C^2(\mathbb{R}^2 \setminus \bar{D}) \cap C(\mathbb{R}^2 \setminus D)$ satisfies

- 1 the Helmholtz equation $\Delta u^s + k^2 u^s = 0$, in $\mathbb{R}^2 \setminus \bar{D}$
- 2 the Dirichlet boundary condition(BC)

$$u^s = -u^i \quad \text{on } \Gamma := \partial D \quad (15)$$

- 3 the Sommerfeld radiation condition(SRC)

$$\lim_{r \rightarrow \infty} \sqrt{r} \left(\frac{\partial u^s}{\partial r} - i k u^s \right) = 0, \quad r := |x|, \hat{x} := \frac{x}{|x|}$$

Well-posedness of DP

Theorem 10

The direct problem has a unique solution given by

$$u^s(x) = \int_{\Gamma} \frac{\partial \Phi(x, y)}{\partial \nu(y)} \varphi(y) ds(y) + i \int_{\Gamma} \Phi(x, y) \varphi(y) ds(y) \quad x \in \mathbb{R}^2 \setminus \bar{D}. \quad (16)$$

where the density function $\varphi \in C(\Gamma)$ is the (unique) solution to the following boundary integral equation

$$\varphi(x) + 2 \int_{\Gamma} \frac{\partial \Phi(x, y)}{\partial \nu(y)} \varphi(y) ds(y) + 2i \int_{\Gamma} \Phi(x, y) \varphi(y) ds(y) = -2u^i(x) \quad (17)$$

for $x \in \Gamma$.

Operator equation

We define for $x \in \Gamma$ the operators

$$(S\varphi)(x) := 2 \int_{\Gamma} \Phi(x, y) \varphi(y) ds(y)$$

and

$$(K\varphi)(x) := 2 \int_{\Gamma} \frac{\partial \Phi(x, y)}{\partial \nu(y)} \varphi(y) ds(y)$$

The boundary integral equation (17) in the operator form reads

$$(I + K + iS)\varphi = -2u^i \quad (18)$$

Main idea of the proof

- Functional analytical approach
- Uniqueness by Rellich Lemma and Radiation condition
- Existence and stability by Riesz Theory

Far field pattern u_∞

The far field pattern or the scattering amplitude is given by

$$u^s(x) = \frac{e^{ik|x|}}{\sqrt{|x|}} \left\{ u_\infty(\hat{x}) + O\left(\frac{1}{|x|}\right) \right\} \quad |x| \rightarrow \infty$$

uniformly for all directions $\hat{x} \in \Omega := \{x \in \mathbb{R}^2 \mid |x| = 1\}$.

The far field pattern for the Dirichlet problem is :

$$u_\infty(\hat{x}) = \lambda_1 \int_\Gamma \langle \nu(y), \hat{x} \rangle e^{-ik\langle \hat{x}, y \rangle} \varphi(y) ds(y) + i\lambda_2 \int_\Gamma e^{-ik\langle \hat{x}, y \rangle} \varphi(y) ds(y) \quad (19)$$

with the constants $\lambda_1 = \frac{1-i}{4} \sqrt{\frac{k}{\pi}}$, $\lambda_2 = \frac{1+i}{4\sqrt{k\pi}}$ and the density function φ given by theorem 10.

Inverse Problem

Definition 7 (IP)

Determine the scatterer D if the far field pattern $u_\infty(\cdot, d)$ is known for one incident direction d and for one wave number $k \in \mathbb{R}$.

Uniqueness

Theorem 11 (Schiffer)

If D_1 and D_2 are the solutions to the inverse problem with the same far field pattern for a fixed wave number k , then $D_1 = D_2$.

Comments on Existence

- Solving the inverse problem means to solve the far field equation

$$F(\Gamma) = u_\infty \quad (20)$$

- However
 - (21) is an equation of the first kind
 - The operator F is compact
 - F is nonlinear in Γ .

To remain in our framework, we need

- Linearization
- Regularization

Newton's Method

Solve the nonlinear ill-posed far field equation:

$$F(\Gamma) = u_\infty \quad (21)$$

where the far field operator F is given by equation (19).

Linearization:

$$F(\gamma) + F'(\gamma)h = u_\infty \quad (22)$$

Newton iteration:

$$\gamma_{\nu+1} = \gamma_\nu + h, \quad \nu = 0, 1, 2, \dots$$

Regularization is needed in solving (22).

Regularization

Instead of solving (22), we solve the regularized equation

$$(\alpha I + F'(\gamma)F'(\gamma)^*) h = F'(\gamma)^*(u_\infty - F(\gamma)) \quad (23)$$

where $\alpha > 0$ is a regularization parameter.

Newton iteration:

$$\gamma_{\nu+1} = \gamma_\nu + h, \quad \nu = 0, 1, 2, \dots$$

Numerical Settings

Define the space :

$$V_m := \text{span}\{1, \cos t, \cos 2t, \dots, \cos mt; \sin t, \dots, \sin(m-1)t\}$$

The solution space for $\Gamma := (\gamma_1(t), \gamma_2(t))$ is taken to be $V_m \times V_m$.

The solution space for the density function φ is V_n .

Stopping criterion for the Newton's method:

Discrepancy Principle:

$$\|u_{\infty,k} - u_\infty\| < \epsilon$$

Examples

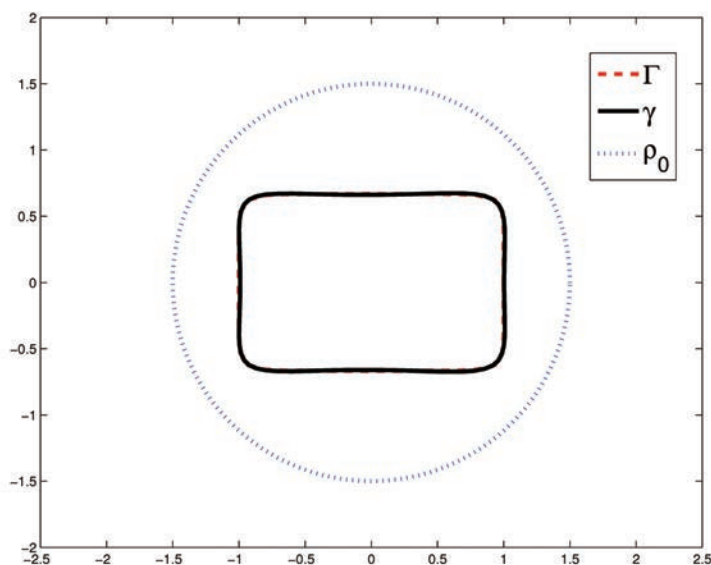
For the numerical examples, we take obstacles of the following form

$$\Gamma = \gamma(t)(\cos t, \sin t)$$

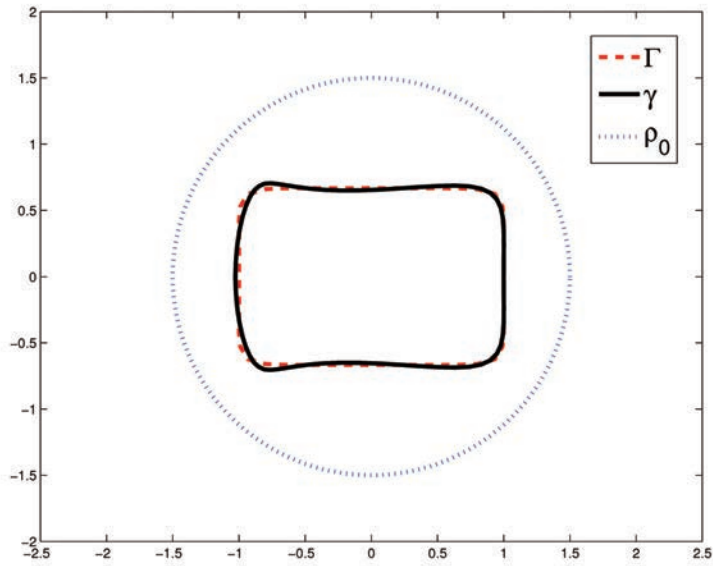
with different γ

- 1 Rectangle $\gamma(t) = \frac{2}{3} \left[\sin^{10} t + \left(\frac{2}{3} \cos t \right)^{10} \right]^{-0.1}$
- 2 Peanut $\gamma(t) = \sqrt{\cos^2 t + 0.25 \sin^2 t}$
- 3 Bean $\gamma(t) = \frac{1+0.9 \cos t+0.1 \sin(2t)}{1+0.75 \cos t}$

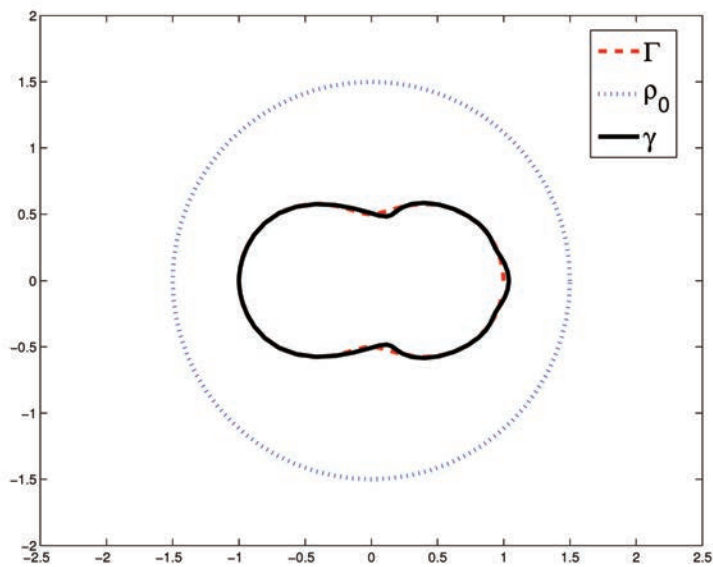
Rectangle



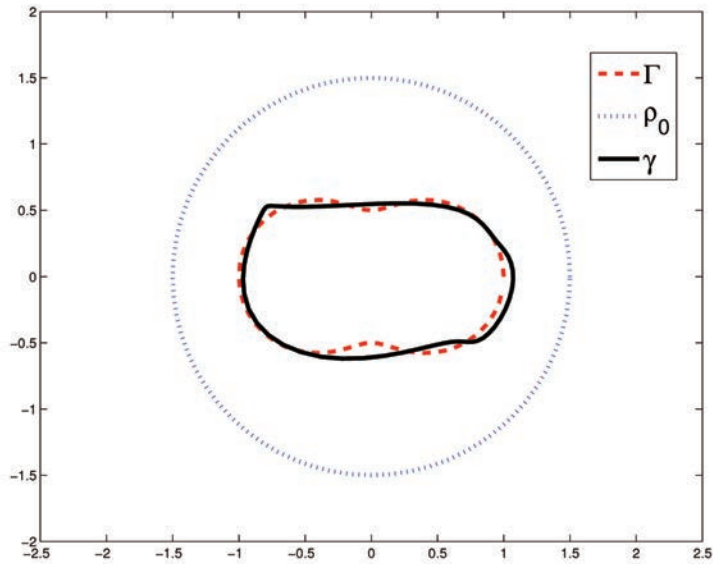
Rectangle with 3% noise



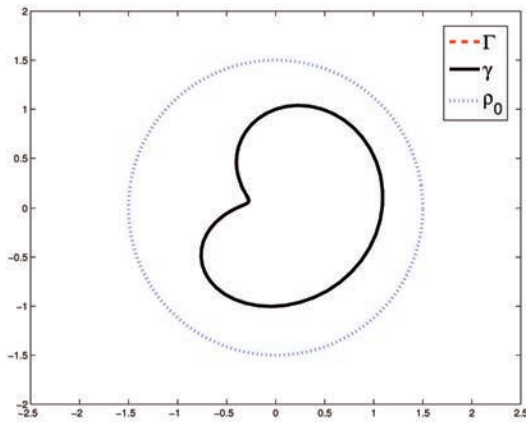
Peanut



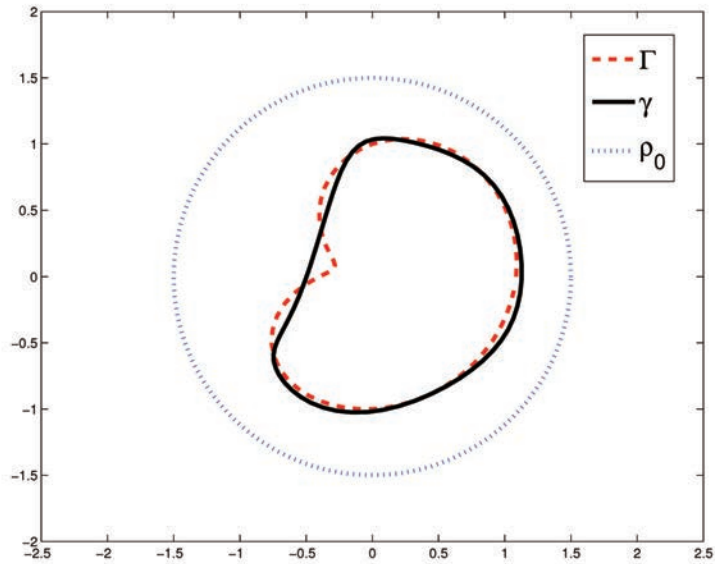
Peanut with 3% noise



Bean



Bean with 3% noise



ON CURRENT DENSITY BASED IMPEDANCE IMAGING WITH MINIMAL DATA

ALEXANDRU TAMASAN

ABSTRACT. In this paper we survey some recent progress in conductivity imaging that uses the magnitude of one current density field, with particular interest in the Complete Electrode Model.

1. INTRODUCTION

In electrical impedance imaging one seeks quantitative information on the electrical conductivity σ and the permittivity distribution inside a body. Original formulations of the problem used boundary measurements of electric voltage potential and currents [27, 59, 9]. Due to high contrast in biological materials a renewed interest in conductivity imaging started in mid 1980s geared by applications in the medical field [17, 5], which soon exploded in developments on both the mathematics and engineering field. Among some of the most remarkable results on the mathematical facet of we mention [49, 36, 8]. For an understanding on the breadth of these development we refer to the reviews [10],[7]. By now, however, it is well understood that the problem is severely ill-posed, where changes of the conductivity inside induce exponentially small perturbations in the measured boundary data (inverse with the distance to the boundary) [11], [33]. Controlled by the level of noise, the ill-posedness impose serious limitations on the resolution of the image away from the boundary. Current research, including the ones reviewed here, considers coupled physical phenomena to restore the well-posedness, see, e.g., [3],[12],[2],[4].

Current Density Impedance Imaging (CDII) is one of the hybrid methods in which the classical model based on Maxwell system is augmented by some interior knowledge of the Current Density field \mathbf{J} induced by the applied current (or voltage) at the boundary. While still nonlinear, under reasonable sufficient assumptions the conductivity imaging problem becomes well-posed. Currently, the interior field data is obtained from Magnetic Resonance measurements as found by M. Joy at al. in their pioneering work in Current Density Imaging [19, 46]. They show that the magnetic flux density \mathbf{B} induced by an applied current can be determined from magnetic resonance. For very low frequency currents (a few kHz) the effects of permittivity are negligible, and the current density field is determined from the Maxwell equation $\mathbf{J} = \frac{1}{\mu_0} \nabla \times \mathbf{B}$, where the magnetic permeability of the tissue μ_0 may be assumed constant and known; see Section 2 for a brief description.

AMS Subject Classification: 35R30, 35J60, 31A25, 62P10.

The first work proposing to use the knowledge of \mathbf{J} to image electrical conductivity appeared in [61]. In [16] a perturbation method recovers the conductivity in the linearized case. Based on the fact that \mathbf{J} is normal to equipotential lines, the method in [26] recovers two dimensional conductivities. In [22] Seo et al. reduce the conductivity imaging problem to the Neumann problem for the 1-Laplacian, show examples of non-uniqueness and non-existence, and propose the “ J -substitution” algorithm to image conductivity from knowledge of the magnitude of two current density fields $|\mathbf{J}_1|, |\mathbf{J}_2|$; see also [21]. While this iterative algorithm is shown to be convergent [23], there is no proof of independence of the starting guess. As a corollary of a result in here, we will see that the magnitude of two currents does determine the conductivity uniquely. In [44] the problem is reduced to a first order system of PDEs and several numerical reconstructions based on solving this system are proposed. A local formula based on two transversal fields (6 functions) appeared in [20] (see also [15]), and independently in [28].

Each magnetic resonance experiment determines only the component of the magnetic field along the longitudinal axis of the MRI gantry. To obtain the current density field \mathbf{J} (by taking the curl), one currently performs two further rotations of the object, fact which limits its medical applications. To avoid such rotations, Seo et al. have developed several methods (known under the name Magnetic Resonance Electrical Impedance Tomography) for conductivity imaging using the B_z - component of the magnetic field, see e.g., [43, 45, 25, 29, 60]. While performing well in numerical simulations and phantom experiments, the unique determination of the conductivity from just one component of \mathbf{B} is still an open problem, except for some special axial symmetry [30], or under some posteriori assumptions [31]. Most recent results in MREIT at Larmor frequency show that one can determine $H_x + iH_y$ inside (where both components H_x , and H_y are complex valued) and under further axial assumptions an isotropic conductivity is uniquely determined [48]. This is a directions of intense activity in current mathematical and engineering research and we refer to the survey [52] for further details.

In Section 3 we survey some of collaborative work of the author in [37],[38] and [39] on imaging conductivity from the knowledge of the magnitude $|\mathbf{J}|$ of just one current density field when the voltage potential is (partially) known at the boundary.

In Section 4 we review the Complete Electrode Model (CEM) of Somersalo-Cheney and Isaacson [47] from a minimization point of view introduced in [41, Appendix]. In Section 5 we announce the most recent results obtained in [41] for the conductivity imaging with complete electrode model boundary conditions. The pictures at the end are part of a numerical experiment for the inverse problem for the complete electrode model based on the theoretical results in Section 5, see [41] for details.

2. INTERIOR DATA ACQUISITION

In this section we briefly describe the way the interior data is obtained. The notations used in here are not essential for the other sections of the paper.

In the three dimensional space, assume that z is the longitudinal axis (along the main static magnetic field) of an MRI machine. Upon injecting a current I_+ into

a body Ω the induced magnetic field $\mathbf{B} = (B_x, B_y, B_z)$ alters the spin of protons (and their precession time) thus producing a phase change in the Magnetic Resonance signal M . More precisely, the phase change in the transversal plane $z = z_0$ is proportional with the component B_z and with the duration T of the pulse (injection):

$$M_+(x, y, z_0) = M(x, y, z_0)e^{i\gamma B_z(x, y, z_0)T + i\varphi_0}, \quad (x, y, z_0) \in \Omega;$$

here φ_0 is the phase due to the static magnetic field and γ is the magnetogyric ratio. By applying the inversely polarized current I_- for the same duration T , one obtains

$$M_-(x, y, z_0) = M(x, y, z_0)e^{-i\gamma B_z(x, y, z_0)T + i\varphi_0}, \quad (x, y, z_0) \in \Omega.$$

Therefore,

$$B_z(x, y, z_0) = \frac{1}{2\gamma T} \Im m \log \left(\frac{M_+(x, y, z_0)}{M_-(x, y, z_0)} \right),$$

where \log denotes a continuous branch of the complex logarithm. In practice, one uses a “phase unwrapping” algorithm to determine such a branch.

3. IMAGING FROM THE INTERIOR DATA $|\mathbf{J}|$

In this section we assume that a conductive body $\Omega \subset \mathbb{R}^n$, $n \geq 2$, has connected Lipschitz boundary $\partial\Omega$. The (unknown) conductivity $\sigma \in L^\infty(\Omega)$ is isotropic and bounded away from zero. Further regularity will be assumed as stated in the results. Let \mathbf{J} be the current density field, u be the induced electric potential and $\mathbf{E} = -\nabla u$ be the induced electric field in Ω . We assume that knowledge of $|\mathbf{J}|$ is available inside.

For ideal data, Ohm’s law ($\mathbf{J} = -\sigma\mathbf{E}$) implies that $|\mathbf{J}|/|\nabla u| \in L^\infty(\Omega)$ and

$$(1) \quad \sigma(x) = \frac{|\mathbf{J}(x)|}{|\nabla u(x)|}, \quad x \in \Omega.$$

In the absence of charge sources/sinks the conservation law $\nabla \cdot \mathbf{J} = 0$ together with (1) lead to the singular, quasilinear, degenerate elliptic equation

$$(2) \quad \nabla \cdot \left(\frac{|\mathbf{J}|}{|\nabla u|} \nabla u \right) = 0.$$

The equation (2) appears first in [22] together with examples of non-uniqueness and non-existence for the associated Neumann problem.

In [37] the equipotential sets of regular solutions of (2) were shown to be minimal surfaces with respect to the metric $g = |\mathbf{J}|^{2/(n-1)}I$, the same geometric property enjoyed by solutions of the classical 1-Laplacian, where $|J| \equiv 1$. Let

$$(3) \quad \mathbf{A}(\Sigma) = \int_{\Sigma} |\mathbf{J}| dS,$$

be the surface area of Σ induced by the metric $g = |\mathbf{J}|^{2/(n-1)}I$. In [37] the equipotential sets were shown to be minimal surfaces with respect to the metric $g = |\mathbf{J}|^{2/(n-1)}I$. In fact they are not just critical surfaces but they are minimizers. Below we denote by H^{n-1} the $(n-1)$ -Hausdorff measure and describe (compact) distortions of level sets of u by level sets of arbitrary functions with the same trace as u at the boundary.

Theorem 3.1 ([39]). *Let $u \in C^{2,\delta}(\Omega)$ be the electric potential inside a $C^{1,\delta}$ -smooth conductive body, generated while maintaining the voltage $f \in C^{2,\delta}(\partial\Omega)$ at the boundary, $0 < \delta < 1$. Assume $|\mathbf{J}| > 0$ in $\bar{\Omega}$. Let $\lambda \in \text{Range}(f)$ be such that $H^{n-1}(f^{-1}(\lambda) \cap \partial\Omega) = 0$ (valid a.e. $\lambda \in \text{Range}(f)$).*

Then, for any $v \in C^2(\bar{\Omega})$ with $v|_{\partial\Omega} = f$ and $|\nabla v| \neq 0$, we have

$$(4) \quad \mathbf{A}(u^{-1}(\lambda)) \leq \mathbf{A}(v^{-1}(\lambda)),$$

where \mathbf{A} is defined in (3).

In the plane the level sets are geodesics, for smooth data, they can be recovered as solutions of the system

$$(5) \quad \begin{aligned} \ddot{x} &= -\dot{x}^2 \frac{|J_x|}{|J|}(x, y) - 2\dot{x}\dot{y} \frac{|J_y|}{|J|}(x, y) + \dot{y}^2 \frac{|J_x|}{|J|}(x, y), \\ \ddot{y} &= \dot{x}^2 \frac{|J_y|}{|J|}(x, y) - 2\dot{x}\dot{y} \frac{|J_x|}{|J|}(x, y) - \dot{y}^2 \frac{|J_y|}{|J|}(x, y), \end{aligned}$$

In the Cauchy case we have the following:

Theorem 3.2 ([40]). *Let $\Omega \subset \mathbb{R}^2$ be a simply connected, bounded domain with a piecewise C^1 -smooth boundary and $\Gamma \subset \partial\Omega$. Given $f \in C^2(\Gamma)$, $g \in C^1(\Omega)$, and $|\mathbf{J}| \in C^1(\bar{\Omega}) \cap C^2(\Omega)$, there exists a uniquely defined subregion $\tilde{\Omega} \subset \Omega$ and a unique pair $(\sigma, u) \in C^2(\tilde{\Omega}) \times C^2(\tilde{\Omega})$ such that u is σ -harmonic and $\sigma|\nabla u| = |\mathbf{J}|$ in $\tilde{\Omega}$, and $u|_{\Gamma} = f$ and $\partial_\nu u|_{\Gamma} = g$. Moreover, if f is almost two-to-one and Γ is a maximal arc of monotony, then the above holds with $\tilde{\Omega} = \Omega$.*

Note that in practice the reconstruction method based on Theorem 3.2 needs the current \mathbf{J} , the voltage potential, and σ along the boundary arc Γ . The next method, based on the Dirichlet boundary value problem associated with (5) only requires knowledge of the voltage on parts of the boundary:

Theorem 3.3 ([39]). *Let $\Omega \subset \mathbb{R}^2$ be a simply connected domain with $C^{2,\delta}$ -boundary, $0 < \delta < 1$. For $i = 1, 2$ let $\sigma_i \in C^{2,\delta}(\Omega)$, u_i be σ_i -harmonic with $u_i|_{\partial\Omega} \in C^{3,\delta}(\partial\Omega)$ almost two-to-one, and $|J_i| = |\sigma_i \nabla u_i|$. For $\alpha < \beta$ let*

$$(6) \quad \Omega_{\alpha,\beta} := \{x \in \bar{\Omega} : \alpha < u_1(x) < \beta\} \text{ and } \Gamma := \Omega_{\alpha,\beta} \cap \partial\Omega.$$

(i) *Assume $u_1|_{\Gamma} = u_2|_{\Gamma}$ and $|J_1| = |J_2|$ in Ω . Then*

$$\begin{aligned} u_1 &= u_2 \text{ in } \Omega_{\alpha,\beta} \text{ and} \\ \sigma_1 &= \sigma_2 \text{ in } \Omega_{\alpha,\beta}. \end{aligned}$$

(ii) *Assume $u_1|_{\Gamma} = u_2|_{\Gamma}$ and $|J_1| = |J_2|$ in the interior of $\Omega_{\alpha,\beta}$. Then*

$$(7) \quad \{x \in \bar{\Omega} : \alpha < u_2(x) < \beta\} = \Omega_{\alpha,\beta},$$

$$(8) \quad u_1 = u_2 \text{ in } \Omega_{\alpha,\beta} \text{ and}$$

$$(9) \quad \sigma_1 = \sigma_2 \text{ in } \Omega_{\alpha,\beta}.$$

The reconstruction is based on solving two point boundary value problems to find geodesics joining pairs of equipotential points at the boundary. Note that, in general, such boundary value problems may have none or multiple solutions even for the geodesic system.

Theorem 3.4 ([39]). *Let $\Omega \subset \mathbb{R}^2$ be a simply connected domain with $C^{2,\delta}$ -boundary, $0 < \delta < 1$. Let $(f, |\mathbf{J}|) \in C^{2,\delta}(\partial\Omega) \times C^{1,\delta}(\Omega)$ be an admissible pair with f almost two-to-one and let $(x_0, y_0), (x_1, y_1) \in \partial\Omega$ be such that $f(x_0, y_0) = f(x_1, y_1)$. Then the system (5) subject to the boundary conditions*

$$(10) \quad (x(0), y(0)) = (x_0, y_0) \text{ and } (x(1), y(1)) = (x_1, y_1),$$

has a unique solution $\gamma : [0, 1] \rightarrow \Omega$, $\gamma(t) = (x(t), y(t))$. Moreover, the map $u : \Omega \rightarrow \mathbb{R}$ is constant along γ :

$$(11) \quad (u \circ \gamma)(t) = \lambda, \quad t \in [0, 1].$$

The results above provide reconstruction methods for the planar case. In theory they can be extended to three dimensional models, but recovering the potential level set by level set is not practical. An alternate method based on a variational problem is proposed. This method is valid in any dimension.

We consider the minimization problem

$$(12) \quad \min \left\{ \int_{\Omega} |\mathbf{J}| |\nabla v| dx : v \in S, v|_{\partial\Omega} = f \right\},$$

where S is an appropriate space of competitors (ideally $H^1(\Omega)$), $\mathbf{J} \in L^2(\Omega)$ is the current density field induced in Ω while maintaining a voltage potential $f \in H^{1/2}(\partial\Omega)$; we call such a pair $(|\mathbf{J}|, f)$ *admissible*. This problem was first studied for the case $|\mathbf{J}| \equiv 1$ in [55, 54, 56] where existence of a unique minimizer was proved under the assumption that f is continuous and $\partial\Omega$ has positive mean curvature on a dense subset of $\partial\Omega$. Existence for the case when $S = BV(\Omega)$ is the space of functions of bounded total variation has been established recently in [18] for $|\mathbf{J}| \in C^{1,1}(\bar{\Omega})$ bounded away from zero and $f \in C(\Omega)$. However, for the admissible case occurring in the conductivity imaging problem, the minimization problem above is shown to have at least one solution in $H^1(\Omega)$, namely the potential u [38]. Note also that formally, the Euler-Lagrange equation associated with the (non-smooth) functional in (12) is the 1-Laplacian equation (2).

Uniqueness results in [38, 39, 34] assume a space of competitors of increasing generality, with the most general case treated in [35]. In the theorem below $|Du|$ is the Radon measure induced by the total variation of u (which coincides with $|\nabla u|$ if $u \in W^{1,1}(\Omega)$).

Theorem 3.5 ([35]). *Let $\Omega \subset \mathbb{R}^n$ be a bounded Lipschitz domain with connected boundary, $f \in C(\partial\Omega)$, and $|\mathbf{J}| \in C(\bar{\Omega})$. If $|\mathbf{J}| > 0$ in $\bar{\Omega}$ and*

$$(13) \quad \min \left\{ \int_{\Omega} |\mathbf{J}| |Du| : u \in BV(\Omega), u|_{\partial\Omega} = f \right\},$$

has a minimizer $u \in C^1(\bar{\Omega})$ with $|\nabla u| > 0$ in $\bar{\Omega}$, then u is the unique minimizer of (13) in $BV(\Omega)$.

For the admissible data $(|\mathbf{J}|, f) \in L^2(\Omega) \times H^{1/2}(\partial\Omega)$ a minimization scheme in [42] shows stability of the minimum value in (12) with respect to the interior data $a \in L^2(\Omega)$ nearby $|\mathbf{J}|$. Note that arbitrary (a, f) may not be admissible and the

corresponding minimization problem for $\int_{\Omega} a |\nabla v| dx$ may not have solutions in $H^1(\Omega)$. The stability property of the minimizer of (12) is still an open problem closely related to the uniqueness question.

The uniqueness result in Theorem 3.5 above, can now be applied to show convergence of the regularized minimization scheme in [42]. In order to state this new result, let us recall some assumptions in [42]. The domain $\Omega \subset \mathbb{R}^d$ is bounded with $C^{1,\alpha}$ -smooth boundary, the boundary voltage $f \in C^{1,\alpha}(\partial\Omega)$, and the conductivity σ is unknown but assumed in $C^\alpha(\overline{\Omega})$, for some $0 < \alpha < 1$. The magnitude $|\mathbf{J}|$ of the current density field (which by elliptic regularity is in $C^\alpha(\overline{\Omega})$) is assumed bounded away from zero. Let $u \in H^1(\Omega)$ denote the unknown σ -harmonic map with trace f at the boundary (again, elliptic regularity insures $u \in C^{1,\alpha}$), and let u_0 be the harmonic map with same trace f as u .

The minimization scheme will seek the unknown potential $u = u_0 + h$ for some $h \in H_0^1(\Omega)$ to be determined.

Set

$$(14) \quad \delta := \frac{\min_{\overline{\Omega}} |\mathbf{J}|}{\max_{\overline{\Omega}} \sigma} > 0.$$

For $\epsilon > 0$ to be specified, δ as in (14), and some $a \in L^2(\Omega)$ consider the following regularized functional $F_\epsilon^\delta[\cdot; a] : H_0^1(\Omega) \rightarrow \mathbb{R}$ by

$$(15) \quad F^\delta[h; a] := \int_{\Omega} a \max\{|\nabla(u_0 + h)|, \delta\} dx + \epsilon \int_{\Omega} |\nabla h|^2 dx.$$

In [42, Proposition 5] it is shown that $F^\delta[\cdot; a]$ has a unique minimizer. As a consequence of Theorem 3.5 we have

Theorem 3.6. *Assume that the data $(|\mathbf{J}|, f) \in C^\alpha(\overline{\Omega}) \times C^{1,\alpha}(\partial\Omega)$ is as described above. Let $\{a_n\} \subset L^2(\Omega)$ be a sequence with $a_n \rightarrow \mathbf{J}$ in $L^2(\Omega)$.*

For $n \in \mathbb{N}$, let $\epsilon_n = \sqrt{\| |\mathbf{J}| - a_n \|_{L^2}}$, and h_n be the unique solution of the minimization problem

$$h_n = \operatorname{argmin}\{F_{\epsilon_n}^\delta[h; a_n] : h \in H_0^1(\Omega)\}.$$

Then, on a subsequence, $\{h_n\}$ converges in $L^q(\Omega)$ to some $h^ \in L^q(\Omega) \cap BV_0(\Omega)$, $1 \leq q < d/(d-1)$. Moreover, $h^* \in C_0^{1,\alpha}(\overline{\Omega})$, the sum*

$$(16) \quad u = u_0 + h^*,$$

is the corresponding voltage potential with $|\nabla(u_0 + h^)| > \delta$, and the conductivity is recovered by*

$$(17) \quad \sigma = \frac{|\mathbf{J}|}{|\nabla(u_0 + h^*)|}.$$

A complete proof of this theorem will appear elsewhere.

4. A MINIMIZATION APPROACH FOR THE COMPLETE ELECTRODE MODEL

In this section we review the Complete Electrode Model for the conductivity equation introduced by Somersalo, Cheney and Isaacson in [47]. The approach is less general than the one given in [47] since we assume a real valued conductivity and positive electrode impedances. However it explains how we are led to the specific functional essential in solving the CDII problem for this model. For proofs of the results in this section we refer to [41, Appendix].

Let $e_k \subset \partial\Omega$ denote the surface electrode of impedance z_k through which one injects a net current I_k , $k = 0, \dots, N$. The CEM assumes the voltage potential u inside and the constant voltages U_k 's on the surface of the electrodes distribute according to the boundary value problem

$$(18) \quad \nabla \cdot \sigma \nabla u = 0, \quad \text{in } \Omega,$$

$$(19) \quad u + z_k \sigma \frac{\partial u}{\partial \nu} = U_k \quad \text{on } e_k, \quad \text{for } k = 0, \dots, N,$$

$$(20) \quad \int_{e_k} \sigma \frac{\partial u}{\partial \nu} ds = I_k, \quad \text{for } k = 0, \dots, N,$$

$$(21) \quad \frac{\partial u}{\partial \nu} = 0, \quad \text{on } \partial\Omega \setminus \bigcup_{k=0}^N e_k,$$

where ν is the outer unit normal. For brevity. we refer to the problem (18), (19), (20), and (21) as to the *forward problem*.

If a solution exists, an integration of (18) over Ω together with (20) and (21) show that

$$(22) \quad \sum_{k=0}^N I_k = 0$$

is necessary. Physically, the zero sum of the boundary currents account for the absence of sources/sinks of charges. The constants U_k appearing in (19) represent *unknown* voltages on the surface of the electrodes, and the difference from the traces $u|_{e_k}$ of the interior voltage potential governs the flux of the current through the skin to the electrode.

For conductivities of real part bounded away from zero and infinity, the problem has a unique solution $(u; \langle U_0, \dots, U_N \rangle) \in H^1(\Omega) \times \mathbb{C}^{N+1}$ up to an additive constant, as shown in [47]. We normalize a constant by imposing the electrode voltages $U = \langle U_0, \dots, U_N \rangle$ to lie in the hyperplane

$$(23) \quad \Pi := \{U \in \mathbb{R}^{N+1} : U_0 + \dots + U_N = 0\}.$$

Let $H^1(\Omega)$ be the space of functions which together with their gradients lie in $L^2(\Omega)$, and Π be the hyperplane in (23). We seek weak solutions to (18), (19) (20), (21), and (22) in the Hilbert space $H^1(\Omega) \times \Pi$, endowed with the product

$$\langle (u, U), (v, V) \rangle := \int_{\Omega} uv dx + \int_{\Omega} \nabla u \cdot \nabla v dx + \sum_{k=0}^N U_k V_k,$$

and the induced norm

$$(24) \quad \|(u, U)\| := \langle (u, U), (u, U) \rangle^{1/2}.$$

We'll need the following variant of the Poincaré inequality, suitable for the complete electrode model.

Proposition 4.1. *Let $\Omega \subset \mathbb{R}^n$, $n \geq 2$, be an open, connected, bounded domain with Lipschitz boundary $\partial\Omega$, and Π be the hyperplane in (23). For $k = 0, \dots, N$, let $e_k \subset \partial\Omega$ be disjoint subsets of the boundary of positive $(n-1)$ - Hausdorff measure: $|e_k| > 0$.*

There exists a constant $C > 0$, dependent only on Ω and the e_k 's, such that for all $u \in H^1(\Omega)$ and all $U = (U_0, \dots, U_N) \in \Pi$, we have

$$(25) \quad \int_{\Omega} u^2 dx + \sum_{k=0}^N U_k^2 \leq C \left(\int_{\Omega} |\nabla u|^2 dx + \sum_{k=0}^N \int_{e_k} (u - U_k)^2 ds \right).$$

Let Ω , Π , and $e_k \subset \partial\Omega$, $k = 0, \dots, N$ be as above. Let z_k 's be satisfying (??), σ be satisfying (34), and $I = (I_0, \dots, I_N) \in \mathbb{R}^{N+1}$.

The forward problem will be treated via a minimization for the energy functional $F_{\sigma} : H^1(\Omega) \times \Pi \rightarrow \mathbb{R}$ defined by

$$(26) \quad F_{\sigma}(u, U) := \frac{1}{2} \int_{\partial\Omega} \sigma |\nabla u|^2 dx + \frac{1}{2} \sum_{k=0}^N \int_{e_k} \frac{1}{z_k} (u - U_k)^2 ds - \sum_{k=0}^N I_k U_k.$$

The following establishes some of the properties of F_{σ} needed later.

Proposition 4.2. *Let Ω , Π , and $e_k \subset \partial\Omega$, $k = 0, \dots, N$ be as in Proposition 4.1. For z_k 's satisfying (??), σ satisfying (34), and $I = (I_0, \dots, I_N) \in \mathbb{R}^{N+1}$, let us consider the quadratic functional $F_{\sigma} : H^1(\Omega) \times \Pi \rightarrow \mathbb{R}$ defined by*

$$(27) \quad F_{\sigma}(u, U) := \frac{1}{2} \int_{\partial\Omega} \sigma |\nabla u|^2 dx + \frac{1}{2} \sum_{k=0}^N \int_{e_k} \frac{1}{z_k} (u - U_k)^2 ds - \sum_{k=0}^N I_k U_k.$$

Then

(i) F_{σ} is strictly convex

(ii) F_{σ} is Gateaux differentiable in $H^1(\Omega) \times \Pi$, and the derivative at (u, U) in the direction (v, V) is given by

$$(28) \quad \begin{aligned} \langle DF_{\sigma}(u, U); (v, V) \rangle &= \int_{\Omega} \sigma \nabla u \cdot \nabla v dx + \sum_{k=0}^N \int_{e_k} \frac{1}{z_k} (u - U_k)(v - V_k) ds \\ &\quad - \sum_{k=0}^N I_k V_k \end{aligned}$$

(iii) F_{σ} is coercive, more precisely,

$$(29) \quad F_{\sigma}(u, U) \geq \frac{c}{2} \|(u, U)\|^2 - \frac{1}{2c} \sum_{k=0}^N I_k^2,$$

for some constant $c > 0$ dependent on the lower bound for the conductivity, on the lowest surface impedance and on the constant C appearing in the Poincaré inequality (25).

The proposition below revisits [47, Proposition 3.1.] and separates the role of the conservation of charge condition (22). This becomes important in our minimization approach, where we shall see that F_σ has a unique minimizer independently of the condition of (22) being satisfied. However, it is only for currents satisfying (22), that the minimizer satisfies (20). This result does not use the reality of σ and of z_k 's. Recall that the Gateaux derivative of DF_σ is given in (28).

Proposition 4.3. *Let Ω , Π , $e_k \subset \partial\Omega$, z_k , $k = 0, \dots, N$, and σ be as in Proposition 4.2.*

(i) *If $(u, U) \in H^1(\Omega) \times \Pi$ is a weak solution to (18), (19), (20) and (21), then (22) holds and*

$$(30) \quad \langle DF_\sigma(u, U); (v, V) \rangle = 0, \quad \forall (v, V) \in H^1(\Omega) \times \Pi.$$

(ii) *If $(u, U) \in H^1(\Omega) \times \Pi$ satisfies (30), then it solves (18), (19) and (21). In addition, if I_k 's satisfy (22), then (20) also holds.*

The existence and uniqueness of the weak solution to the forward CEM problem; now follows by classical arguments.

Theorem 4.4. *Let Ω , Π , $e_k \subset \partial\Omega$, z_k , for $k = 0, \dots, N$, and σ be as in Proposition 4.2. Let $F_\sigma : H^1(\Omega) \times \Pi \rightarrow \mathbb{R}$ be defined in (27).*

(i) *Then F_σ has a unique minimizer $(u, U) \in H^1(\Omega) \times \Pi$. If, in addition, the injected currents I_k 's satisfy (22) the minimizer is the weak solution of the problem (18), (19), (20), and (21).*

(ii) *If the problem (18), (19), (20),(21) has a solution, then it is a minimizer of F_σ in the whole space $H^1(\Omega) \times \Pi$ and hence unique. Moreover, the current I_k 's satisfy (22).*

Proof. (i) Let

$$d = \inf_{H^1(\Omega) \times \Pi} F_\sigma(u, U),$$

and consider a minimizing sequence $\{(u_n, U^n)\}$ in $H^1(\Omega) \times \Pi$,

$$(31) \quad d \leq F_\sigma(u_n, U^n) \leq d + \frac{1}{n}.$$

Since $\inf F_\sigma \geq -\frac{1}{4c} \sum_{k=0}^N I_k^2$ we have $d \neq -\infty$. Following (29),

$$\lim_{\|(u, U)\| \rightarrow \infty} F_\sigma(u, U) = \infty.$$

Thus the minimizing sequence must be bounded, hence weakly compact. In particular, for a subsequence (relabelled for simplicity) there is some $(u_*, U^*) \in H^1(\Omega) \times \Pi$, such that

$$(32) \quad u_n \rightharpoonup u_* \text{ in } H^1(\Omega), \quad \text{and } U_n \rightarrow U^* \text{ in } \Pi, \text{ as } n \rightarrow \infty.$$

On the other hand since F_σ is convex, and Gateaux differentiable at (u_*, U^*) in the direction $(u_n - u_*, U^n - U^*)$, we have

$$(33) \quad F_\sigma(u_n, U^n) \geq F_\sigma(u_*, U^*) + \langle DF_\sigma(u_*, U^*); (u_n - u_*, U^n - U^*) \rangle.$$

We take the limit as $n \rightarrow \infty$. The weak convergence in (32) yields

$$\langle DF_\sigma(u_*, U^*), (u_n - u_*, U^n - U^*) \rangle \rightarrow 0.$$

Thus $d \geq F_\sigma(u_*, U^*) \geq d$ which shows that (u_*, U^*) is a global minimizer. Strict convexity of F_σ implies it is unique. At the minimum (u_*, U^*) the Euler-Lagrange equations (30) are satisfied. An application of Proposition 4.3 part (ii) shows that (u_*, U^*) is a weak solution to the forward problem.

(ii) Proposition 4.3 part (i) shows that (u_*, U^*) solves the Euler-Lagrange equations, and due to the convexity it is a minimizer of F_σ . Due to the strict convexity of the functional the minimizer is unique, hence the weak solution is unique. \square

5. CONDUCTIVITY IMAGING FOR THE COMPLETE ELECTRODE MODEL

All the results of this sections are from [41], where refer to for their proofs.

In the inverse problem we seek to determine a conductivity σ satisfying

$$(34) \quad \epsilon < \sigma < 1/\epsilon,$$

for some $\epsilon > 0$, given the magnitude $|\mathbf{J}|$ of one current density field inside Ω ,

$$(35) \quad a := |\mathbf{J}| = |\sigma \nabla u|,$$

where $(u, U) \in H^1(\Omega) \times \Pi$ is the solution of the forward problem. The electrodes $e_k \subset \partial\Omega$ and their constant impedances $z_k > 0$, for $k = 0, \dots, N$, are known. The injected currents I_0, \dots, I_N satisfy (22). We normalize a constant by imposing the electrode voltages $U = \langle U_0, \dots, U_N \rangle$ to lie in the hyperplane Π as in(23).

Similar to the inverse problem for the Dirichlet data, where the reconstruction was based on the minimization of the functional in (12), for the complete electrode boundary data problem we introduce the functional $G_a : H^1(\Omega) \times \Pi \rightarrow \mathbb{R}$, by

$$(36) \quad G_a(u, U) := \int_{\partial\Omega} a |\nabla u| dx + \frac{1}{2} \sum_{k=0}^N \int_{e_k} \frac{1}{z_k} (u - U_k)^2 ds - \sum_{k=0}^N I_k U_k,$$

which is defined in terms of the data available in the inverse problem. The connection below between the solutions of the forward problem and global minimizers of G_a is crucial.

Proposition 5.1. *Let $\Omega \subset \mathbb{R}^n$, $n \geq 2$, be a bounded domain with Lipschitz boundary. Let σ satisfy (34) and, for $k = 0, \dots, N$, let e_k be disjoint subsets of the boundary of positive $(n-1)$ -Hausdorff measure, with impedances z_k satisfying (??), and I_k satisfy (22). Let $(u, U) \in H^1(\Omega) \times \Pi$ be the unique solution of the forward problem (18), (19), (20), (21). If $a := \sigma |\nabla u|$, then*

$$(37) \quad G_a(v, V) \geq G_a(u, U), \quad \forall (v, V) \in H^1(\Omega) \times \Pi.$$

Let us remark first that there is non-uniqueness in the inverse problem stated above, as can be seen in the following example: Let $\Omega = (0, 1) \times (0, 1)$ be the unit square. We inject the current $I_1 = 1$ through the top electrode $e_1 = \{(x, 1) : 0 \leq x \leq 1\}$ of impedance $z_1 > 0$, “extract” the current $I_0 = -1$ through the bottom electrode $e_0 = \{(0, x) : 0 \leq x \leq 1\}$ of impedance $z_0 = z_1 + 1$, and measure the magnitude $a \equiv 1$ of the current density field in Ω . Then, for every $\varphi : [0, 1] \rightarrow [\varphi(0), \varphi(1)]$ an increasing Lipschitz continuous function, satisfying $\varphi(0) + \varphi(1) = 1$, the function $u_\varphi(x, y) := \varphi(y)$ solves the forward problem (18), (19), (20), and (21) corresponding to a conductivity $\sigma_\varphi(x, y) = 1/\varphi'(y)$, yet the magnitudes of the corresponding current densities yield the same interior measurements $\sigma|\nabla u| = \sigma_\varphi|\nabla u_\varphi| \equiv 1$.

The following result shows that this uniqueness is locally generic.

Theorem 5.2 ([41]). *Let $\Omega \subset \mathbb{R}^d$, $d \geq 2$ be a bounded, connected $C^{1,\alpha}$ -domain, for some $0 < \alpha < 1$, and let e_k , $k = 0, \dots, N$, be disjoint subsets of the boundary of positive $(n-1)$ -Hausdorff measure. Assume that the corresponding impedances z_k satisfy (??), and that the given currents I_k are such that (22) holds. Let $(u, U), (v, V) \in H^1(\Omega) \times \Pi$, be the solutions of the forward problem (18), (19), (20), and (21) corresponding to unknown conductivities $\sigma, \tilde{\sigma} \in C^\alpha(\Omega)$ satisfying (34). Assume that*

$$(38) \quad \sigma|\nabla u| = \tilde{\sigma}|\nabla v| > 0 \text{ a.e. in } \Omega.$$

Then, for a.e. $x^0 \in \Omega$, there exists a neighborhood O_0 of x^0 and an function $\varphi \in C^1(v(O_0))$, such that

$$(39) \quad u = \varphi \circ v, \quad \text{in } O_0,$$

and

$$(40) \quad \tilde{\sigma} = \frac{\sigma}{\varphi' \circ v}, \quad \text{in } O_0.$$

Moreover, for each $k = 0, \dots, N$,

$$(41) \quad u|_{e_k} - U_k = v|_{e_k} - V_k, \text{ a.e. on } e_k.$$

The above theorem shows that knowledge of the input currents at the boundary is sufficient to recover the direction of the current density field.

Corollary 5.3 (Phase retrieval). *Let $\Omega \subset \mathbb{R}^d$, $d \geq 2$ be a bounded connected $C^{1,\alpha}$ -domain, for some $0 < \alpha < 1$. Let I_k be known currents on the electrodes $e_k \subset \partial\Omega$ of impedances z_k , $k = 0, \dots, N$, which satisfy (22). Let $J := \sigma\nabla u$ and $\tilde{J} := \tilde{\sigma}\nabla v$, where $(u, U), (v, V) \in H^1(\Omega) \times \Pi$ are the solutions of the forward problem (18), (19), (20), and (21) corresponding to some unknown $\sigma, \tilde{\sigma} \in C^\alpha(\Omega)$ satisfying (34). If*

$$(42) \quad |J| = |\tilde{J}| > 0 \text{ a.e. in } \Omega,$$

then

$$(43) \quad J = \tilde{J} \text{ in } \Omega.$$

The proof is immediate: For $x^0 \in \Omega \setminus S$ arbitrarily fixed, let O_0 and $\varphi : v(O_0) \rightarrow \mathbb{R}$ be the corresponding function provided by Theorem 5.2. From (40) and (39) we have for all $x \in O_0$,

$$\tilde{J}(x) = \tilde{\sigma}(x) \nabla v(x) = \frac{\sigma(x)}{\varphi' \circ v(x)} \nabla v(x) = \sigma(x) \nabla u(x) = J(x).$$

Since J, \tilde{J} are continuous in Ω , and $\Omega \setminus S$ is dense in Ω , the result follows.

In order to determine the conductivity uniquely we identify next some additional data. It will be sufficient to measure the voltage potential u along a boundary curve Γ which connects all the electrodes. The main idea of the proof will be to show that the range of u on the union of this curve and the electrodes is the same as the range of u in $\overline{\Omega}$, fact which follows from a maximum principle for the Complete Electrode Model.

Proposition 5.4 (Maximum principle for CEM[41]). *Let Ω , σ , e'_k 's, z_k 's, and I_k 's, for $k = 0, \dots, N$ be as in Theorem 5.2, and let u be a solution of the forward problem. Then u achieves its minimum and maximum on the electrodes $e_0 \cup \dots \cup e_N$. Moreover, if $\Gamma \subset \partial\Omega$ is a curve connecting the electrodes, then the range of u over $\Gamma \cup e_0 \cup \dots \cup e_N$ coincides with the range of u over $\overline{\Omega}$.*

Theorem 5.5 (Unique determination[41]). *Let $\Omega \subset \mathbb{R}^d$, $d \geq 2$ be a bounded, connected $C^{1,\alpha}$ -domain, for some $0 < \alpha < 1$. Let $e_k \subset \partial\Omega$ denote the electrode with impedance z_k satisfying (??), for $k = 0, \dots, N$ and Γ be a curve on the boundary connecting the electrodes. For currents I_k which satisfy (22), let $(u, U), (v, V) \in H^1(\Omega) \times \Pi$ be the solutions of the forward problem (18), (19), (20), and (21) corresponding to unknown conductivities $\sigma, \tilde{\sigma} \in C^\alpha(\Omega)$ satisfying (34).*

Assume that

$$(44) \quad \sigma |\nabla u| = \tilde{\sigma} |\nabla \tilde{u}| > 0, \text{ a.e. in } \Omega,$$

$$(45) \quad u|_\Gamma = \tilde{u}|_\Gamma,$$

for some constant C . Then

$$(46) \quad u = \tilde{u} \text{ in } \overline{\Omega},$$

$$(47) \quad \sigma = \tilde{\sigma} \text{ in } \Omega.$$

6. A NUMERICAL EXPERIMENT

In [41] the following algorithm is shown to produce a minimizing sequence for the functional G_a , see [41, Lemma 5.1]. We assume the current density never vanishes, more precisely, that

$$(48) \quad \min_{\overline{\Omega}} |\mathbf{J}| > 0.$$

Let $\epsilon > 0$ be the lower bound in (34), and $\delta > 0$ a measure of error to be used in the stopping criteria.

- Step 1: Solve (18, 19, 20) and (21) for $\sigma = 1$, and let u_0 be its unique solution. Define

$$\sigma_1 := \min \left\{ \max \left\{ \frac{a}{|\nabla u_0|}, \epsilon \right\}, \frac{1}{\epsilon} \right\};$$

- Step 2: For σ_n given: Solve (18, 19, 20) and (21) for the unique solution u_n ;
- Step 3: If

$$\|\nabla u_n - \nabla u_{n-1}\|_{C(\bar{\Omega})} > \delta \frac{\epsilon}{\text{ess\,inf} a},$$

then define

$$(49) \quad \sigma_{n+1} := \min \left\{ \max \left\{ \frac{a}{|\nabla u_n|}, \epsilon \right\}, \frac{1}{\epsilon} \right\}$$

and repeat Step 2;

- Else STOP.

We illustrate the theoretical results on a numerical simulation in two dimensions. The numerical solutions for the forward problem (18), (19), (20), and (21) is being solved by a finite element method adapted to the CEM boundary conditions, see [41] for details.

We consider a simulated planar conductivity σ which models the cross section of a torso embedded in the unit box $[0, 1] \times [0, 1]$; see Figure 6 on the left. The values of the conductivity range from 1.0 S/m to 1.8 S/m .

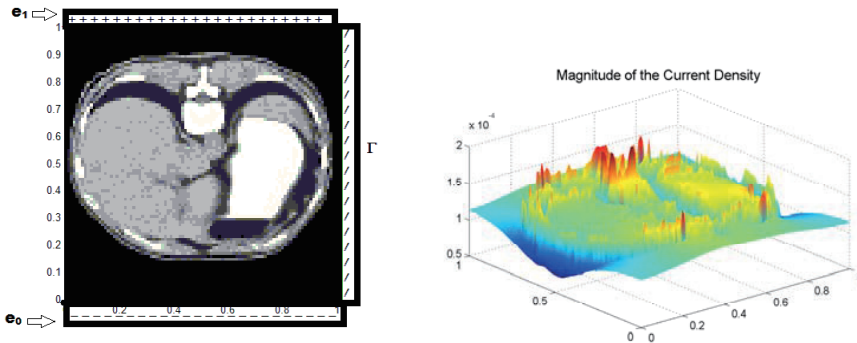


FIGURE 1. The exact conductivity with the electrode set up (left). The simulated magnitude a of the current density field (right).

Two currents $-I_0 = I_1 = 3 \text{ mA}$ are respectively injected/extracted through the electrodes

$$e_0 = \{(x, y) \in [0, 1] \times [0, 1] : y = 0\} \quad \text{and} \quad e_1 = \{(x, y) \in [0, 1] \times [0, 1] : y = 1\}$$

of equal impedances $z_0 = z_1 = 8.3 \text{ m}\Omega \cdot \text{m}^2$.

For the given σ we solve the forward problem (18), (19), (20),(21) for (u, U) . The interior data of the magnitude $|\mathbf{J}|$ of the current density field (defined by $\sigma|\nabla u|$) is shown in the Figure 6 on the right.

Knowing the injected currents I_0 and I_1 , the electrode impedances z_0 and z_1 , and the corresponding magnitude a of the current density we find an approximate minimizer of G_a via the iterative algorithm above. The iterations start with the guess $\sigma_0 \equiv 1$. An approximate solution v is computed on a 90×90 grid. The stopping criterion (49) for this experiment used $\delta = 10^{-7}$, and was attained with 320 iterations. A pseudo-conductivity $\sigma_v := a/|\nabla v|$ in Figure 2 can be computed using this minimizer v .

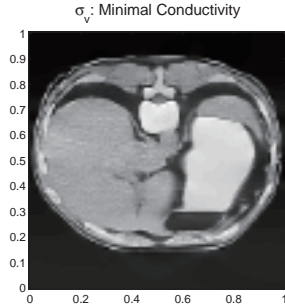


FIGURE 2. Without any boundary measurement a pseudo conductivity can be recovered

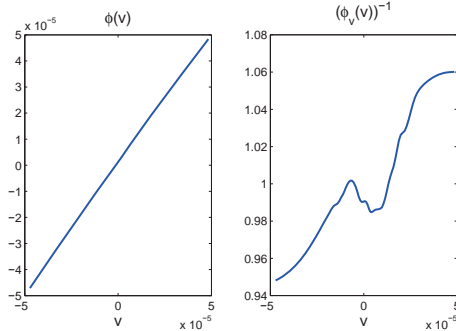


FIGURE 3. Computed voltage on Γ shown as a function of the computed values of v (left) vs. Its derivative is needed to reconstruct σ (right).

Since the geometry of the level sets is shown to create global coordinates, we know from Theorem 5.2 that the correct voltage potential is related to v via the scaling $u(x) = \varphi(v(x))$, for some unknown scaling φ . To apply Theorem 5.5 we use the additional measurement $u|_{\Gamma}$ on the curve $\Gamma = \{(1, y) : 0 \leq y \leq 1\}$. Since $\varphi(v) = u|_{\Gamma}(v)$ (see Figure 3 on the left), an application of the chain rule recovers the conductivity σ by

$$\sigma(x) = \frac{1}{\varphi'(v(x))} \sigma_v(x), \quad x \in \Omega.$$

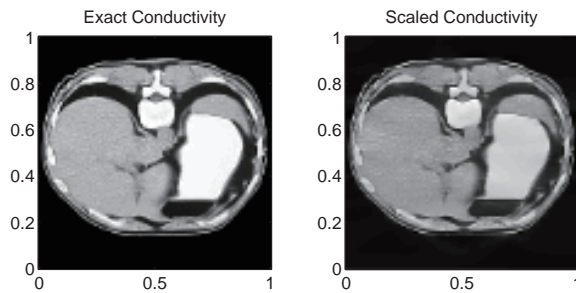


FIGURE 4. Exact conductivity (left) vs. Reconstructed conductivity (right)

In Figure 6 the reconstructed conductivity σ is shown on the right against the exact conductivity on the left. The L_2 error of the reconstruction is 0.04.

ACKNOWLEDGMENTS

Theorem 3.6 was inspired by discussions during the author's visit to the Institute for Mathematics in Industry, Kyushu University, Fukuoka, Japan, during the *IMI Workshop on Mathematical Backgrounds and Future Progress of Practical Inverse Problems*, November 10-13, 2016. The author is grateful to the organizers of the workshop, and acknowledges the financial support from IMI, which made his visit possible. The results in Sections 4 and 5 were obtained while the author was partially supported by the NSF Grant DMS-1312883.

REFERENCES

- [1] G. ALESSANDRINI, *An identification problem for an elliptic equation in two variables*, Annali di matematica pura ed applicata, **145** (1986), pp. 265–295.
- [2] H. AMMARI, Y. CAPDEBOSCQ, H. KANG, AND A. KOZHEMIK, *Mathematical models and reconstruction methods in magneto-acoustic imaging*, European J. Appl. Math., **20**(2009), pp. 303–317.
- [3] H. AMMARI, E. BONNETIER, Y. CAPDEBOSCQ, M. TANTER, AND M. FINK, *Electrical Impedance Tomography by Elastic Deformation*, SIAM J. Appl. Math., **68** (2008), pp.1557–1573.
- [4] G. BAL AND J.C. SCHOTLAND, *Inverse Scattering and Acousto-Optic Imaging*, Phys. Rev. Letters **104**(2010), 043902.
- [5] R. H. BAYFORD, *Bioimpedance Tomography (Electrical impedance tomography)*, Annu. Rev. Biomed. Eng., 2006, 8, 63–91.
- [6] E. BOMBIERI, E. DE GIORGI AND E. GIUSTI, *Minimal Cones and the Bernstein Problem*, Inventiones Math. **7** (1969), pp. 243–268.
- [7] L. BORCEA, *Electrical impedance tomography*, Inverse Problems **18**(2002), R99–R136.
- [8] A. L. BUKHGEIM, RECOVERING A POTENTIAL FROM CAUCHY DATA IN THE TWO-DIMENSIONAL CASE, J. Inverse Ill-Posed Probl. **16**(2008), 19-33.

- [9] A. P. CALDERON, *On an inverse boundary value problem*, Seminar on Numerical Analysis and Its Applications to Continuum Physics (Rio de Janeiro: Soc. Brasil. Mat.), 1980, 65–73.
- [10] M. CHENEY, D. ISAACSON, AND J. C. NEWELL, *Electrical Impedance Tomography*, SIAM Rev. **41**(1999), no.1, 85–101.
- [11] D. ISAACSON AND M. CHENEY, *Effects of measurement precision and finite numbers of electrodes on linear impedance imaging algorithms*, SIAM J. Appl. Math. **51** (1991), no. 6, 1705–1731.
- [12] B. GEBAUER AND O. SCHERZER, *Impedance-acoustic tomography*, SIAM J. Appl. Math., **69** (2008), pp. 565–576.
- [13] D. GILBARG AND N. S. TRUDINGER, *Elliptic Partial Differential Equations*, 2nd ed., Springer-Verlag, NY, 2001.
- [14] H. FEDERER, *Curvature measures*, Trans. Amer. Math. Soc. **62** (1959), pp. 418–491.
- [15] K. F. HASANOV, A. W. MA, A. I. NACHMAN, AND M. J. JOY, *Current Density Impedance Imaging*, IEEE Trans. Med. Imag. **27**(2008), pp. 1301–1309.
- [16] Y.Z. IDER AND Ö. BIRGÜL, *Use of the magnetic field generated by the internal distribution of injected currents for Electrical Impedance Tomography(MR-EIT)*, Elektrik **6** (1998), 215–225
- [17] D ISAACSON, Distinguishability of Conductivities by Electric Current Computed Tomography, IEEE Trans. on Medical Imaging, 1986, Vol. MI-5, No. 2, 91-95.
- [18] R.L. JERRARD, A. MORADIFAM, A. NACHMAN, *Existence and uniqueness of minimizers of general least gradient problems*, J. Reine Angew. Math., to appear (2015).
- [19] M. L. JOY, G. C. SCOTT, AND M. HENKELMAN, *In vivo detection of applied electric currents by magnetic resonance imaging*, Magnetic Resonance Imaging, **7** (1989), pp. 89–94.
- [20] M. J. JOY, A. I. NACHMAN, K. F. HASANOV, R. S. YOON, AND A. W. MA, *A new approach to Current Density Impedance Imaging (CDII)*, Proceedings ISMRM, No. 356, Kyoto, Japan, 2004.
- [21] H.S. KHANG, B.I. LEE, S. H. OH, E.J. WOO, S. Y. LEE, M.H. CHO, O. I. KWON, J.R. YOON, AND J.K. SEO, *J-substitution algorithm in magnetic resonance electrical impedance tomography (MREIT): Phantom experiments for static resistivity images*, IEEE Trans. Med. Imag., **21**(2002), no. 6, pp. 695–702.
- [22] S. KIM, O. KWON, J. K. SEO, AND J. R. YOON, *On a nonlinear partial differential equation arising in magnetic resonance electrical impedance tomography*, SIAM J. Math. Anal., **34** (2002), pp. 511–526.
- [23] Y.J. KIM, O. KWON, J. K. SEO, AND E. J. WOO, *Uniqueness and convergence of conductivity image reconstruction in magnetic resonance electrical impedance tomography*, Inverse Problems **19**(2003), no. 5, 1213-1225.
- [24] O. KWON, E. J. WOO, J. R. YOON, AND J. K. SEO, *Magnetic resonance electric impedance tomography (MREIT): Simulation study of J-substitution algorithm*, IEEE Trans. Biomed. Eng., **49** (2002), pp. 160–167
- [25] O. KWON, C. J. PARK, E.J. PARK, J. K. SEO, AND E. J. WOO, *Electrical conductivity imaging using a variational method in B_z -based MREIT*, Inverse Problems **21** (2005), pp. 969–980.
- [26] O. KWON, J. Y LEE, AND J. R. YOON, *Equipotential line method for magnetic resonance electrical impedance tomography*, Inverse Problems. **18** (2002), pp. 1089-1100
- [27] Langer R E, *An inverse problem in differential equations*, Bull. Amer. Math. Soc., 1933, 39, 814820.
- [28] J. Y. LEE *A reconstruction formula and uniqueness of conductivity in MREIT using two internal current distributions*, Inverse Problems, **20** (2004), pp. 847–858
- [29] J. J. LIU, H. C. PYO, J. K. SEO, AND E. J. WOO, *Convergence properties and stability issues in MREIT algorithm*, Contemporary Mathematics **25** (2006), 168–176.
- [30] J. J. LIU, J. K. SEO, M. SINI AND E. J. WOO, *On the convergence of the harmonic B_z Algorithm in Magnetic Resonance Imaging*, SIAM J. Appl. Math. **67** (2007), 1259–1282.

- [31] J. J. LIU, J. K. SEO, AND E. J. WOO, *A Posteriori Error Estimate and Convergence Analysis for Conductivity Image Reconstruction in MREIT*, SIAM J. Appl. Math. **70**(2010), Issue 8, pp. 2883–2903.
- [32] Q. MA AND B. HE, *Investigation on magnetoacoustic signal generation with magnetic induction and application to electrical conductivity reconstruction*, Phys. Med. Biol., **52** (2007), pp. 5085–5099.
- [33] N. MANDACHE, *Exponential instability in an inverse problem for the Schrödinger equation*, Inverse Problems **17** (2001), pp. 1435–1444.
- [34] A. MORADIFAM, A. NACHMAN, AND A. TAMASAN, *Conductivity imaging in the presence of perfectly conducting and insulating inclusions from one interior measurement*, SIAM J. Math. Anal. **44** (2012), no. 6, 3969–3990
- [35] A. MORADIFAM, A. NACHMAN, AND A. TAMASAN, *Uniqueness of minimizers of weighted least gradient problems arising in hybrid inverse problems*, under review.
- [36] A. NACHMAN, *Global uniqueness for a two-dimensional inverse boundary value problem*, Ann. of Math. (2) **143** (1996), no. 1, 71–96.
- [37] A. NACHMAN, A. TAMASAN, AND A. TIMONOV, *Conductivity imaging with a single measurement of boundary and interior data*, Inverse Problems, **23** (2007), pp. 2551–2563.
- [38] A. NACHMAN, A. TAMASAN, AND A. TIMONOV, *Recovering the conductivity from a single measurement of interior data*, Inverse Problems, **25** (2009) 035014 (16pp).
- [39] A. NACHMAN, A. TAMASAN, AND A. TIMONOV, *Reconstruction of Planar Conductivities in Subdomains from Incomplete Data*, SIAM J. Appl. Math. **70**(2010), Issue 8, pp. 3342–3362.
- [40] A. NACHMAN, A. TAMASAN, AND A. TIMONOV, *Current density impedance imaging*, in Tomography and Inverse Transport Theory, Contemp. Math. **559**, pp. 135–149, AMS, Providence, RI, 2011
- [41] A. NACHMAN, A. TAMASAN, AND J. VERAS, *A weighted minimum gradient problem with complete electrode model boundary conditions for conductivity imaging*, under review.
- [42] M. Z. NASHED AND A. TAMASAN, *Structural stability in a minimization problem and applications to conductivity imaging*, Inverse Problems and Imaging **5**(2011), 219–236.
- [43] S.H. OH, B. I. LEE, E. J. WOO, S. Y. LEE, M. H. CHO, O. KWON, AND J. K. SEO, *Conductivity and current density image reconstruction using B_z algorithm in magnetic resonance electrical impedance tomography*, Phys. Med. Biol. **48**(2003), pp. 3101–3116.
- [44] S. ONART, Y.Z. IDER, AND W. LIONHEART, *Uniqueness and reconstructions in magnetic resonance -electrical impedance tomography (MR-EIT)*, Physiol. Meas. **24**(2003), pp. 591–604.
- [45] C. PARK, O. KWON, E.J. WOO, AND J. K. SEO, *Electrical conductivity imaging using gradient B_z decomposition algorithm in magnetic resonance electrical impedance tomography (MREIT)*, IEEE Trans. Med. Imag. **23**(2004), pp. 388–394.
- [46] G. C. SCOTT, M. L. JOY, R. L. ARMSTRONG, AND R. M. HENKELMAN, *Measurement of nonuniform current density by magnetic resonance*, IEEE Trans. Med. Imag., **10** (1991), pp. 362–374
- [47] E. SOMERSALO, M. CHENEY, AND D. ISAACSON, *Existence and uniqueness for electrode models for electric current computed tomography*, SIAM J. Appl. Math. **54**(1992), 1023–1040.
- [48] Y. SONG AND J.K. SEO, *Conductivity and permittivity image reconstruction at the Larmor frequency using MRI*, SIAM J. Appl. Math., 2013, 73, no. 6, 22622280.
- [49] J. SYLVESTER AND G. UHLMANN, *A global uniqueness theorem for an inverse boundary value problem*, Ann. Math., **125**, 153–169.
- [50] J K SEO, J R YOON, E J WOO ET AL., *Reconstruction of conductivity and current density images using only one component of magnetic field measurements*, IEEE Trans. Biomed. Eng., 2003, 50, 1121–1124.
- [51] J. K. SEO, K. JEON, C.O. LEE ET AL., *Non-iterative harmonic B_z algorithm in MREIT*, Inverse Problems, 2011, 27, 085003.
- [52] J.K. SEO AND E. J. WOO, *Magnetic resonance electrical impedance tomography*, SIAM Rev., 2011, 53, 40–68.

- [53] J. K. SEO, D-H KIM, J. LEE ET AL., Electrical tissue property imaging using MRI at dc and Larmor frequency, *Inverse Problems*, 2012, 28, 084002 (26pp).
- [54] P. STERNBERG, G. WILLIAMS, AND W. P. ZIEMER, *Existence, uniqueness and regularity for functions of least gradient*, *J. Rein Angew. Math.* **430** (1992), 35–60.
- [55] P. STERNBERG AND W. P. ZIEMER, *Generalized motion by curvature with a Dirichlet condition*, *J. Differ. Eq.*, **114**(1994), pp. 580–600.
- [56] P. STERNBERG AND W. P. ZIEMER, *The Dirichlet problem for functions of least gradient. Degenerate diffusions* (Minneapolis, MN, 1991), 197–214, in *IMA Vol. Math. Appl.*, **47**, Springer, New York, 1993.
- [57] A TAMASAN AND J VERAS, *Conductivity imaging by the method of characteristics in the 1-Laplacian*, *Inverse Problems*, **28**(2012), 084006, 13pp.
- [58] A TAMASAN, A TIMONOV, AND J VERAS, *Stable reconstruction of regular 1-Harmonic maps with a given trace at the boundary*, *Appl. Anal.* **94** (2015), no. 6, 1098-1115.
- [59] A N TICHONOV AND R J TURKISHER, *The influence of an intermediate layer in vertical electric soundation*. (Russian) *Bull. Acad. Sci. URSS. Sr. Gograph. Gophys. [Izvestia Akad. Nauk SSSR]*, 1942, 219227.
- [60] E. J. WOO AND J. K. SEO, *Magnetic resonance electrical impedance tomography (MREIT) for high resolution conductivity imaging*, *Physiol. Meas.*, **29** (2008), pp. R1-R26.
- [61] N. ZHANG, *Electrical impedance tomography based on current density imaging*, M.Sc. Thesis: University of Toronto, Canada, 1992.
- [62] W. P. ZIEMER, *Weakly Differentiable Functions*, New York, Springer, 1069.

ALEXANDRU TAMASAN, DEPARTMENT OF MATHEMATICS, UNIVERSITY OF CENTRAL FLORIDA,
4000 CENTRAL FLORIDA BLVD., ORLANDO, FL, 32816, USA

E-mail address: tamasan@math.ucf.edu

Current density based impedance imaging from minimal data

Alexandru Tamasan

Collaborators: A. Nachman, Z. Nashed, A. Moradifam, & J. Veras

University of Central Florida

IMI Workshop on *Mathematical Backgrounds and Future Progress of Practical Inverse Problems*, Fukuoka,
Japan, November 10-13, 2015

Outline

In motivation

- Hybrid methods in Inverse Problems
- Current density based EIT
- Acquiring the interior data

The 1-Laplacian

- 1-Laplacian in Conductivity Imaging
- The Dirichlet problem

The Complete Electrode Model

- A boundary value problem for the Complete Electrode Model

Inverse Problem for Complete Electrode Model

- Characterization of non-uniqueness
- Phase retrieval
- Restoring uniqueness
- A numerical algorithm and experiment
- Conclusions

Outline

In motivation

- Hybrid methods in Inverse Problems
- Current density based EIT
- Acquiring the interior data

The 1-Laplacian

- 1-Laplacian in Conductivity Imaging
- The Dirichlet problem

The Complete Electrode Model

- A boundary value problem for the Complete Electrode Model

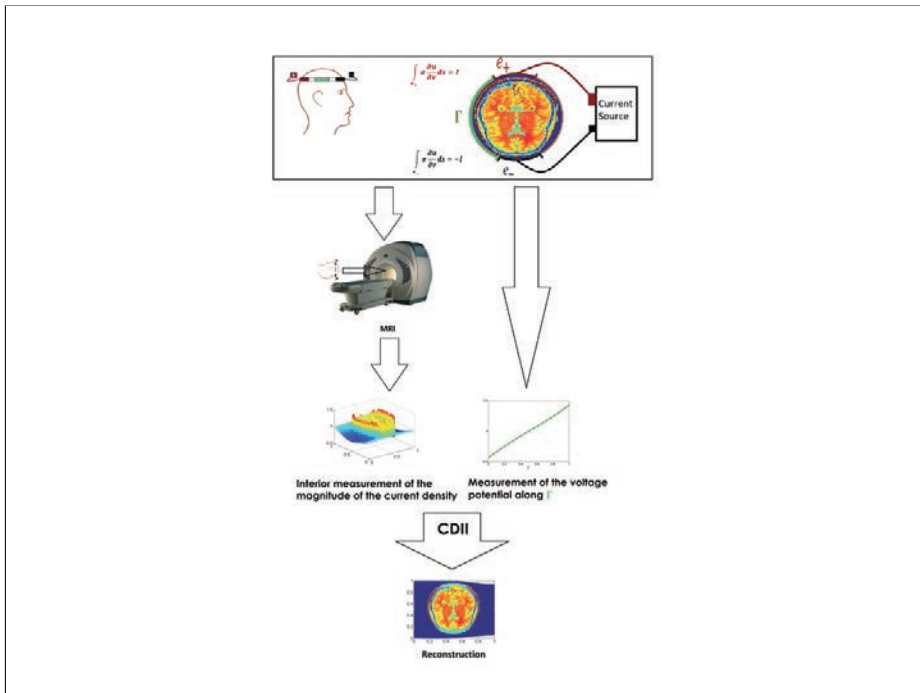
Inverse Problem for Complete Electrode Model

- Characterization of non-uniqueness
- Phase retrieval
- Restoring uniqueness
- A numerical algorithm and experiment
- Conclusions

Coupled Physics Imaging Methods

Combine high contrast & high resolution

- ▶ Elastography: elastic waves & ultrasound/MRI \Rightarrow stiffness
- ▶ Thermo/PhotoAcoustic: UV light & sound \Rightarrow embedded acoustic sources
- ▶ AcoustoOptics: light & sound \Rightarrow absorption and scattering
- ▶ **Coupled Physics Electrical Impedance Tomography**
 - ▶ Current density impedance imaging **CDII**: Joy & Nachman since 2002, Seo et al. 2002
 - ▶ MREIT (B_z -methods): Seo et al. since 2003
 - ▶ Ultrasound modulated EIT: Capdebosq et al. 2008, Bal et al. 2009
 - ▶ Impedance acoustic: Scherzer et al. 2009
 - ▶ Lorentz force driven EIT: Ammari et al. since 2013
 - ▶ ...



Current density tracing inside an object

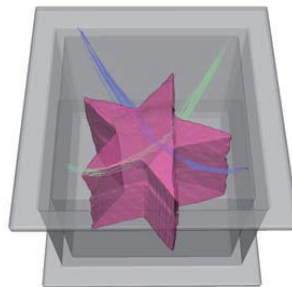


Figure : Courtesy: Joy's group, U Toronto

Magnetic resonance data: $M : \Omega \rightarrow \mathbb{C}$



Figure : $M_{\pm}(x, y, z_0) = M(x, y, z_0) \exp(\pm i\gamma B_z(x, y, z_0)T + i\varphi_0)$

Aquiring the interior data

One MR scan \Rightarrow longitudinal component B_z (along gantry) of the magnetic field $\mathbf{B} = (B_x, B_y, B_z)$

$$B_z(x, y, z_0) = \frac{1}{2\gamma T} \text{Im} \log \left(\frac{M_+(x, y, z_0)}{M_-(x, y, z_0)} \right)$$

- ▶ MREIT (Seo et al. since 2003): Does B_z uniquely determine the electrical conductivity? In general, not known.
- ▶ CDII (Nachman et al since 2002, Seo (2002)) : + two rotation of the object

$$\Rightarrow \mathbf{B} \Rightarrow \mathbf{J} = \frac{1}{\mu_0} \nabla \times \mathbf{B}$$

- ▶ Anisotropic case: Bal & Monard (2013), unique determination Hoell-Moradifam-Nachman (2014, within conformal class)

Today: the magnitude $|\mathbf{J}|$ is assumed known inside .

Outline

In motivation

- Hybrid methods in Inverse Problems
- Current density based EIT
- Acquiring the interior data

The 1-Laplacian

- 1-Laplacian in Conductivity Imaging
- The Dirichlet problem

The Complete Electrode Model

- A boundary value problem for the Complete Electrode Model

Inverse Problem for Complete Electrode Model

- Characterization of non-uniqueness
- Phase retrieval
- Restoring uniqueness
- A numerical algorithm and experiment
- Conclusions

How it appears

J = current density, E = electric field, σ = (isotropic) conductivity

- ▶ Ohm's law: $J = \sigma E \implies \sigma = \frac{|J|}{|E|}$
- ▶ Charge conservation: $\nabla \cdot J = 0$
- ▶ Maxwell's eq. (zero frequency): $\nabla \times E = 0 \implies E = -\nabla u$

Yield:

- ▶ Conductivity eq.: $\nabla \cdot \sigma \nabla u = 0$
- ▶ 1-Laplacian eq.:

$$\nabla \cdot \frac{|J|}{|\nabla u|} \nabla u = 0$$

The equipotential sets of u are minimal surfaces in the metric $|J|^{\frac{n}{n-1}}$ Identity!

Basic Properties

$$\nabla \cdot \frac{|J|}{|\nabla u|} \nabla u = 0$$

- ▶ Degenerate elliptic (no coercivity)
- ▶ Singular (where $\nabla u = 0$)
- ▶ Solutions defined in the viscosity sense (limits of sub/super solutions of regularized equation)
- ▶ Case $|J| = 1$ well understood (Sternberg, Ziemer, Williams 1990s)
- ▶ Our problem needs regular solutions:

$$\epsilon \leq \frac{|J|}{|\nabla u|} \leq \frac{1}{\epsilon}$$

Imaging from $|J|$: a brief history on BVP for 1-Laplacian

Neumann: $\partial_\nu u = \text{given}$ is not well posed in general. Examples of non-uniqueness or non-existence (Seo et al. '02)

Cauchy: $u = \text{given}$ and $\partial_\nu u = \text{given}$ on the same part of the boundary: *Reconstruction & conditional stability* (Nachman-T-Timonov '07, T-Veras '12)

Dirichlet: $u = \text{given}$ on the entire boundary

- ▶ Uniqueness & Reconstruction (Nachman-T-Timonov '09, Moradifam-Nachman-Timonov '12, Moradifam-Nachman-T'14, Gerard-Moradifam-Nachman '14)
- ▶ Local stability for u (Nashed-T'10) + corollaries (Moradifam-Nachman-T '14)
- ▶ Local stability for σ (T-Veras'12 ($n = 2$), Montalto-Stefanov'15 ($n \geq 3$))

CEM: Characterization of non-uniqueness (Nachman-T-Veras: under review)

Sternberg-Ziemer's example

Case $|J| \equiv 1$:

$$\nabla \cdot \left(\frac{1}{|\nabla u|} \nabla u \right) = 0$$

$$u(x, y) = x^2 - y^2$$

For each $\lambda \in [0, 1] \exists u^\lambda$
viscosity solution $u^\lambda \equiv \lambda$ in an
inscribed rectangle.

Note: u^λ cannot be voltage
potentials in some conductive
body!

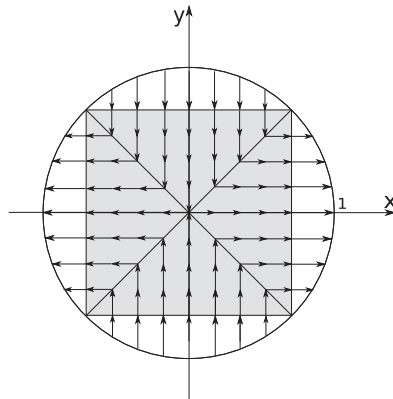


Figure : The viscosity solution u^0 .

Variational approach to 1-Laplacian

Consider the functional $F : H^1(\Omega) \rightarrow \mathbb{R}$, defined by

$$F_{|J|}[u] := \int_{\Omega} |J| |\nabla u| dx.$$

- ▶ If $u \in H^1(\Omega)$, with $\epsilon \leq \frac{|J|}{|\nabla u|} \leq \frac{1}{\epsilon}$, then $F_{|J|}$ is Gateaux diff. at u and

$$DF_{|J|}[u](\phi) = \int_{\Omega} \frac{|J|}{|\nabla u|} \nabla u \cdot \nabla \phi dx, \quad \forall \phi \in H^1(\Omega).$$

- ▶ If u is σ -harmonic and $a := |\sigma \nabla u|$, then

$$F_a[u] \leq F_a[v], \quad \forall v \in H^1(\Omega), \quad v|_{\partial\Omega} = u|_{\partial\Omega}.$$

Remark: In SZ -example only u^0 is a minimizer of
 $v \mapsto \int_{\Omega} |\nabla v| dx$, $v(x, y) = x^2 - y^2$ on ∂D .

Unique determination

Theorem: (Nachman-T-Timonov'09, Moradifam- Nachman-T '12)
Let $(f, |J|) \in C^{1,\alpha}(\partial\Omega) \times C^\alpha(\Omega)$ be admissible, generated by some unknown $\sigma \in C^\alpha(\Omega)$. Assume $|J| > 0$. Then the corresponding voltage potential

$$u \in \operatorname{argmin} \left\{ \int_{\Omega} |J| |\nabla v| dx : v \in W^{1,1}(\Omega)/BV(\Omega), v|_{\partial\Omega} = f \right\}.$$

and $\sigma = \frac{|J|}{|\nabla u|}$.

Remark: $|J|$ may be allowed to vanish in open sets. Then σ can be recovered outside the zeros of $|J|$.

Outline

In motivation

- Hybrid methods in Inverse Problems
- Current density based EIT
- Acquiring the interior data

The 1-Laplacian

- 1-Laplacian in Conductivity Imaging
- The Dirichlet problem

The Complete Electrode Model

- A boundary value problem for the Complete Electrode Model

Inverse Problem for Complete Electrode Model

- Characterization of non-uniqueness
- Phase retrieval
- Restoring uniqueness
- A numerical algorithm and experiment
- Conclusions

Complete Electrode Model (Somersalo-Cheney-Isaacson '92)

$\Omega \subset \mathbb{R}^n$ bounded with Lipschitz boundary $\partial\Omega$,

$N + 1$ electrodes: $e_k \subset \partial\Omega$, $k = 0, \dots, N$,

$\epsilon \leq \operatorname{Re}\{\sigma\} \leq 1/\epsilon$,

$\epsilon \leq \operatorname{Re}\{z_k\} \leq 1/\epsilon$, $k = 0, 1, \dots, N$,

$$\nabla \cdot \sigma \nabla \mathbf{u} = 0, \quad \text{in } \Omega,$$

$$\mathbf{u} + z_k \sigma \frac{\partial \mathbf{u}}{\partial \nu} \equiv \text{const} = U_k \quad \text{on } e_k, \quad \text{for } k = 0, \dots, N,$$

$$\int_{e_k} \sigma \frac{\partial \mathbf{u}}{\partial \nu} ds = I_k, \quad \text{for } k = 0, \dots, N,$$

$$\frac{\partial \mathbf{u}}{\partial \nu} = 0, \quad \text{on } \partial\Omega \setminus \bigcup_{k=0}^N e_k,$$

Well-posedness

Based on Lax-Milgram lemma:

Theorem (Somersalo- Cheney- Isaacson '92) Provided

$$\sum_{k=0}^N I_k = 0,$$

there is a unique solution $\langle u(x), (U_0, \dots, U_N) \rangle \in H^1(\Omega) \times \mathbb{C}^{N+1}$
up to a constant.

Normalization

Uniqueness up to a constant:

$\langle u(x) + c, (U_0 + c, \dots, U_N + c) \rangle$ also a solution.

$$\nabla \cdot \sigma \nabla(u + c) = 0, \quad \text{in } \Omega,$$

$$(u + c) + z_k \sigma \frac{\partial(u + c)}{\partial \nu} \equiv \text{const} = U_k + c \quad \text{on } e_k, \quad \text{for } k = 0, \dots, N,$$

$$\int_{e_k} \sigma \frac{\partial(u + c)}{\partial \nu} ds = I_k, \quad \text{for } k = 0, \dots, N,$$

$$\frac{\partial(u + c)}{\partial \nu} = 0, \quad \text{on } \partial\Omega \setminus \bigcup_{k=0}^N e_k,$$

Normalization: fix a constant by seeking $\mathbf{U} = (U_0, \dots, U_N)$ with $\sum_{k=0}^N U_k = 0$.

New properties in the real valued case

$$\sigma(x), z_0(x), \dots, z_N(x) \in \mathbb{R}$$

$$\mathbf{U} \in \Pi := \{(U_0, \dots, U_N) \in \mathbb{R}^{N+1} : \sum_{k=0}^N U_k = 0\}$$

- ▶ Maximum Principle for CEM: The maximum and minimum of the voltage potential u occur on the electrodes.
- ▶ A Poincaré Inequality (not necessarily connected with CEM): $\exists C > 0$ dependent only on Ω and $e_k \subset \partial\Omega$ such that $\forall u \in H^1(\Omega)$ and $\forall \mathbf{U} = (U_0, \dots, U_N) \in \Pi$:

$$\int_{\Omega} u^2 + \sum_{k=0}^N U_k^2 \leq C \left(\int_{\Omega} |\nabla u|^2 dx + \sum_{k=0}^N \int_{e_k} (u - U_k)^2 ds \right)$$

The Dirichlet principle for the CEM

Consider the functional

$$F_\sigma(u, \mathbf{U}) := \frac{1}{2} \int_{\partial\Omega} \sigma |\nabla u|^2 dx + \frac{1}{2} \sum_{k=0}^N \int_{e_k} \frac{1}{z_k} (u - U_k)^2 ds - \sum_{k=0}^N l_k U_k.$$

Recall Ω , Π , $e_k \subset \partial\Omega$, z_k , for $k = 0, \dots, N$, σ , and

$$\sum_{k=0}^N l_k = 0 \quad (*)$$

Theorem(Nachman-T-Veras '14)

(i) Independently of (*):

$$\exists! (u, \mathbf{U}) = \operatorname{argmin}_{H^1(\Omega) \times \Pi} F_\sigma$$

(ii) If (*) holds:

$$(u, \mathbf{U}) = \operatorname{argmin}_{H^1(\Omega) \times \Pi} F_\sigma \Leftrightarrow (u, \mathbf{U}) \text{ solves CEM}$$

Formulation of an Inverse Problem

Given: Ω , $e_k \subset \partial\Omega$ with $z_k > 0$, and l_1, \dots, l_N ,
(then $l_0 := -\sum_{k=1}^N l_k$),
and $|\mathbf{J}| = \sigma |\nabla u|$ inside Ω ,

Find σ .

Formulation of an Inverse Problem

Given: Ω , $e_k \subset \partial\Omega$ with $z_k > 0$, and l_k , $k = 1, \dots, N$ (then $l_0 := -\sum_{k=1}^N l_k$), and $|\mathbf{J}| = \sigma|\nabla u|$ inside,

Find σ .

Not possible:

$\Omega = (0, 1) \times (0, 1)$,

Top side: e_1 with $z_1 > 0$, inject $l_1 = 1$

Bottom side: e_0 with $z_0 = z_1 + 1$, extract $l_0 = -1$

Measure the magnitude $|\mathbf{J}| \equiv 1$ inside.

Arbitrary $\varphi : [0, 1] \rightarrow [\varphi(0), \varphi(1)]$ increasing, Lipschitz with $\varphi(0) + \varphi(1) = 1$.

Then: $u_\varphi(x, y) := \varphi(y)$ voltage for $\sigma_\varphi(x, y) = 1/\varphi'(y)$.

Yet for all such φ ,

$$\sigma_\varphi |\nabla u_\varphi| \equiv 1!$$

Generic non-uniqueness

Let $(u, U) \in H^1(\Omega) \times \Pi$ be the solution of CEM for some σ .
 $\varphi \in Lip(u(\bar{\Omega}))$ be an increasing function of one variable,
 $\varphi(t) = t + c_k$ whenever $t \in u(e_k)$, for each $k = 0, \dots, N$, and
 constants c_k satisfying $\sum_{k=0}^N c_k = 0$. Then

$$u_\varphi := \varphi \circ u \tag{1}$$

is a voltage potential for CEM with

$$\sigma_\varphi := \frac{\sigma}{\varphi' \circ u}, \tag{2}$$

and has the same interior data

$$\sigma |\nabla u| = \sigma_\varphi |\nabla u_\varphi|.$$

Characterization of Non-uniqueness

Theorem (Nachman-T-Veras '14) Recall assumptions on $\Omega \subset \mathbb{R}^d$ be bounded, connected $C^{1,\alpha}$, $e_k \subset \partial\Omega$, $z_k > 0$, l_k , $k = 0, \dots, N$.

Let $(u, U), (v, V) \in H^1(\Omega) \times \Pi$, be the CEM solutions for unknown conductivities $\sigma, \tilde{\sigma} \in C^\alpha(\Omega)$ with

$$|\mathbf{J}| := \sigma |\nabla u| = \tilde{\sigma} |\nabla v| \geq \delta > 0 \text{ in } \Omega.$$

Then $\exists \varphi \in C^1(u(\Omega))$, with $\varphi'(t) > 0$ a.e. in Ω , such that

$$v = \varphi \circ u, \quad \text{in } \Omega,$$

$$\tilde{\sigma} = \frac{\sigma}{\varphi' \circ u}, \quad \text{a.e. in } \Omega.$$

Moreover, for each $k = 0, \dots, N$ and $t \in v(e_k)$,

$$\varphi(t) = t + (U_k - V_k).$$

Idea: reduction to a minimization problem

Inverse hybrid problem: Consider

$$G_{|\mathbf{J}|}(v, V) = \int_{\Omega} |\mathbf{J}| |\nabla v|^2 dx + \frac{1}{2} \sum_{k=0}^N \int_{e_k} \frac{1}{z_k} (v - V_k)^2 ds - \sum_{k=0}^N l_k V_k,$$

- ▶ solutions of CEM are global minimizers of $G_{|\mathbf{J}|}$ over $H^1(\Omega) \times \Pi$.
- ▶ Geometry of the equipotential sets are uniquely determined! Contrast with Dirichlet

Contrast with functional in the forward model

$$F_{\sigma}(v, \mathbf{V}) := \frac{1}{2} \int_{\partial\Omega} \sigma |\nabla v|^2 dx + \frac{1}{2} \sum_{k=0}^N \int_{e_k} \frac{1}{z_k} (v - V_k)^2 ds - \sum_{k=0}^N l_k V_k.$$

Corollaries

- ▶ **Phase retrieval** (Nachman-T-Veras'14) Same hypotheses (recall).

$$|\mathbf{J}| = |\tilde{\mathbf{J}}| \Rightarrow \mathbf{J} = \tilde{\mathbf{J}}.$$

- ▶ There is uniqueness (and a reconstruction method) from the magnitudes of **two** currents via a local formula (Nachman et al., Lee 2004)
- ▶ The J -substitution algorithm via magnitudes of **two** currents (Seo et al 2002) converges to the unique solution.

Knowledge of the potential on a boundary curve joining the electrodes restores uniqueness

Theorem (Nachman-T-Veras '14) In addition to the hypotheses of the characterization theorem if

$$u|_{\Gamma} = \tilde{u}|_{\Gamma} + C,$$

for some C , and Γ a curve joining the electrodes, then

$$\begin{aligned} u &= \tilde{u} + C \text{ in } \bar{\Omega}, \\ \sigma &= \tilde{\sigma} \text{ in } \Omega. \end{aligned}$$

A minimization algorithm for G

$$G_{|\mathbf{J}|}(v, V) = \int_{\Omega} |\mathbf{J}| |\nabla v| dx + \sum_{k=0}^N \int_{e_k} \frac{1}{2z_k} (v - V_k)^2 ds - \sum_{k=0}^N I_k V_k,$$

Lemma Assume that $v \in H^1(\Omega)$ satisfies

$$\epsilon \leq \frac{a}{|\nabla v|} \leq \frac{1}{\epsilon},$$

for some $\epsilon > 0$, and let $(u, U) \in H^1(\Omega) \times \Pi$ be the unique solution for CEM with $\sigma := a/|\nabla v|$. Then

$$G_a(u, U) \leq G_a(v, V), \quad \text{for all } V \in \Pi.$$

Moreover, if equality holds then $(u, U) = (v, V)$.

A minimization algorithm

- ▶ With σ_n given: Solve CEM for the unique solution (u_n, \mathbf{U}^n) ;
- ▶ If

$$\text{essinf} \|\nabla u_n - \nabla u_{n-1}\| > \delta \frac{\epsilon}{\text{essinf} |\mathbf{J}|},$$

update

$$\sigma_{n+1} := \min \left\{ \max \left\{ \frac{|\mathbf{J}|}{|\nabla u_n|}, \epsilon \right\}, \frac{1}{\epsilon} \right\}$$

and repeat;

- ▶ else STOP.

Enough for the phase retrieval:

$$\mathbf{J} \approx |\mathbf{J}| \frac{\nabla u_n}{|\nabla u_n|}$$

Using the voltage on Γ

Let n be the last iteration and set

$$\sigma_{n+1} := \frac{|\mathbf{J}|}{\nabla u_n}.$$

The Characterization Theorem

$$\Rightarrow u(x) \approx f(u_n(x)).$$

Read off the measured data on Γ to determine the scaling function $f : u(\Gamma) \rightarrow u_n(\Gamma)$.

Then

$$\sigma(x) \approx \frac{1}{f'(u_n(x))} \sigma_{n+1}(x).$$

Reconstruction results in a numerical experiment

$$1\text{S/m} \leq \sigma \leq 1.8\text{S/m}, -I_0 = I_1 = 3\text{mA}, z_0 = z_1 = 8.3\text{m}\Omega \cdot \text{m}^2$$

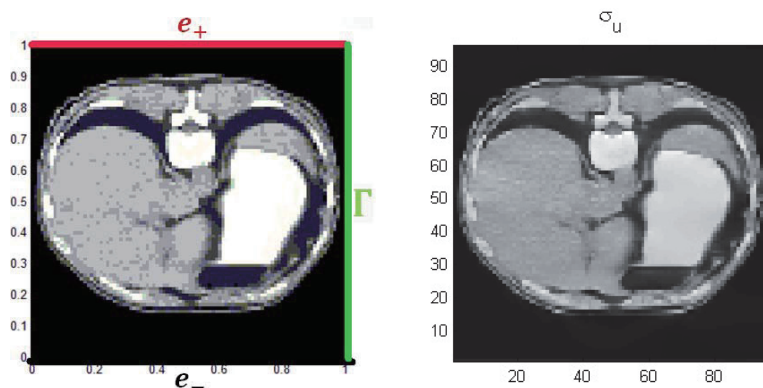


Figure : Exact conductivity (left) vs. reconstructed conductivity (right)

Voltage potential scaling along Γ

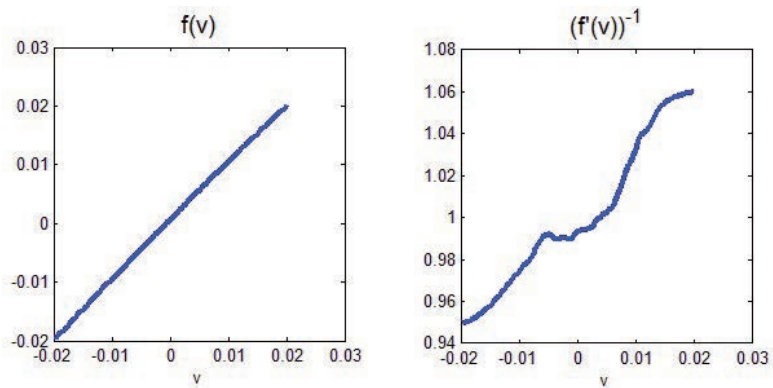


Figure : The scaling function f and its derivative.

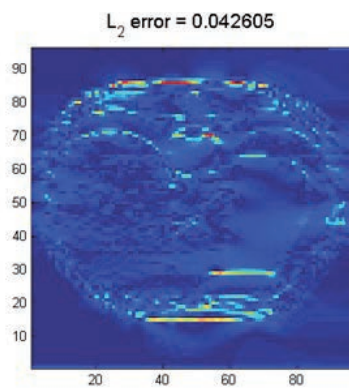


Figure : L^2 -Error: Understood from the stability in the linearized case Kuchment&Steinhauer (2011), Bal (2012)

Some learnings and open questions

- ▶ knowledge of the magnitude of one current and of boundary voltage potential is sufficient to determine an isotropic conductivity
- ▶ in the more realistic CEM. the magnitude of one current density by itself cannot determine an isotropic conductivity
- ▶ but the magnitude recovers the phase ! (not known in the anisotropic case)
- ▶ the magnitude of two currents uniquely determine the conductivity (up to an additive constant)
- ▶ knowledge of the voltage potential along a curve joining electrodes restores uniqueness in a well determined region inside.
- ▶ in the isotropic case: the phase of the current is uniquely determined from its magnitude (not known in the anisotropic case)
- ▶ Develop efficient algorithms for the 1-Laplacian
- ▶ What can be recovered in the anisotropic case from the magnitudes of the current? How many such currents?

Thank you!

Hierarchical Bayesian estimation method for diffuse optical tomography

Takeaki Shimokawa

ATR Neural Information Analysis Laboratories

Abstract

Functional near-infrared spectroscopy (fNIRS) is a technique that non-invasively measures human hemodynamic responses to neuronal activation in the cerebral cortex. In fNIRS measurements, optical topography has been widely used as an imaging method, but recently diffuse optical tomography (DOT) has collected much attention as an advanced technique for visualizing the cortical activities. The large number of overlapping measurement channels due to the use of high-density probe arrays permits the reconstruction of the internal activities. However, accurate three-dimensional reconstruction is still a challenging problem because of highly diffusive nature of the photon propagation in biological tissue. It has also been a problem that the observation signal is contaminated by the artifact signal from the hemodynamic response in the scalp.

To address these difficulties, we have been developing a hierarchical Bayesian estimation methods. Firstly, we introduced sensitivity-normalized regularization and sparsity into the Bayesian method to improve depth accuracy and spatial resolution of DOT [1]. Secondly, we extended it to be able to estimate scalp blood flow as well as cortical activity by introducing different types of regularization models for the cortex and the scalp [2]. We show several estimation results of our methods through computer simulations, phantom experiments, and human experiments [3].

References

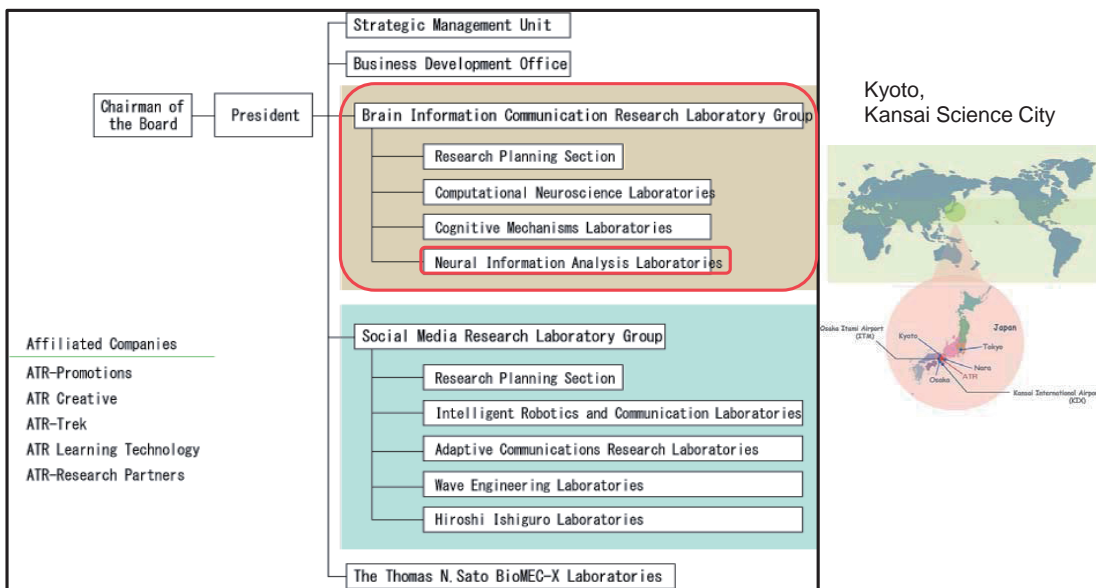
- [1] T. Shimokawa, T. Kosaka, O. Yamashita, N. Hiroe, T. Amita, Y. Inoue, and M. Sato, “Hierarchical Bayesian estimation improves depth accuracy and spatial resolution of diffuse optical tomography,” *Opt. Express* **20**, 20427–20446 (2012).
- [2] T. Shimokawa, T. Kosaka, O. Yamashita, N. Hiroe, T. Amita, Y. Inoue, and M. Sato, “Hierarchical Bayesian estimation improves depth accuracy and spatial resolution of diffuse optical tomography,” *Biomed. Opt. Express* **4**, 2411–2432 (2013).
- [3] O. Yamashita, T. Shimokawa, T. Kosaka, T. Amita, Y. Inoue, and M. Sato, “Hierarchical Bayesian model for diffuse optical tomography of the human brain: human experimental study,” *Journal of Advanced Computational Intelligence and Intelligent Informatics* **18**, 1026–1033 (2014).

Hierarchical Bayesian estimation method for diffuse optical tomography

IMI Conference on Inverse Problems
 Nov. 12th @ Kyushu Univ.
 Takeaki Shimokawa (ATR)



(株)国際電気通信基礎技術研究所

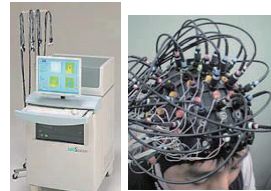


Neuroimaging devices in ATR

fMRI



fNIRS



© Shimadzu corp.

MEG



© ATR-BAIC

EEG



© biosemi

Neuroimaging devices in ATR

fMRI



© ATR-BAIC

- high spatial resolution: $\sim 2\text{mm}$
(no need to solve inverse problem)
- low time resolution: $\sim 1\text{s}$

MEG



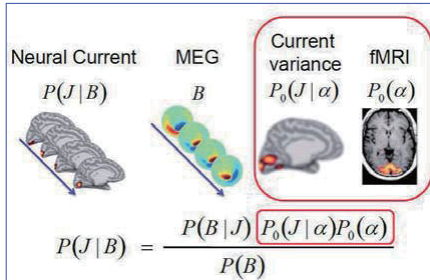
© ATR-BAIC

- high time resolution: $\sim 1\text{ms}$
- need to solve inverse problem

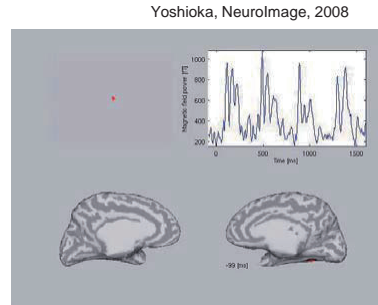
ATR Neural Information Laboratory

- Develop methods for neuroscientist

Hierarchical Bayesian estimation method
from MEG data with fMRI prior
[Sato, NeuroImage, 2004]



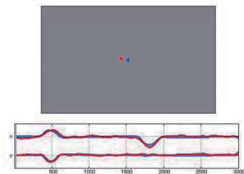
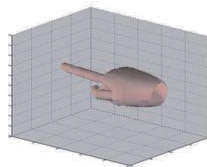
validation



↓ application



Toda, NeuroImage, 2011



For application study

fMRI



MEG



fNIRS



EEG



Portable & Low cost

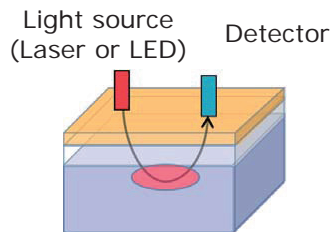
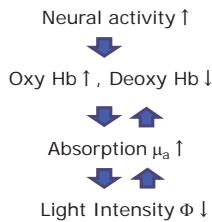
fNIRS and its advantages

- functional Near-InfraRed Spectroscopy (fNIRS)
- Advantages • • • small and portable device, safety, low cost, few physical restrictions

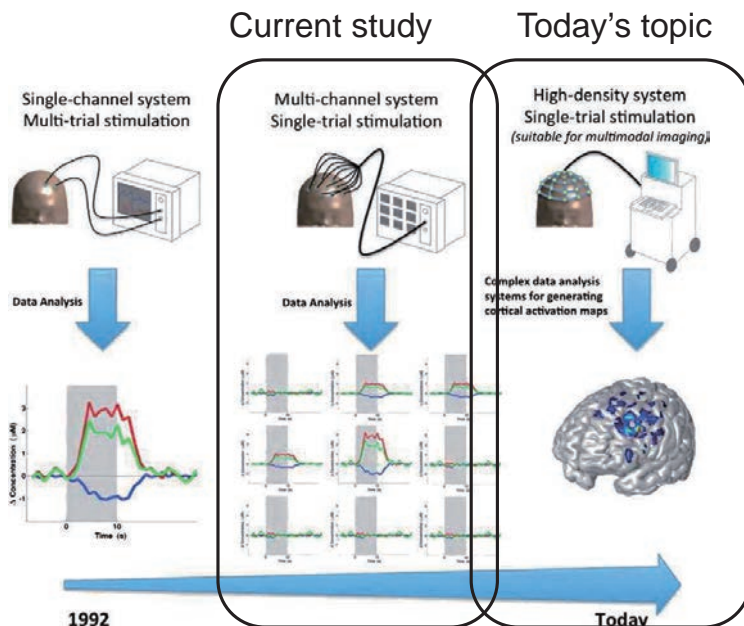
Near Infrared light easily go through biological tissue



Shimadzu corp.



History of fNIRS

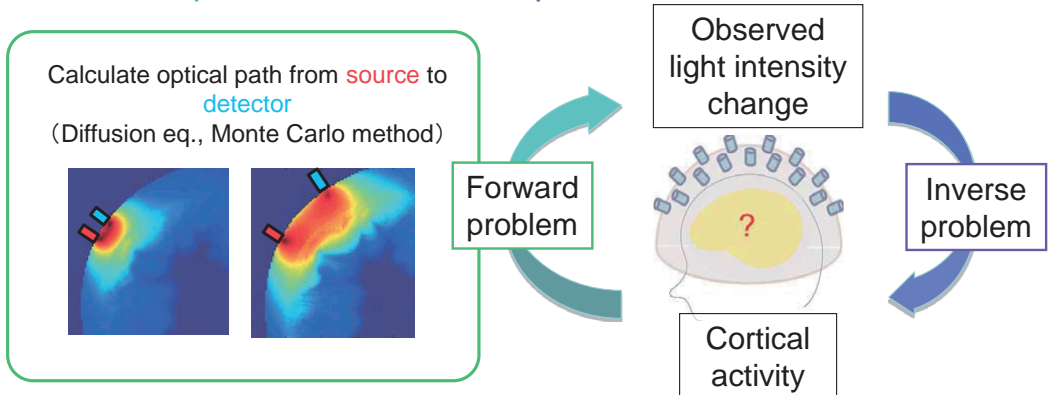


Ferrari, NeuroImage, 2012

Called as "Diffuse Optical Tomography (DOT)"

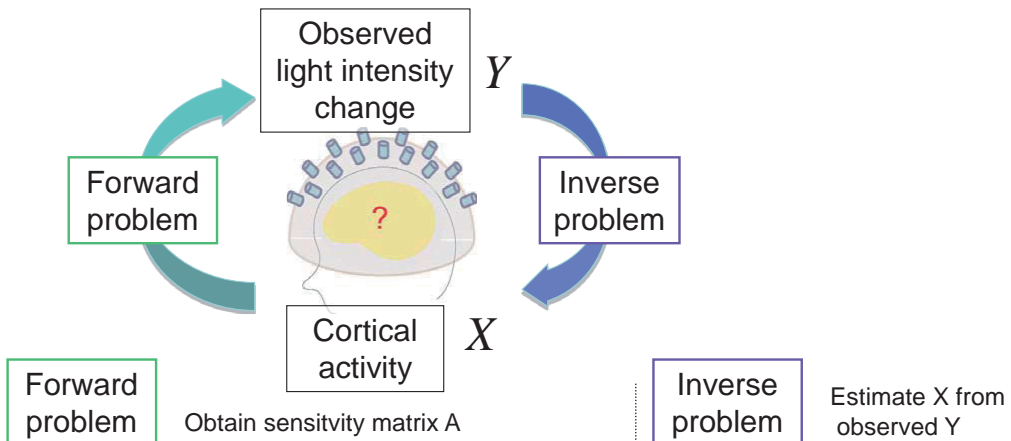
Diffuse optical tomography (DOT)

- Estimate inner brain activity from light intensity change observed outside the head
- DOT consists of two steps:
forward problem and inverse problem



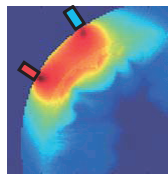
- We develop the inversion methods

DOT by Linear approximation



$$\left(\nabla^2 - \frac{\nu \mu_a}{D} \right) \Phi_0(\vec{r}_s, \vec{r}) = -\frac{S}{D} \delta(\vec{r} - \vec{r}_s)$$

Use Rytov approximation to diffusion equation $Y = AX$ Sensitivity matrix Map of sensitivity

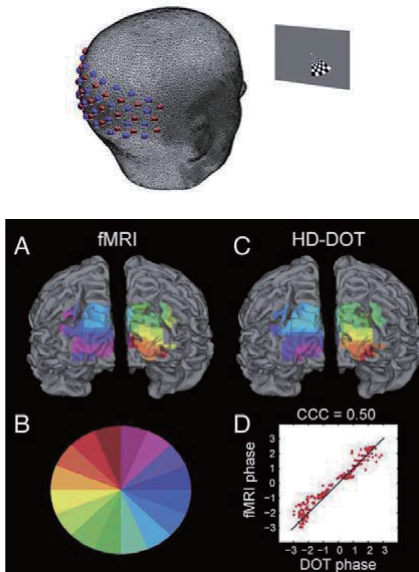


$$Y = AX + \xi$$

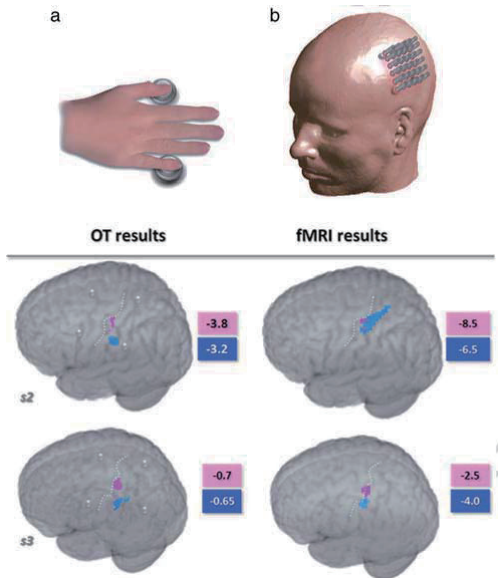
$$X = ?$$

Dim of X is large.
 Dim of Y is small.
 → ill-posed problem

Recent DOT studies



Eggebrecht, NeuroImage 2012

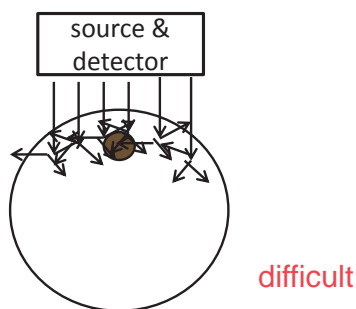


Habermehl, NeuroImage 2011

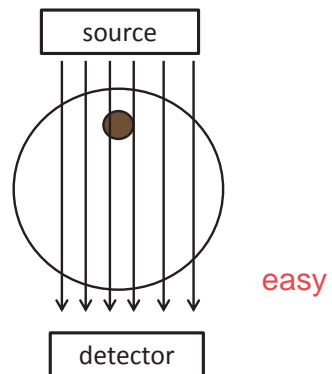
- Remarkable results. However, the 3D estimation remains incomplete

3D tomography by NIR light is difficult

Diffuse Optical Tomography (DOT)
by near-infrared light

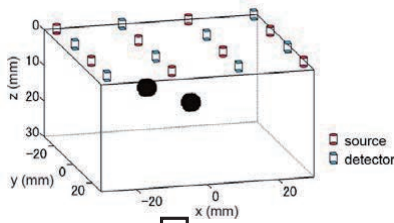


Computed Tomography (CT)
by X-ray



- NIR light does not penetrate large tissues
→ difficulty of estimation in depth direction
- NIR light scatters in biological tissues
→ blurred. Low spatial resolution.

Problems of conventional inversion method

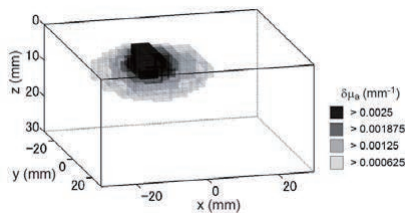


observe



Light intensity

reconstruct



Tikhonov Regularization

$$\hat{X} = \min_X \left[\underbrace{\|\Sigma_y^{-1}(Y - AX)\|^2}_{\text{observation error}} + \lambda \underbrace{\sum_i X_i^2}_{\text{penalty}} \right]$$

1. biased toward surface
2. low spatial resolution

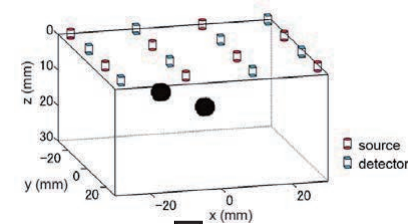


improve by two steps

Proposed 3D estimation method

[Shimokawa et al, Opt Express, 2012]

① Weighted regularization

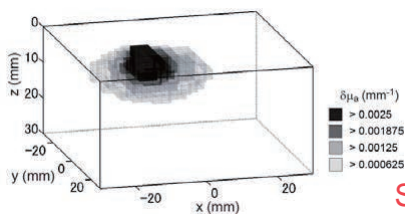


observe



Light intensity

reconstruct



Tikhonov regularization

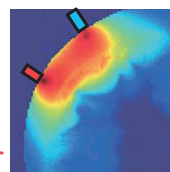
$$\hat{X} = \min_X \left[\left\| \Sigma_y^{-1} (Y - AX) \right\|^2 + \lambda \left\| X \right\|^2 \right]$$

observation error penalty

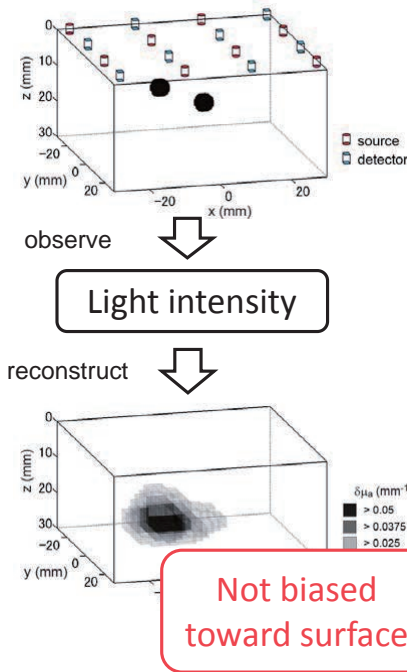


Biased because this penalty is homogeneous

Sensitivity A:
Very strong in shallow layer
Very weak in deep layer



① Weighted regularization



Sensitivity-normalized Tikhonov Regularization

$$\hat{X} = \min_X \left[\|\Sigma_y^{-1}(Y - AX)\|^2 + \lambda \sum_i D_{ii} X_i^2 \right]$$

weighted penalty

$$D = \text{diag}(A^T \Sigma_y^{-1} A + \beta I)$$

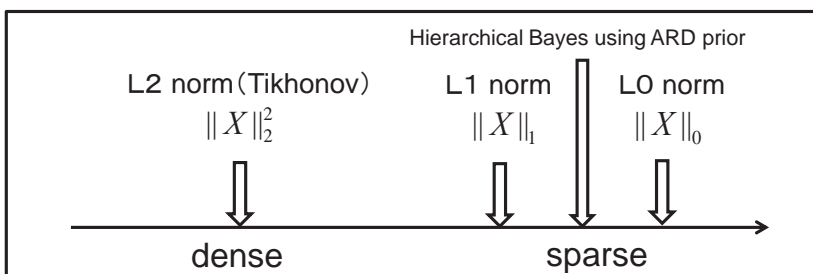
Penalize shallow layers strongly and deep layers weakly

[Pogue 1999, Culver 2003, Niu 2010]

② Introduce sparsity

- Each Brain function is localized.
- The sparse estimation can increase spatial resolution if true solution is sparse.
- The sparseness of solution depends on regularization term

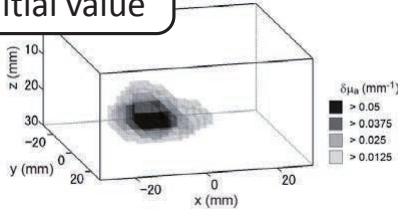
$$\hat{X} = \min_X \left[\|\Sigma_y^{-1}(Y - AX)\|^2 + (\text{regularization}) \right]$$



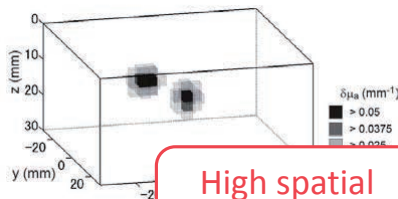
$$\|X\|_p = \lim_{\epsilon \rightarrow 0} \sum_{i=1}^N |x_i|^{p+\epsilon}$$

Hierarchical Bayesian estimation

Use as an initial value



Iteratively optimize



Sensitivity-normalized Tikhonov Regularization

2. low spatial resolution

Hierarchical Bayesian estimation with ARD prior

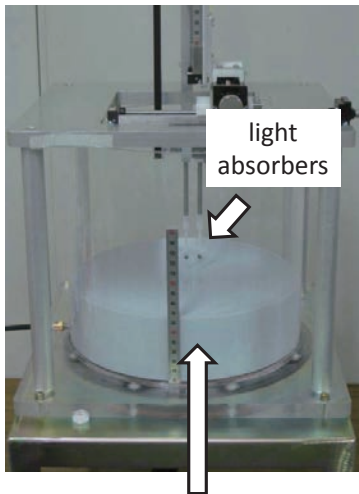
$$\hat{X} = \min_X \left[\|\Sigma_y^{-1}(Y - AX)\|^2 + \sum_i \lambda_i X_i^2 \right]$$

each voxel regularization

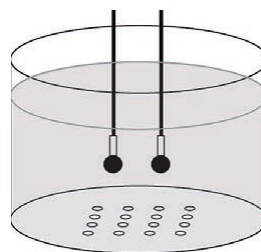
initial value → iteratively optimized

The solution become sparse [Faul, 2002].
Remove unimportant activities

Phantom experiment



optical parameter
Absorption: $\mu_a = 0.019 \text{ mm}^{-1}$,
Scattering: $\mu_s' = 1.1 \text{ mm}^{-1}$
(similar to cerebral cortex)



Sources & Detectors
at the bottom
(probe interval:
18mm)

Extended method for removing scalp artifact

[Shimokawa et al, Biomed Opt Express, 2013]

Extension of the method

3D estimation was possible



estimate both cortical activity and scalp activity

- We assumed sparsity to the cortical activity
- However, hemodynamic response in scalp is not sparse but global.

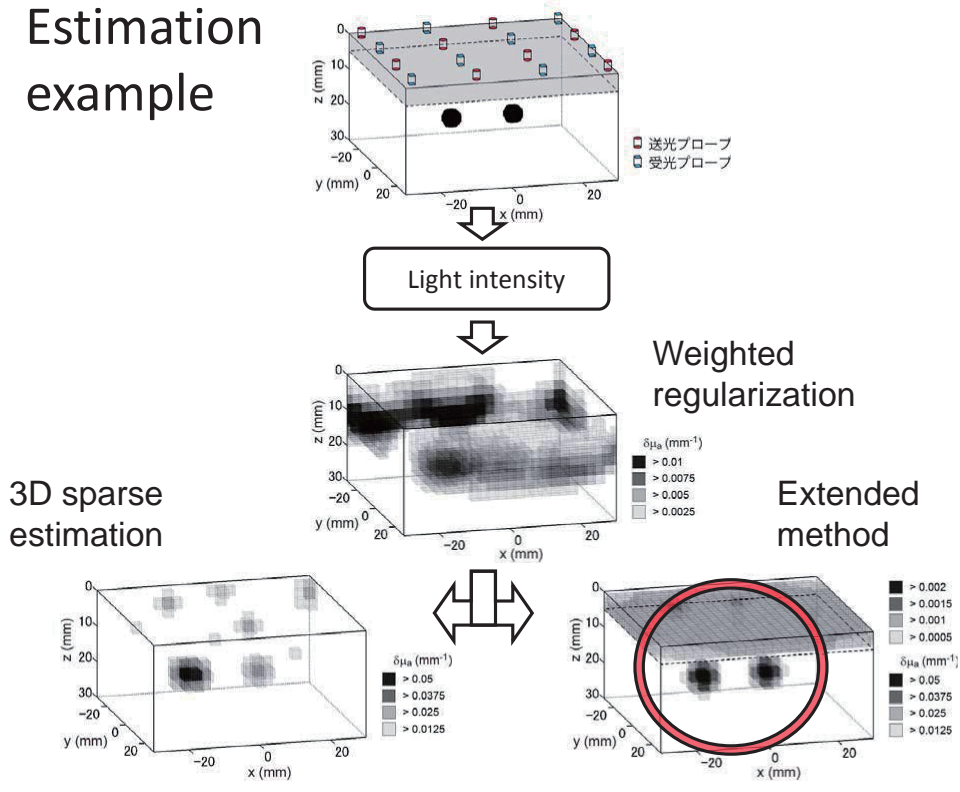
⇒ Apply different types of regularizations

$$Y = A_{cortex} \underline{X}_{cortex} + A_{scalp} \underline{X}_{scalp}$$

introduce sparsity
by ARD prior

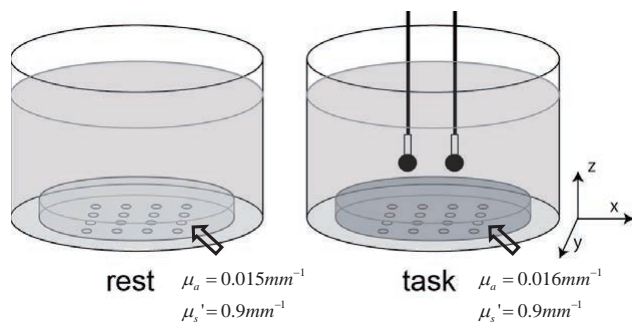
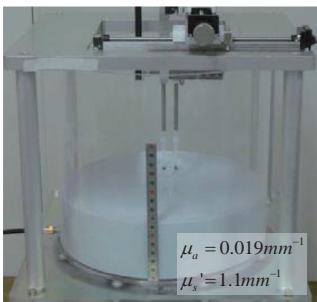
penalize Laplacian of the activity
 $\min \|\nabla X_{scalp}\|^2$

Estimation example



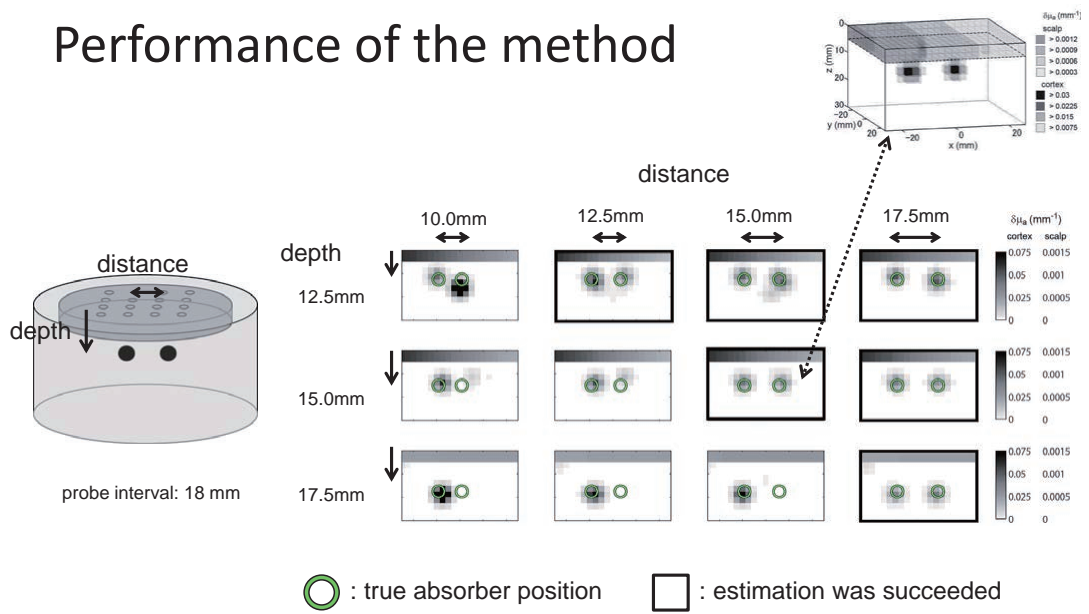
Validation

- 2-layer phantom experiment



- Cortical activity is mimicked by absorber
- Scalp activity is mimicked by replacing the silicone plate

Performance of the method

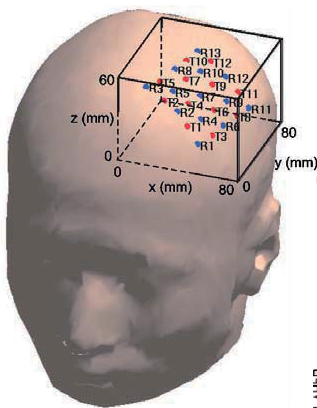


Two absorbers of 12.5 mm distance can be discriminated with 18 mm interval probe arrangement.

Realistic Simulation Study

[Shimokawa et al, Biomed Opt Express, 2013]

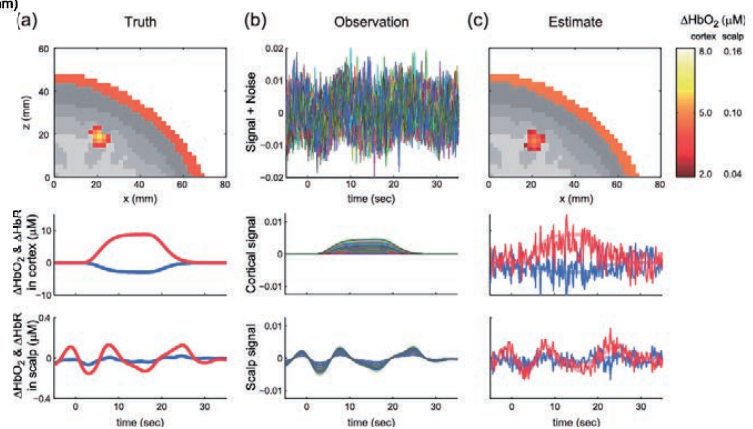
Validation by MRI-based head-model simulations



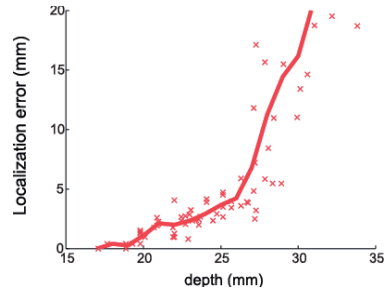
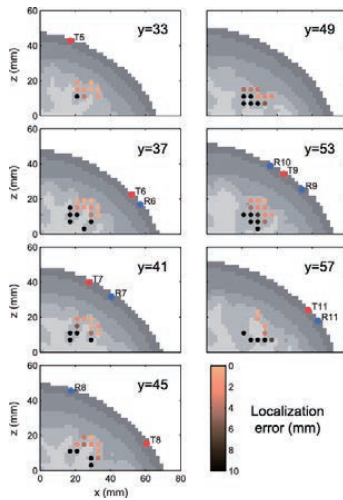
MRI image



- 5-layer head model
- scalp (active)
 - skull
 - CSF
 - gray matter (active)
 - white matter



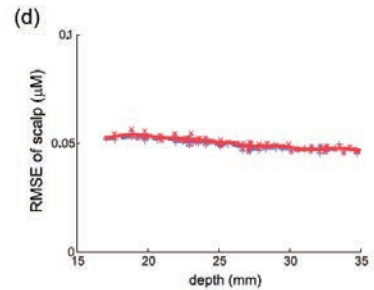
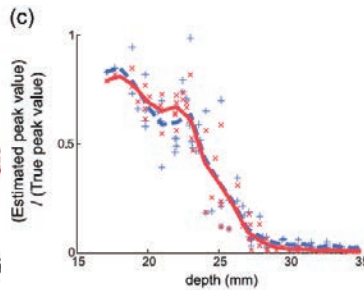
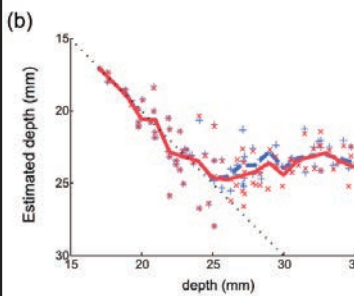
Validation by MRI-based head-model simulations



Depth of cortical activity

We tested the localization error changing the position of cortical activity

Validation by MRI-based head-model simulations

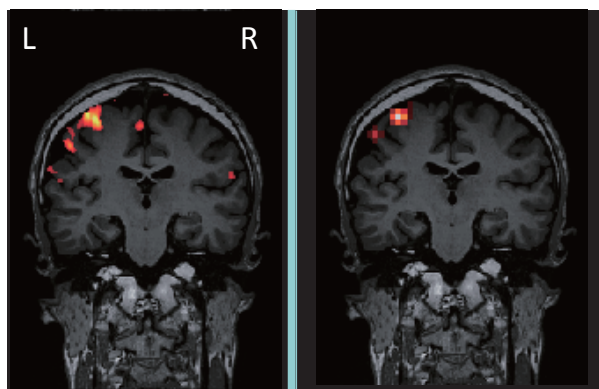
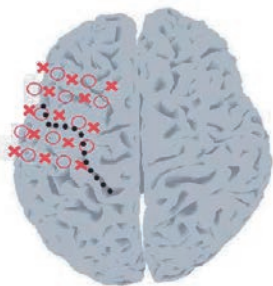


Human Experiment

[Yamashita et al, JACIII, 2014]

Validation by human experiment

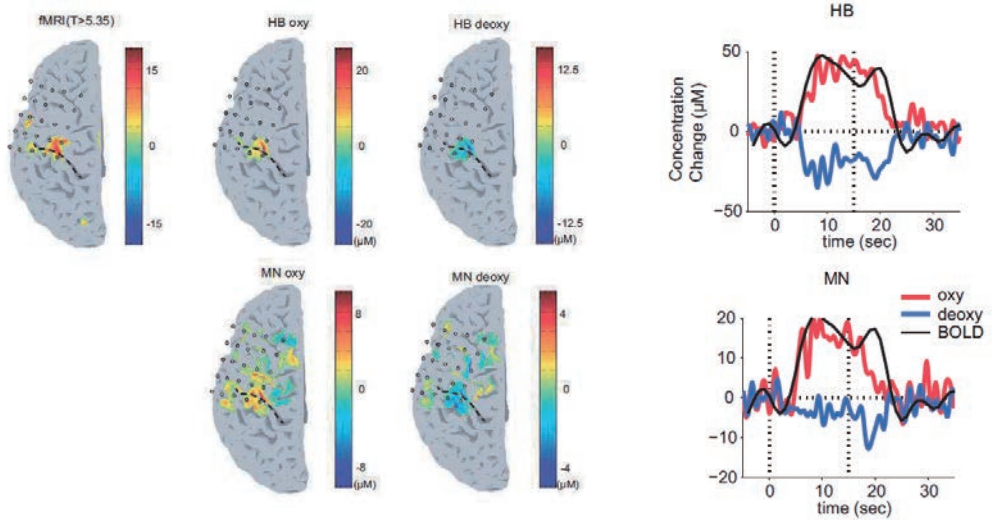
- Right-finger-tapping



fMRI

DOT
(proposed
method)

Validation by human experiment



Summary

- We developed the diffuse optical tomography method for visualizing the 3-dimensional distribution of hemodynamic changes inside the brain.
- The methods introduced the following two idea:
 - ①weighted regularization
 - ②sparsity
- We extended it for removing scalp artifact
- We validated the proposed method through phantom experiments, realistic simulations, and human experiments.

Acknowledgement

- collaborator
 - Okito YAMASHITA (ATR)
 - Takashi KOSAKA (ATR & NAIST)
 - Ryota AISU (ATR & NAIST)
 - Nobuo HIROE (ATR)
 - Takashi AMITA (Shimadzu corp.)
 - Yoshihiro INOUE (Shimadzu corp.)
 - Masa-aki SATO (ATR)

References

- [1] M. Sato, T. Yoshioka, S. Kajihara, K. Toyama, N. Goda, K. Doya, and M. Kawato, “Hierarchical Bayesian estimation for MEG inverse problem,” *NeuroImage* **23**, 806–826 (2004).
- [2] T. Yoshioka, K. Toyama, M. Kawato, O. Yamashita, S. Nishina, N. Yamagishi, and M. Sato, “Evaluation of hierarchical bayesian method through retinotopic signal reconstruction from MEG measurement,” *NeuroImage* **42**, 1397–1413 (2008).
- [3] A. Toda, H. Imamizu, M. Kawato, and M. Sato, “Reconstruction of two-dimensional movement trajectories from selected magnetoencephalography cortical currents by combined sparse Bayesian methods,” *NeuroImage* **54**, 892–905 (2011).
- [4] M. Ferrari and V. Quaresima, “A brief review on the history of human functional near-infrared spectroscopy (fNIRS) development and fields of application,” *NeuroImage* **63**, 921–935 (2012).
- [5] A. T. Eggebrecht, B. R. White, S. L. Ferradal, C. Chen, Y. Zhan, A. Z. Snyder, H. Dehghani, and J. P. Culver, “A quantitative spatial comparison of high-density diffuse optical tomography and fMRI cortical mapping,” *NeuroImage* **61**, 1120–1128 (2012).
- [6] C. Habermehl, S. Holtze, J. Steinbrink, S. P. Koch, H. Obrig, J. Mehnert, and C. H. Schmitz, “Somatosensory activation of two fingers can be discriminated with ultrahigh-density diffuse optical tomography,” *NeuroImage* **59**, 3201–3211 (2011).
- [7] B. W. Pogue, T. O. McBride, J. Prewitt, U. L. Österberg, and K. D. Paulsen, “Spatially variant regularization improves diffuse optical tomography,” *Appl. Opt.* **38**, 2950–2961 (1999).
- [8] J. P. Culver, T. Durduran, D. Furuya, C. Cheung, J. H. Greenberg, and A. G. Yodh, “Diffuse optical tomography of cerebral blood flow, oxygenation, and metabolism in rat during focal ischemia,” *J. Cereb. Blood Flow Metab.* **23**, 911–924 (2003).
- [9] H. Niu, F. Tian, Z. J. Lin, and H. Liu, “Development of a compensation algorithm for accurate depth localization in diffuse optical tomography,” *Opt. Lett.* **35**, 429–431 (2010).
- [10] A. C. Faul and M. E. Tipping, “Analysis of sparse Bayesian learning,” *Adv. Neural Inf. Process. Syst.* **14**, 383–389 (2002).

Gentaro Taga

Graduate School of Education, The University of Tokyo

"Phase dynamics of spontaneous activity in the cerebrovascular system of human infants"

While the structural network of the white matter pathways in the human brain is mostly established during the fetal period, the local hemodynamics in relation to the neural activation and the global functional network of the brain are postnatally generated in daily life activity such as sleeping, moving and interacting with the environment. Empirical evidences have shown that dynamic changes occur in local cerebral hemodynamics and global network of the cortex in the first few months of life after birth. The safe and non-invasive method of neuroimaging based on multi-channel (94CH) near infrared spectroscopy (NIRS) has been used to measure spontaneous fluctuations (0.01-0.1 Hz) in oxygenated and deoxygenated hemoglobin (oxy- and deoxy-Hb) in the cerebral blood, which are assumed to change in response to neural activation while infants were sleeping. I will first focus on the phase dynamics in oxy- and deoxy-Hb signals, which are extracted by performing Hilbert transformation. While newborn infants showed in-phase oscillations between local oxy- and deoxy-Hb changes, 3-month-old infants showed anti-phase oscillations between the same signals. To understand the physiological mechanisms underlying this change, I will demonstrate a biophysical model for the systemic and cerebral circulation, gas exchange and neurovascular coupling, which are described as nonlinear differential equations and present preliminary results of simulation. The second focus is on state-dependent changes in the global functional networks shown in the form of correlation and/or phase synchronization of oxy-Hb signals over different channels. Empirical data showed that the oxy-Hb signals over the global regions of the cortex exhibited synchronous and asynchronous fluctuations during active and quiet sleeping, respectively. I will discuss the mechanism for the sleep-state-dependent changes in phase dynamics of the hemodynamics of the brain in infants.

Development of ultrasonic tomography for concrete structures

Noriyuki MITA* and Takashi TAKIGUCHI†

Abstract

In this article, we first review the basic theory of concrete from the viewpoint of the building material. It is our motivation for this article is to establish a determinate non-destructive inspection method for concrete structures by application of integral geometry. It would enable us to detect the interior structure of the concrete structures concretely, which has not been developed yet, unfortunately. For our purpose, we study how to establish an acoustic tomography by ultrasonic waves, where we pose a mathematical problem of integral geometry based on our experiments on the concrete structures and their review-examination. We also discuss how important our problem is and introduce several examples in practical applications to which the researches on our problem should be applied. We shall study this problem in view of both theoretical mathematics and practical applications.

Keywords: non-destructive inspection of concrete structures, inverse problems, acoustic tomography, integral geometry

2010 Mathematics Subject Classification ; Primary 35R30, Secondary 74J25, 53C65

*Faculty of Human Resources Development, Polytechnic University of Japan, 2-32-1, OgawaNishimachi, Kodaira, Tokyo, 187-0035, JAPAN. email: mitanori@uitech.ac.jp

†Supported in part by JSPS Grant-in-Aid for Scientific Research (C) 26400184.
Department of Mathematics, National Defense Academy of Japan, 1-10-20, Hashirimizu, Yokosuka, Kanagawa, 239-8686, JAPAN. email: takashi@nda.ac.jp

1 Introduction

In this article, we first review the outline of concrete theory, with which most of the readers may not be familiar. For the general theory of concrete, confer [1]. We also recommend [3] for Japanese readers. It is one of our main purposes is to establish a determinate non-destructive inspection method for concrete structures, which has not been developed yet for the time being. For this purpose, we propose a problem in integral geometry the solution of which would yield the development of a new non-destructive inspection method for concrete structures applying acoustic tomography. For the development of the acoustic CT for our purpose, we studied how the ultrasonic waves and the electromagnetic acoustic pulses propagate in the cement paste, the mortar and the concrete by experiments. By the results of our experiments, we study the propagation of the ultrasonic waves and the electromagnetic acoustic pulses in the cement paste, the mortar and the concrete, which yields an inverse problem of the acoustic tomography applied to the determinate non-destructive inspection method for concrete structures we are trying to establish. It is interesting that the main problem (Problem 4.1 below) posed in this paper is very interesting in view of theoretical study of integral geometry. Having the above argument in mind, we shall discuss the importance of our main problem (Problem 4.1 below) in view of both practice and theory.

This article consists of the following sections.

- §1. Introduction
- §2. Basic properties of concrete
- §3. Propagation of the ultrasonic waves and the electromagnetic acoustic pulses
- §4. An inverse problem of the acoustic tomography
- §5. Examples in practice
- §6. Conclusion

In this section, as the introduction of this article, we introduce the outline of our article. In the next section, we shall review basic properties of concrete. We also discuss how we understand the concrete in this paper, we claim that this understanding (Claim 2.1 below) is very important for the study of concrete as a building material. In the third section, we study how the ultrasonic waves and the electromagnetic acoustic pulses propagate in the cement paste, the mortar and the concrete by the experiments, which is a key to discuss our main purpose, to study how to establish a determinate non-destructive inspection method for concrete structures, in Section 4. We first introduce our experiments to study the propagation the ultrasonic waves and the electromagnetic acoustic pulses in the cement paste, the mortar and the concrete. By examining the results of our experiments, we conclude that we can treat the ultrasonic waves and the electromagnetic acoustic pulses as linear elastic waves for our purpose if we only focus on the first arriving waves and ignore all the other waves. Section 4 is devoted for the main purpose of this article. We shall pose an inverse problem for establishment of a determinate non-destructive inspection method for concrete structures, for which we shall apply the results of our experiments and their examination discussed in Section 4. The problem posed in this section is also

interesting in view of pure mathematics, especially, in view of integral geometry. In the fourth section, as well as posing the main problem (Problem 4.1), we also give some studies on it, especially in view of theoretical mathematics. In the section five, we shall introduce some applications of our main problem and discuss how to solve them, where we study our main problem (Problem 4.1) from the viewpoint of practical applications. In the final section, we shall summarize our conclusions and mention some open problems left to be solved for further development.

As the origin of this research, we would like the readers to confer [5] published in the proceedings of the conference “Collaboration between theory and practice in inverse problems” held at IMI, Kyushu University, Japan, from Dec. 16th to Dec. 19th, 2014.

At the end of Introduction of this article, the authors would express their gratefulness to Professors Hisashi Yamasaki for his devoted help for our experiments.

2 Basic properties of concrete

In this section, we shall review basic properties of concrete. Before reviewing the definition and some basic properties of concrete, the authors claim that

Claim 2.1. *The concrete materials are artificial (gigantic) stones or megaliths.*

Let us first discuss why the authors claim Claim 2.1. Take Valley Temple, Egypt (BC2500?) and Parthenon, Athens (BC447-432), for example, which are made of megaliths. At that period around those areas, there were plenty of megaliths available, therefore they made Valley Temple and Parthenon of megaliths which are very suitable for edifices. On the other hand, let us turn to Colosseum, Rome (AD70-80). Its bailey or external wall being made of megaliths, its interior structure is infilled with stones bricks and sand, which we take as an origin of the concrete. It may be because of the shortage of the megaliths in Rome about 2000 years ago. Note that the structure of Colosseum safely exists after about 2000 years after its foundation. Hence we can say that the primitive concrete materials applied to the interior infillment of Colosseum have played their important role as the substitute for the megaliths very well for a long time, which is one of the reasons why the authors claim Claim 2.1. Though we still have many other reasons, we would not mention them in detail, since they directly have little to do with our main purpose in this article.

Let us define what the concrete is.

Definition 2.1. The concrete is the mixture of the four materials, the cement (C), the water (W), the sand (fine aggregate :S) and the gravel (coarse aggregate: G). Sometimes, if necessary, we add some admixture to the above mixture of the four materials to make harder concrete.

Remark 2.1.

- (i) The mixture of the cement and the water is called the cement paste.
- (ii) The mixture of the cement, the water, and the sand (the cement paste and the sand) is called the mortar.
- (iii) The concrete can be understood as the mixture of the mortar and the gravel.
- (iv) It being usually said that the concrete is the mixture of the four materials, the cement, the water, the sand and the gravel as mentioned above, it is very important to add the air as the fifth component of the concrete, especially for the main purpose in this article. Since concrete is a porous medium, as is well known, it is very important to study how the air is included in a concrete structure for its non-destructive inspection, for typical examples of which, confer Problems 5.1, 5.2 and 5.3 and thier solutions in the fifth section.

Let us introduce the merits of the concrete.

Property 2.1 (Merits of the concrete).

The merits of the concrete as a building material are as follows.

- (a) *Excellent durability against the weather, the chemical materials and the mechanical force.*
- (b) *High fire-resistance and water-resistance.*
- (c) *High compressive strength.*
- (d) *High corrosion resistance for steel.*
- (e) *The coefficients of thermal expansion (CTE) of the concrete and the steel are exactly the same.*
- (f) *Easily made and shaped in any form because of its fluidity before it gets hard.*
- (g) *Its cost is very cheap.*

Let us give some remarks on Property 2.1. The first three properties are very close to the ones of the stones and the megaliths, which is one of the reasons why the authors claimed Claim 2.1. The properties (d) and (e) are essentially important for the reinforced concrete (RC) structures. The property (d) is by the chemical property of the cement. Very roughly speaking, the main component of the cement is calcium oxide (CaO), whose combination with the water yields



which is known as the hydration reaction of the cement. It is well known that calcium hydroxide ($Ca(OH)_2$) shows strong alkalinity, which prevents the steel from getting oxidized. We claim that this property is much better than “being artificial stones or megaliths”, especially as the material of the RC structures. If the CTE of the concrete and the steel are different, the RC structure easily have some cracks in their interior by the change of the temperature. By the properties (d) and (e), the RC was called as “the miracle and the permanent material” at its initial stage of application to the buildings. It turned out, however, that it was neither miracle nor permanent. The concrete gets neutralized by the carbon dioxide (CO_2) in the air a few decades after its placing, whose chemical reaction is represented by



After the neutralization of the concrete, a part of the steel inside the RC structure gets corroded by the water contained in its interior. The corroded steel intumescens very much, which would make cracks or ruin the structure. Therefore the life span of the RC structure is called about a half century, these days. In spite of it, it is true that the reinforced concrete is very cheap, durable and easily treated material for the buildings before the steel in its interior gets corroded. By these facts, it is very important to study how to find the defects in the concrete structures and how to repair and maintain them. We also note that the properties (f) and (g) are very good, important and superior to the megaliths as the building material.

Of course, there are demerits of the concrete.

Property 2.2 (Demerits of the concrete).

The demerits of the concrete as a building material are as follows.

- (α) *Low tensile strength.*
- (β) *It easily gets cracks in and on itself.*
- (γ) *It is very heavy in the RC structures.*

Let us give some remarks on Property 2.2. As for (α), the tensile strength of the concrete is about 1/10 of its compressive one. It is very weak compared to its bending strength which is about a third of its compressive one. In view of this argument, there arises the necessity to reinforce the concrete. The demerit (β) causes problems in the load bearing ability and durability. It also causes the water leakage. The RC structures are generally said to be weak to the damage by the earthquake because of the demerit (γ). The demerits (α) and (β) are inferior to the megaliths as the building material. The demerit (γ) is the same one as the megaliths.

For the time being, in order to improve the demerit (α), concrete is reinforced by steel included in the interior of concrete structures. As we have claimed in Claim 2.1, we would like concrete materials to be alternatives for megaliths. In this context, the lifespan of RC materials, about 50 to 75 years is much shorter than the one of megaliths. For the solution to this problems, we pose the following problems.

Problem 2.1 (Concrete as alternatives for the megaliths).

For the lifespan of RC materials to be much longer, we have to solve either of the following problems.

- (i) *Develop a method to make solid, stubborn and stable concrete without reinforcement, by which we can literally make artificial megaliths.*
- (ii) *Develop a method to maintain RC structures in order that their lifespan can be much longer.*

The problem Problem 2.1 (i) is very important and challenging where we are try to make very cheap, easily shaped in any form, and easily transportable artificial megaliths, literally. Therefore, the solution of Problem 2.1 (i) yields that the concrete material would be much superior building materials to the megaliths. We claim that the solution to this problem would give a big breakthrough in the study and application of building materials, which is under investigation by the authors. Since Problem 2.1 (i) is very hard problem to solve, for the time being, it is much more likely that we solve Problem 2.1 (ii) and apply our solution to practice, where we admit the defects of RC materials and try to keep them staying safe as long as possible by application of suitable maintenance.

In view of the above argument about Problem 2.1, we pose the following problems.

Problem 2.2. *From the viewpoint of Problem 2.1, we pose the following two problems.*

- (1) *How to establish a determinate non-destructive inspection technique for RC structures*

- (2) *How to repair the RC structures in order that they would safely live for a very long time*

By Problem 2.2, we mean that it is very important to establish a good method to check RC structures without destructing them and to develop a nice method to maintain the RC structures in order that their lifespan would be very long, in order for RC materials to play a role as substitutes of megaliths. It is our main theme to study how to solve the problem (1) in Problem 2.2, for which we shall study how acoustic waves propagate in concrete materials in the next section, by which we pose our main problem (Problem 4.1) in the fourth section in order to give a solution to Problem 2.2 (1). Confer Section 5, for application of an answer to Problem 2.2 (1) to practice, for example, confer Problems 5.1, 5.3 and 5.4 below.

3 Propagation of the ultrasonic waves and the electromagnetic acoustic pulses

As we have mentioned at the end of the last section, we shall apply the properties of the sound as a tool of the non-destructive inspection for concrete structures. In this section, as a preparation for the next section, we study how the ultrasonic waves and the electromagnetic acoustic pulses propagate in the cement paste, the mortar and the concrete by the experiments. We first introduce our experiments to study the propagation the ultrasonic waves and the electromagnetic acoustic pulses propagate in the cement paste, the mortar and the concrete. By the examining the results of our experiments, we shall study the propagation of the ultrasonic waves and the electromagnetic acoustic pulses in concrete structures of the length about $1m$ or less.

Let us introduce the outline of our experiments.

Outline of our experiments

- Velocity of the sound;
 - Velocity of the ultrasonic wave is denoted by V_s (m/s).
 - Velocity of the electromagnetic acoustic pulse is denoted by V_e (m/s).
- Length of test pieces;
We prepared test pieces of the length 100, 200, 300, 400, 800 and 1200 mm in order to check
 - the decay of the acoustic velocity
 - the propagation of the sound
- Inclusions;
We prepared two types of test pieces.
 - Normal test pieces
 - Test pieces with styrofoam of the length 200 and 300 mm included in their inside

These test pieces are made use of to determine the propagation of the sound.

We first made the test pieces made of cement paste and mortar as shown in Table 1.

Table 1: Components of the test pieces

Table 1 : Mix Proportion of Cement Paste

	Water	Cement	Air	Total
Weight(kg)	553	1382	–	1935
Volume(ℓ)	553	437	10	1000

※W/C=40% , Air=1%

Table 2 : Mix Proportion of Cement Mortar

	Water	Cement	Sand	Air	Total
Weight(kg)	331	828	1035	–	2195
Volume(ℓ)	331	262	397	10	1000

※W/C=40% , S/C=1.25 , Air=1%

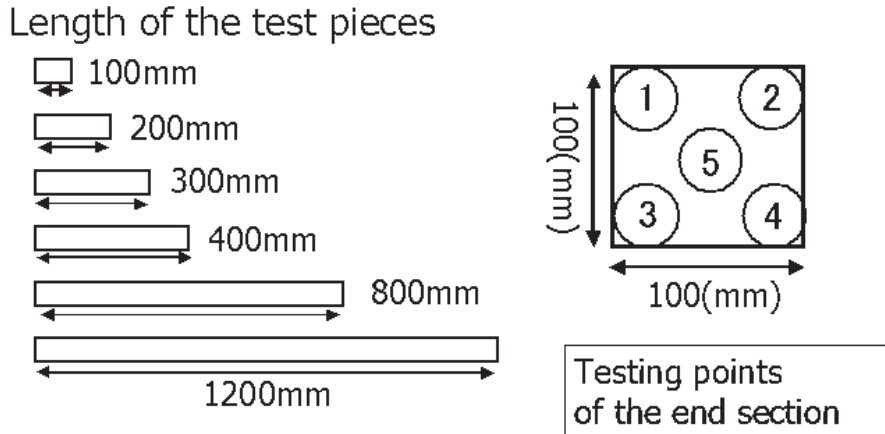


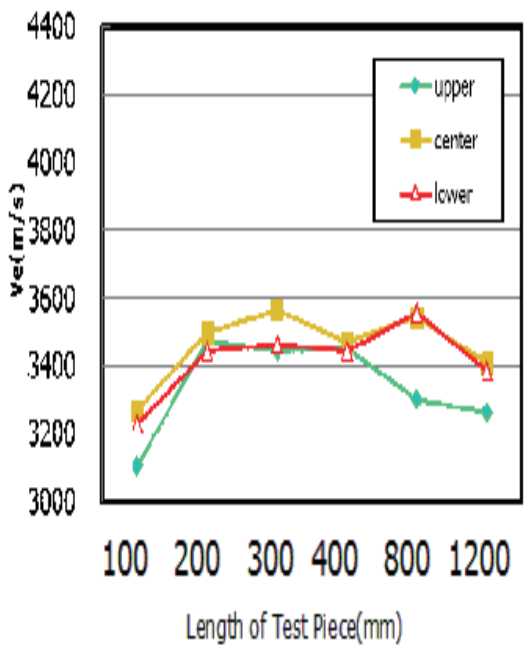
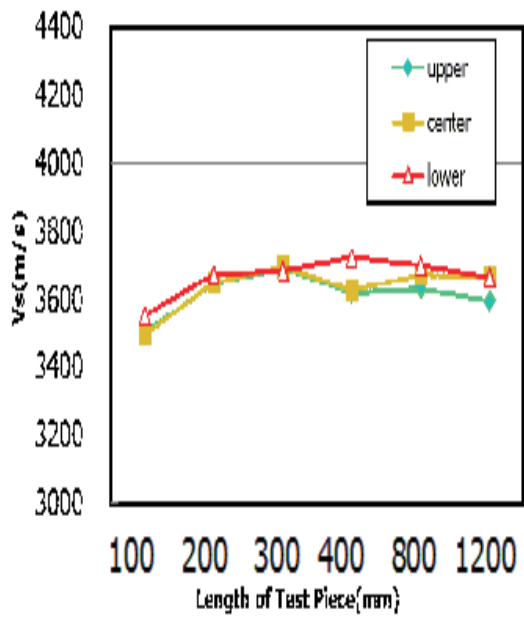
Figure 1: Length of the test pieces and inspection points

Experiment 1.

We first experimented on the normal test pieces. We projected the ultrasonic waves and the electromagnetic acoustic pulses from the inspection points numbered ①, \dots , ⑤ on one end square of the test pieces (see figure 1). We name them as ‘source points’. We received them at the same-numbered inspection points on the other end square. We name them as ‘observation points’. We have measured the time for the sound to travel between the source and the observation points. The results of these experiments are summed up in Figures 2 and 3, where we mean that the age of the test pieces is x weeks by the term ‘ xW ’.

Remark that the average of the results on the point ① and ② are treated as ‘upper points’, the average of the results on the point ③ and ④ are treated as ‘lower points’ and the point ⑤ is denoted by the center point.

Cement Paste (1W)



Cement Mortar (1W)

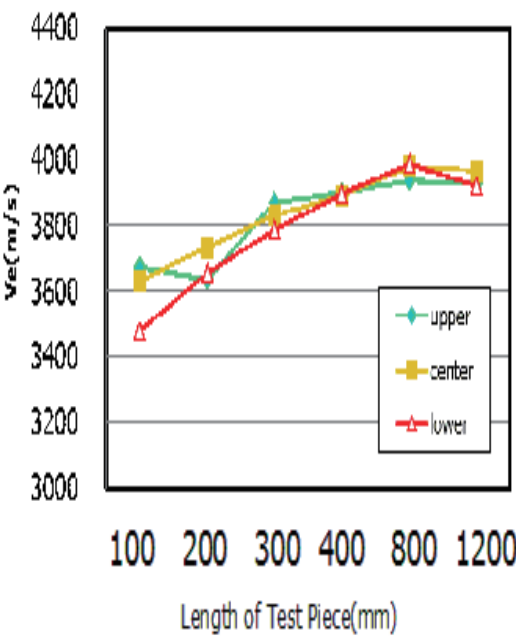
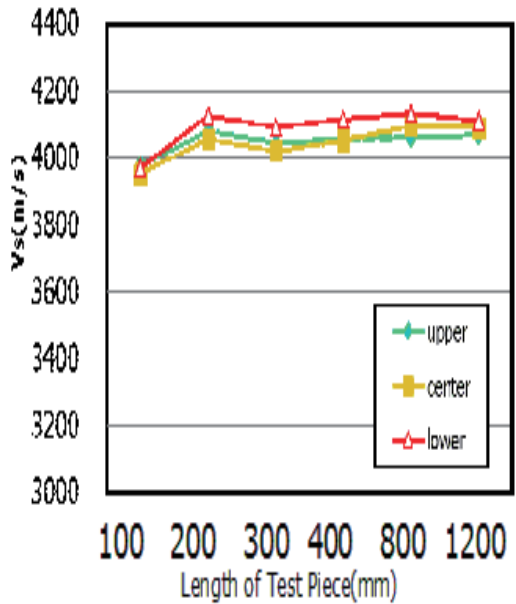
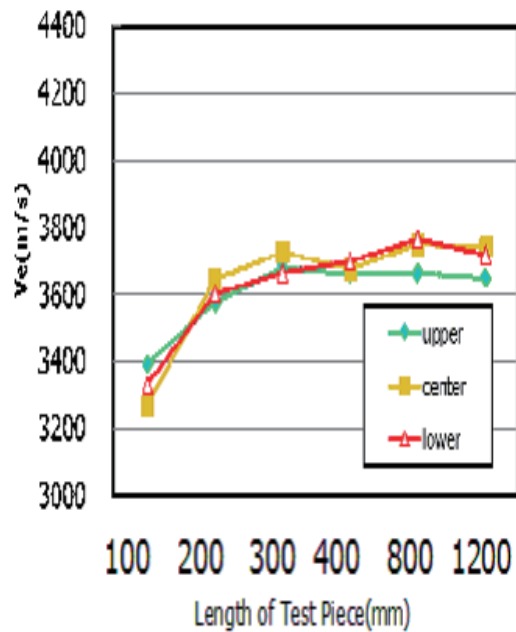
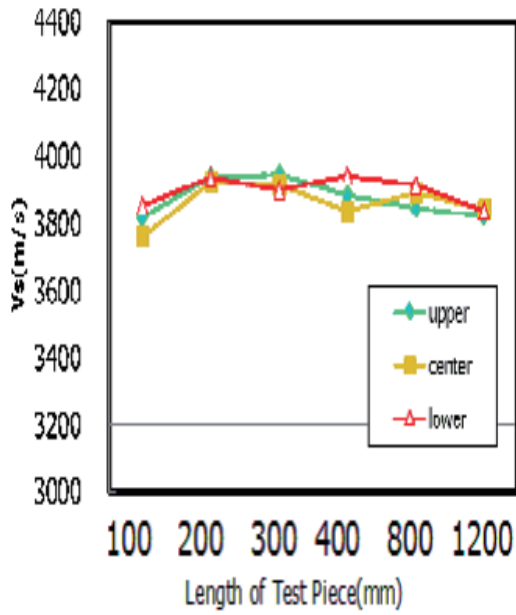


Figure 2: Normal test pieces (age of a week)

Cement Paste (4W)



Cement Mortar (4W)

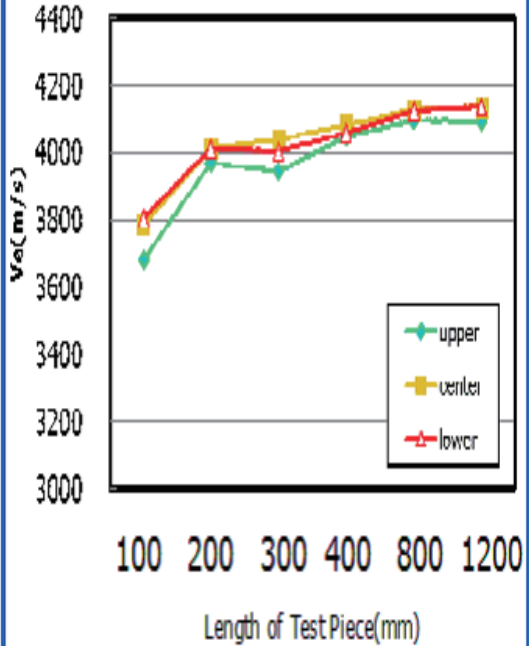
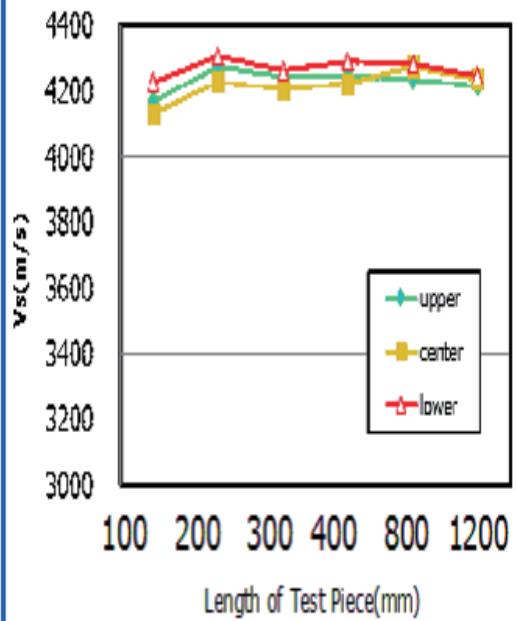


Figure 3: Normal test pieces (age of 4 weeks)

By reviewexamining the results by Experiment 1, we obtain the following properties.

Property 3.1.

- We have rediscovered the well known basic property of concrete; the more time goes by, the harder the test pieces are, which is caused by the reaction of hydration of concrete.
- We also have rediscovered the well known basic property, the gravity settling of cement, in terms of the acoustic velocity; the lower the inspection points are, the faster the acoustic velocity is, which is because of the fact that the lower the points are, the larger their density is, which is caused by the gravity settling of cement.
- We can conclude that for the test pieces of the length less than 1200mm, there is no decay of the acoustic velocity from the viewpoint of its first arriving time.

The last property is essentially important for our study.

Experiment 2.

We simultaneously made the test pieces of the length 400mm (100mm × 100mm × 400mm) with styrofoam of the length 200 and 300mm included in their inside (confer Figure 4). We performed the same experiments as Experiment 1, whose results are re-viewexamined in the following .

**Test pieces with styrofoam inside :
normal, styrofoam (200mm, 300mm)**

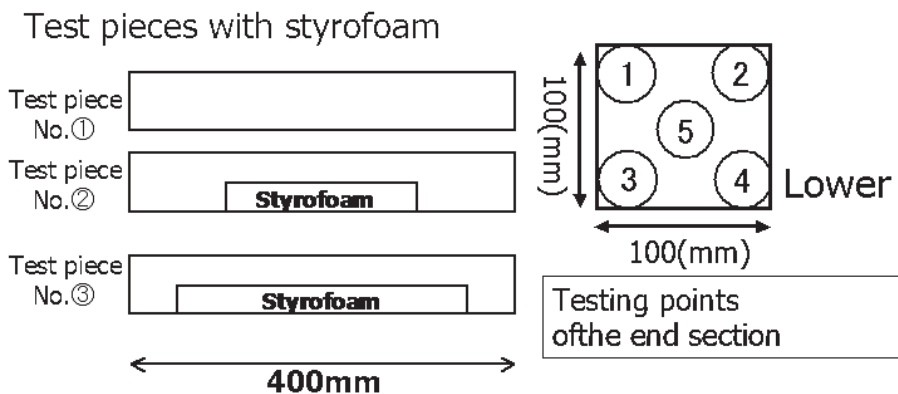


Figure 4: Test pieces with styrofoam

In Experiment 2, the (formal) velocity, which is calculated by

$$\frac{\text{length of the test piece (meters)}}{\text{arriving time (seconds)}}, \quad (3)$$

in the lower points is smaller than that of upper points, applying which we studied the propagation of the sound in the test pieces. We hypothesized that the propagation of the sound in the test pieces is as the following Hypothesis which is also shown in Figure 5.

Hypothesis 3.1. The first arrival wave of the ultrasonic one and the electromagnetic acoustic pulse takes the fastest route in the test pieces of the cement paste, the mortar and the concrete.

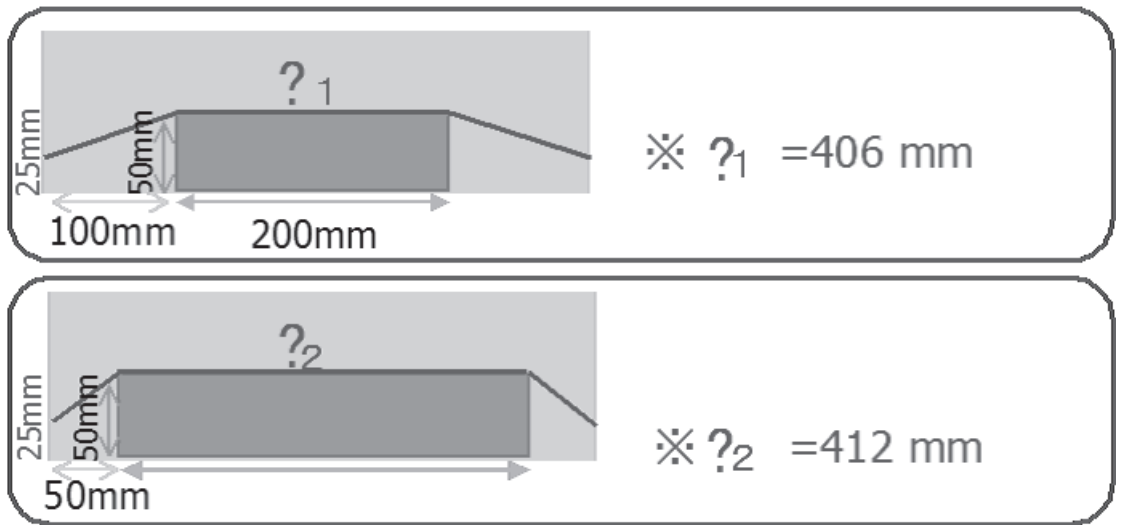


Figure 5: Propagation of the sound

Applying Hypothesis 3.1, we have modified the length of the orbit along which the sound propagates, that is, V'_s and V'_e are given by

$$\frac{0.00406 \text{ (meters)}}{\text{arriving time (seconds)}} \quad (4)$$

for the lower points in the test pieces with styrofoam of the length 200mm and by

$$\frac{0.00412 \text{ (meters)}}{\text{arriving time (seconds)}} \quad (5)$$

for the lower points in the test pieces with styrofoam of the length 300mm. Confer Figure 5 for the image of these modifications. The results of Experiment 2 with the modification of the velocities are summarized in Figures 6, 7 and 8.

Table 3 : Modified Data of Cement Paste

Test Piece	Testing Point	Vs(m/s)	Vs'(m/s)	Ve(m/s)	Ve'(m/s)
No-Styrofoam	Upper	3777	-	3506	-
	Center	3788	-	3626	-
	Lower	3808	-	3648	-
Styrofoam 200mm	Upper	3800	-	3508	-
	Center	3824	-	3663	-
	Lower	3701	3831	3540	3595
Styrofoam 300mm	Upper	3867	-	3664	-
	Center	3873	-	3695	-
	Lower	3731	3866	3496	3686

Table 4 : Modified Data of Cement Mortar

Test Piece	Testing Point	Vs(m/s)	Vs'(m/s)	Ve(m/s)	Ve'(m/s)
No-Styrofoam	Upper	4223	-	3952	-
	Center	4203	-	4022	-
	Lower	4229	-	4021	-
Styrofoam 200mm	Upper	4207	-	3968	-
	Center	4160	-	3999	-
	Lower	4079	4186	3918	4009
Styrofoam 300mm	Upper	4222	-	3983	-
	Center	4191	-	4034	-
	Lower	4035	4239	3893	4085

※Vs', Ve' : Modified Data

Figure 6: Tables of modification of the velocity

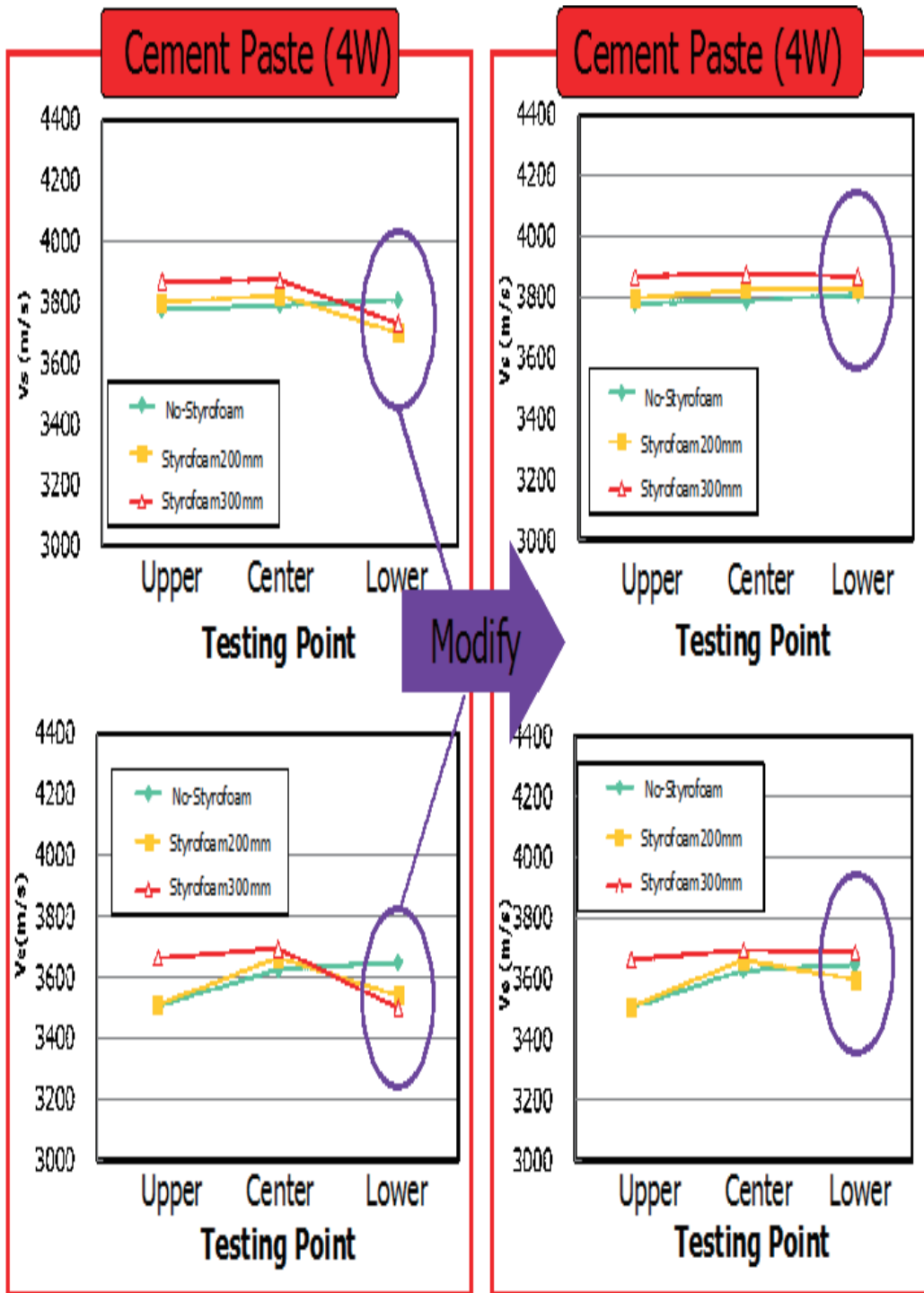


Figure 7: Test pieces of cement paste with styrofoam (age of 4 weeks)

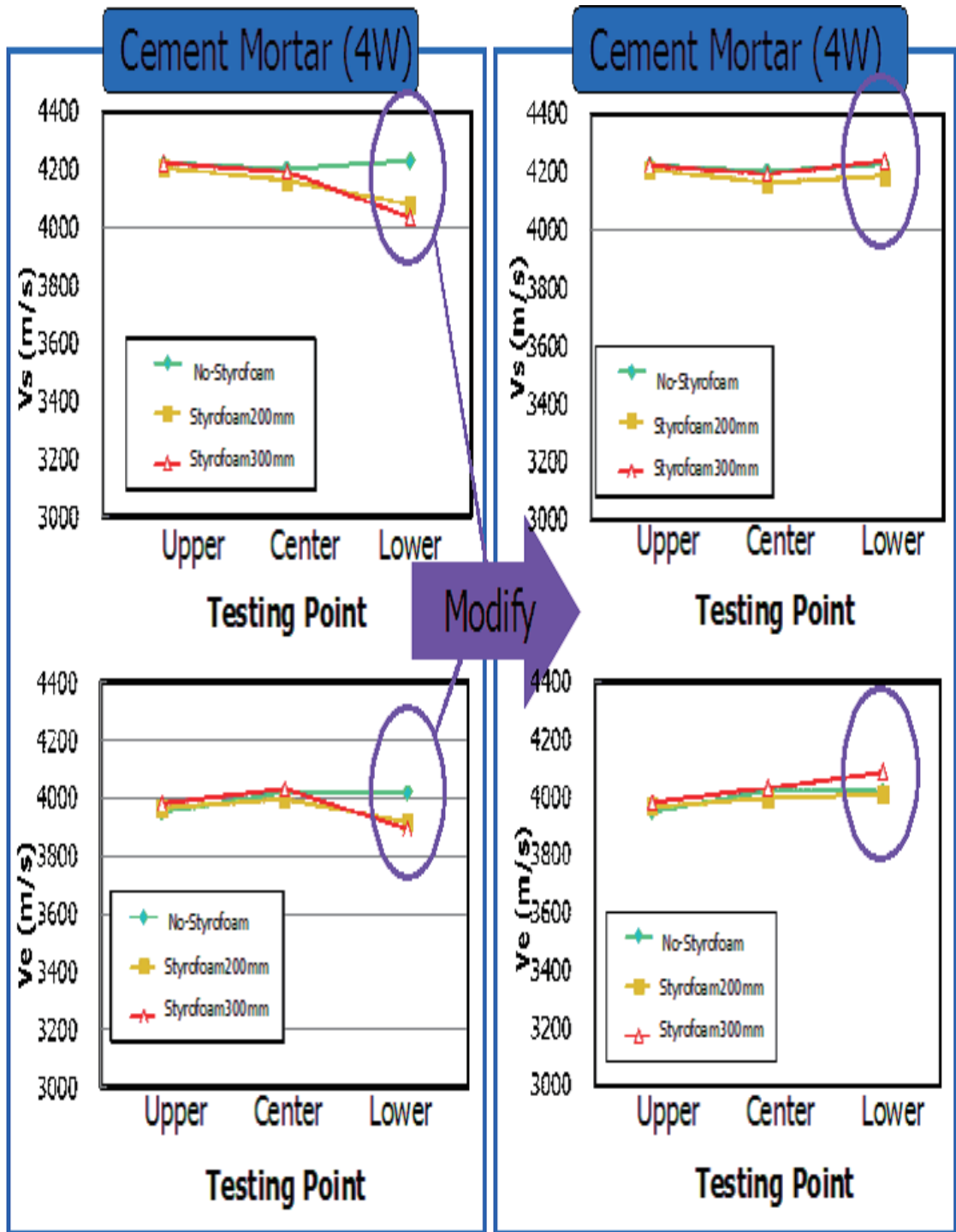


Figure 8: Test pieces of mortar with styrofoam (age of 4 weeks)

Let us summarize the conclusions of Experiments 1 and 2.

Conclusion 3.1 (Conclusion of Experiments 1 and 2).

- *The first arrival wave of the ultrasonic one and the electromagnetic acoustic pulse takes the fastest route in the test pieces of the cement paste, the mortar and the concrete.*
- *In the test pieces of the length less than 1200mm, there is no decay of the speed of the ultrasonic waves and the electromagnetic acoustic pulses with respect to the length of the test pieces.*

Remark 3.1. For the time being, there does not exist determinate non-destructive inspection method for concrete structures. It is our newer idea than the existing ones [2, 4] to focus on the first arrival time of the sound and pose a problem for the development of the acoustic CT, which may yield a determinate non-destructive inspection method. We shall discuss this problem in the next section.

The first conclusion in Conclusion 3.1 is so important for our main purpose that we summarized it as an important property.

Property 3.2. *The first arrival wave of the ultrasonic one and the electromagnetic acoustic pulse takes the fastest route in the test objects of the cement paste, the mortar and the concrete.*

Property 3.2 plays an important role to pose a problem for establishment of determinate non-destructive inspection method in the next section.

Remark 3.2. Having introduced the results of our experiments mainly on the data of ultrasonic waves, we have almost the same results on electromagnetic acoustic pulses, which shall be introduced in our forthcoming paper.

4 An inverse problem of the acoustic tomography

As was studied in the previous section, we know that the the first arrival wave of the ultrasonic one and the electromagnetic acoustic pulse takes the fastest route in the concrete structures of the length less than $1.2m$ and there is no decay in the velocity of the sound with the length of $1.2m$, which is what Conclusion 3.1 claims. In view these properties, we pose the following problem in order to establish a determinate non-destructive inspection method for concrete structures, which is the main purpose in this article.

Problem 4.1 (Problem for non-destructive inspection for concrete structure).

Let $\Omega \subset \mathbb{R}^3$ be a domain and $f(x)$, ($x \in \Omega$) be the propagation speed of the sound. For $\alpha, \beta \in \partial\Omega$, we denote by $\gamma_{\alpha, \beta}$ a route from α to β through Ω . Reconstruct $f(x)$ ($x \in \Omega$) out of the data

$$\min_{\gamma_{\alpha, \beta}} \int_{\gamma_{\alpha, \beta}} 1/f(x)d\gamma, \quad (6)$$

for $\forall \alpha, \beta \in \partial\Omega$.

By Problem 4.1 we mean the problem “Reconstruct the acoustic velocity $f(x)$ at the all points $x \in \Omega$ out of the data of the acoustic arrival time between the all pairs of the points on the boundary.” Study of Problem 4.1 is very important to establish a determinate non-destructing inspection method for concrete structures including RC ones, for which confer the examples in the next section. Let us give some remarks on Problem 4.1.

Remark 4.1 (Remarks on Problem 4.1).

- It is impossible to reconstruct the information of some points x 's where $f(x)$'s are very small. For example, we cannot reconstruct the acoustic velocity of the styrofoam if it is included near the center of the test piece since no acoustic wave would go through it because of Property 3.2. However, it does not matter very much, since what we focus on in Problem 5.3 is the part damage by salt where the density (accordingly the acoustic velocity) is relatively large.
- It is an interesting problem to determine the optimal subset of reconstructible by the acoustic CT established by the application of Problem 4.1.

Study of this problems would be applied for non-destructive investigation of concrete structures, as examples of which, we shall discuss the following problems in the next section.

- Non-destructive inspection for the damage by salt on the expressway bridges
- Non-destructive inspection for RC pillars

As we have discussed above, study of Problem 4.1 is very important in view of the maintenance of concrete structures, which would play an important role in redevelopment and prolonging life of infrastructures. It is also important in view of both pure and applied mathematics, especially in integral geometry. Let us mention how important the study of Problem 4.1 is in view of pure and applied mathematics.

Remark 4.2 (Importance of Problem 4.1 in mathematics).

- It is a very interesting problem to establish an reconstruction formula for Problem 4.1 in view of integral geometry.
- It is another interesting problem in Problem 4.1 to determine the subset of Ω where the reconstruction is impossible because it was no intersection with any γ giving (6). This problem is also interesting in view of integral geometry.
- In practice, we have to study various incomplete data problems of Problems 4.1 by the restriction arisen from various reasons, which is interesting in view of pure mathematics, especially in view of integral geometry, which is also very important in applied mathematics.

In the rest of this section, let us study some mathematical problems relating to Problem 4.1.

We first introduce that the unique solvability in Problem 4.1 would not hold in general.

Theorem 4.1. *In general, unique solvability of Problem 4.1 would not hold.*

Let us remember Experiment 2 in the third section. The ultrasonic waves would not go through the styrofoam. We obtain the exactly the same data if we replace the styrofoam in Experiment 2 by the cavity, which proves the non-unique solvability of Problem 4.1. By this argument, we can easily imagine that there are a number of examples of the non-unique solvability of Problem 4.1.

Next, let us study a simple problem. For simplicity, let us assume that there is a cavity of a disc whose center and radius are unknown in the two dimensional homogeneous object. The motivation to study this problem is as follows. Almost all standards of concrete materials are determined based on the mortar structure since it is the most important that how to make the mortar part in the construction of the concrete materials. The authors claim that we can take the mortar as a homogeneous material since the particles of the cement and the fine gravel are so small that together with the water and the air they make a homogeneous material from macro viewpoint. It can be very basic and important problem to study a cavity of a disc in the mortar, which yields the following problem.

Theorem 4.2. *Let us study the 2-dimensional case. Assume that a homogeneous rectangle contains a cavity of a disk in its interior. In this case, the cavity is reconstructed by appropriate three data of our acoustic tomography.*

In this theorem, by the term ‘‘appropriate three data’’ we mean the data which would determine the disc. For simplicity, we assume the acoustic velocity in the homogeneous rectangle is 1 and the cavity is of radius r and centered at (x_0, y_0) . In Figure 9 below, the length of the detour of the acoustic wave is given by

$$L_i = \left((X_i^1 - x_i^1)^2 + (Y_i^1 - y_i^1)^2 \right)^{\frac{1}{2}} + \left((X_i^2 - x_i^2)^2 + (Y_i^2 - y_i^2)^2 \right)^{\frac{1}{2}} + r\theta_i, \quad (7)$$

where $i = 1, 2, 3$, $j = 1, 2$, (x_i^j, y_i^j) are the points where we project the acoustic wave and (x_i^2, y_i^2) are the points where receive the acoustic wave ($x_i^1 = -R$, $x_i^2 = R$).

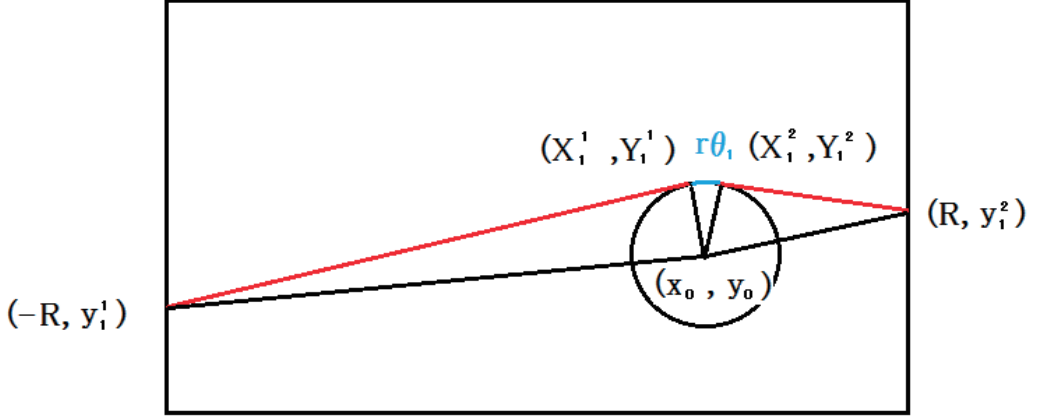


Figure 9: A cavity of a circle in the 2-dimensional molar structure

We can solve the system (7) of three equations to determine x_0 , y_0 and r , since we can determine X_i^j, Y_i^j by

$$\begin{cases} (X_i^j - x_0)^2 + (Y_i^j - y_0)^2 = (X_i^j - x_i^j)^2 + (Y_i^j - y_i^j)^2 + r^2 \\ (X_i^j - x_0)(X_i^j - x_i^j) + (Y_i^j - y_0)(Y_i^j - y_i^j) = 0. \end{cases} \quad (8)$$

and θ_i by

$$\theta_i = \cos^{-1} \frac{(X_i^1 - x_0)(X_i^2 - x_0) + (Y_i^1 - y_0)(Y_i^2 - y_0)}{\sqrt{(X_i^1 - x_0)^2 + (Y_i^1 - y_0)^2} \sqrt{(X_i^2 - x_0)^2 + (Y_i^2 - y_0)^2}}. \quad (9)$$

Note that there being quadratic equations in the systems (7) and (8), they have two solutions, however, by virtue of the condition that the detour is the shortest way we can determine the unique solution. We also note that θ_i in (9) must be acute.

It is very easy to extend Theorem 4.2 to the 3-dimensional case.

Theorem 4.3. *In the three dimensional case, a cavity of a ball in its interior of a homogeneous object is reconstructed by appropriate four data of our acoustic tomography.*

In this case, what we have to do is determine the four unknowns, the coordinate (x_0, y_0, z_0) of the center and the radius r . It is sufficient to have appropriate four data. The reconstruction algorithm is easily obtained by extending the algorithm for the 2-dimensional case.

5 Examples in practice

In this section, we shall introduce some examples where the study of Problem 4.1 is very important.

Let us first discuss a problem of the damage by salt on the expressway bridges. First, we consider the expressway bridges over the sea. By the wind or a tide, sea water blows up and pours on the expressway bridge. As a result, the salt soaks into the interior of the bridge. In the interior of an expressway bridge, there are a number of steel wires inbedded for reinforcement. The electric erosion induced by the soaked salt promotes the corrosion of the steel by oxidization very fast. In this process, the corrosion of the steel wires is much faster than the usual corrosion by oxidization induced by the neutralization of concrete, since oxidization induced by electric erosion cannot be helped by the alkalinity of the cement. It may happen before the concrete gets neutralized. This damage by the salt is one of the severest problems on the maintenance of the expressway bridges over the sea. It is also very severe to maintain the expressways in the cold season and areas, where they use much road surface antifreezing agent containing much chlorine compound ($CaCl_2$), where the mechanism of the steel wire to get corroded is exactly the same as the above argument. For the time being, people in the companies to maintain the expressways check the damage of the expressway damaged by salt by application of a destructive inspection. They first pull out some pieces of concrete from the brides. By checking whether they contain the salt or not, they determine the parts of the bridge damaged by salt. This is a typical example of the destructive inspection, which costs much time and labor. For development of the better inspection methods, we pose the following problem.

Problem 5.1. *Establish a good non-destructive inspection method for the expressways damaged by salt within the distance less than 40cm from each edge surface, which also works to cut off the inspection time and the labor costs for the inspection.*

There are many steel wires inbedded into the expressway bridges for their reinforcement. The closest steel wire to the boundary surface of the bridge locates about 40cm away from the boundary. That is why we pose Problem 5.1.

As an application of the study of Problem 4.1, we have Problem 5.1 in mind. In Problem 5.1, we have to detect detect the $2 \sim 3kg$ of salt included in the $1m^3$ of concrete in order to detect the damaged parts of the expressway bridges by salt, which yields the following problem.

Problem 5.2 (Another problem to solve Problem 5.3).

Is it possible to detect the $2 \sim 3kg$ of salt included in the $1m^3$ of concrete, by the acoustic tomography as an application of Problem 4.1?

By an experiment, we conclude that the answer to Problem 5.2 is positive. In Table 2, we summaries the result of our experiment. In this experiment, we have included salt in the concrete when cast it, in the rate of $3kg$ per $1m^3$. Therefore our experiment is different from the real damage of expressway bridges by salt. In the damage of expressway bridges by salt, the image of the damage is that the air of the concrete is replaced by salt, after the concrete itself gets completed or gets hard 4 weeks or more after it was cast.

In our experiment, we have obtained good data on the upper points where the acoustic velocity is faster in the test pieces with salt. The authors are afraid that the gravity

settlement of cement was prevented by salt, especially in the middle and lower points, in the test pieces with salt.

Anyway, the real damage of expressway bridges by salt, is caused by the phenomenon that the air in the concrete is replaced by salt, by which we mean the trend in the upper points in our experiment (Table 2) would be much clearer in the real damage of expressway bridges by salt. Therefore we conclude that the answer to Problem 5.2 is positive.

Table 2: Test pieces with and without salt

	Without salt		With salt	
age	4w	19w	4w	19w
	Velocity (m/s)			
upper	4331.8	4503.4	4488.0	4554.3
middle	4420.4	4549.0	4381.2	4582.1
lower	4487.8	4602.3	4419.3	4549.0

Now we are experimenting more practical experiments of the damage of expressway bridges by salt, whose result shall be presented and studied in our forthcoming paper.

Remark 5.1. Note that if we solve Problems 5.1 then we could cut off the the inspection time and the labor costs for the inspection as well as the damage to the bridge by the inspection. We also note that by application of the research of Problem 4.1, we can exactly determine the place damaged by salt in a non-destructive way, which is one of the reasons why the authors claim that the study of Problem 4.1 is very important.

For simplicity, assume that the bridge is a rectangular parallelepiped. Its damage by salt must be detected before the salt soaks into the interior of the bridges longer than $1m$ from each edge surface, otherwise the steel wire inside the bridge might get damaged by corrosion with chloridation.

Therefore, we pose our problem concretely in the following way.

Problem 5.3. *Establish a good non-destructive inspection method to determine the place damaged by salt inside the expressway within the distance less than 40cm from each edge surface.*

By virtue of the third property in Property 3.1, the study of Problem 4.1 is applicable to solve Problem 5.3.

We can solve Problem 5.3 by our acoustic CT.

Theorem 5.1. *We can establish a non-destructive inspection method to determine the place damaged by salt inside the expressway within the distance less than 40cm from each edge surface.*

If we project the acoustic wave from the point on the boundary, close to the wire, it would propagate in the image shown in Figure 10.

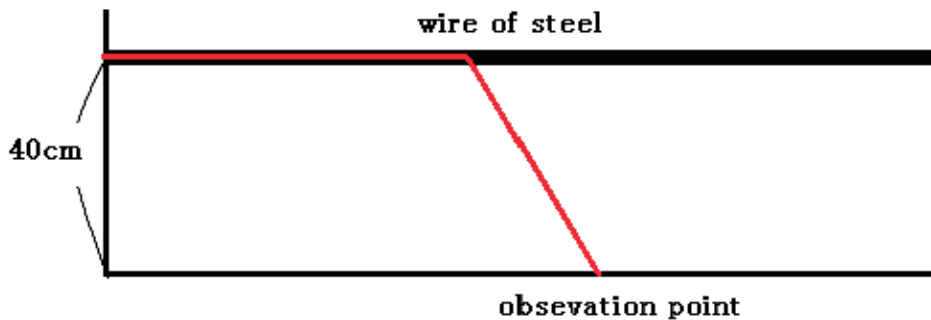


Figure 10: Propagation of ultrasonic waves in the bridge

Therefore we can detect the place damaged by salt as the place where the acoustic velocity is relatively large since the place of air is replaced by salt.

Remark 5.2. In Theorem 5.1, we do not have to determine the place damaged by salt very precisely. What is required is to give a rough sketch of the damaged place including the whole damaged area, by which they cut off the whole area supposed to be damaged and patch it with new mortar or concrete in order that the lifespan of the bridge would be longer.

As another application of the study of Problem 4.1, we take non-destructive inspection of RC structures, for which we have to study the propagation of the sound in the longer concrete structures.

Problem 5.4 (Another problem for non-destructive inspection of concrete structures).

- (i) *Establish a non-destructive inspection method to detect the corroded steel in RC buildings.*
- (ii) *Detest the cavity in RC pillars.*

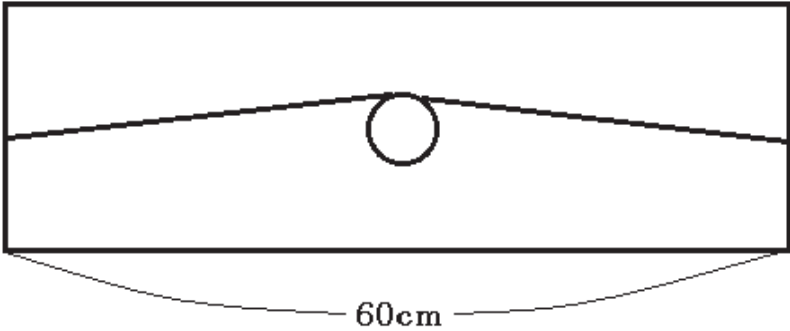
For the study Problem 5.4 (i), by application of the research of Problem 4.1, we know not only whether the steel in the interior of the concrete structure is corroded or not, but also the exact place where the steel is corroded, which is much better and newer than the existing non-destructive inspection for concrete structures and may yield a good method how to fix or repair such corroded steel in the interior of RC structures. The study of this problem can be very helpful for non-destructive inspection for more general concrete structures, especially to detect the corroded steel in RC structures. The width of the wall and pillar in RC buildings being usually less than $1m$, the third property in Property 3.1 is very essential for the solution to Problem 5.4 by application of Problem 4.1. By application of the research of Problem 4.1, we know not only whether the steel in the interior of the concrete structure is corroded or not, but also the exact place where

the steel is corroded, which is much better and newer than the existing non-destructive inspection for concrete structures and may yield a good method how to fix or repair such corroded steel in the interior of RC structures.

In the casting RC structures, concrete sometimes does not pour well and there makes some cavities near the steel. The radius of the cavity being not so large, it would not damage the strength of the structure very much, it would be very serious if the radius of a cavity is very large. Having this argument in mind for studying Problem 5.4 (ii), let us note the following two important points.

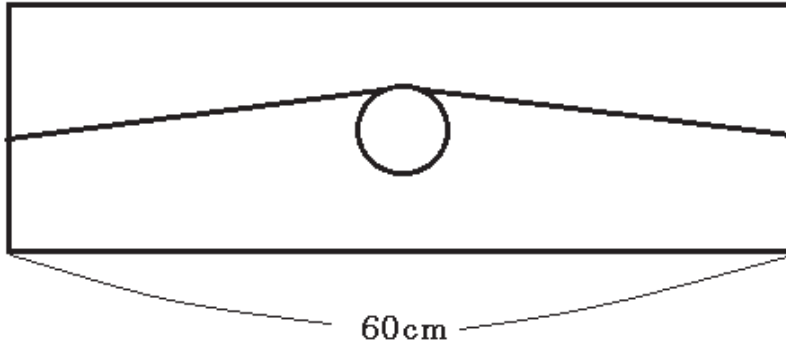
- The width of RC pillars is more than 50 centimeters.
- It is serious if the radius of the cavity is larger than 10 centimeters.

Let us consider the worst case to be reconstructed. Look at Figures 11 and 12 below.



The length of the detour (diversion) is about 60.30cm

Figure 11: A cavity of radius 6cm



The length of the detour is more than 60.84cm

Figure 12: A cavity of radius 10cm

In the case in Figure 11, the length of the detour is 100.5% of the route where there is no cavity in the interior, which cannot be detected by our acoustic CT since the gap of 0.5% is included in the errors in the Experiments shown in the third section.

On the other hand, in the case in Figure 12, the length of the detour is more than 101%. We can detect the gap more than 1% by our acoustic CT.

Therefore, we conclude the following.

Theorem 5.2. *We can detect the serious cavities in RC pillars by our acoustic CT.*

Remark 5.3. It is very important to develop the study of Problems 2.1, 2.2, 5.3, and 5.4, especially in view of redevelopment and prolonging life of infrastructures.

6 Conclusion

In this section, we summarize our conclusions in the article.

Conclusion 6.1 (Conclusion of this paper).

- (i) *For development of the acoustic CT, we studied how the first arrival wave propagates in the cement paste and the mortar.*
- (ii) *Applying the property of the first arriving wave, we have posed a problem (Problem 4.1) for the development of the acoustic CT.*
- (iii) *We have studied basic problems relating Problem 4.1 (Theorems 4.1, 4.2 and 4.3)*
- (iv) *The acoustic CT for concrete structure may be the first determinate non-destructive inspection method for concrete structures.*
- (v) *The problems posed in this study are interesting in view of the study of mathematics.*
- (vi) *We have proved that our acoustic CT can be theoretically allied to the non-destructive inspection for expressway bridges damaged by salt (Theorem 5.1) and RC pillars (Theorem 5.2), though no concrete reconstruction algorithm has been developed yet.*

We still have too many unsolved problems for the study of Problem 4.1 to be applied to both practice and mathematics, some of which have already been discussed throughout this paper.

At the end of this paper, we shall introduce some open problems left to be solved for our acoustic CT to develop further.

At the end of the fourth section, we discussed reconstruction of a ball (or a disc) in a homogeneous object, which can be a basic theory for reconstruction of general cavities.

Problem 6.1. *Approximate cavities in a homogeneous medium by a joint of balls (or discs) and approximately reconstruct the cavities by such a joint of balls (or discs) by application of Theorems 4.2 and 4.3.*

In the previous section, we posed three examples of non-destructive inspection of concrete structures;

- expressway bridges damaged by salt
- corroded steel in RC structures
- cavities in RC pillars

We have studied the first and the third problems but we gave no concrete result for the second problem, in view of which we pose the following.

Problem 6.2. *Give a concrete study of Problem 5.4 (i).*

Though we have some studies on the first and the third problems, they are a little far from being applied for practice, in view of which we pose the following problem.

Problem 6.3. *Give concrete reconstruction formulas for Problem 5.3 and Problem 5.4 (ii).*

Since our acoustic CT is a quite new study, there are many open problems in view of both theory and practice. We would like to solve them by collaboration between academia and industry and by interdisciplinary collaboration in order that our study would contribute to theoretical and applied mathematics, civil engineering, building materials and practical industry.

References

- [1] Dunham C. W. : *The theory and practice of reinforced concrete (third edition)*, McGraw-Hill, New York, (1953).
- [2] Jones R. and Facaoaru I. : *Materials and Structures*, Research and Testing, **2**, (1969) p. 275.
- [3] 國府勝郎, 辻幸和, 下山善秀: 『コンクリート工学 (I) 施工 (新訂第七版)』, 彰国社 (2010).
- [4] Motooka S. and Okujima M. : *Study on Detection of Buried Steel Bar in Concrete with Electromagnetic Impact Driving Method*, Proceedings of 2nd Symposium on Ultrasonics Electronics, (1981) pp.144-146.
- [5] Mita N. and Takiguchi T. : *Basic propertiers of concrete and its non destructive testing*, MI研究 **2**, “Collaboration between theory and practice in inverse problems”, (2015) pp. 117-137.

Noriyuki MITA
Faculty of Human Resources Development,
Polytechnic University of Japan,
2-32-1, OgawaNishimachi, Kodaira,
Tokyo, 187-0035, JAPAN
e-mail: mitanori@uitech.ac.jp

Takashi TAKIGUCHI
Department of Mathematics,
National Defense Academy of Japan,
1-10-20, Hashirimizu, Yokosuka,
Kanagawa, 239-8686, JAPAN
e-mail: takashi@nda.ac.jp

「マス・フォア・インダストリ研究」シリーズ刊行にあたり

本シリーズは、平成 23 年 4 月に設立された九州大学マス・フォア・インダストリ研究所 (IMI) が、平成 25 年 4 月に共同利用・共同研究拠点「産業数学の先進的・基礎的共同研究拠点」として、文部科学大臣より認定を受けたことにもない刊行するものである。本シリーズでは、主として、マス・フォア・インダストリに関する研究集会の会議録、共同研究の成果報告等を出版する。各巻はマス・フォア・インダストリの最新の研究成果に加え、その新たな視点からのサーベイ及びレビューなども収録し、マス・フォア・インダストリの展開に資するものとする。

平成 26 年 10 月
マス・フォア・インダストリ研究所
所長 福本康秀

Mathematical Backgrounds and Future Progress of Practical Inverse Problems

マス・フォア・インダストリ研究 No.5, IMI, 九州大学

ISSN 2188-286X

発行日 2016 年 3 月 1 日

編集 藤原宏志, 滝口孝志

発行 九州大学マス・フォア・インダストリ研究所

〒819-0395 福岡市西区元岡 744

九州大学数理・IMI 事務室

TEL 092-802-4402 FAX 092-802-4405

URL <http://www.imi.kyushu-u.ac.jp/>

印刷 社会福祉法人 福岡コロニー

〒811-0119 福岡県糟屋郡新宮町緑ヶ浜 1 丁目 11 番 1 号

TEL 092-962-0764 FAX 092-962-0768

シリーズ既刊

Issue	Author / Editor	Title	Published
マス・フォア・インダストリ 研究 No.1	穴田 啓見 安田 貴徳 Xavier Dahan 櫻井 幸一	Functional Encryption as a Social Infrastructure and Its Realization by Elliptic Curves and Lattices	26 February 2015
マス・フォア・インダストリ 研究 No.2	滝口 孝志 藤原 宏志	Collaboration Between Theory and Practice in Inverse Problems	12 March 2015
マス・フォア・インダストリ 研究 No.3	寛 三郎	非線形数理モデルの諸相：連続，離散，超離散， その先 (Various aspects of nonlinear mathematical models : continuous, discrete, ultra-discrete, and beyond)	24 March 2015
マス・フォア・インダストリ 研究 No.4	穴田 啓見 安田 貴徳 櫻井 幸一 寺西 勇	Next-generation Cryptography for Privacy Protection and Decentralized Control and Mathematical Structures to Support Techniques	29 January 2016



Institute of Mathematics for Industry
Kyushu University

九州大学マス・フォア・インダストリ研究所

〒819-0395 福岡市西区元岡744
URL <http://www.imi.kyushu-u.ac.jp/>